CARDIFF UNIVERSITY

SCHOOL OF BIOSCIENCES

DALE BOORMAN

MULTIMODAL COHERENT ANTI-STOKES RAMAN SCATTERING (CARS) MICROSCOPY FOR THE DETECTION OF ISOTOPE-LABELLED MOLECULES

A THESIS SUBMITTED TO CARDIFF UNIVERSITY FOR THE DEGREE OF DOCTOR OF PHILOSOPHY

OCTOBER 2019

ACKNOWLEDGEMENTS

The completion of this thesis would not have been possible without the continued support of those around me, both inside and outside of the lab.

I would like to thank Dr Pete Watson for all of the professional and personal support which he has provided throughout this journey, for the many hours that he has sacrificed to proof-reading reports, discussing results, planning experiments and the like, and, overall, for making the last four years an incredible experience for which I will always be grateful.

I would also like to thank Prof. Paola Borri and Prof. Wolfgang Langbein for granting me use of their CARS system throughout this project, as well as providing me with the accompanying physics knowledge (at a level suitable for a biologist!). I would like to thank Dr Iestyn Pope for being the fountain of knowledge for all things hardware-based and for always being willing to answer my questions, regardless of the number of times they had already been asked. I would like to thank Dr Francesco Masia for providing the ingenious HIA software that has been utilised throughout this project.

I would also like to thank Dr Steve Hood for dealing with all GSK-related affairs, and for providing me with the opportunity to conduct research at both GSK and at the University of Illinois Urbana-Champaign. On that note, I would also like to thank Dr Aneesh Alex, Dr Chi Zhang and Prof Stephen Boppart, along with everybody else in the Boppart Lab at the Beckman Institute, for their hospitality during my UIUC visit.

Thanks also to all members of the Watson, Borri and Dale Labs for making office E3.12 an extremely pleasant and often entertaining environment in which to work.

It goes without saying that my biggest thank you of all goes to my friends and family whose incredible support stretches beyond the last four years. I would like to say a special thank you to my partner, Grace, whose understanding and patience over the last few months had been exceptional – I promise we can have our evenings and weekends back now!

TABLE OF CONTENTS

ABSTRACT

Coherent anti-Stokes Raman scattering (CARS) microscopy utilises intrinsic vibrational resonances of molecules to drive inelastic scattering of light. This eradicates the need for exogenous fluorescent labelling, which can be perturbative to the study of many small molecules, whilst providing high-resolution three-dimensional images with chemical specificity. Isotopic substitution of hydrogen atoms with deuterium presents a labelling strategy that introduces minimal change to molecular structure but can achieve chemical contrast when coupled with CARS microscopy. This is due to an induced down-shift of the CH_2 peak into the cell-silent region of the Raman spectrum which does not contain contributions from other chemical species, thus giving contrast against other cellular components.

A novel data analysis methodology, named Factorisation into Susceptibilities and Concentrations of Chemical Components (FSC^3), has been developed for application with hyperspectral CARS data to generate concentration maps of chemical components. Within this thesis, the ability of FSC^3 to observe a range of exogenously applied deuterium-labelled molecules within a cell has been assessed. Hyperspectral CARS datasets were initially acquired from lipid droplets of HeLa cells incubated with deuterium-labelled fatty acids, and FSC^3 analysis was applied to identify and spatially resolve a chemical component corresponding to carbon-deuterium bond vibrations. Identification of a deuterium-associated component enabled quantitative study of the uptake, storage and turnover of deuterated fatty acids within cytosolic lipid droplets based on changes in the carbon-deuterium signal intensity. The ability of FSC^3 to visualise lipid droplets containing deuterated lipid was also utilised for non-invasive tracking of cells of interest within mixed populations. FSC^3 identification of non-lipid-based molecules was more challenging, with limited intracellular visualisation of deuterium-labelled biomolecules and small molecule compounds achieved. However, some evidence suggested detection of the compound, D7-HCMVi, within cells.

The imaging capabilities of the custom-built multimodal CARS microscopy system at Cardiff University were also evaluated in the context of a similar system at the Beckman Institute, University of Illinois Urbana-Champaign and a commercially available system developed by Leica. The results of this indicated multimodal advantages of the Beckman system, accessibility advantages of the Leica system, but specifically for nonlinear imaging capabilities, the Cardiff system was the most technologically advanced.

LIST OF ABBREVIATIONS

2PE	Two-photon excitation
3PE	Three-photon excitation
AOM	Acousto-optic modulator
BE	Beam expander
BSA	Bovine serum albumin
C	Carbon
C≡C	Alkyne
C-D	Carbon-deuterium
C-N	Nitrile
CARS	Coherent anti-Stokes Raman scattering
CCD	Charge-coupled device
CH_3	Methyl
COMI	Centre for Optical Molecular Imaging
COX-1/-2	Cyclooxygenase-1/-2
CRS	Coherent Raman scattering
D	Deuterium
D3-TPMP	Methyl-D3-triphenylphosphonium
D4-/D6-SA	D4-/D6-Succinic acid
D4-Para	D4-paracetamol
D5-Trp	D5-L-tryptophan
D7-HCMVi	D7-human cytomegalovirus DNA synthesis inhibitor
D8-H_2Ri	D8-histamine$_2$-receptor antagonist
D9-COX2i	D9-COX-2 inhibitor
D11-LA	D11-linoleic acid

D14-LNA	D14-α-linolenic acid
D17-OA	D17-oleic acid
DAPI	4’, 6-diamidino-2-phenylindole
D-CARS	Dual-frequency differential CARS
DESI	Desorption electrospray ionisation
Dex-488	AlexaFluor488-labelled dextran
DIC	Differential interference contrast
DM	Dichroic mirror
EGFR	Epidermal growth factor receptor
EOM	Electro-optic modulator
ER	Endoplasmic reticulum
FAD	Flavin adenine dinucleotide
FBS	Foetal bovine serum
FITC	Fluorescein isothiocyanate
FLIM	Fluorescence lifetime imaging microscopy
FSC^3	Factorisation into susceptibilities and concentrations of chemical components
GFP	Green fluorescent protein
GORD	Gastro-oesophageal reflux disease
GVD	Group velocity dispersion
H	Hydrogen
HCMV	Human cytomegalovirus
HeLa	Human cervical carcinoma cell line
HIA	Hyperspectral Imaging Analysis
HPLC	High-performance liquid chromatography

IFD	Instantaneous frequency difference
IMS	Industrial methylated spirit
IR	Infrared
LA	Linoleic acid
LC-MS(/MS)	Liquid chromatography-(tandem) mass spectrometry
LNA	α-Linolenic acid
M	Mirror
MALDI	Matrix-assisted laser desorption/ionisation
MEM	Minimum essential medium
MS	Mass spectrometry
NA	Numerical aperture
NAD	Nicotinamide adenine dinucleotide
Nd:YVO4	Neodymium:Vanadate
NIR	Near infrared
NNMF	Non-negative matrix factorisation
NSAID	Non-steroidal anti-inflammatory drugs
OA	Oleic acid
OCT	Optical coherence tomography
OPO	Optical parametric oscillator
PBS	Phosphate buffered saline
PCKK	Phase-corrected Kramers-Kronig
PFA	Paraformaldehyde
PMT	Photomultiplier tube
R	Reflecting prism
RFP (DsRed)	Red fluorescent protein

ROS	Reactive oxygen species
SA	Succinic acid
SERS	Surface-enhanced Raman scattering
SHG	Second harmonic generation
SRG	Stimulated Raman gain
SRL	Stimulated Raman loss
SRS	Stimulated Raman scattering
SVD	Singular value decomposition
THG	Third harmonic generation
Ti:Sa	Titanium:Sapphire
ToF-SIMS	Time-of-flight secondary ion mass spectrometry
TPF	Two-photon fluorescence
TPMP	Methyltriphenylphosphonium
Trp	L-tryptophan
WD	Working distance

LIST OF FIGURES

Chapter 2

Chapter 3

Chapter 4

Chapter 5

Chapter 6

LIST OF TABLES

1. INTRODUCTION

1.1. Background and Motivation

Biological systems, such as cells, are chemically complex, comprising mixtures of many different molecules, and thus progression towards a holistic understanding of these systems relies on the ability to distinguish chemicals of interest from all others within the mutual environment. This requirement for specific chemical identification is evident regardless of whether the target molecules exist endogenously or if they are exogenously applied to the biological system. Consequently, numerous methodologies have been developed over the last century to generate contrast between a molecule of interest and the chemical environment in which it is located, providing valuable insights into cell function and dysfunction, and paving the way for investigation of molecular uptake, distribution and turnover. Within pharmacological research, the venture to achieve efficient and specific delivery of therapeutic agents is ongoing[1], with development of subcellular targeting strategies for a range of therapeutic agents[2–4], and ever-present concerns regarding the relationship between off-target accumulation and cellular toxicity[5]. Thus, the ability to distinguish and track molecules within cells is paramount if delivery strategies are to be evaluated and improved.

1.1.1. Fluorescence microscopy

Fluorescence microscopy remains the most widely used optical tool for imaging cellular components with high spatial resolution, with technologies such as super-resolution light microscopy achieving resolution in the submicrometre range[6–8]. However, most fluorescence-based imaging modalities are limited by a necessity for exogenous label incorporation to enable chemical specificity[9,10], the majority of which share a similar molecular weight with many small biological and chemical molecules, consequently affecting the biological activity, cellular localisation and dynamics of the parent small molecules[11–13]. Specifically, organic fluorophores have been shown to interfere with the binding kinetics of proteins with their associated receptors[14], whilst labelling artefacts and non-specific binding are common problems in the fluorescent study of lipids[15–17]. Furthermore, despite their high sensitivity, fluorescent markers permit the investigation of only the target structure, limiting the extent of information which may be obtained, and due to their broad emission spectra, such labels are poorly compatible with multiplex detection[18,19]. Fluorophores also generate reactive oxygen species (ROS) upon

excitation[20–22], which can induce photobleaching[23–25] and phototoxic cell damage[26–29] with prolonged excitation, leading to difficulties in observing samples over longer timescales[30,31]. Fluorescent proteins, such as green fluorescent protein (GFP) and red fluorescent protein (RFP/DsRed), have been shown to cause growth defects[32–35] and induce apoptosis[36,37] in cells, with the cytotoxicity of some fluorescent proteins having been proposed for specific cell-killing purposes, e.g. KillerRed[38,39]. Cell damage through immunogenicity induced by fluorescent proteins has also been observed within *in vivo* models[40]. Quantum dots present an alternative fluorescent labelling strategy, but these too have been shown to perturb cell function, owing to the release of heavy metals following their degradation[41–43]. Consequently, there is a necessity for development of label-free techniques which can be used to visualise biological and chemical samples without incorporation of a potentially problematic fluorescent label. An overview of existing microscopy techniques for cellular imaging is provided in Table 1.1 and each will be discussed in the following paragraphs.

Some molecules naturally fluoresce due to their chemical structure and thus lend themselves to visualisation by techniques which can exploit their autofluorescence, permitting effective imaging without the requirement for exogenous label incorporation. Fluorescence lifetime imaging microscopy (FLIM) is a fluorescence-based technique which does not rely on the intensity of fluorescence, but instead utilises the fluorescent lifetime of a fluorophore to achieve contrast[44]. The fluorescent decay of a fluorophore following illumination by a pulsed laser varies with the type of molecule, the conformation of the molecule, and the interaction between a molecule and its environment. The technique has been utilised extensively to observe nicotinamide adenine dinucleotide (NADH) within cells, due to the intrinsic fluorescence which it displays, permitting label-free imaging, and the different lifetimes it shows depending on whether it exists in a free or bound state[45]. FLIM can therefore provide information regarding the interaction between a molecule and its environment, offering an insight into ongoing cellular functions[46,47], and hence, for certain molecules which show intrinsic fluorescence, FLIM presents an effective label-free imaging method[47].

1.1.2. Linear optical techniques

Linear optical microscopy techniques, such as phase contrast and differential interference contrast (DIC) microscopy also offer label-free alternatives to conventional fluorescence microscopy which can provide images with high resolution. This is achieved by detecting variations in sample thickness and refractive index which alter the optical path length of the

incident light. Similarly, optical coherence tomography (OCT) utilises interference to extrapolate information about sample depth, permitting acquisition of three-dimensional image data at video-rate speed[48]. However, these linear techniques are limited by their inability to provide the chemical specificity possible with fluorescence-based imaging[49]. Detailed information about chemical composition of cell extracts can be obtained through application of various analytical methods, however these techniques fail to provide spatial information due to their invasive nature. Hence, the ideal imaging modality would combine high-resolution spatial imaging with the ability to accurately identify specific chemical groups in the absence of a bulky fluorescent marker.

Vibrational micro-spectroscopy techniques have emerged as an effective method to bridge the gap between spatial imaging and chemical profiling by exploiting the vibrational resonances of molecules within a specimen, which relate to the mass of the constitutive atoms and the strength of the chemical bonds between those atoms[50]. This will be discussed in detail in Chapter 2, where the physical theory which underlies this concept will be described. Spectra of vibrational resonances can be produced either by infrared(IR)-absorption[51] or through Raman scattering[52]. The non-invasive imaging potential of these techniques is extremely promising, providing an effective means of studying endogenous small biomolecules which are poorly compatible with fluorescence-based modalities. However, both techniques have disadvantages which limit their translation into a biological context. IR microscopy uses long wavelengths for excitation and consequently suffers from poor spatial resolution in comparison to the techniques described above, and water molecules show IR absorptions which overlap with bands of several other chemical components[53–56], limiting application for studying molecules within the aqueous environment within cells. Raman-based techniques overcome these problems by utilising shorter excitation wavelengths, however, spontaneous Raman scattering is instead limited by a small cross-sectional area and a weak response signal from biological materials. Consequently, high excitation energies and long integration times are necessary to achieve a sufficient signal-to-noise ratio, which is not always compatible with living systems[57]. The scattered Raman field is also detected within the Stokes region, which overlaps with fluorescence emissions from endogenous molecules and can obscure the signal of interest. It is possible to dramatically improve Raman sensitivity by adsorbing investigated molecules onto a metal nanostructured substrate, e.g. Au, Ag or Cu nanoparticles, to enhance the local field, as in surface enhanced Raman spectroscopy (SERS)[58]. The improved Raman scattering cross-section can be attributed primarily to electromagnetic field enhancement due to excitation of localised surface plasmon resonances of the underlying metallic substrate. Chemical enhancement also provides a smaller contribution to the improved Raman signal, where energetically favourable charge-transfer states are created between the adsorbed molecule and metallic substrate, providing a pathway for resonant

excitation and hence increasing the probability of a Raman transition. The resulting enhancement in Raman sensitivity can be as high as 10^{11}, permitting single molecule detection[58]. However, the necessity for a nanostructured substrate complicates sample preparation, and the applicability of the method is limited to thin regions near the substrate[49].

1.1.3. Nonlinear optical techniques

Multiphoton microscopy techniques, including second-harmonic generation (SHG) and third-harmonic generation (THG), have also been employed to image biological samples in a label-free manner. Unlike IR absorption and Raman scattering, SHG and THG are based on nonlinear optical effects. In SHG, light is emitted by a sample at half of its incident wavelength (twice its incident frequency), provided the sample does not show inversion symmetry. Much of the research which has utilised SHG has involved the study of collagen matrices, due to its favourable, non-centrosymmetric molecular organisation[59–62]. Similarly, in THG, excitation light is emitted by a sample at a third of its incident wavelength (triple its incident frequency), and signal is generated by discontinuities in refractive index, i.e. the change from lipid-rich vesicles to cell cytosol[63,64]. Due to their nonlinear nature, SHG and THG only give efficient responses at high incident energies, which are found at the focal centre, thus permitting three-dimensional spatial resolution without the need for a pinhole to reject the out-of-focus light, as is the case with confocal microscopy. Whilst these nonlinear multiphoton techniques generate strong image contrast, they utilise wavelengths well below the vibrational wavelength range, and thus do not provide chemical specificity[65].

Table 1.1 | Summary of advantages and disadvantages of cellular imaging techniques.

	Advantages	**Disadvantages**
Fluorescence	✓ High resolution ✓ Chemical specificity	× Label requirement – photobleaching; phototoxicity
FLIM	✓ Label-free ✓ High resolution	× Only effective for certain molecules × Requirement for a pulsed laser and a time-resolved detection system
Phase contrast; DIC	✓ Label-free ✓ High resolution ✓ Ease of acquisition ✓ Simple, cost-effective setup	× No chemical specificity
OCT	✓ Fast, 3D acquisition	× No chemical specificity
IR	✓ Label-free ✓ Chemical specificity	× Low resolution × Interference from water
Raman	✓ Label-free ✓ Chemical specificity	× Weak signal × Overlaps between signal and samples autofluorescence
SERS	✓ Label-free ✓ Chemical specificity ✓ Strong signal	× Requirement for nanostructured substrate × Limited to thin regions near to substrate
SHG	✓ Label-free	× No chemical specificity
THG	✓ Label-free	× No chemical specificity
CARS	✓ Label-free ✓ Chemical specificity	× Non-resonant background
SRS	✓ Label-free ✓ Chemical specificity ✓ Background-free	× Requirement for laser modulation × Specialised detection systems

1.1.4. Coherent Raman scattering techniques

Coherent Raman scattering (CRS) techniques have emerged as an effective method for addressing the sensitivity problems associated with spontaneous Raman scattering. By using two incident light fields to coherently drive molecular vibration of chemical bonds with a resonance which is equal to the frequency difference between the two light fields, specific chemical groups can be probed and spatially resolved, hence permitting chemical sensitivity[66]. As identical vibrating bonds in the focal volume are driven coherently, the corresponding Raman scattering fields constructively interfere, giving a marked enhancement in detectable anti-Stokes signal compared to spontaneous Raman scattering[67].

Coherent anti-Stokes Raman scattering (CARS) microscopy is a widely utilised branch of CRS technology which, despite having been first implemented over half a century ago[68] and used frequently in chemistry and material science applications over the following 30 years[69], was not employed as a microscopy technique in biological systems until 1999, when Zumbusch and colleagues applied the technique to observe live, unlabelled cells[70]. From this point onwards, CARS has emerged as a valuable analytical technique within biology and biomedicine, offering both intrinsic chemical specificity and three-dimensional sectioning capabilities due to an excitation that is limited to the focal volume[49]. Consequently, CARS has been employed for the label-free study of various biological molecules, including nucleic acids[71], proteins[72–75], water[76–78] and lipids[79–85] via excitation of phosphate, amide I, oxygen-hydrogen and carbon-hydrogen chemical groups, respectively. In addition to the visualisation of endogenous cellular material, CARS microscopy has also been applied within analysis of pharmaceuticals, including assessment of small molecule compound distribution within tablet formulations[86] and on carrier particles within adhesive mixtures for inhalation[87]. CARS has also been employed for observation of *in situ* release of small molecule compounds from polymeric films[88–90] and to image compound distribution in lipid dosage forms for oral administration[91,92]. However, evidence for the ability of CARS to visualise small molecule compounds within cells is still under investigation and will comprise a major component of this thesis.

Hyperspectral and multiplex CARS are progressions of the CARS technology which permit simultaneous excitation and probing of multiple vibrational resonances, expanding the volume of chemical information obtained and offering superior chemical specificity compared to single-frequency CARS[93]. This can be achieved either through acquisition of a series of spatially resolved images at different vibrational frequencies (hyperspectral CARS)[94], or through acquisition of full-range spectra at each spatial point (multiplex CARS)[93], with both techniques giving spectra for every pixel of the XY image. A major limitation of CARS microscopy is the

non-resonant background signal that is generated in addition to the resonant signal from targeted molecular bonds, which will be discussed in more detail in Chapter 2. Furthermore, both multiplex and hyperspectral CARS methodologies require relatively long imaging times for acquisition of full datasets. Dual-frequency differential CARS (D-CARS) is a method that has been developed to address these two difficulties which involves separating the incident light fields into two pairs, one of which is temporally delayed so that on- and off-target resonances are probed simultaneously. The intensity difference between the two resonances provides the D-CARS signal, which shows suppressed non-resonant background and requires a shorter acquisition time, more comparable to that of single-frequency CARS[79,95,96].

Stimulated Raman scattering (SRS) microscopy is a second CRS technique which has received increasing interest in recent years, owing to a number of advantages which it shows over CARS microscopy. SRS was first observed in 1962[97], although it has only recently been realised as an alternative Raman imaging platform[98]. Like CARS, SRS uses two incident light fields, pump and Stokes, which interact at the sample to drive vibration of all molecular bonds with a resonance frequency that matches the frequency difference between the incident fields, amplifying the Raman signal through stimulated excitation. However, instead of driving inelastic scattering of a probe field as in CARS, SRS generates its signal from an observed reduction in the intensity of the pump beam (stimulated Raman loss, SRL) and an observed increase in the intensity of the Stokes beam (stimulated Raman gain, SRG)[99]. Contrast can be achieved via modulation of one of the laser beams (typically the Stokes beam), using either an electro-optic modulator (EOM) or an acousto-optic modulator (AOM), and the change in the other beam (typically the pump beam) can be measured using radio-frequency lock-in detection, and an image can be formulated[99].

As previously described, CARS microscopy is limited by its associated non-resonant background, which can limit detection sensitivity and give CARS spectra with distorted line-shapes when compared to spontaneous Raman spectra, making interpretation of data challenging without spectral processing techniques. A non-resonant background is observed in CARS due to emission of the energy difference between pump and Stokes fields at the anti-Stokes frequency, which permits the occurrence of CARS processes even in the absence of resonant molecules[100]. In SRS, when the frequency difference between the incident fields does not match any vibrational resonance of molecular bonds, SRG and SRL cannot occur, and thus a non-resonant background is not observed, giving improved detection sensitivity in comparison to CARS microscopy, and spectra which appear similar to those acquired by spontaneous Raman[100]. Furthermore, SRS shows a linear concentration dependence, i.e. SRS signal is directly proportional to molecular concentration, which permits quantitative analysis of chemical components within the focal volume, whilst CARS shows a non-linear concentration dependence, which necessitates data

processing strategies if quantitative assessments are to be performed[99,101]. CARS does, however, benefit from a simpler configuration than SRS, as excitation lasers do not require modulation or specialised detectors, and sophisticated frequency-selective amplifiers, such as lock-in or tuned amplifiers, are not required[101], thus CARS is often favourable within multimodal imaging systems. Furthermore, CARS can theoretically achieve higher spatial resolution due to a higher-order nonlinear dependence on the excitation laser intensity[102]. CARS intensity shows a quadratic dependence on the pump field's intensity and a linear dependence on the Stokes field's intensity; hence signal is generated in a small focal volume, permitting three-dimensional sectioning with high spatial resolution[103] (see Section 2.2 of Chapter 2 for detailed description of CARS signal composition). Conversely, SRS intensity shows linear dependency on both pump and Stokes fields, and consequently, both generated intensity and achievable spatial resolution are not as high[101].

Multiplex and hyperspectral SRS have also been developed to enable high-speed image acquisition, whilst maintaining the fingerprinting capabilities of Raman spectroscopy. To achieve multiplex SRS imaging, Fu et al. utilised a broadband Ti:Sa fs laser to provide the pump beam, which was divided into wavelength bands, each corresponding to a different Raman shift, before combination with an electrically synchronised ps laser at 1064 nm and passage into a laser scanning microscope[104]. A Fourier-transform was then applied to extract each Raman band, thus enabling simultaneous probing and detection from multiple vibrational resonances[104]. Hyperspectral SRS data can be acquired in the same way as hyperspectral CARS data, through acquisition of XY images at a series of spectral positions, generating spectra for each spatial point, however these spectra do not require subsequent processing as the spectral line-shape and peak positioning are comparable to those observed by spontaneous Raman[101,105].

Despite the advantages which SRS microscopy shows over CARS microscopy, the application of data processing and analysis techniques to CARS data enables generation of images with spatial resolution and quantitative chemical specificity comparable to the most advanced SRS outputs. Acquired CARS spectra can be processed to retrieve spectra which are more comparable to those of spontaneous Raman and are linear in concentration of chemical components, thus overcoming the limitation of a distorted, non-trivial line-shape which is associated with CARS due to interference between vibrationally resonant and non-resonant terms[106,107]. Furthermore, data analysis algorithms have recently been developed to maximise the chemical information which can be obtained from hyperspectral CARS images, i.e. the number of different chemical groups which can be spatially resolved, providing quantitative maps of independently varying chemical components[73]. This analysis method has proved a useful tool in

the study of chemical changes associated with the different stages of the cell cycle[75], as well as the lipid composition of adipocytes[79,80], and will be utilised frequently within this project.

1.1.5. Raman-sensitive labelling

With the promise of non-invasive Raman-based imaging techniques as analytical tools now realised, interest is developing in expanding the scope of information which can be obtained even further. Whilst Raman-based imaging techniques can be effectively employed to identify specific chemical groups within a sample, the spectra of many chemical bonds overlap, thus making identification of a spectrum corresponding to a particular chemical component challenging. For example, an abundance of vibrational resonances exists within the "CH-stretch" region of the Raman spectrum (2600-3400 cm^{-1}) due to modes of methine (CH), methylene (CH_2), methyl (CH_3) and vinyl (=CH-) groups[108]. Consequently, the use of chemical isotopologues as Raman-sensitive probes has emerged to provide improved chemical contrast and expand the volume of chemical information that can be obtained from biological samples[98]. These vibrational probes are designed to shift the position of Raman peaks away from congested areas of the spectrum and into regions where prevalence of peaks is at a minimum or where they are absent altogether, whilst also minimizing the associated structural change from the endogenous forms of the chemicals of interest. As previously discussed, the incorporation of large fluorescent markers is unfavourable for observing small chemical and biological molecules, whose ability to traverse cell membranes and structures can be largely altered with label incorporation[11–14]. The minimal degree of structural change induced by Raman-sensitive probes makes them a useful tool for intracellular visualization of molecules within biomedical research and pharmacological assessment of compounds in the drug development pipeline.

A frequently utilised target of such labelling strategies is the silent region of the Raman spectrum (1800-2600 cm^{-1}), which is characterized by an absence of vibrational peaks corresponding to naturally occurring bioactive molecules. Bioorthogonal Raman-sensitive probes consist of chemical groups which give rise to sharp Raman peaks within the cell-silent region, including alkyne (C≡C), azide (N_3), nitrile (C≡N) and carbon-deuterium (C-D) groups[109]. Within this project, deuterium, the neutron-containing heavier isotope of hydrogen, is investigated and assessed as a potential Raman reporter for intracellular molecule visualization. Of all the bioorthogonal probes, deuterium presents the Raman-sensitive chemical moiety with the smallest associated structural change to parent small molecules and is thus the most biocompatible[110]. Although it has been shown that alkyl groups offer a potentially more effective alternative to

deuterium with a larger Raman cross-section[19], the induced structural change is larger than for isotope substitution (although still only minimal), with higher potential for altering chemical activity[111]. Thus, isotope substitution presents the most suitable Raman-sensitive reporter for observing small but abundant biomolecules that are easily perturbed by structural alteration[112].

The potential of deuterium and alkyne incorporation for investigation of endogenous molecules within biological systems has been shown across various studies, all of which are described in a concise overview by Zhao et al.[112]. Deuterium- and alkyne-modulation of endogenous biological molecules, including nucleic acids, amino acids, lipids and glucose, has enabled their intracellular visualisation by Raman-based imaging techniques, permitting study of their synthesis, uptake, storage, metabolism and turnover[112]. The use of alkyne incorporation as a labelling strategy has historically relied upon ligation of the alkyne-tagged molecule to a fluorescent dye and subsequent fluorescence imaging[113,114], but recently alkyne labelling has been coupled with Raman-based imaging techniques to enable non-invasive observation of endogenous biological molecules[111,115,116]. Alkyne-tagged analogues of thymidine, uridine, methionine and glucose permit observation of DNA synthesis, RNA synthesis, protein metabolism and glucose uptake, respectively[111,115,116], whilst similar analogues of cholesterol, choline and palmitic acid have enabled visualisation and study of lipid uptake, storage and metabolism[110,116,117].

As discussed, isotopic substitution of hydrogen with deuterium presents another Raman-sensitive labelling strategy, with deuterated isoforms of phenylalanine (D5-phenylalanine) and glucose (D7-glucose) permitting study of protein synthesis and glucose metabolism, respectively[118,119]. Deuterated analogues of 20 different amino acids have enabled development of a general platform for investigation of protein metabolism across a variety of biological systems[120–122]. Deuterium incorporation has also been utilised extensively for the study of intracellular lipids, in particular with the growing acceptance of the importance of cytosolic lipid droplet regulation in both lipid and protein homeostasis[123], with numerous deuterium-containing analogues of lipid molecules, including D6- and D38-cholesterol; D2- and D33-oleic acid; D8-arachidonic acid; and D31-palmitic acid, having been employed to investigate lipid uptake and storage[124–131].

In addition to the study of endogenous biological molecules, both of the aforementioned Raman-sensitive labelling approaches have also been employed to visualise exogenously applied small molecule compounds, owing to the minimal structural change associated with Raman probe incorporation. Useful information can be obtained from observing the subcellular localisation of a small molecule, such as whether intracellular target sites are reached, or whether the molecule accumulates within off-target cellular compartments, potentially giving rise to toxicity[5]. Erlotinib,

an FDA-approved cancer drug, naturally possesses an alkyne group in its chemical structure, which permits the use of spontaneous Raman imaging to observe its localisation at the cell membrane, where it has been shown to cluster with EGFR to induce receptor internalisation[98,132]. Deuterium-containing small molecules have been synthesised and imaged by both spontaneous Raman and CARS, however, despite a strong Raman signal observed within the cell-silent region for powder preparations, detection of each of the molecules within an aqueous solution lacked detection sensitivity against the solvent background[133], thus indicating the necessity for cells to take up and accumulate a deuterium-labelled molecule if sufficient signal above noise is to be achieved. Such localisation-based enhancement of Raman signal was observed for two tyrosine-kinase inhibitors, imatinib and nilotinib, whose 1000-fold accumulation within lysosomes enabled distinction from a mixed chemical background without necessity for incorporation of a Raman tag, instead relying on peak variations within the fingerprint region of the Raman spectrum (<1800 cm^{-1})[134].

One of the main driving forces behind development of Raman-sensitive reporters is the potential to maximise the volume of chemical information obtained, and consequently Raman probes are being developed for simultaneous incorporation within the same sample to permit multiplex imaging. This is made possible by the sharpness of the Raman peaks produced by the probes and the subtle variations in peak position within the cell-silent region, hence giving value to each of the bioorthogonal probes within its own right[110]. Recently, Hu et al. showed the possibility of controlling Raman peak position within the cell-silent region through manipulation of the chain length of alkyne labels, which was used in combination with fluorescent labels to generate a 15-channel image of living cells[135]. The engineered probes were also conjugated to organelle-targeting moieties, which were utilised to produce a 10-channel image, mapping subcellular structures in live cells[135].

1.1.6. Hypothesis

The work described in this thesis aims to assess the ability of an in-house-developed multimodal CARS microscopy system, combined with the novel data analysis algorithm, factorisation into susceptibilities and concentrations of chemical components (FSC^3), for intracellular observation of deuterium-labelled biological and chemical molecules which show limited compatibility with fluorescence imaging. The analytical potential of this image acquisition and analysis strategy is considered in the context of existing state-of-the-art non-invasive imaging technologies, both custom-built and commercially available. Overall, this thesis will provide

evidence which will prove or disprove that the use of hyperspectral CARS and FSC^3 data analysis permits the identification of deuterated molecules within mammalian cells.

1.2. Thesis Outline

This thesis will be organised with the following structure:

Chapter 2 will provide the theoretical background for existing Raman-based imaging technologies, beginning with a physical description of spontaneous Raman scattering, before progressing to explain the principles underlying CARS microscopy, as well as the experimental realisation of CARS employed within this project.

Chapter 3 will describe the sample preparation; the set-up of the in-house-developed multimodal CARS system at Cardiff, permitting spontaneous Raman and hyperspectral CARS acquisition; the subsequent data processing procedures; and the applied FSC^3 algorithm for quantitative data analysis.

Chapter 4 will provide an assessment of the ability of the FSC^3 data analysis algorithm to identify and spatially resolve an intracellular chemical component corresponding to a deuterium-labelled molecule, in this case deuterated lipids, from hyperspectral CARS datasets.

Chapter 5 will explore the potential for the combination of deuterium-labelling and FSC^3 analysis to serve as a transferable tool, utilised in this chapter for observation of lipid dynamics and non-invasive tracking of cell lines within a mixed population.

Chapter 6 will assess the ability of hyperspectral CARS combined with FSC^3 data analysis to distinguish a deuterium-labelled small molecule from a cellular background, thus facilitating investigation of molecular uptake, distribution, accumulation and turnover.

Chapter 7 will utilise a common set of samples to provide a systematic comparison of the possible data outputs from custom-built multimodal CARS systems at Cardiff University and the Beckman Institute in the University of Illinois Urbana-Champaign, which differ in their stage of system development, multimodal capabilities, and the availability of supporting data analysis techniques. Outputs from these systems will also be compared to those obtained from the commercially available Leica TCS SP8 CARS microscope, evaluating whether data generated by an off-the-shelf system can meet the demands of pharmaceutical companies, or whether collaboration with state-of-the-art research institutes provides the most effective way to employ nonlinear optical techniques within the small molecule compound development process.

Chapter 8 will collate and summarise the findings of this thesis, whilst providing an outlook for future development and application of the investigated technologies.

2. THEORETICAL BACKGROUND

2.1. The Raman Scattering Principle

Upon interaction with matter, light can either be absorbed by atoms and converted into internal excitation energy or scattered with an identical (elastic) or altered (inelastic) photon energy. The process of vibrational Raman scattering was first observed experimentally by C. V. Raman and K. S. Krishnan in 1928[136]. The phenomenon occurs when light inelastically collides with a vibrating molecule and is scattered with an altered frequency. The frequency difference between incident and scattered photons is equal to the vibrational energy gained or lost by the molecule, with a reduction in frequency of scattered light referred to as a Stokes shift and a gain in frequency referred to as an anti-Stokes shift[137] (Figure 2.1). The observed variations in photon energy, and consequently vibrational frequency, are determined by the type of chemical bonds present, thus permitting utilisation of vibrational Raman scattering as an analytical tool for assessing the chemical composition of a material.

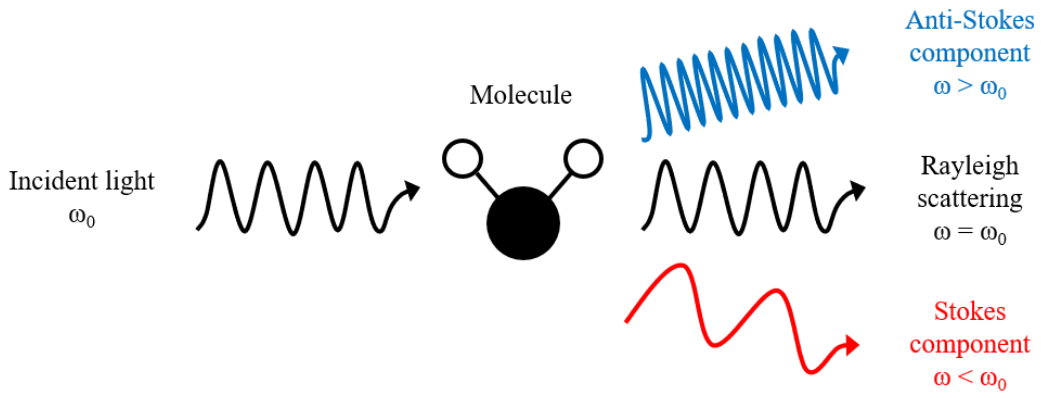

Figure 2.1 | Illustration of Raman scattering showing Stokes and anti-Stokes components following interaction of incident light with a molecule.

To explain this concept in its most basic terms, a diatomic molecule can be considered as two masses connected by a spring[138]. According to Hooke's Law, application of an external force will impart vibration to the system with a frequency defined by both the mass of the associated atoms and the spring constant. Hence, different molecules exhibit different vibrational frequencies due to variations in these two parameters. Molecules with more complex chemical structures display many different types of vibrations, referred to as vibrational modes. It is generally accepted that an N-atomic nonlinear molecule will have 3N - 6 vibrational modes, with

each mode characterized by a well-defined frequency, thus giving rise to vibrational spectra with many different bands which can provide the distinctive chemical signature of a molecule[67,139]. Within this thesis, two groups of vibrational normal modes are introduced: bending/deformation modes, where bond angle is altered but the bond lengths remain unaffected, and stretching modes, which involve a change in bond length but not bond angle (Figure 2.2). Each of the groups can be further categorised into more specific normal vibrations, including scissoring, rocking, twisting and wagging subdivisions of the bending/deformation motions, whilst the stretching motions can either be symmetric or asymmetric.

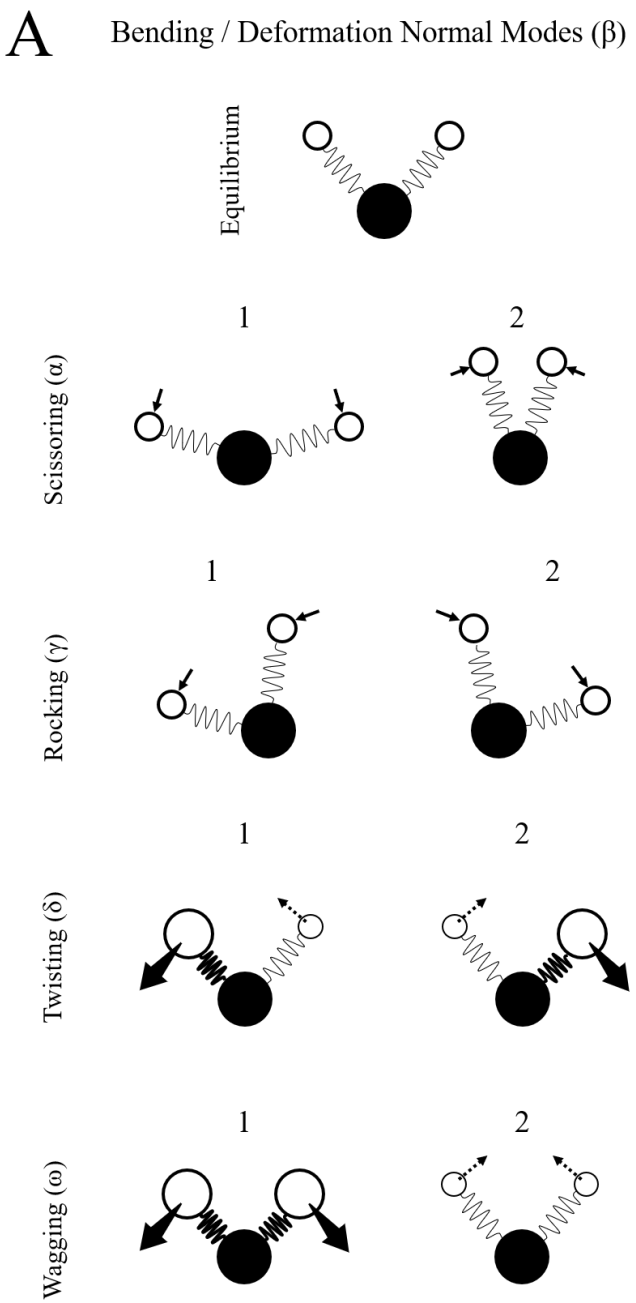

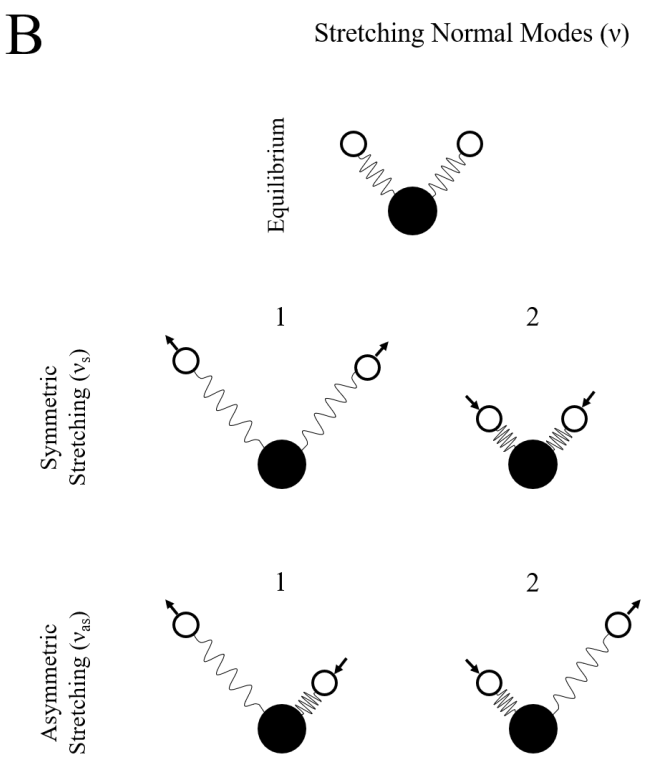

Figure 2.2 | Illustration of normal vibrational modes using the masses connected by springs representation of molecules. Molecules are shown at two different positions (1 and 2), illustrating displacement from the equilibrium position. In twisting and wagging modes, broader arrows indicate motion out of the page, whilst dashed arrows indicate motion into the page.

In a classical description, a molecule is composed of two or more atoms which are covalently bound to each other and surrounded by an inter-nuclei electron cloud[140,141]. When molecules interact with light, the electric component of the incident light displaces the electrons from their equilibrium position and causes them to oscillate with the same frequency as the "driving" light field. This introduces a dipole moment, *p(t)*, within the molecule, given by:

$$p(t) = \alpha(t)\, E(t) \tag{2.1}$$

where $\alpha(t)$ is the electric polarisability and $E(t)$ is the electric field amplitude. As a result, the molecule becomes polarised, with positive charges moving in the direction of the electric field and negative charges moving in the opposite direction, and the extent by which the electrons are displaced will depend on how strongly the electrons are bound to the positive nuclei and the strength of the electric field. The macroscopic polarisation, *P*, is obtained by considering the combined contribution of all *N* electric dipoles per unit volume:

$$P(t) = N\, p(t) \tag{2.2}$$

If the incident electric field is weaker than the field binding the electrons to the nuclei of the atoms, the displacement is directly proportional to the electric field strength, and the polarisation, *P*, can be rewritten as:

$$P(t) = \varepsilon_0\, \chi\, E(t) \tag{2.3}$$

where ε_0 is the electric permittivity in a vacuum and χ is the susceptibility of the material, a parameter describing the ease with which a dielectric material can become polarised in the presence of an applied field. However, as the incident field becomes stronger, and electrons are displaced further from their equilibrium, the linear relation expressed by Equation 2.3 becomes invalid and the polarisation, *P(t)*, can instead be expressed as a power series in the electric field, *E(t)*:

$$P(t) = \varepsilon_0 \left[\chi^{(1)}\, E(t) + \chi^{(2)}\, E^2(t) + \chi^{(3)}\, E^3(t) + \cdots\right] \tag{2.4}$$

$$= P^{(1)}(t) + P^{(2)}(t) + P^{(3)}(t) + \cdots \tag{2.5}$$

where $\chi^{(n)}$ is the *n*-th order susceptibility and $P^{(n)}$ is the *n*-th order contribution to the polarisation[140]. Thus, the displacement of the electron is no longer linearly dependent on the field strength.

Raman micro-spectroscopy provides a valuable analytical tool, generating spectra of frequency-shifted peaks from different vibrational modes of molecules without a requirement for detection markers. However, as discussed in Chapter 1, the technique suffers from an extremely small cross-section, typically 10^{-29} cm^2 per vibrational mode, which is approximately 14 orders-of-magnitude smaller than typical absorption cross-sections for electronic transitions (organic fluorophores)[67]. Therefore, Raman micro-spectroscopy demands high excitation powers (~ 100 mW at sample, ~ 5-fold higher than CARS, see Section 3.7.1 in Chapter 3) and long integration times (in excess of 30 mins per image) to achieve a sufficient signal-to-noise ratio[142], neither of which are compatible with data acquisition from live cell samples. Coherent Raman scattering (CRS) techniques offer a solution to the limitations associated with spontaneous Raman scattering by exploiting a coherent enhancement effect resulting from driven oscillations of modes. One branch of CRS technology is coherent anti-Stokes Raman scattering (CARS), which is described in the following section.

2.2. Coherent anti-Stokes Raman scattering

Coherent anti-Stokes Raman scattering (CARS) is a third-order nonlinear process in which two laser fields, referred to as pump and Stokes beams, with frequencies, ω_P and ω_S, respectively, are combined to give a beating field which coherently drives molecular vibration at a resonance equal to the frequency difference between the two fields, given by:

$$\omega_{vib} = \omega_P - \omega_S \tag{2.6}$$

Oscillating molecules are probed via a third beam, referred to as the probe beam with frequency, ω_{PB}, which is inelastically scattered by the driven molecular vibration, undergoing an anti-Stokes shift in frequency:

$$\omega_{AS} = \omega_{PB} + \omega_{vib} \tag{2.7}$$

Experimentally, the probe beam is often derived from the pump beam, hence giving:

$$\omega_{AS} = 2\omega_P - \omega_S \tag{2.8}$$

The resulting blue-shifted anti-Stokes signal can be easily filtered from the excitation wavelengths, as well as any sample autofluorescence[49]. Importantly, the frequency of the beating pump/Stokes field ($\omega_P - \omega_S$) coherently drives all identical vibrations within the focal volume, hence the generated anti-Stokes Raman fields constructively interfere, giving a coherent superposition of all the vibrating bonds. The resulting anti-Stokes (CARS) intensity, I_{AS}, can be expressed in terms of the aforementioned induced polarisation, P, in the material, and as CARS is a four-wave mixing process, with two pump fields, one Stokes field and one anti-Stokes field, I_{AS} is proportional to the module squared of the third-order polarisation, $P^{(3)}$[143]:

$$I_{AS} \propto \left|P^{(3)}\right|^2 \tag{2.9}$$

which has a magnitude determined by the strength of the pump (E_P) and Stokes (E_S) fields, as well as the third-order susceptibility, $\chi^{(3)}$, and therefore, from equation 2.3, this gives:

$$P^{(3)} \propto \chi^{(3)} E_P^2 E_S^*. \tag{2.10}$$

$\chi^{(3)}$ quantifies the efficiency of the nonlinear four-wave mixing processes, considering all possible third-order resonant processes, both vibrational and electronic[66], and it can be generally expressed by[144,145]:

$$\chi^{(3)} = \frac{A_R}{\Omega - (\omega_P - \omega_S) - i\Gamma_R} + \chi_{NR}^{(3)} + \frac{A_t}{\omega_t - 2\omega_P - i\Gamma_t} \tag{2.11}$$

where A_R and A_t are constants representing the Raman scattering and two-photon absorption cross-sections, respectively; Γ_R and Γ_t are the half-width at half-maximum of the Raman line and the two-photon electronic transition, respectively; Ω is the vibrational frequency; $\chi_{NR}^{(3)}$ is the non-resonant susceptibility; and ω_t is the frequency of the electronic transition. The first term is the contribution from vibrationally resonant states, the second term is the non-resonant contribution (non-resonant background), which is independent of the Raman shift, and the third term is the enhanced non-resonant contribution due to two-photon electronic resonance. Each of these terms is illustrated in the form of an energy level diagram in Figure 2.3.

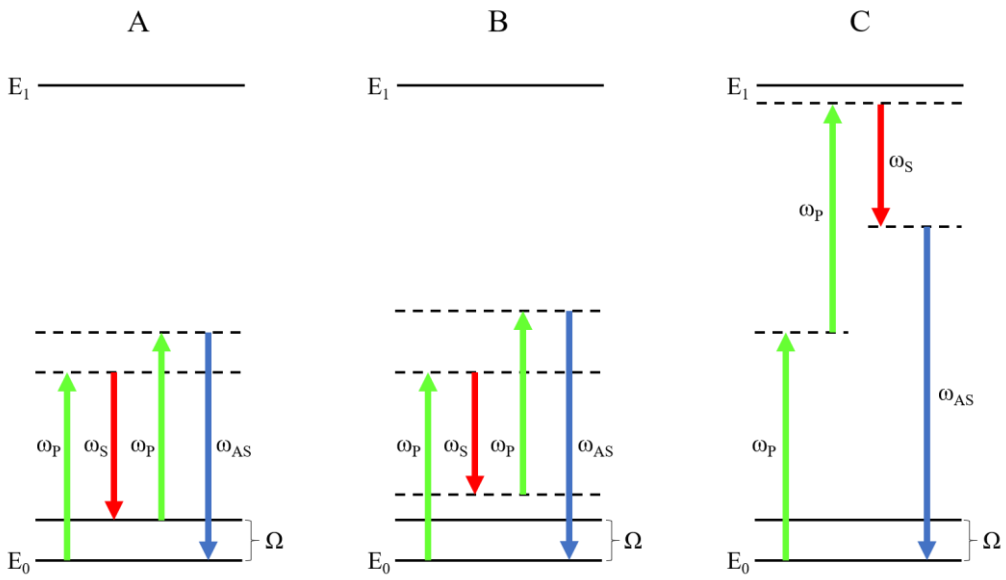

Figure 2.3 | Energy level diagrams illustrating all possible third-order processes in CARS: (A) resonant contribution; (B) non-resonant contribution; and (C) two-photon enhanced electronic non-resonant contribution associated with an excited electronic state. E_0 and E_1 indicate electronic levels, dashed lines indicate virtual energy states, Ω is the frequency difference between vibrational modes, and ω_P, ω_S and ω_{AS} are frequencies of pump, Stokes and anti-Stokes fields, respectively.

By solving the wave equation, assuming plane pump and Stokes waves, the anti-Stokes signal intensity, I_{AS}, can be obtained as follows[142]:

$$I_{AS} \propto \left|\chi^{(3)}\right|^2 I_P^2 I_S \left(\frac{\sin\left(\frac{\Delta k z}{2}\right)}{\frac{\Delta k}{2}} \right)^2 \tag{2.12}$$

where z is sample thickness; I_P and I_S are the pump and Stokes intensities, respectively; and $\Delta k = k_{AS} - (2k_P - k_S)$ is the wavevector mismatch (see Section 2.3.1 below). Within the above equation, it can be observed that although $\chi^{(3)}$ is linearly dependent on the number of vibrating bonds, the anti-Stokes intensity scales as $|\chi^{(3)}|^2$, giving CARS its improved signal strength compared to that of Raman scattering when a large number of identically vibrating bonds are probed. Equation 2.12 can be rewritten in terms of both resonant and non-resonant parts of $\chi^{(3)}$, giving:

$$I_{AS}(\Delta) \propto \left|\chi_{NR}^{(3)}\right|^2 + \left|\chi_R^{(3)}(\Delta)\right|^2 + 2\chi_{NR}^{(3)} Re\, \chi_R^{(3)}(\Delta) \tag{2.13}$$

where $\Delta = \omega P - \omega S - \Omega$ is the detuning (Raman shift); and $Re\, \chi_R^{(3)}$ is the real part of $\chi_R^{(3)}$. The first term describes the constant contribution from non-resonant background which is independent of Raman shift, the second term describes the resonant vibrating modes, and the third term is a mixing term between the resonant and non-resonant contributions and contains the real part of the vibrational response[145]. Each of these terms can be illustrated as spectral responses, as shown in Figure 2.4, and their respective contributions to the generated anti-Stokes signal can be visualised. The dispersive shape of the third term causes the maximum of the CARS spectral peak to be slightly red-shifted (towards lower frequencies) and creates a negative dip at the blue (higher frequency) side of the peak[142], which, when combined with the presence of non-resonant background, makes interpretation of CARS data non-trivial and challenging. It is possible to extract $\chi^{(3)}$ through interferometry to give spectra that are more comparable to those obtained by spontaneous Raman techniques[146,147], although this brings further complications to CARS imaging systems[142].

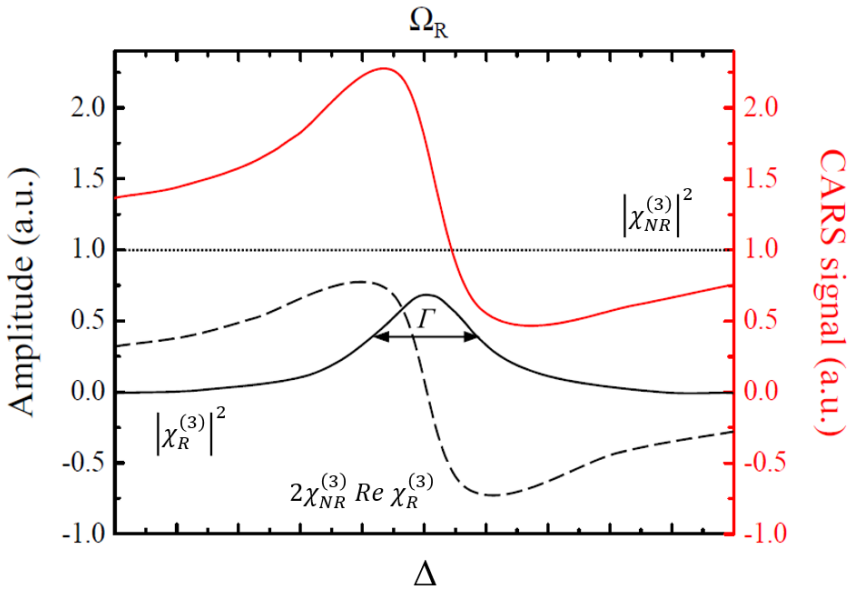

Figure 2.4 | Components of the CARS signal (reprinted from C. Di Napoli PhD thesis[148], adapted from ref[142]). The resonant term, $\left|\chi_R^{(3)}\right|^2$ (*black solid line*), the non-resonant term, $\left|\chi_{NR}^{(3)}\right|^2$ (*black dotted line*), and the mixed term, $2\chi_{NR}^{(3)}\ Re\ \chi_R^{(3)}$ (*black dashed line*) are plotted as a function of detuning, Δ. The non-resonant term shows a constant amplitude, independent of Δ, whilst the mixed term shows a dispersive line shape. The summative CARS signal, which is a combination of the other three terms, is shown as a red solid line. The displayed curve is plotted for $\chi_{NR}^{(3)} = 1.2\chi_R^{(3)}$ when $\Delta = 0$. Ω_R is the centre frequency of a homogenously broadened Raman line, *R*, and Γ is the half-width at half-maximum of the Raman line.

An understanding of the physical principles which have been outlined within this section are fundamental if CARS is to be employed as an investigative tool within a biological context. The chemical specificity offered by CARS is explained by Equations 2.11-2.13, which show that when the frequency difference, $\omega_P - \omega_S$, between pump and Stokes fields matches the frequency of a molecular vibration, Ω, the resonant term, $\chi_R^{(3)}$, is maximised, giving an enhancement of the CARS (anti-Stokes) signal, thus permitting chemical contrast. Furthermore, as A_R in Equation 2.11 is proportional to the number of dipoles present, all of the anti-Stokes fields generated by the identically driven molecules constructively interfere with one another (coherent scattering), giving an enhancement in the intensity of the generated CARS signal of approximately 10^9 compared to the corresponding spontaneous Raman signal[67]. The main complication associated with CARS microscopy is the presence of a non-resonant background, which arises due to contribution from the non-resonant term, $\chi_{NR}^{(3)}$, of the susceptibility, limiting spectral sensitivity and image contrast. From a spectroscopy perspective, the non-resonant background is responsible

for distortion of spectral line-shapes, compromising interpretation of spectra and subsequent molecular assignment of features, whilst from a microscopy perspective, it introduces an offset background which reduces image contrast, and generates a negative contrast at the observed dip at the higher frequency end of CARS peaks[142]. Thus, suppression of the non-resonant background has been a major venture in the development of CARS instrumentation for application within a biological context, and this will be discussed further in Section 2.3.3.

2.3. Experimental realisation of CARS

As described in Chapter 1, CARS was first employed as an analytical technique in 1965, when Maker and Terhune utilised the third-order nonlinear effect to investigate benzene derivatives on a macroscopic scale whilst working for the Ford Motor Company[68]. A pulsed ruby laser was used to study the polarisation of electron clouds induced by the strong electric field component of the laser beam. CARS thus became recognised as an analytical technique which could permit high resolution chemical analysis of materials, and it found application in the qualitative and quantitative study of gas-phase and plasma systems, in particular within combustion diagnostics, over the following 17 years[69].

It was not until 1982 that the CARS process was incorporated into a microscope-based system, where it was employed for visualisation of the distribution of deuterated water (D_2O) in onion-skin cells[149], although image quality was severely hampered by the limited technology available at the time, with the strong non-resonant background presenting a major setback to the technique. However, despite the associated challenges, the work pioneered the use of a scanning microscope connected to a camera-tube detector. Almost two decades of further laser system development was required before CARS microscopy began to realise its full potential, with Zumbusch and colleagues utilising the technology to visualise biological molecules in living cells with high spatial resolution, sensitivity and three-dimensional sectioning capabilities, owing to use of a high numerical aperture objective and near-infrared laser sources[70]. This work reinstated CARS microscopy as a widely applicable imaging strategy capable of providing label-free chemical information of biological systems. Whilst the theoretical description of the physical processes underlying CARS micro-spectroscopy has remained unchanged over this time, recent developments in CARS microscopy have shown that its experimental requirements differ greatly from those of CARS spectroscopy, mainly concerning excitation geometry and the laser source[143]. The following section will outline some of the developments in CARS instrumentation, which

have aimed to maximise the generated resonant CARS signal and enable its realisation as an effective microscopy technique.

2.3.1. Phase-matching

In CARS, signal generation must fulfil the phase-matching condition (Figure 2.5), meaning that the sum of the wavevectors (term describing the direction of wave propagation) of the absorbed photons must equal the sum of the wavevectors of the emitted photons, given by:

$$k_{AS} = 2k_P - k_S \tag{2.14}$$

or equivalently

$$\Delta k = k_{AS} - (2k_P - k_S) = 0 \tag{2.15}$$

where k_P, k_S and k_{AS} are the wavevectors of pump, Stokes and anti-Stokes, respectively, and Δk is the wavevector mismatch, as described in Equation 2.12, where the sinc function is maximised when Δkz is close to zero[142]. Practically, Δk will not have a value of zero due to the different refractive indexes that pump, Stokes and anti-Stokes photon experience whilst propagating through the medium at different frequencies, and thus the wavevector mismatch, Δk, is generated[150].

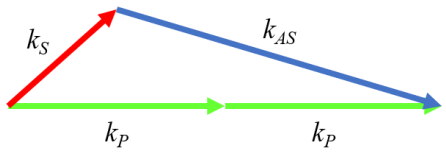

Figure 2.5 | Phase-matching condition for CARS emitted in the forward direction. k_P, k_S and k_{AS} represent the wavevectors of pump, Stokes and anti-Stokes, respectively.

The term which was described as sample thickness (z) in Equation 2.12 can be considered as length. Using a high numerical aperture (NA) objective lens (>0.8) to focus the pump and Stokes beams onto the sample, creates a small focal volume (z) and hence a good spatial resolution[67].

2.3.2. Laser excitation

The development of CARS-based imaging techniques in recent years has been facilitated by the development of new light sources. Near-infrared (NIR) laser sources, with a wavelength range from 800 nm to 1300 nm, are able to minimise the two-photon electronic interaction, which contributes towards non-resonant background enhancement[70], and avoid multiphoton absorption from ultraviolet electronic resonances, thus decreasing associated photo-damage[151]. Additionally, they show reduced Rayleigh scattering in thick material, permitting deeper penetration depth in tissues[70]. Consequently, NIR lasers have become the excitation source of choice within CARS microscopy applications[142,145].

As previously described, the generated CARS signal scales cubically with the intensity of the incident laser light, i.e. high peak powers are required, but moderate average power is desirable[145], particularly for biological applications. Therefore, CARS utilises pulsed laser sources which provide high peak intensities but moderate average powers. The width of these pulses is another important criterion in the selection of the optimum excitation source for CARS microscopy. Vibrational linewidths are typically 10-20 cm^{-1}, whereas femtosecond (fs, 10^{-15}s) pulses are generally much broader (a ~ 100 fs pulse has a bandwidth of ~ 150 cm^{-1} [142]), hence only a small part of their spectral components will be used to pump the narrow Raman line, and the remaining part will contribute to the non-resonant background, thus hampering chemical contrast[152]. Picosecond (ps, 10^{-12}s) pulses offer an alternative to femtosecond pulses which match the Raman linewidth of typical biomolecules, and can thus efficiently excite the resonant signal of interest without contributing so heavily to the non-resonant background, consequently providing improved spatial resolution[153]. The relationship between pulse width (spectral and temporal), resonant signal and non-resonant background is shown in Figure 2.6, where non-resonant background is seen to increase with a quadratic dependence on pulse width, whilst CARS signal remains constant, thus explaining how picosecond pulses give a higher resonant signal to non-resonant background ratio compared to femtossecond pulses.

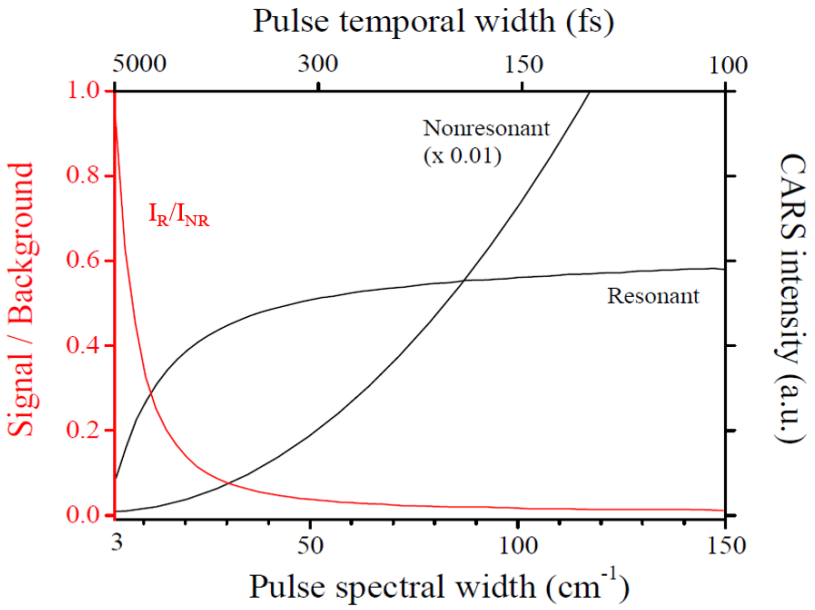

Figure 2.6 | Relationship between pulse width, resonant signal and non-resonant background (reprinted from C. Di Napoli PhD thesis[148], adapted from ref[145]). The ratio of resonant signal, I_R, to non-resonant background, I_{NR}, is plotted in red, and is observed to be much higher when the pulse duration is longer, and the spectral width is shorter.

Picosecond CARS systems typically use either two electronically synchronised Titanium:Sapphire (Ti:Sa) oscillators[152] or an optical parametric oscillator (OPO) pumped by a mode-locked Neodymium:Vanade (Nd:YVO4) laser[142], however both of these approaches demand higher costs than femtosecond laser systems. Furthermore, femtosecond systems are more versatile in that they permit quasi-instantaneous multiphoton processes such as two-photon fluorescence (TPF) and second harmonic generation (SHG), presenting the opportunity for implementation of multimodal imaging[49]. Therefore, the ideal CARS laser source would employ femtosecond pulses without generating the associated non-resonant background signal.

Spectral focusing is a procedure which makes this possible by shaping the pump and Stokes pulses in time in order to drive a narrow vibrational frequency range, despite the individual pulses being spectrally broad[154]. This can be implemented very simply by utilising glass elements of known chromatic dispersion to apply chirp (frequency change with time) to the pulses[95,155,156]. Chromatic dispersion is a phenomenon where the refractive index of a dispersive medium, such as glass, changes with wavelength (frequency). When a laser pulse passes through glass, its different wavelength components travel at different speeds, with longer wavelengths traveling faster and leaving the glass first, hence giving chirp (Figure 2.7). This stretches out the pulse from its initial width, τ_{G_0}, to a new width, τ_G. If E_0 is the electric field of a Gaussian pulse entering a

glass block of thickness, *d*, the associated electrical field, *E*, of the pulse leaving the glass can be expressed as follows:

$$E(t) = E_0\, exp\left(-\left(\frac{t}{\tau_G}\right)^2 + \mathrm{i}t\,(\omega_0 + \beta t)\right) \tag{2.16}$$

with $\beta = \dfrac{2k"d}{\tau_{G_0}^2\,\tau_G^2}$ and $k" = \dfrac{\lambda^3}{2\pi c^2}\dfrac{d^2n}{d\lambda^2}$

where ω_0 is the pulse centre frequency, t is time, β is the chirp parameter, d is the thickness of the dispersive medium, c is the speed of light, λ is the wavelength and $k"$ is the group velocity dispersion (GVD). From Equation 2.16, the instantaneous frequency, $\omega(t)$, can be defined as $\omega(t) = \omega_0 + 2\beta t$, where βt is the temporal phase gradient. For spectral focussing in CARS, pump and Stokes pulses have the same linear chirp parameter, β, hence:

$$\omega_p(t) = \omega_{P_0} + 2\beta t$$
$$\omega_S(t) = \omega_{S_0} + 2\beta t \tag{2.17}$$

and the instantaneous frequency difference (IFD) between them, $\Delta\omega = \omega_P(t) - \omega_S(t)$, remains constant over time (Figure 2.7B). The practical realisation of this concept will be described in the context of the CARS system utilised within this project in Section 3.6 of Chapter 3.

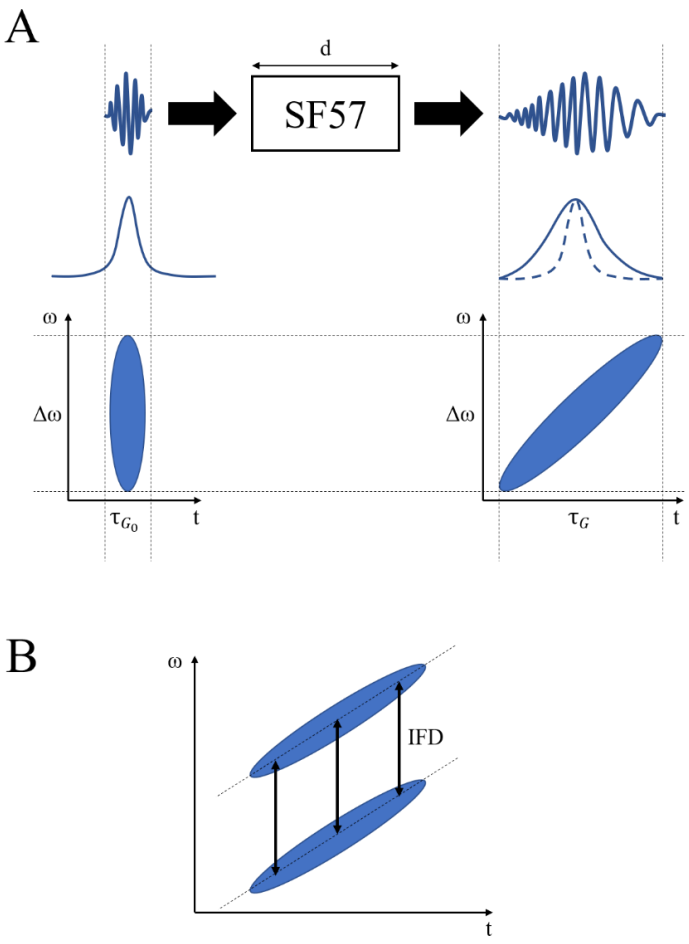

Figure 2.7 | Illustration of spectral focussing (chirping), adapted from ref[49]. As a pulse propagates through a SF57 glass block, it becomes stretched in time as longer wavelengths emerge first. As the same linear chirp is applied to both pump and Stokes pulses, the IFD between them remains constant with time. *d* is distance; ω is frequency; *t* is time; τ_{G_0} is initial pulse width; τ_G is final pulse width.

2.3.3. Non-resonant background suppression

Equation 2.13 describes how the CARS signal comprises both a resonant ($\chi_R^{(3)}$) and a non-resonant term ($\chi_{NR}^{(3)}$). As discussed in Section 2.2, the background signal, for which the non-resonant term is primarily responsible, presents a major challenge within CARS micro-spectroscopy, reducing image contrast and distorting spectral line-shapes in relation to those acquired by spontaneous Raman methods, thus limiting interpretation of CARS data outputs. Strategies have been implemented to reduce or eliminate the non-resonant contribution to the

CARS signal, and in turn improve the contrast of the signal generated by the targeted vibrational modes[143,150].

The different polarisation dependencies of $\chi_{NR}^{(3)}$ and $\chi_{R}^{(3)}$ can be exploited through use of different polarisation angles for pump and Stokes beams, giving the non-resonant background a different polarisation also, thus enabling it to be removed through use of polarisation filters within the detection path[72]. However, this strategy has been employed more frequently within CARS spectroscopy and has found only limited use within CARS microscopy[143]. One reason for this is that along with removal of the non-resonant contribution to the CARS signal, some attenuation of the resonant contribution is also observed due to the angle between the polarisations of the two contributions being very small[143].

As well as different polarisation properties, $\chi_{NR}^{(3)}$ and $\chi_{R}^{(3)}$ also exhibit different temporal behaviour. Whilst the non-resonant component shows an instantaneous response to the incident field due to its purely electronic nature, the response of the resonant component is determined by the vibrational lifetime and the phase-relaxation time of the vibrational modes involved. Therefore, the resonant and non-resonant components can be separated based on differences in temporal behaviour, which can be achieved by applying pump and probe pulses separately, with a tuneable temporal delay between them[157]. However, this strategy shows the same limitations as polarisation CARS in that attenuation of the resonant component is also observed[143].

Interferometric strategies have also been developed where CARS signal is mixed with a local oscillator to measure the real part, $Re\left\{\chi_{R}^{(3)}\right\}$, and the imaginary part, $Im\left\{\chi_{R}^{(3)}\right\}$, of the resonant component ($\chi_{R}^{(3)}$) of the CARS signal separately[146,147,158,159], thus the non-resonant contribution can be excluded, and $Im\left\{\chi_{R}^{(3)}\right\}$, which is directly proportional to the spontaneous Raman scattering spectrum[106], can be utilised. Another simple, yet effective approach which has been taken to suppress the non-resonant background involves initially splitting the pump and Stokes pulse pair into two pairs and delaying one of the pairs by half the laser repetition rate and applying a small amount of additional chirp so that the two pairs probe slightly different vibrational frequencies, i.e. one pair probes at the target frequency, whilst the other probes slightly off-target, and the corresponding intensity difference in the signal generated by each pair is utilised for suppression of the non-resonant background. This technique is referred to as dual-frequency differential CARS (D-CARS)[79,95,96].

This chapter has described some of fundamental physical principles behind Raman-based technologies, as well as discussing some of the advances in instrumentation that have permitted

realisation of CARS as an effective imaging technique. Within the following chapter, the configuration of the CARS system used within this project and the supporting data processing and analysis methodologies are described.

3. MATERIALS AND METHODS

3.1. Lipids

Within Chapters 4, 5 and 7 of this thesis, deuterated fatty acids were utilised to investigate the potential of hyperspectral CARS imaging and FSC^3 data analysis to visualise deuterium-labelled molecules within cells. Deuterated and non-deuterated isoforms of three different fatty acids were investigated which differed in their degree of unsaturation. These include oleic acid (OA), a monounsaturated 18C molecule with a cis double bond at the ninth carbon; D17-oleic acid (D17-OA), a deuterated isoform of OA with 17 deuterium atoms attached to carbons 11-18; linoleic acid (LA), a biunsaturated 18C molecule with two cis double bonds at the ninth and twelfth carbons; D11-linoleic acid (D11-LA), a deuterated isoform of LA with 11 deuterium atoms attached to carbons 14-18; α-linolenic acid (LNA), a triunsaturated 18C molecule with cis double bonds at the ninth, twelfth and fifteenth carbons; and D14-α-linolenic acid (D14-LNA), a deuterated isoform with 14 deuterium atoms attached to carbons 2-8. Pure (>95%) samples of the investigated fatty acids were purchased from Cayman Chemical (MI, USA) and their chemical structures are displayed in Figure 3.1.

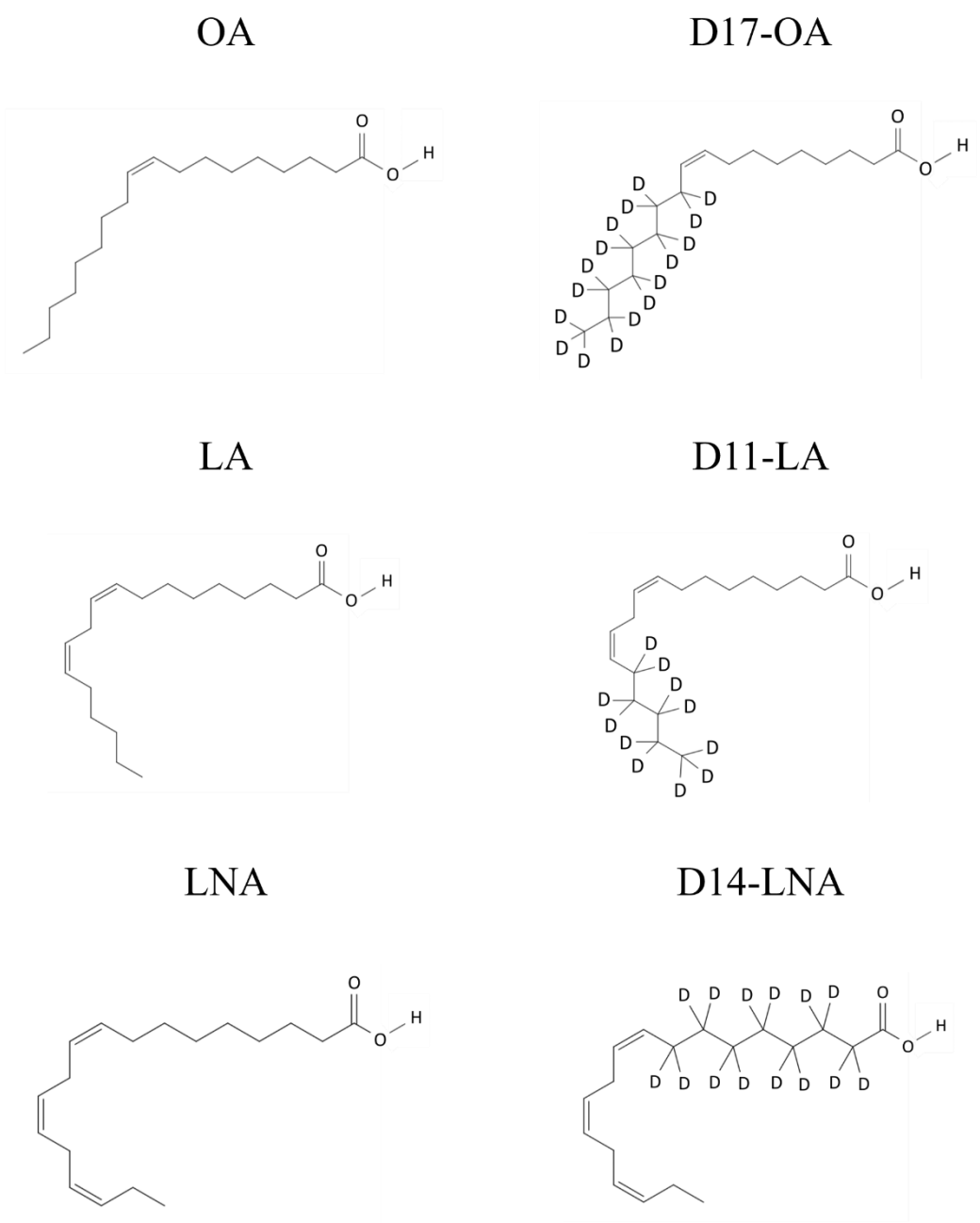

Figure 3.1 | Chemical structures of the six investigated fatty acid variants. Deuterium atoms are located within the aliphatic chain of the deuterated fatty acids and are represented by 'D'. MolView was used as a molecule editor to generate the two-dimensional representations.

3.2. Small molecule compounds

Within Chapter 6 of this thesis, seven deuterium-labelled molecules were investigated to assess the ability of hyperspectral CARS and FSC^3 data analysis for visualising deuterated molecules of different types within cells. Table 3.1 gives an overview of the investigated compounds, which included D5-L-tryptophan (D5-Trp) and D4-/D6-succinic acid (D4-SA/D6-SA), deuterated isoforms of an amino acid and a carbohydrate, respectively, as well as five small molecule compounds, namely methyl-D3-triphenylphosphonium iodide (D3-TPMP); D4-paracetamol (D4-Para); D8-histamine H_2 receptor antagonist (D8-H_2Ri); D9-COX-2 inhibitor (D9-COX2i); and D7-HCMV DNA synthesis inhibitor (D7-HCMVi). The chemical structures for each of these molecules are displayed in Figure 3.2, and each will be described in more detail within Chapter 6. Pure powder preparations of D5-Trp, D4-SA, D6-SA and D3-TPMP, as well as their associated non-deuterated parent molecules, were purchased from Sigma Aldrich (UK), whilst the remaining four small molecule compounds were provided by GlaxoSmithKline (UK).

Table 3.1 | Chemical data for investigated deuterium-labelled small molecule compounds.

Parent Compound	Label	Label Position	Molecular weight
L-Tryptophan (Trp)	D5	Aromatic	209.25
Succinic acid (SA)	D4/D6	Aliphatic	122.11/124.30
Methyltriphenylphosphonium iodide (TPMP)	D3	Aliphatic	407.24
Paracetamol	D4	Aromatic	155.19
Histamine H_2 Receptor Antagonist	D8	Aromatic	350.44
COX-2 Inhibitor	D9	Aliphatic	383.39
HCMV DNA Synthesis Inhibitor	D7	Aliphatic	383.28

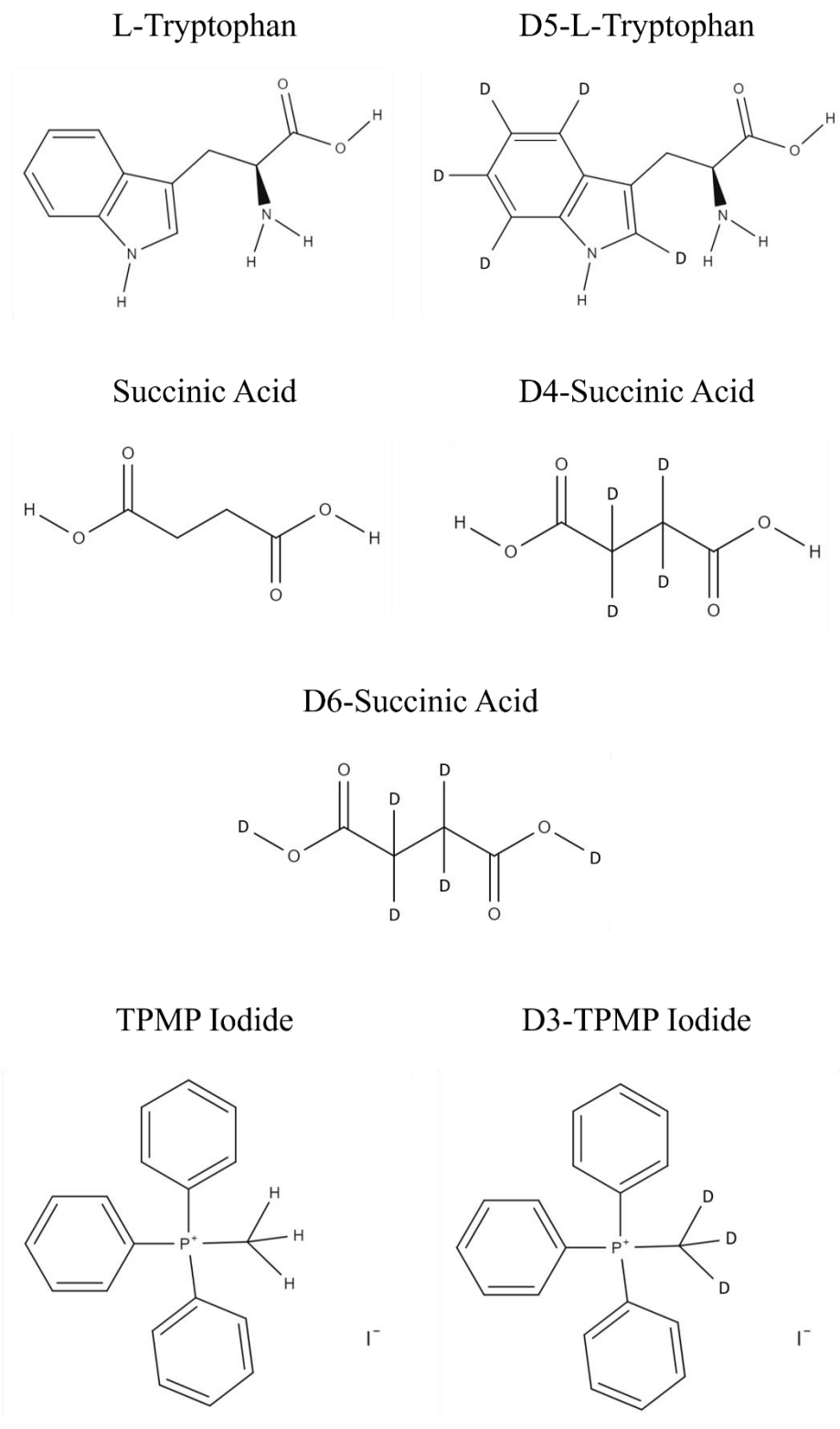

Figure 3.2 | Chemical structures of investigated deuterium-labelled molecules and their non-deuterated parent molecules generated using MolView as a molecule editor. Deuterium atoms are represented by 'D'.

D4-Paracetamol

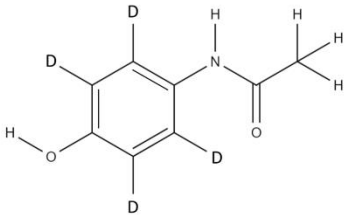

D7-HCMV DNA Synthesis Inhibitor

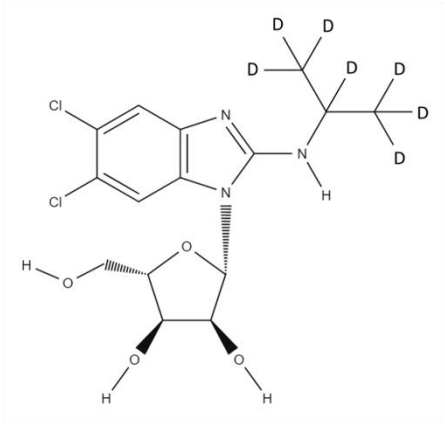

D9-Cox-2 Inhibitor

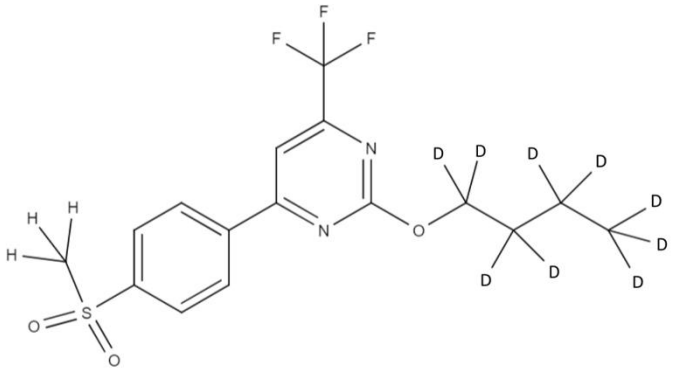

D8-Histamine H2 Receptor Antagonist

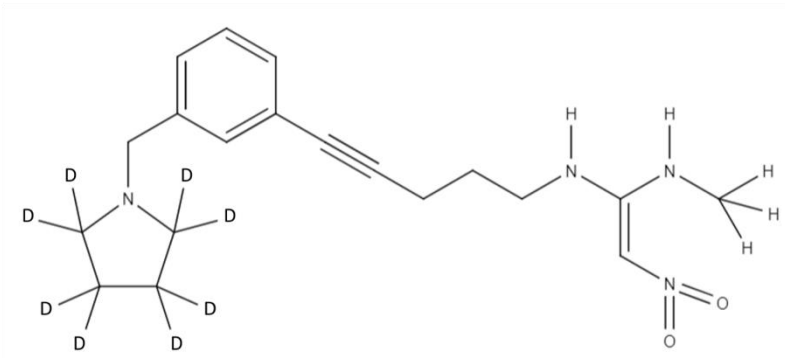

Figure 3.2 cont. | Chemical structures of investigated deuterium-labelled small molecule compounds generated using MolView as a molecule editor. Deuterium atoms are represented by 'D'.

3.3. Cell culture and treatment

3.3.1. Cell culture

The human cervical carcinoma cell line, HeLa, was obtained from the American Type Culture Collection (ATCC) (UK), which had undergone prior mycoplasma testing. These cells were routinely cultured at a temperature of 37°C and a CO_2 concentration of 5% within a humidified incubator, and their growth was monitored daily via brightfield microscopy. Cells were grown in minimum essential medium (MEM) and GlutaMAX™ (Life Technologies, UK) supplemented with 10% (v/v) foetal bovine serum (FBS) (Life Technologies, UK) within cell culture petri dishes with a surface area of 55 cm^2 and were passaged every 3-4 days when a confluency of approximately 75% had been reached. All solutions were pre-warmed to 37°C in a water bath and the routine passage procedure was performed in sterile conditions via a cell culture hood, which was disinfected with 70% industrial methylated spirit (IMS) prior to and following use. During the passaging procedure, cells were washed once with phosphate buffered saline (PBS) (Thermofisher, UK) and incubated with 1 ml of 0.25% trypsin/EDTA (Thermofisher, UK) for 5 min at 37°C, inducing detachment of cells from the culture dish, which was confirmed via brightfield microscopy. The detached cells were then resuspended in 9 ml of culture media and the suspension was transferred to a 15 ml tube, before centrifugation at 250G for 4 min. The supernatant was discarded, and the remaining pellet was resuspended in 10 ml of fresh cell culture media. Cell concentration was determined using a haemocytometer, which featured a grid with eight squares of volume, 1 x 1 x 0.1 mm = 0.1 mm^3 = 0.0001 ml, from which an average cell number was calculated. Hence, the following equations were used to determine the required volume of cell suspension to be added to the new culture dish to achieve the desired cell concentration:

1) Number of cells per ml = Average cell number per square x Volume of square (ml)

2) Volume of cell suspension (ml) = Desired cell number per ml / Number of cells per ml

A concentration of $1x10^5$ cells per ml was used at each passage, and the calculated volume of the cell suspension was added to growth media to give a final volume of 10 ml.

3.3.2. Lipid starvation and treatment

Human cervical carcinoma (HeLa) cells (ATCC, UK) were cultured in minimum essential medium (MEM) supplemented with GlutaMAX™ (Life Technologies, UK) and 10% (v/v) foetal bovine serum (FBS) (Life Technologies, UK) directly onto glass coverslips (thickness #1.5, 25 mm diameter, PA, VWR International, USA). Following 8 hours incubation in MEM + GlutaMAX™ with 10% FBS, cells were transferred to MEM + GlutaMAX™ supplemented with fatty acid-free FBS (Biowest, France) to deplete cells of lipid droplets. After 18 hours incubation, cells were transferred to MEM + GlutaMAX™ supplemented with lipid-free FBS and a complex of bovine serum albumin (BSA) (Sigma Aldrich, UK) and the investigated fatty acid at a concentration of 47 μg/ml. Fatty acid-BSA complexes were formed by adapting a published protocol[160], which involved combining 5% BSA/PBS solutions with 20 mM sodium-fatty acid solutions to form fatty acid-BSA complexes with a final concentration of 1.656 mg/ml.

A stock of 5% BSA/PBS solution was made by dissolving 0.5 g of fatty acid-free BSA (Biowest, France) in 10 ml of PBS (Thermofisher, UK) in a 15 ml tube. To form the sodium-fatty acid solutions, the solvents in which the fatty acids were dissolved were first evaporated using a gentle stream of nitrogen, leaving droplets of the pure lipids. The purchased fatty acids were packaged in 2 ml glass vials, which provided a suitable vessel in which each sodium-fatty acid solution could be prepared following evaporation of the solvent. Six lots of 2 μl of 1M NaOH and 157 μl of water were combined in separate 2 ml glass vials and heated to 70°C in a water bath, before the solutions were combined with the pure fatty acids. Each NaOH/water/fatty acid solution was incubated at 70°C for 30 mins, with mixing at every 5 mins, before a further 3 μl of NaOH was added to each solution as six separate 0.5 μl aliquots with a gap of 5 mins between each, giving 20 mM solutions of sodium oleate, sodium D17-oleate, sodium linoleate, sodium D11-linoleate, sodium α-linolenate and sodium D14-α-linolenate. Six aliquots of 464 μl of the 5% BSA/PBS solution were transferred into six separate 2 ml glass vials and warmed to 37°C in a water bath, before each sodium-fatty acid solution was added dropwise to the 5% BSA-PBS solutions, with mixing after each drop. Thus, stock fatty acid-BSA solutions were produced with a concentration of 1.656 mg of fatty acid per 1 ml of BSA. To achieve a final lipid concentration of 47.3 μg/ml, 57 μl of the fatty acid-BSA complex was added to 1943 μl of MEM + GlutaMAX™ supplemented with 10% lipid-free FBS, giving a total volume of 2 ml, which was transferred onto cells within a sterile cell culture hood using a 4 mm diameter, 0.22 μm filter (Corning, USA) and a 2 ml syringe (Becton Dickinson, USA).

Following an 18-hour incubation period in fatty acid-BSA-supplemented media, coverslips were fixed in a 4% formaldehyde-PBS solution (Affymetrix, UK) for 20 minutes and

mounted onto standard glass microscope slides using a 9 mm diameter, 120 μm thick adhesive imaging gasket (Grace BioLabs, OR, USA) filled with water. Control cells used for widefield analysis were incubated in GlutaMAX™ supplemented with lipid-free FBS for the full 36-hour period.

3.3.3. Small molecule compound treatment

Human cervical carcinoma (HeLa) cells (ATCC, UK) were cultured in minimum essential medium (MEM) supplemented with GlutaMAX™ (Life Technologies, UK) and 10% (v/v) foetal bovine serum (FBS) (Life Technologies, UK) directly onto glass coverslips (thickness #1.5, 25 mm diameter, PA, VWR International, USA). Initially, high concentration stock solutions of each investigated small molecule compound were prepared. D4-Para, D8-H_2Ri and D7-HCMVi were each dissolved in a 50:50 mixture of water and methanol to give a final concentration of 10 mM, whilst D9-COX2i was less soluble and was thus dissolved at a concentration of 1 mM. The incorporation of methanol within solutions containing each of the compounds listed above was required due to their immiscibility in water alone. Due to their higher solubility, D5-Trp, D4-/D6-SA and D3-TPMP could be dissolved in water alone, and stock solutions of each were prepared with a final concentration of 10 mM. The mass of powder compound to be dissolved within each of the stock solutions was calculated as follows:

Mass (g) = Concentration (M) x Volume (L) x Molecular Mass (Mr).

For small molecule compounds dissolved in 50:50 solutions of water and methanol, compounds were first dissolved in methanol before water was added. Stock solutions of compounds were diluted to the desired concentration in MEM + GlutaMAX™ supplemented with 10% lipid-free FBS before the compound-containing media was administered to cells within a sterile cell culture hood using a 4 mm diameter, 0.22 μm filter (Corning, USA) and a 2 ml syringe (Becton Dickinson, USA). Vehicle control cells received the equivalent volume of either 50:50 water:methanol or water alone, corresponding to the small molecule compound being investigated.

Following the desired incubation period in compound-containing media, samples were either fixed in a 4% formaldehyde-PBS solution (Affymetrix, UK) for 20 minutes and mounted onto standard glass microscope slides using a 9 mm diameter, 120 μm thick adhesive imaging gasket (Grace BioLabs, OR, USA) filled with water, or, for live imaging, coverslips were mounted in the same way within gaskets filled with HEPES-buffered live cell imaging solution (Life Technologies, UK) and imaged immediately.

3.4. Widefield fluorescence imaging

Following fixation, samples selected for fluorescence imaging were incubated in a 2 mg/ml solution of glycine (Sigma Aldrich, UK) in PBS for 30 minutes to quench unreacted aldehyde groups which can cause an increase in background fluorescence. Cells were then incubated in a staining solution containing DAPI (ThermoFisher Scientific, UK) at 0.5 mg/ml, LipidTOX Red neutral lipid stain (ThermoFisher Scientific, UK) at 0.2 μl/ml and FITC-labelled concanavalin A (ThermoFisher Scientific, UK) at 5 μl/ml in PBS for 1 hour. Samples were imaged using an Olympus IX 73 inverted widefield microscope. Images were acquired using an ORCA Flash 4.0 Camera (Hamamatsu) using HCImaging software and a Prior Lumen200Pro light source. Fluorescence emission was separated by a multiband dichroic filter set #69002 (Chroma). Table 3.2 shows the excitation and emission wavelengths for each of the utilised fluorescence markers. All widefield images were acquired using a 100x, 1.4 NA oil immersion objective and image processing was performed using the software, ImageJ[161].

Table 3.2 | Excitation and emission wavelengths for utilised fluorescent markers.

Fluorescent Marker	λ Excitation (nm)	λ Emission (nm)
DAPI	350/50	455/50
FITC	490/20	525/36
LipidTOX Red	555/25	605/52

3.5. Spontaneous Raman imaging

The spontaneous Raman spectra shown in Chapters 4 and 6 were acquired using a custom-built multimodal micro-spectroscopy system, which is described in detail in the next section (Section 3.6). Horizontal (Thorlabs VA100, 0-6.4 mm) and vertical (internal to the spectrometer, Horiba iHR550) slits enable confocal Raman spectroscopy. A 40x, 0.95 NA, 0.21 mm WD dry objective (Nikon CFI Plan Apochromat IR λS Series, MRD00405) and a 0.72 NA, 12.5 mm WD condenser (Nikon Ti-C-CLWD, MEL56100) were used for acquisition of spectra. The excitation beam from a 532 nm laser (Laser Quantum GEM) was initially passed through a filter (Semrock LL01-532) to exclude lower wavelengths, preventing interference with the signal,

before it was coupled into the microscope via a dichroic mirror (Semrock LPD01-532RS). Raman scattering was collected in epi-direction, filtered with a long pass filter (Semrock BLP01-523R), dispersed by an imaging spectrometer (Horiba iHR550) with a grating of 300 lines/mm, and detected with a CCD camera (Andor Newton DU971N-BV). All measurements were performed at room temperature.

3.6. Multimodal CARS microscope configuration

All CARS data within Chapters 4, 5 and 6 was acquired using a custom-built multimodal laser scanning CARS microscope within Cardiff University's School of Biosciences[94]. A schematic overview of the CARS system configuration is shown in Figure 3.3. A single 5 fs Ti:Sa broadband (660 nm to 970 nm) pulsed laser (Venteon, Pulse:One PE) was pumped by a Nd:vanadate laser (Laser Quantum, Finesse) at 4.5 W to generate < 8 fs pulses with a spectral width of 310 nm at 10% of the maximum intensity at a repetition rate of 80 MHz and with an average output power of ~ 500 mW. The laser power was set using a computer-controlled achromatic half-wave plate and a Glan-laser polariser. A long-pass filter (two 3 mm thick RG645 in Brewster angle) was used to reject the tail of the laser spectrum, which would otherwise overlap with the CARS detection range. A short-pass dichroic mirror (Eksma Optics) (DM1a) reflected wavelengths above 900 nm to be used for TPF/SHG excitation and the resulting pulse was centred at 940 nm with a bandwidth of 70 nm. The transmitted beam was separated into pump and Stokes components by a second dichroic mirror (CVI Melles Griot) (DM2), and the resulting pump and Stokes pulses were centred at 682 nm and 806 nm with a bandwidth at 10% of the maximum of 65 nm and 200 nm, respectively, permitting excitation of molecular vibrations over the spectral range, 1200-3780 cm^{-1}. As shown by the side view of the highlighted section within Figure 3.3, Dichroic mirror 1a (DM1a) and mirror 1 (M1) were cut in half, enabling pump and Stokes beams to be recombined by dichroic mirror 2 (DM2) after passing through a vertically displacing prism reflector (R). Each of the separated pump, Stokes and TPF/SHG components carried approximately one third (one sixth for SHG) of the laser power (~ 500 mW). Following recombination by DM2, the pump/Stokes pair was recombined with the TPF/SHG beam by dichroic mirror 1b (DM1b), before entering the scan (galvo) mirrors (Cambridge Technology, 6210HSM40), which were responsible for guiding the laser beam focus across the sample in horizontal lines (raster scanning).

The excitation beam entered a commercial inverted microscope (Nikon Ti-U), equipped with different objectives and condensers. For all samples investigated within this thesis, a 60x,

1.27 NA, 0.17 mm WD water immersion objective (Nikon CFI Plan Apochromat IR λS series, MRD70650) was used with a 1.4 NA, 1.95 mm WD oil condenser (Nikon T-C-HNAO, MEL41410) and a 1x tube lens, enabling high resolution imaging (~ 0.3 μm spatial resolution). All CARS data shown within this thesis was acquired in the forward direction, however, the utilised CARS system also had epi-detection capabilities. For forward detection, the signal collected by the condenser was projected upwards to three photomultiplier tubes (PMTs). A dichroic mirror (Semrock FF520-Di02) (DM4) transmitted the CARS emission at > 540 nm and reflected the shorter wavelength TPF/SHG signal. Different bandpass filters were applied to the CARS pathway to reject pump and Stokes emissions and transmit CARS signal over specific spectral ranges, which could be selected based on the vibrational range being investigated. The transmitted CARS signal was detected by a Hamamatsu H7422-40 PMT. The signal reflected by DM4 was separated into SHG and TPF components by another dichroic mirror (Chroma t495lp) (DM5), which were detected by Hamamatsu H107210-210 and Hamamatsu H10721-20 PMTs, respectively. Table 3.3 provides an overview of the bandpass filters and PMTs utilised in CARS, SHG and TPF detection. The epi-detected CARS, TPF and SHG signals were first collected by the microscope objective and propagated back along the excitation pathway, before they were reflected by a dichroic mirror (Semrock FF660-Di02) (DM3) into a collection of bandpass filters and PMTs with an identical layout to the forward-detection configuration described above (see Figure 3.3).

The microscope was also equipped with differential interference contrast (DIC) optics, which were utilised within this project to locate regions of interest within samples, prior to CARS imaging. DIC imaging was undertaken using the same objective and condenser combination used for CARS. The condenser assembly was fitted with a polariser (MEN51941) and Wollaston prism (MEH52500, T-C DIC Module HNA N2 Oil). A second Wollaston prism (Nikon, MBH76260) was located after the objective, followed by a DIC analyser block (MEN51980, Ti-A-E DIC Analyser Block). DIC images were acquired using a CCD camera (Hamamatsu Orca-285). Both XY sample motion (Prior, H117N2NN stage) and objective motion in Z-direction (Prior, H122 with direct fine drive coupling kit (H122KON)) were controlled via a Prior Proscan III controller (V31XYZ) using a hand controller (PS3J100) or direct PC control. Whilst an overview of the entire multimodal CARS microscopy system has been provided, not all modalities were implemented within this project, however, a knowledge of the whole system is important for understanding how image data is generated by each modality individually. Specifically, only images generated by forward-detected CARS and DIC feature within this thesis, and CARS data was only acquired from the CH-stretch (2600-3300 cm^{-1}) and cell-silent (1800-2700 cm^{-1}) regions of the Raman spectrum.

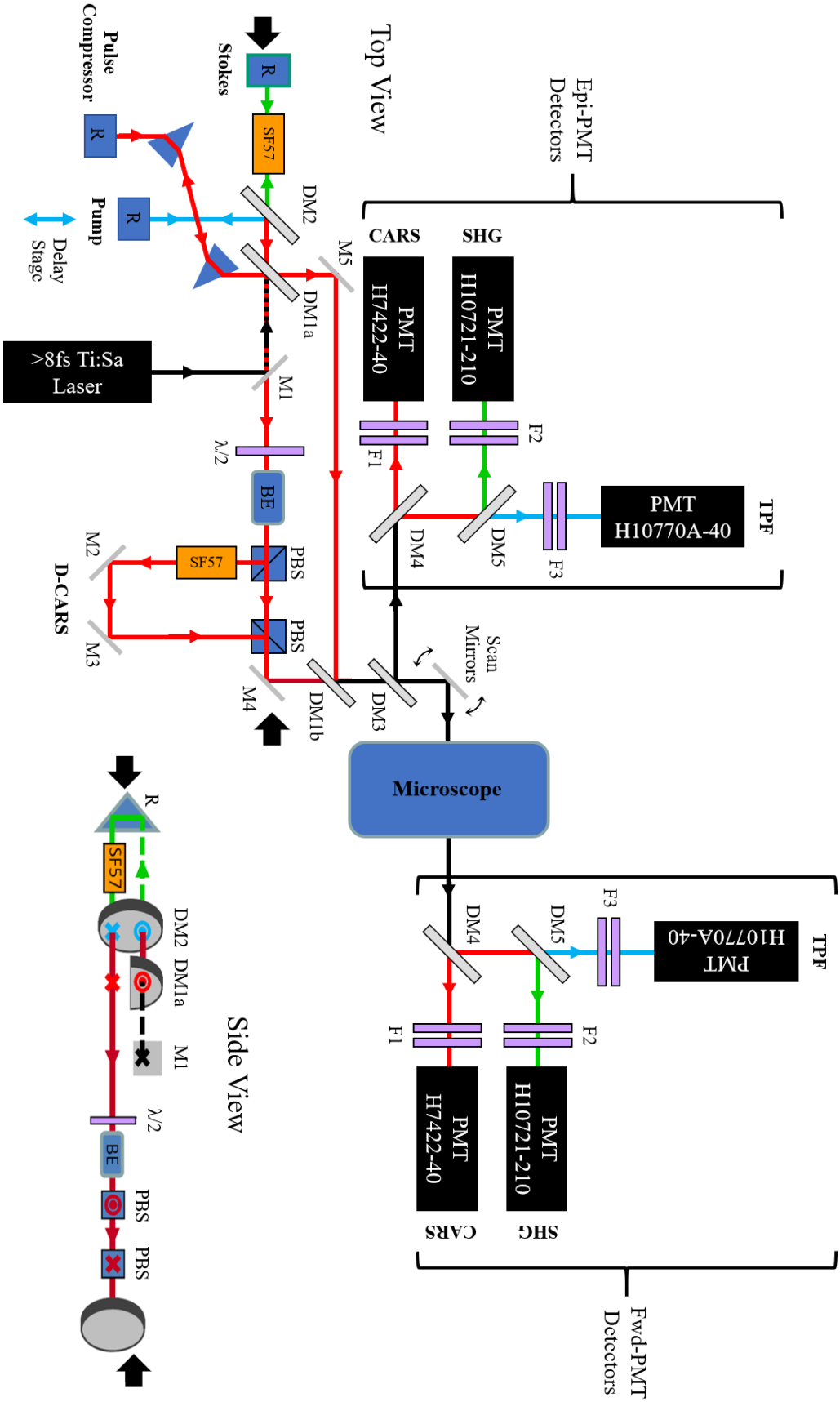
Top View
Epi-PMT Detectors
CARS
SHG
PMT H7422-40
PMT H10721-210
F1
F2
F3
PMT H10770A-40
TPF
DM4
DM5
Pulse Compressor
Stokes
Pump
Delay Stage
SF57
DM2
DM1a
M5
M1
>8fs Ti:Sa Laser
λ/2
BE
PBS
M2
M3
M4
DM1b
DM3
Scan Mirrors
D-CARS
Microscope
Side View
Fwd-PMT Detectors

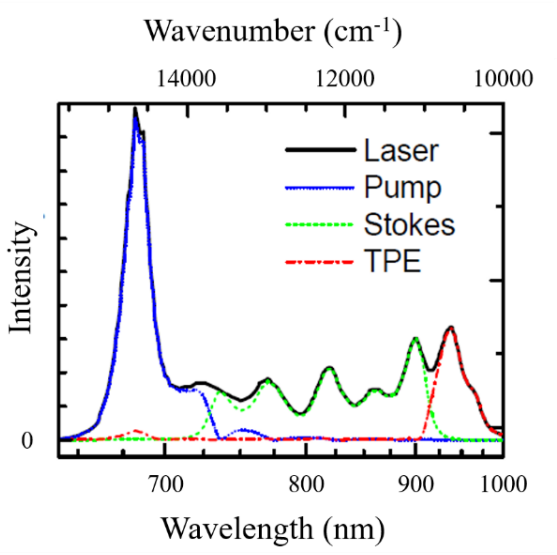

Figure 3.3 | Overview of multimodal, multiphoton, laser scanning CARS microscope configuration, adapted from ref[94]. The full beam path is shown for CARS, SHG and TPF signal generation from the laser source to the detectors. A side view is provided of the central section of the configuration (black arrows), illustrating how the beams are displaced vertically to bypass the half-cut dichroic mirror 1a (DM1a) and mirror 1 (M1). Dichroic mirrors (DM) are used to separate and recombine the CARS, SHG and TPF components, SF57 glass blocks are used to apply linear chirp to the pump and Stokes pulses, the delay stage is used to tune the IFD to target vibrational resonances, the scan mirrors guide the focus of the laser beam across the sample, and a half-wave plate (λ/2) and polarising beam splitters (PBS) enable D-CARS. The graph shows the typical spectra of the laser, indicating the pump, Stokes and SHG/TPF (TPE) components. M is mirror; DM is dichroic mirror; R is reflecting prism; SF57 is glass block; λ/2 is half-wave plate; BE is beam expander; PBS is polarising beam splitter; F is filter; PMT is photomultiplier tube.

Table 3.3 | Bandpass filters and PMTs employed in forward and epi detection of CARS, SHG and TPF, adapted from ref[94]. All filters purchased from Semrock. All PMTs purchased from Hamamatsu. The targeted spectral range permitted by each of the CARS filters is also shown. Three interchangeable CARS filters (F1(1-3)) are implemented within the system, represented by F1 in Figure 3.3.

Detection	Figure 3.3 Label	Filters	PMT	Transmission Range	Signal
Forward	F1(1)	FF01-562/40 x2	H7422-40	542-582 nm 3787-2519 cm^{-1}	CARS (CH)
	F1(2)	FF01-593/40 x2		573-613 nm 2789-1650 cm^{-1}	CARS (CD)
	F1(3)	SP01-633RS FF01-609/57 x2		582-630 nm 2519-1210 cm^{-1}	CARS (FP)
	F2	FF01-510/84 FF01-469/35	H107210-210	468-487 nm	SHG
	F3	FF01-510/84 x2	H10721-40	468-552 nm	TPF
Epi	F1(1)	FF01-562/40 x2	H7422-40	542-582 nm 3787-2519 cm^{-1}	CARS (CH)
	F1(2)	FF01-593/40 x2		573-613 nm 2789-1650 cm^{-1}	CARS (CD)
	F1(3)	FF01-609/54 FF01-609/57		582-637 nm 2519-1210 cm^{-1}	CARS (FP)
	F2	FF01-469/35 x2	H107210-210	449-488 nm	SHG
	F3	FF01-510/84 x2	H10721-40	468-552 nm	TPF

As discussed in Section 2.3.2 of Chapter 2, the bandwidth of a fs pulse is much larger than typical Raman bandwidths, reducing spectral selectivity and increasing non-resonant background. This limitation is overcome in the described CARS system through application of linear chirp to both pump and Stokes beams to stretch the beams in time so that the temporal difference between them drives vibrations over a narrower frequency range[154]. This procedure, referred to as spectral focussing, is implemented through use of SF57 glass elements (Changchun Fortune Optronic Inc.) of known chromatic dispersion, where the refractive index changes with wavelength (frequency) so that longer wavelengths propagate faster and leave the glass first [95,155,156]. In the described CARS system, the Stokes beam propagates through an additional block of SF57 glass to correct for its smaller group velocity dispersion (GVD) compared to the pump beam, before both beams are recombined, thus ensuring the linear chirp parameter of the pump and Stokes beams are the same. The other optical elements within the setup (particularly the objective) are sufficient to chirp the beams to a picosecond. The molecular vibration is driven at the beat frequency, $\omega_P - \omega_S$, centred at the IFD, $\omega_{P_0} - \omega_{S_0}$, and has a spectral width given by the Fourier limit of the temporal envelope of the pulses. This spectral width can be elongated by the applied linear chirp to a few picoseconds (τ_G), enabling a spectral resolution of 10 cm^{-1} to be achieved[94].

Spectral tuning to drive resonance at specific frequencies is achieved by controlling the arrival time of the pump beam through use of a mechanical delay stage (Physik Instrumente M-404.42S) with a travel distance of 150 mm and a minimum incremental motion of 0.2 μm, permitting a precision of 5 fs in the temporal delay. Tuning the delay shifts the IFD between the equally linearly chirped pump and Stokes pulses, enabling vibrational spectroscopy to be performed without a requirement for multiplex detection or laser tuning (Figure 3.4).

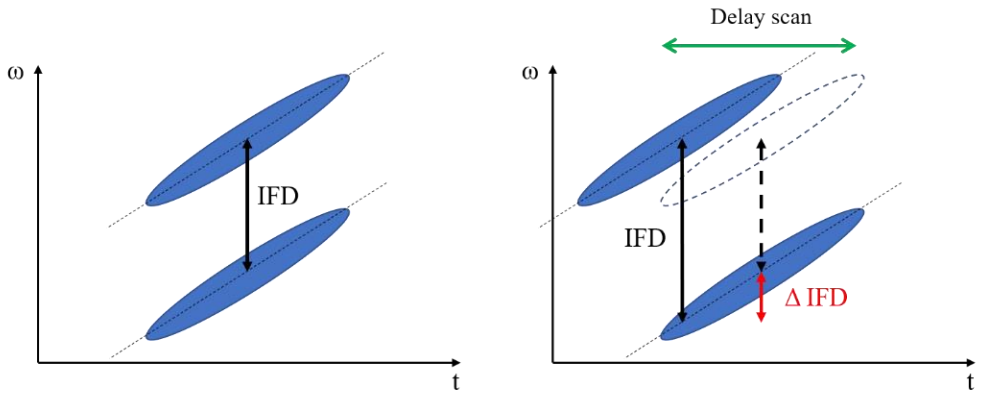

Figure 3.4 | Illustration of instantaneous frequency difference (IFD) tuning via delay scanning. Varying the overlap of the two equally chirped pulses changes the IFD, thus permitting targeting of specific vibrational resonances. ω is frequency; t is time.

D-CARS was introduced in Section 2.3.3 in Chapter 2 as a strategy to suppress non-resonant background and reduce acquisition times. This technique is implemented within the described CARS system via a half-wave plate (λ/2) and polarising beam splitter (PBS), which are used to split the pump/Stokes pair into two orthogonally polarised pairs. The second pair travels along an additional path, which gives a delay equal to half of the laser repetition rate, before it is recombined with the first pair via a second PBS. The use of a thin SF57 glass element within the beam path of the second pair permits control of its IFD, enabling simultaneous detection of the sum and difference of the CARS intensities at two IFDs (wavenumbers) separated by 20 cm^{-1} to 150 cm^{-1}. However, D-CARS is not employed as a CARS technique within this thesis, and so extensive details will be spared.

3.7. Data acquisition, processing and analysis

3.7.1. Data acquisition

Image acquisition using the multimodal CARS microscopy system described in Section 3.6 was performed using a custom-written software called MultiCARS (LabWindows CVI, W. Langbein et al., Cardiff School of Physics and Astronomy) which permitted hardware-software interfacing and remote control of instrumentation. Throughout the project, biological samples were imaged by hyperspectral CARS, where stacks of XY images were acquired at a series of spectral positions in both the CH-stretch region (2600-3300 cm^{-1}) and the cell-silent region (1800-2700 cm^{-1}) of the Raman spectrum with spectral steps of 5 cm^{-1}, producing spectra for each spatial point. For all hyperspectral imaging of biological samples, a power of 50% of the total laser power was used (250 mW based on 500 mW total laser power) and a pixel dwell time of 0.1 ms, however the power at the sample was considerably less than this due to power control settings, separation of laser beams and losses along the beam path. The loss of pump beam power was assessed for a total laser output power of ~ 430 mW with the half-wave plate set to allow transmission of 10% of the total laser power (~ 43 mW). As the laser beam was separated into pump, Stokes and SHG/THG parts, the laser power was also separated three ways, although not equally. The resulting power for the pump beam was recorded at 7.9 mW before entering optics, and at 5.6 mW at the sample plane without inclusion of an objective lens, thus indicating that ~ 71% of the power was transmitted through the optics, with ~ 29% lost along the beam path due to reflection of glass elements and clipping of the laser beam by pinhole components. When the 60x, 1.27 NA objective was used for image acquisition, approximately a further 40% of power was lost, giving a power of ~ 3.36 mW at the sample. Whilst it was important to avoid using excessively high

laser powers in order to prevent cell damage whilst imaging, determination of a specific upper limit for power at sample was difficult to define due to the equal contribution from pixel dwell time and associated energy accumulation within samples. A low power at sample could still have been damaging to cells if a prolonged pixel dwell time was used, whilst a high power at sample may not have induced cell damage with a short cell exposure time, thus, selection of the most suitable imaging conditions accounted for both power at sample and pixel dwell time. Estimations of laser powers which would be non-destructive to live cells were also provided by previous work undertaken using the same multimodal CARS system, where powers at sample of up to 20 mW were routinely utilised for both pump and Stokes beams, achieving sufficient signal to noise with no visible associated cell damage. Thus, for live cell imaging, powers at sample were kept to around 20 mW, whilst for fixed samples, higher laser powers could be employed if necessary.

At the beginning of each measurement session, CARS spectra were acquired from a solid layer of polystyrene and from glass, and a spectrum of the CARS intensity ratio between the two was obtained. This could then be used to calibrate wavenumber based on the well-characterised polystyrene peak positions within the CH-stretch region, correcting against laser fluctuations between different experiments. Similarly, CARS spectra were acquired from a solid layer of 4-Nitrophenyl-acetonitrile, which shows well-characterised peaks within the cell-silent region, and from glass, and a spectrum of the CARS intensity ratio was once again obtained and utilised for wavenumber calibration. For correct quantification of CARS intensity ratios, background contributions from electronics or cell autofluorescence were quantified through measurements under the same excitation and detection conditions, but with pump and Stokes delayed by such a degree in relation to one another that time overlap does not occur, and thus no CARS signal is generated. Images were acquired at 5000 cm^{-1} for CH-stretch region images and at 1000 cm^{-1} for cell-silent region images. These images could then be subtracted from the acquired CARS intensities prior to data analysis.

3.7.2. Regularisation

Acquired CARS images must initially be data regularised into a processing-compatible format via the MultiCARS software. To explain regularisation, an example in the form of a hyperspectral CARS image stack which has been acquired in the CH-stretch region can be considered. The dataset contains both spatial and spectral information in every scan channel of the scan output, specifically, in the scan channel along the x dimension, the scan channel across the y dimension, and the scan channel in the IFD (spectral) dimension. For interpretation, this information must be converted into a multi-dimensional Cartesian data cube of equal sized voxels

(a voxel is a volumetric picture element representing a signal intensity value in a three-dimensional space). Therefore, for the considered example, the hyperspectral CARS XY image is regularised into a three-dimensional cube where X and Y are the orthogonal coordinates at the bottom sides and IFD in height. Regularised data could be exported as ASCII files and/or bitmap images for further data analysis.

3.7.3. Data analysis

Hyperspectral CARS datasets were processed using Hyperspectral Imaging Analysis (HIA) software written by Masia et al.[73], which is an analytical tool that was utilised to extrapolate noise-filtered, quantitative information about chemical composition from hyperspectral images. The software also permitted removal of background contributions through subtraction of 1000 cm^{-1} and 5000 cm^{-1} images. Within the software, three main steps were involved in the processing of hyperspectral CARS data which were based on the following mathematical methods: 1) a singular value decomposition (SVD) algorithm; 2) a phase-corrected Kramers-Kronig (PCKK) retrieval method; and 3) a blind factorisation into susceptibilities and concentrations of chemical components (FSC^3) algorithm.

SVD involved unsupervised noise filtering of hyperspectral CARS data through removal of spectral components which were dominated by noise. For large numbers of photons, CARS intensity, I, scales proportionally to $\sqrt{I}$, and consequently $I/\sqrt{I}$ shows noise independent of intensity. The noise-dominated spectral components could be removed by limiting the number of singular values and a new noise-free matrix was generated. CARS intensity ratios could then be calculated by dividing the background-corrected CARS intensity by the corresponding non-resonant CARS intensity measured in glass under the same excitation and detection conditions. PCKK is a phase-retrieval method which was applied to hyperspectral data to extrapolate the CARS third-order susceptibility, $\chi^{(3)}$, which was normalised with respect to the glass response. This could be achieved by estimating the phase, ϕ, of the CARS field from the CARS intensity ratio, I_{ratio}. As a Kramers-Kronig relationship exists between the real, $Re\left\{\chi_R^{(3)}\right\}$, and imaginary, $Im\left\{\chi_R^{(3)}\right\}$, parts of the resonant contribution, $\chi_R^{(3)}$, to the CARS intensity (see Section 2.2), $Im\left\{\chi_R^{(3)}\right\}$ could be retrieved, which was chemically specific and linear in the concentration of chemical components, permitting quantitative analysis. Thus, this processing step was responsible for generation of Raman-like spectra within hyperspectral CARS datasets.

FSC^3 identified chemical components from the phase-retrieved $\chi^{(3)}$ spectra within the hyperspectral dataset, providing corresponding component spectra and absolute volume concentrations. This was achieved by applying the non-negative matrix factorisation (NNMF) algorithm[162] on a matrix composed of two parts, one of which is related to $Im\left\{\chi_R^{(3)}\right\}$, whilst the other related to the real part, $Re\left\{\chi_R^{(3)}\right\}$. The $Im\left\{\chi_R^{(3)}\right\}$ part took the form of a matrix, D_{Im}, of measured spectral points, given by $D_{Im} = C\,S + E$ where $C > 0$ was the $n\ x\ p$ matrix of absolute volume concentrations, with n being the number of chemical components considered within the algorithm; $S > 0$ was the $s\ x\ n$ matrix of absolute spectra; and E was the $s\ x\ p$ matrix of concentration error residuals. The $Re\left\{\chi_R^{(3)}\right\}$ part took the form of a spectral point with value given by the spectral average of $Re\left\{\chi_R^{(3)}\right\}$ multiplied by $\sqrt{s}$, guaranteeing that $Re\left\{\chi_R^{(3)}\right\}$ and $Im\left\{\chi_R^{(3)}\right\}$ had the same weight. The NNMF algorithm found the matrices C and S, and minimised E in an iterative way, i.e. the algorithm was repeatedly applied, with the condition that the deviation from unity was minimum for the sum of the volume concentrations. Importantly, FSC^3 implemented random initial guesses, and was thus performed in a completely unsupervised, and therefore unbiased, manner, with no user influence other than selection of the number of components considered. Spatial outputs of FSC^3 were generated as .tif files, whilst spectral outputs were given as .dat files. The software programmes, ImageJ and OriginLab were utilised for compiling of figures from FSC^3 analysis.

The application of HIA processing and analysis to CARS hyperspectral images from biological samples identified the complete spatial distribution of CARS intensity ratios and retrieved spectra showing $Im\left\{\chi_R^{(3)}\right\}$, generating spatial maps of the chemical components which could be identified within the applied spectral range. Figure 3.5 shows an example output from HIA analysis acquired within the CH-stretch region of the Raman spectrum, illustrating the layout of the generated results as they will be presented within this thesis.

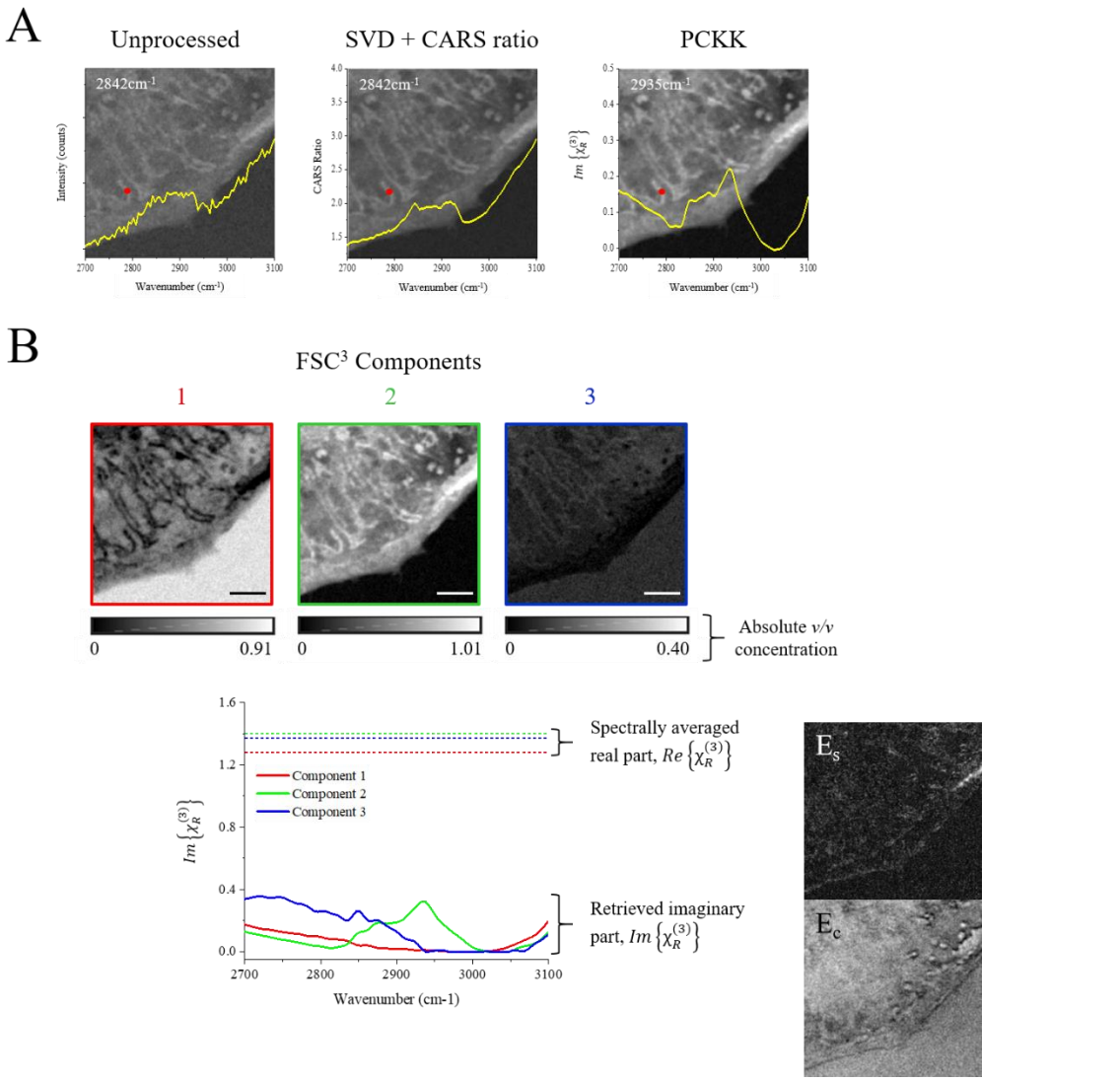

Figure 3.5 | Example FSC^3 spatial and spectral outputs from a HeLa cell sample. Spatial images at the wavenumber giving the maximum intensity and spectra from a single spatial point (*red dot*) are shown for CARS hyperspectral data before processing; after the SVD and CARS ratio calculation steps; and after the PCKK step (A). The results of FSC^3 are also displayed, where three separate chemical components have been considered in the analysis algorithm (B). The spatial outputs of FSC^3 display the distribution of each chemical component with absolute concentrations (*v/v*) given by a grayscale. The respective spectra show the phase-retrieved imaginary part of the normalised CARS susceptibility $Im\left\{\chi_R^{(3)}\right\}$, which are Raman-like in spectral shape, and linear in concentrations of chemical components. The associated real parts of the CARS susceptibility, $Re\left\{\chi_R^{(3)}\right\}$, are given as averages, signified by horizontal dashed lines. The spatial distributions of the spectral and concentration errors are also shown. Based on localisation of signal within spatial images and line-shapes of retrieved spectra, Component 1 is considered to show water, with no observable peaks over the imaged spectral range, and Component 2 is considered to show protein, with a peak present at ~ 2930 cm^{-1}, characteristic of protein-related resonances. Component 3 shows a mixture of all other signals within the image, with some contribution from water and protein, although the signal is weak overall. Scale bars in FSC^3 component images show 4 μm.

4. QUANTITATIVE VISUALISATION OF AN ISOTOPE-LABELLED MOLECULE FROM HYPERSPECTRAL CARS DATASETS USING FSC^3 DATA ANALYSIS

4.1. Introduction

As coherent anti-Stokes Raman scattering (CARS) drives coherent vibration of identical bonds in a sample, structures with dense aggregations of a single type of molecule can be imaged effectively. Lipid droplets have been widely studied by CARS micro-spectroscopy, either in model systems[96] or within cells[79,80,163,164], due to their highly localised structure and abundance of CH-rich triglycerides, both of which contribute to a strong CARS signal. Cytosolic lipid droplets, composed of an organic core of neutral lipid, primarily triglycerides, bound by a monolayer of phospholipids, are formed when a cell is exposed to a high external concentration of lipid and the accessible volume exceeds functional requirement[165].

Given their favourable chemical structure and strong tendency to accumulate into highly concentrated droplets, lipids were selected as a target group of molecules which would be used to assess the capability of a custom-built multimodal CARS system and a novel image analysis strategy, termed "Factorisation into Susceptibilities and Concentrations of Chemical Components" (FSC^3) [73] (see Section 3.7.3 in Chapter 3 for detailed description) for identifying and spatially resolving a deuterium-labelled molecule within a cell. Importantly, FSC^3 identifies the most common chemical groups within a hyperspectral dataset in a completely unsupervised manner and does not require external prompting, thus preventing bias in the analysis and interpretation of data. Uptake and accumulation of deuterium-labelled fatty acids into concentrated lipid droplets ensured maximum signal could be obtained from the carbon-deuterium bonds within the acyl chain of each deuterated fatty acid against the mixed chemical background of the cell. Previous utilisation of the multimodal CARS system and subsequent image analysis has illustrated its ability to detect small changes in lipid droplet composition[79,80,96], owing to the strong signal generated by their high concentrations of carbon-hydrogen bonds. Thus, deuterated fatty acids were studied as proof-of-concept molecules for assessment of deuterium label detection using the multimodal CARS system, laying the foundations for further investigation into distribution, accumulation and turnover of other types of molecules.

Due to their repeating aliphatic chains of carbon and hydrogen, lipids show strong vibrational resonances within the "CH-stretch" region of the Raman spectrum (2600-3400 cm^{-1})

with modes of methine (CH), methylene (CH_2), methyl (CH_3) and vinyl (=CH-) groups[108] (Figure 4.1). However, the presence of so many spectral contributions within this region produces significant overlap, making assignment of individual functional groups challenging. Further information is provided by the fingerprint region (1000-2000 cm^{-1}), with peaks corresponding to carbon and hydrogen groups showing less overlap thus making distinction simpler, although the observed CARS signal within this region is typically one order of magnitude weaker than the CH-stretch region, and thus interference with the non-resonant CARS background can become a problem, reducing signal-to-noise sensitivity and distorting spectral line shapes[166]. Spectral variations within these two regions of the Raman spectra have been used extensively to characterise lipid droplets and obtain information about their chemical composition[79,80,163,164].

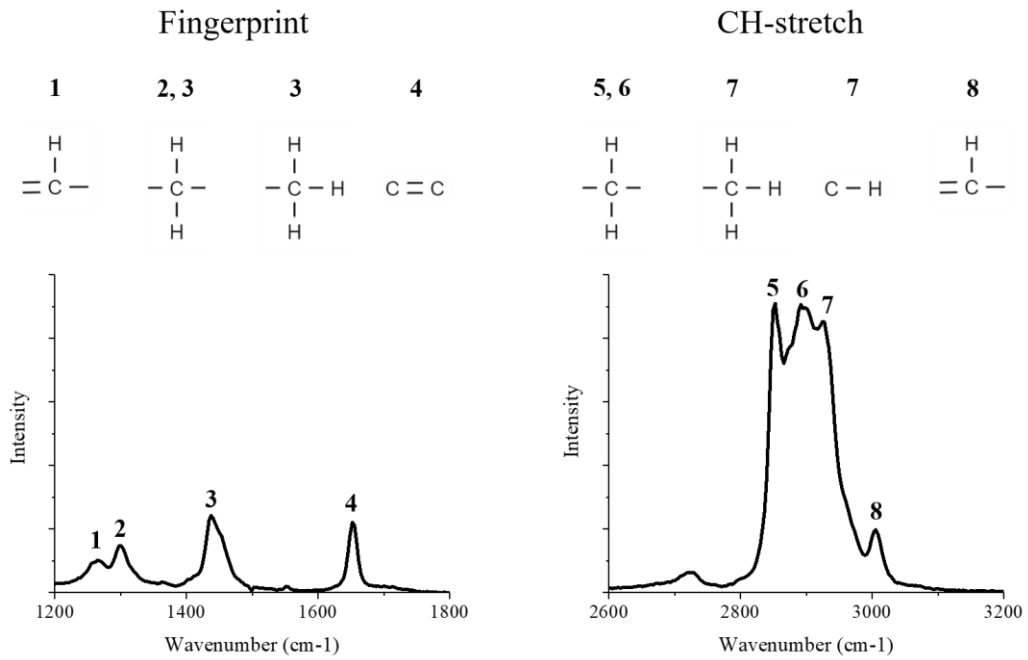

Figure 4.1 | Example Raman spectra from oleic acid showing typical peaks observed within the fingerprint and CH-stretch regions for lipid-based molecules. Spectral overlap within the CH-stretch region can be clearly visualised, and as spectra are plotted on the same intensity scale, the reduced CARS signal intensity within the fingerprint compared to the CH-region can also be observed.

As discussed in Chapter 1, the substitution of hydrogen atoms within the structure of biological molecules with the heavier isotope, deuterium, presents a labelling strategy which, whilst subjecting the molecule to only minimal structural change, offers contrast against a complex chemical background, e.g. the cytosol of a cell. When a hydrogen atom within a

molecular bond is substituted for deuterium, the vibrational resonance of the bond becomes downshifted into the "silent" region of the Raman spectrum (1800-2600 cm^{-1}) (Figure 4.2). Due to the absence of contributions from other endogenous chemical groups within this region, spectral peaks corresponding to carbon-deuterium bonds can be easily distinguished and attributed.

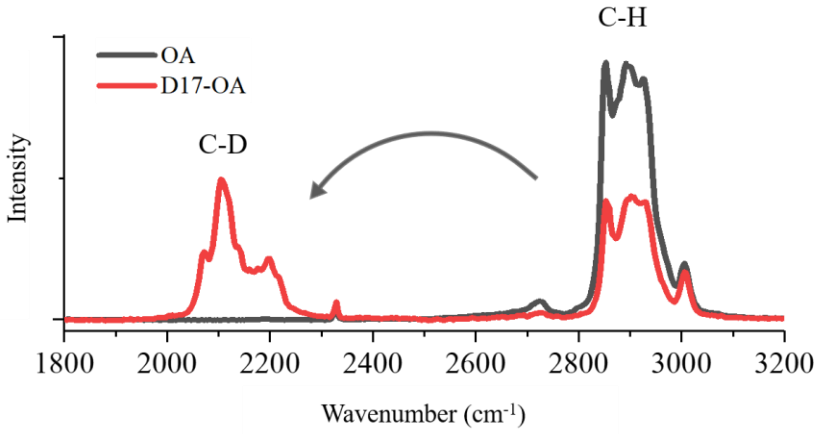

Figure 4.2 | Illustration of CH peak downshift as a result of deuterium incorporation using oleic acid and its deuterated isoform, D17-oleic acid, as an example.

The custom-built multimodal CARS system utilised for all Raman-based data acquisition throughout this project, as well as the novel data processing procedure which is applied to the acquired data for comprehensive analysis, has been discussed in detail in Chapter 3. Through acquisition of hyperspectral CARS datasets, where a series of spatially resolved images were taken at different vibrational frequencies, Raman-like spectra which were linear in concentration of chemical components could be retrieved for each spatial point of the image[94], overcoming the limitation of a non-trivial line-shape characteristic of CARS due to contributions from vibrationally resonant and non-resonant terms[106,107] and enabling detection of small changes in chemical composition.

In this chapter, the novel data analysis method, FSC³ [73,74], was applied to hyperspectral CARS datasets to provide comprehensive, unsupervised and unbiased, quantitative chemical analysis, enabling identification and spatial resolution of a deuterium-labelled fatty acid within cytosolic lipid droplets. The ability of FSC³ to distinguish a chemical component corresponding to carbon-deuterium-related bond vibrations provided evidence for the potential application of a deuterium label for observation of a molecule of interest within a complex chemical cellular environment.

4.2. Raman characterisation of pure deuterated and non-deuterated fatty acids

Raman spectroscopy is a reliable tool for characterisation of biological materials, providing information about intrinsic chemical and physical properties. The technique is driven by inelastic scattering of incident photons by molecular bonds, producing a red-shifted (Stokes) spectrum of scattered light[167]. Acquired spectra provide a reference for interpretation of non-trivial CARS intensity spectra, in which molecular bonds are more difficult to assign due to the interference between resonant and non-resonant terms of the susceptibility $\chi^{(3)}$ [106], as described in detail in Section 2.2 of Chapter 2.

Spontaneous Raman spectra were acquired for pure samples of deuterium-labelled and unlabelled fatty acids to obtain information regarding carbon-deuterium bond-associated peak positions and to observe any other spectral changes resulting from deuterium incorporation. Deuterated and non-deuterated isoforms of three fatty acids were investigated; monounsaturated oleic acid (OA), bi-unsaturated linoleic acid (LA) and tri-unsaturated α-linolenic acid (LNA). Deuterated isoforms of OA, LA and LNA possessed 17, 11 and 14 carbon-deuterium bonds, respectively (see Section 3.1 of Chapter 3 for chemical structures). All fatty acids were imaged in liquid phase, with samples consisting of a droplet of pure lipid mounted between glass, surrounded by air. The acquired spontaneous Raman spectra for each of the six investigated fatty acids are displayed in Figure 4.3 and the attribution of each spectral peak to its associated chemical group is summarised in Table 4.1.

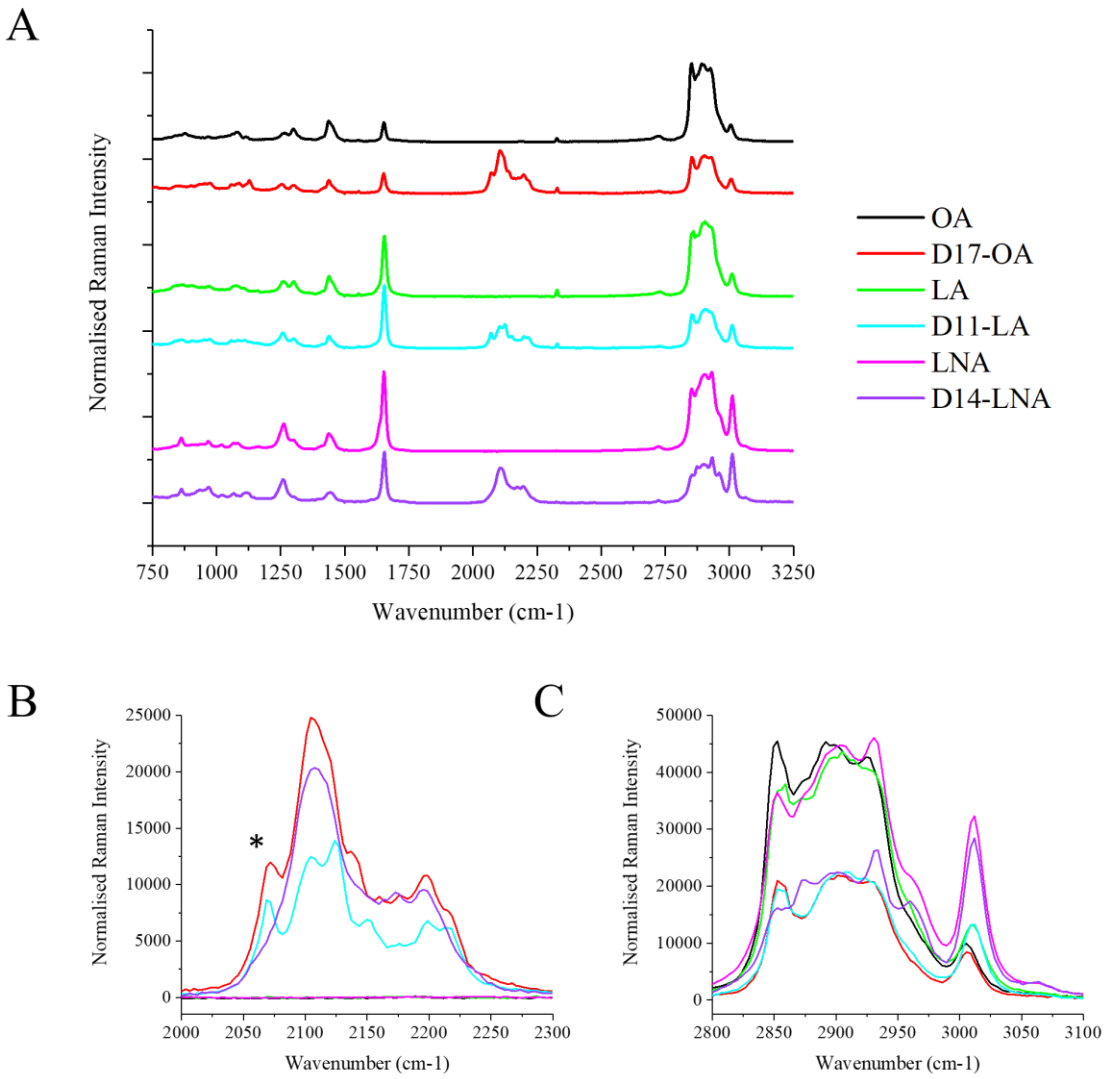

Figure 4.3 | Spontaneous Raman spectra for investigated fatty acids. Full spectra are shown with a spectral range of 750 cm^{-1} to 3250 cm^{-1}, incorporating all three characteristic regions of the Raman spectrum, and spectra are vertically shifted in respect to each other for clarity (A). Spectra are also shown with reduced spectral ranges from 2000 cm^{-1} to 2300 cm^{-1}, targeted around the carbon-deuterium-associated peaks centred at ~ 2100 cm^{-1} within the silent region of the spectrum (B), and from 2800 cm^{-1} to 3100 cm^{-1}, displaying the characteristic carbon-hydrogen-associated peaks within the CH-stretch region of the spectrum (C). Spectra are transposed directly from full spectra but are not vertically shifted, enabling inclusion of Raman intensity values. OA: oleic acid; D17-OA: D17-oleic acid; LA: linoleic acid; D11-LA: D11-linoleic acid; LNA: α-linolenic acid; D14-LNA: D14-α-linolenic acid; colour attributions apply to all spectra within figure.

Table 4.1 | Overview of Raman vibrational resonances for investigated lipids. Assignments are made for peaks from the fingerprint, silent and CH-stretch regions of the Raman spectrum[168–171].

Wavenumber (cm^{-1})	**Assignment**
1260	β =CH
1300	δ CH_2
1400-1500	α CH_2/CH_3
1655	ν C=C
2070-2200	CD-associated resonances
2855	ν_s CH_2
2880	ν_{as} CH_2; Fermi resonance interactions with overtones originating from CH_2 and CH_3 deformations
2930	ν CH_3; ν_{as} CH_2
3010	ν =CH

Symbols for vibrations: ν – stretching (further categorised into ν_s – symmetric stretch; ν_{as} – asymmetric stretch); β – bending/deformation (further categorised into α – scissoring; δ – twisting)

Raman spectra for long-chain fatty acids, such as those investigated within this chapter, have been well-characterised and peak attributions have been reported[168–171]. The fingerprint region from fatty acid spectra typically exhibits peaks at 1300 cm^{-1} and between 1400 cm^{-1} and 1500 cm^{-1}, corresponding to twisting of CH_2 groups and scissoring motions of CH_2/CH_3 groups, respectively. For each of the fatty acids shown in Figure 4.3, the CH_2 twist peak divides into two peaks at 1260 cm^{-1} and 1300 cm^{-1}, attributed to =CH bending and CH_2 twisting, respectively, due to unsaturation within the acyl chain. For LNA, the peak at 1260 cm^{-1} appears larger than the peak at 1300 cm^{-1} due to a greater degree of unsaturation in comparison to both OA and LA. Furthermore, for D14-LNA, the =CH bending peak completely overwhelms the CH_2 twisting peak due to both the high degree of unsaturation and the selective replacement of CH_2 groups with CD_2 groups. Similarly, the peak present at 1660 cm^{-1} corresponds to stretching of C=C bonds, and thus shows increasing intensity with increasing degree of unsaturation. Subtle differences are also apparent when comparing each of the deuterated fatty acids with their non-deuterated counterparts: the peaks at 1300 cm^{-1} and 1400-1500 cm^{-1} show a lower intensity in all deuterated fatty acids due to fewer CH_2 and CH_3 groups present within their chemical structures as a result of deuterium incorporation within the acyl chain.

Peaks within the CH-stretch region are more difficult to attribute due to a large degree of overlap between vibrational resonances. Figure 4.3C shows an overlay of the CH-associated

peaks for each of the investigated fatty acids with a reduced spectral range, enabling clear visualisation of spectral line-shapes. The peak at 2855 cm^{-1} is attributed to CH_2 symmetric stretch; the peak at 2880 cm^{-1} is attributed to a combination of CH_2 asymmetric stretch vibrations and Fermi resonance interactions with overtones originating from CH_2 and CH_3 deformations; and the peak at 2930 cm^{-1} is generated by overlap between CH_3 stretch vibrations and CH_2 asymmetric stretch vibrations[96]. These three peaks show reduced intensity in the Raman spectra from each of the deuterium-containing fatty acids, giving a reduced total area within the CH-stretch region, due to a reduced total number of carbon-hydrogen bonds as a result of deuterium incorporation[163]. Finally, the peak at 3010 cm^{-1} is attributed to stretching of =CH and consequently increases in intensity as degree of unsaturation increases.

As previously discussed, incorporation of a deuterium atom induces a down-shift of the CH-associated peaks from the CH-stretch region of the Raman spectrum into its silent region. Thus, for the deuterated isoform of each fatty acid, a CD-associated peak is present, centred around 2100 cm^{-1}. These peaks can be visualised more clearly in Figure 4.3B, where CD-associated peaks from each of the deuterated fatty acids are overlaid with a reduced spectral range. As is observed in the CH-stretch region, the CD-associated peaks show overlap between vibrational resonances, making assignment of peaks challenging. Literature characterising CD-associated peaks is limited, but through examination of the spontaneous Raman spectra for each of the investigated deuterium-labelled fatty acids, which differ in their chemical structure, some conclusions can be reached. The chemical structures for the deuterated fatty acids, shown in Section 3.1 of Chapter 3, reveal that whilst D17-OA and D11-LA possess a deuterated methyl group (CD_3) at the 18th carbon, D14-LNA contains deuterium at carbons 2-8 at the carboxylic acid end of the acyl chain, and thus does not possess a comparable CD_3 group. The acquired Raman spectra therefore indicate that the peak at 2070 cm^{-1} (indicated by an asterisk in Figure 4.3) corresponds to CD_3-related resonances, owing to its absence from the D14-LNA spectrum. The main peak at 2100 cm^{-1} and the shoulder around 2200 cm^{-1} are present in spectra from all three of the deuterated fatty acids and are therefore considered to correspond to C-H and CH_2 stretching vibrations. It should also be noted that the very small peak at 2330 cm^{-1} corresponds to nitrogen present within the glass of the microscope slide and coverslip and is not related to CD-associated resonances.

4.3. Fluorescence confirmation of lipid droplet depletion and uptake of newly introduced fatty acids

CARS microscopy has become recognised as an imaging strategy which can be employed within biological systems to provide detailed information about the chemical composition of a variety of structures. Consequently, the previously described multimodal CARS microscopy system and FSC^3 data analysis algorithm have been developed and utilised for identification and observation of molecules within cells. The existence of numerous chemical components at unknown concentrations with widely differing vibrational spectra within cell systems makes interpretation of experimental data significantly more challenging compared to working with pure droplets comprising only a single chemical species. Thus, the ability of hyperspectral CARS, combined with subsequent data processing and analysis procedures, to observe intracellular accumulation of deuterated fatty acid into cytosolic droplets within a cellular system was assessed using a HeLa cell line. HeLa cells have been extensively studied for many years and their organelles have been visualised using a wide range of staining techniques. Thus, without the necessity for a study-specific cell type, HeLa cells provided a robust and well-characterised cell line for assessment of intracellular visualisation of deuterated fatty acid molecules.

As a prerequisite to CARS imaging, uptake and storage of exogenously applied deuterated and non-deuterated fatty acids was confirmed using fluorescence imaging. As described in Section 3.3.2 of Chapter 3, HeLa cells were lipid-starved for an 18-hour time period through use of lipid-free foetal bovine serum-supplemented growth media, followed by a further 18-hour incubation period in the same growth medium supplemented with one of the investigated deuterated or non-deuterated fatty acids. A triple-stain of LipidTOX Red, FITC-labelled concanavalin A and DAPI was then applied for visualisation of lipid droplets, cell surface and nuclei, respectively.

Figure 4.4 shows spatially resolved fluorescence images for HeLa cells incubated with each of the investigated fatty acids. Fluorescent signal from DAPI, concanavalin A and LipidTOX Red channels are shown, along with an RGB overlay combining the three stains. Cells treated with deuterated and non-deuterated isoforms of each fatty acid are shown together with corresponding lipid-depleted cells which remained in lipid-depleted growth medium for the full 36-hour duration. These cells illustrate depletion of visible lipid droplets prior to treatment with investigated fatty acids, ensuring that cells form lipid droplets with the maximum amount of the desired fatty acid. Uptake and storage of each deuterated fatty acid is comparable to their non-deuterated counterpart, with all lipid-treated cells forming well-defined cytosolic droplets. These fluorescence images provide evidence for lipid uptake and storage into droplets, but as previously

discussed, they are unable to provide chemical information about the different lipids comprising the visible droplets and thus cannot be used to distinguish deuterated lipid-containing droplets from those comprised of non-deuterated lipid.

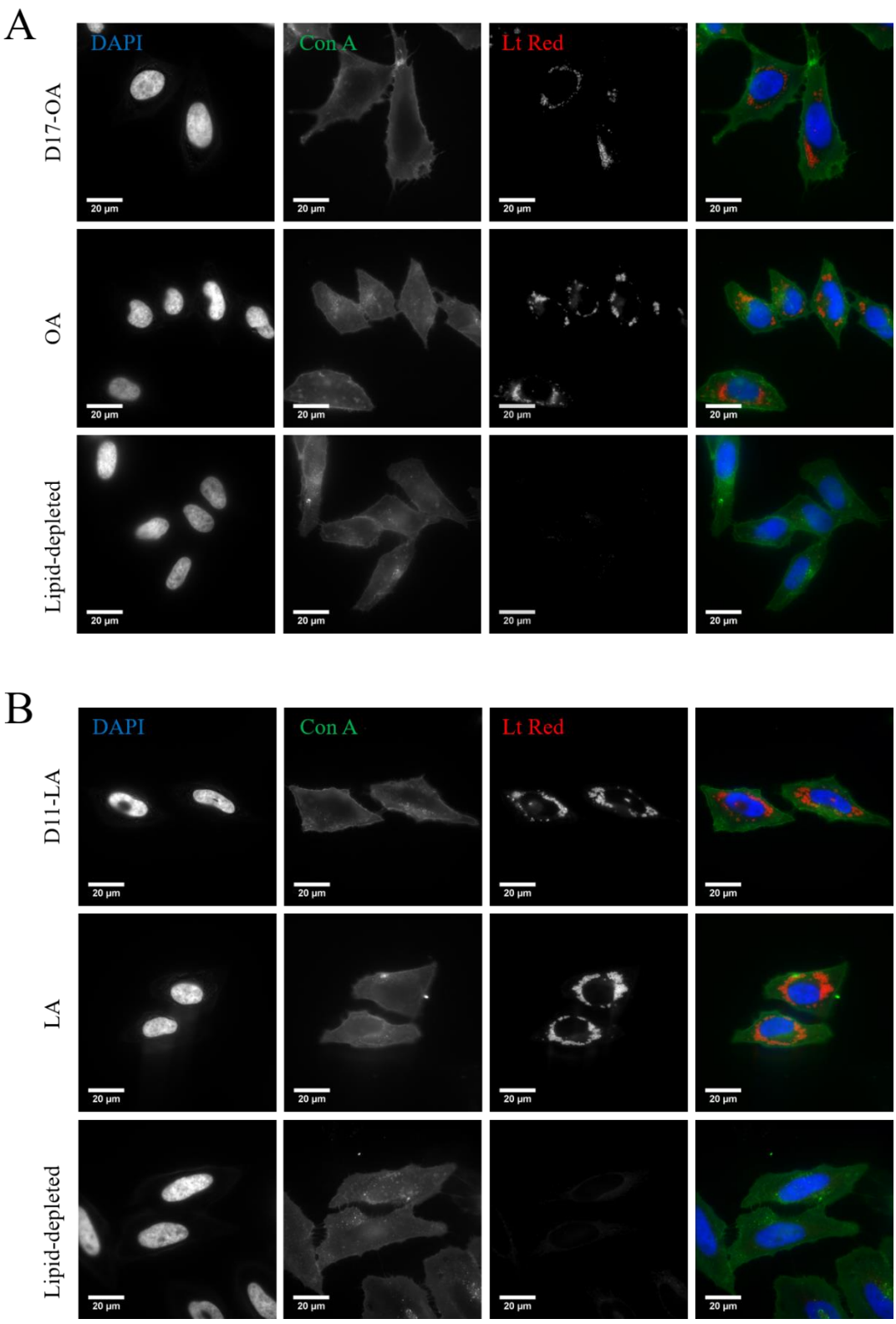

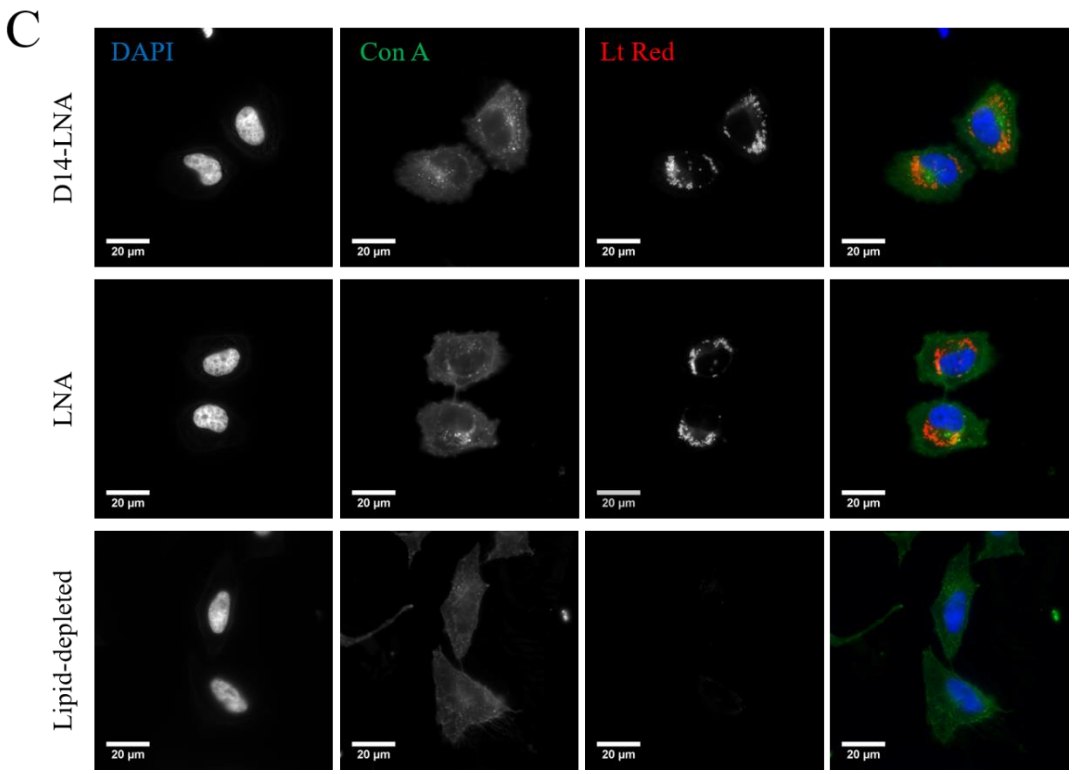

Figure 4.4 | Fluorescence images of triple-stained HeLa cells confirming uptake and storage of OA and D17-OA (A), LA and D11-LA (B), and LNA and D14-LNA (C) into well-defined cytosolic droplets, as well as initial depletion of visible droplets. HeLa cells were fluorescently labelled with the nuclear probe, DAPI (blue channel), the cell surface marker, FITC-labelled concanavalin A (green channel), and the neutral lipid stain, LipidTOX Red (red channel). Images were acquired at 100x, with scale bars showing 20 µm. OA: oleic acid; D17-OA: D17-oleic acid; LA: linoleic acid; D11-LA: D11-linoleic acid; LNA: α-linolenic acid; D14-LNA: D14-α-linolenic acid.

4.4. Hyperspectral CARS and FSC^3 data analysis for quantitative observation of deuterium-labelled lipids

Hyperspectral CARS microscopy provides images with a high spatial resolution and chemical specificity[94], and when combined with data processing and analysis techniques, it can be used to produce quantitative maps of chemical components[73,74]. Thus, the capability of this imaging strategy to identify a chemical component corresponding to carbon-deuterium bond vibrations, and hence a deuterium-labelled molecule, was assessed. HeLa cells were exposed to exogenous deuterated or non-deuterated fatty acids and hyperspectral CARS datasets were acquired from their cytosolic lipid droplets in order to obtain information about their chemical composition, in complete absence of fluorescent markers.

Figure 4.5 shows single wavenumber CARS images acquired from HeLa cells treated with OA and D17-OA (A), LA and D11-LA (B), and LNA and D14-LNA (C) at 2150 cm^{-1} and 2850 cm^{-1}, the vibrational resonances of carbon-deuterium and carbon-hydrogen bonds, respectively. Signal can be observed from lipid droplets within the 2150 cm^{-1} images from cells treated with D17-OA, D11-LA and D14-LNA, but not from the cells treated with OA, LA and LNA, whilst signal is visible within lipid droplets from all investigated cells at 2850 cm^{-1} due to the presence of carbon-hydrogen bonds within the structures of both deuterated and non-deuterated isoforms of each fatty acid. Thus, single wavenumber CARS can be employed to visualise deuterated lipid within a cell and differentiate it from non-deuterated lipid, however, this is the extent of the chemical information provided, and although signal is observed from C-H and C-D bonds within lipid droplets, it is not possible to accurately determine the type of lipid present. Furthermore, the observed signal at 2150 cm^{-1} is weak compared to that observed at 2850 cm^{-1}, which may limit identification of deuterated molecules which are not as well suited to CARS imaging as lipid molecules.

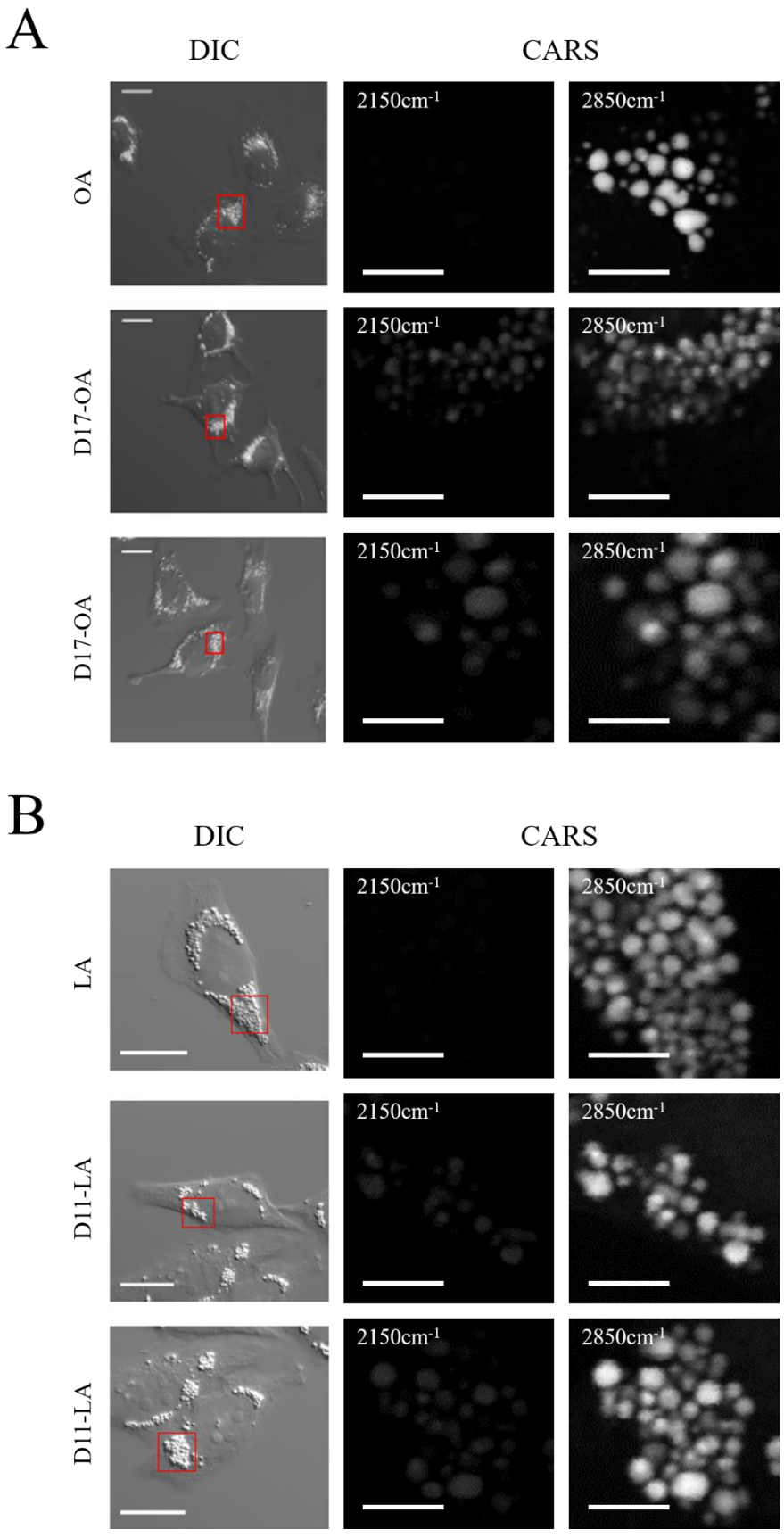
A
DIC
CARS
2150cm-1
2850cm-1
OA
D17-OA
D17-OA
B
DIC
CARS
2150cm-1
2850cm-1
LA
D11-LA
D11-LA

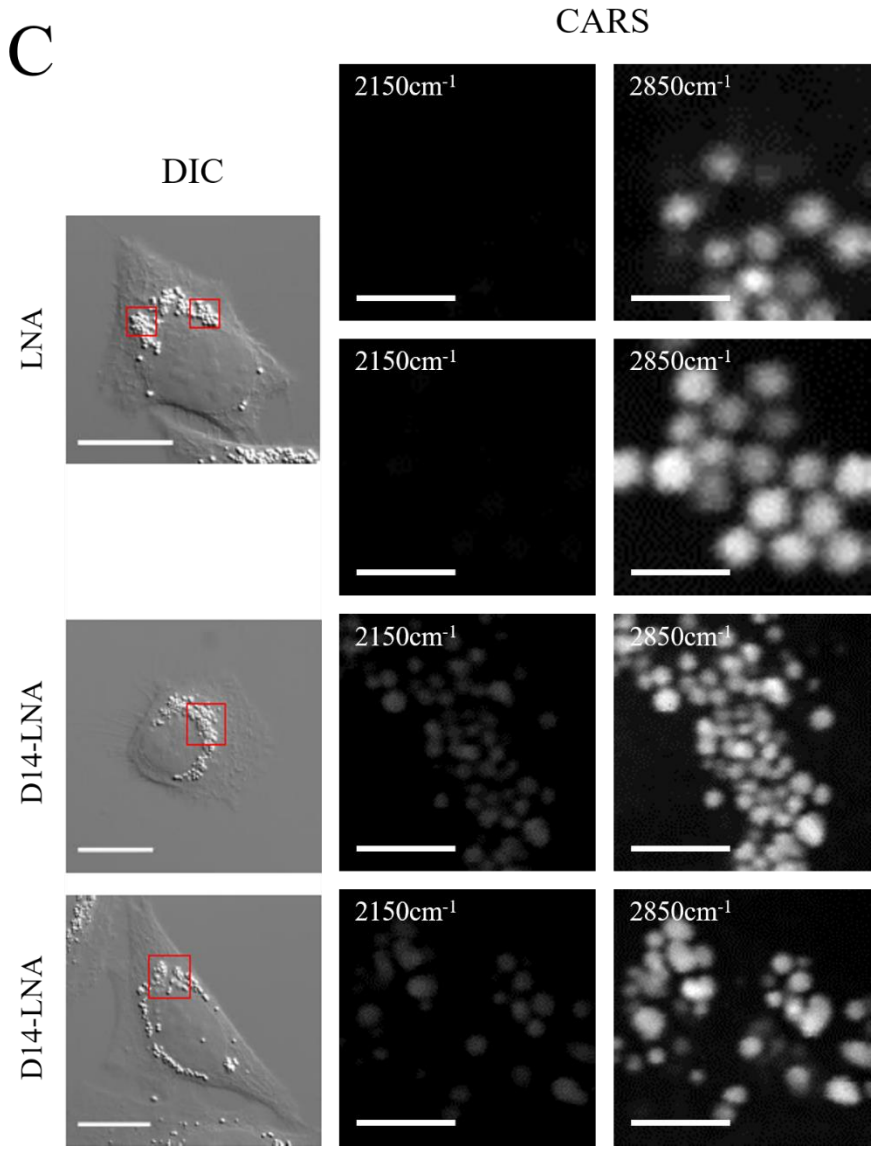

Figure 4.5 | Single wavenumber CARS images acquired from lipid droplets of OA- and D17-OA-treated HeLa cells (A), LA- and D11-LA-treated HeLa cells (B), and LNA- and D14-LNA-treated HeLa cells at 2150 cm^{-1} and 2850 cm^{-1}, targeting C-D and C-H bonds, respectively. DIC images show whole cells and the lipid-rich regions selected for hyperspectral CARS acquisition. Scale bars show 20 µm in DIC images and 4 µm in FSC^3 images (except lowest row of A and upper two rows of C where they instead show 2 µm).

Hyperspectral CARS can achieve superior chemical specificity compared to single wavenumber CARS by generating spectra for each pixel within an image, and the observed peak variations can be utilised to spatially resolve chemical groups. However, as discussed in detail in Chapter 2, spectra acquired by CARS appear altered from those acquired by spontaneous Raman due to the presence of a non-resonant background, and consequently post-acquisition processing is required to generate more Raman-like spectra which are linear in concentrations of chemical components and can be more easily interpreted. The FSC^3 data analysis algorithm can then be applied to the processed hyperspectral CARS data to generate quantitative maps of chemical components. Thus, hyperspectral CARS datasets were obtained from the same fields of view as in Figure 4.5 through acquisition of XY images at a series of wavenumbers, giving a spectrum for each pixel of the spatial image. Following post-acquisition processing of the hyperspectral CARS data to give Raman-like spectra, FSC^3 was applied to the processed hyperspectral CARS data for identification of independent chemical components and their volume concentrations in an unsupervised manner. The chemical composition of lipid droplets from cells treated with deuterated and non-deuterated fatty acids were directly compared to assess the ability of FSC^3 to identify a chemical component corresponding to CD-bond vibrations. As discussed in Section 3.6 of Chapter 3, the multimodal CARS system featured three separate bandpass filters, specifically set up for imaging within each of the three characteristic regions of the Raman spectra, namely the fingerprint, silent and CH-stretch regions. An "intermediate" single-band filter (Semrock FF01-593/40) was utilised to specifically target the silent region of the Raman spectrum (1800-2700 cm^{-1}) where the C-D resonance is situated (~ 2100 cm^{-1}) by excluding light below wavelengths 570 nm and above 620 nm.

Figure 4.6 shows the spatial and spectral outputs of unsupervised FSC^3 analysis applied to lipid droplets from HeLa cells treated with OA and D17-OA, assessing the ability of FSC^3 to identify and spatially resolve a chemical component corresponding to carbon-deuterium bond resonances against the complex chemical background of a cell, whilst also illustrating the steps taken to determine the optimum FSC^3 settings. The spectral output of FSC^3 analysis provided highly accurate chemical specificity, which could not only identify presence or absence of carbon-deuterium bonds, as in single wavenumber CARS, but could also provide more detailed information regarding the type of deuterium-labelled molecule being studied. Figures 4.6A and 4.6B show the results of FSC^3 analysis when applied to OA- and D17-OA-treated cells separately, whilst Figures 4.6C-E show the FSC^3 outputs when OA- and D17-OA-treated cells are analysed together. When FSC^3 analysis was applied to OA- or D17-OA-treated cells separately, the most common spectra within the OA- or D17-OA-treated cells were identified, generating spectra that were unique to each of the groups. In contrast, when FSC^3 is applied to OA- and D17-OA-treated

cells simultaneously, the most common spectra across all of the samples were identified, thus generating a combination of spectra which were unique and common to OA- and D17-OA-treated cells. Furthermore, as described in Section 3.7.3 of Chapter 3, the number of separate chemical components which the FSC^3 algorithm attempted to identify was controlled manually by the user, and consequently the process by which this number was decided upon relied on a combination of prior knowledge of the number of different chemical groups expected to be present within the field of view, and a trial and error process whereby the algorithm was run multiple times considering a range of different numbers of components, thus permitting determination of a suitable number of components which could effectively resolve the chemicals of interest. This process is also illustrated within Figure 4.6, where FSC^3 results are displayed using different numbers of components. FSC^3 outputs from independent analysis of OA- and D17-OA-treated cells are shown with consideration of three and six components in Figures 4.6A and 4.6B, respectively, whilst outputs from combined analysis of OA- and D17-OA-treated cells are shown with consideration of three, four, six and eight components in Figures 4.6C, 4.6D, 4.6E and 4.6F, respectively. All datasets were acquired over the spectral range, 1800-3000 cm^{-1}, incorporating both CD- and CH-associated peaks, enabling identification of chemical components corresponding to both deuterated and non-deuterated lipid, and DIC images were acquired for initial visualisation of whole cells and selection of lipid-rich regions for hyperspectral CARS imaging.

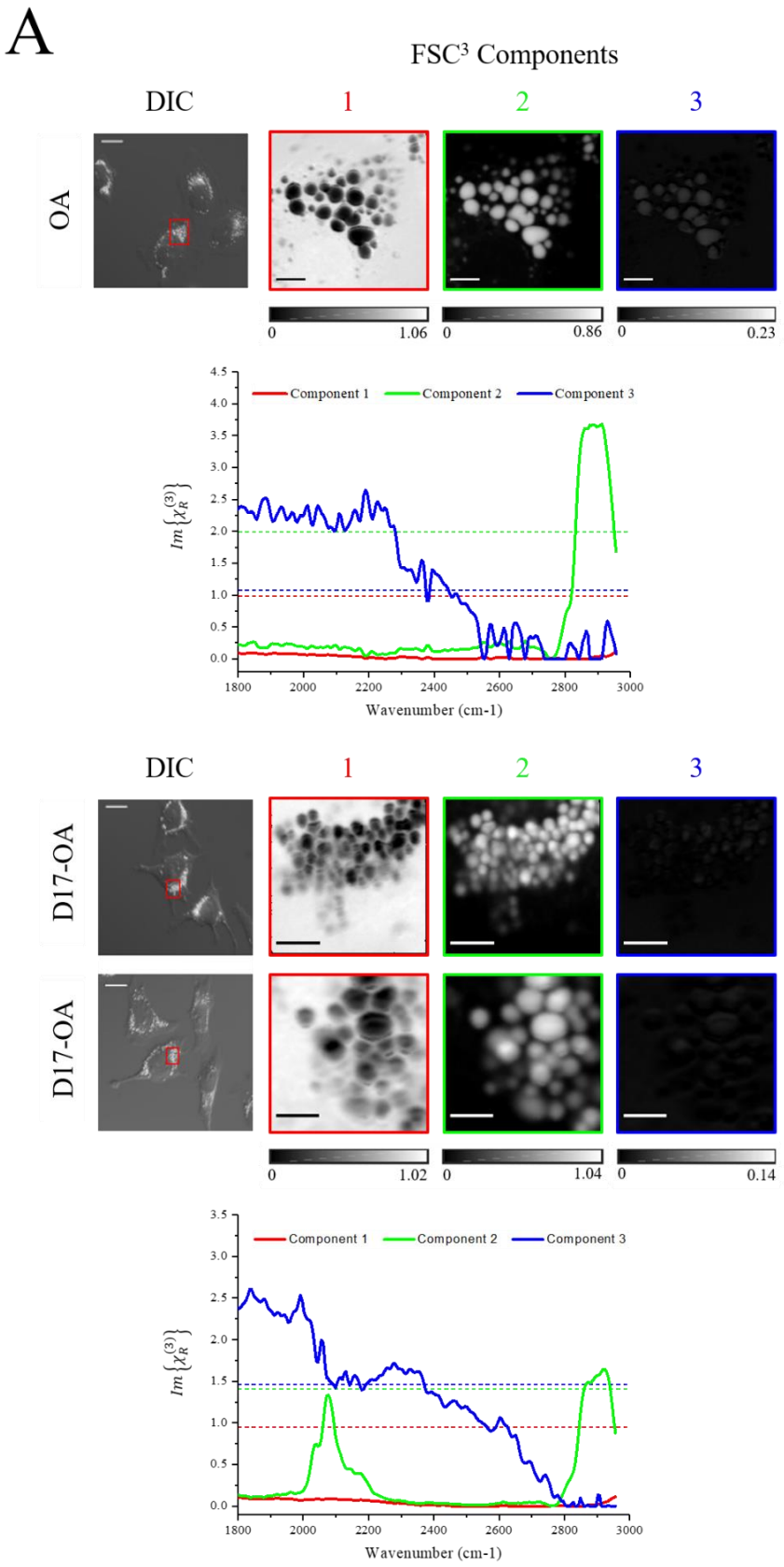
A
FSC3 Components
DIC
1
2
3
OA
0
1.06
0
0.86
0
0.23
Component 1
Component 2
Component 3
Im{χR(3)}
Wavenumber (cm-1)
DIC
1
2
3
D17-OA
D17-OA
0
1.02
0
1.04
0
0.14
Component 1
Component 2
Component 3
Im{χR(3)}
Wavenumber (cm-1)

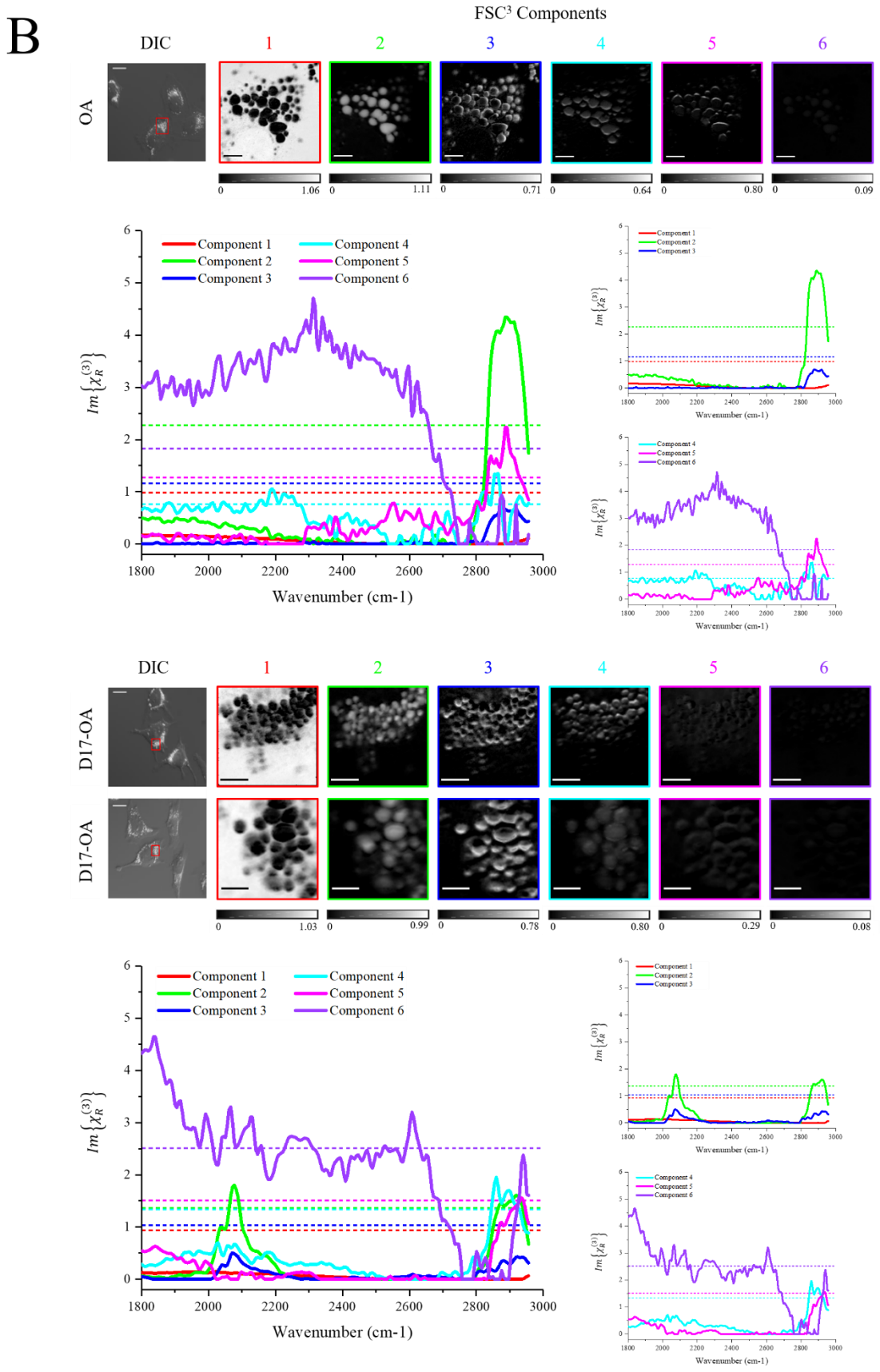
B
FSC³ Components
DIC
1
2
3
4
5
6
OA
0
1.06
0
1.11
0
0.71
0
0.64
0
0.80
0
0.09
Component 1
Component 2
Component 3
Component 4
Component 5
Component 6
Im{χR(3)}
Wavenumber (cm-1)
1800
2000
2200
2400
2600
2800
3000
D17-OA
D17-OA
0
1.03
0
0.99
0
0.78
0
0.80
0
0.29
0
0.08

C

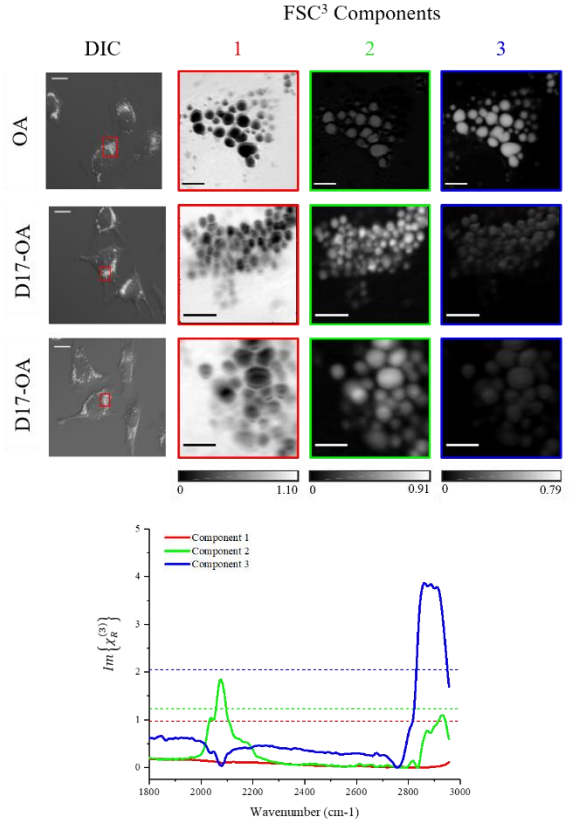
FSC3 Components
DIC
1
2
3
OA
D17-OA
D17-OA
0
1.10
0
0.91
0
0.79
Component 1
Component 2
Component 3
Im{χR(3)}
Wavenumber (cm-1)

D

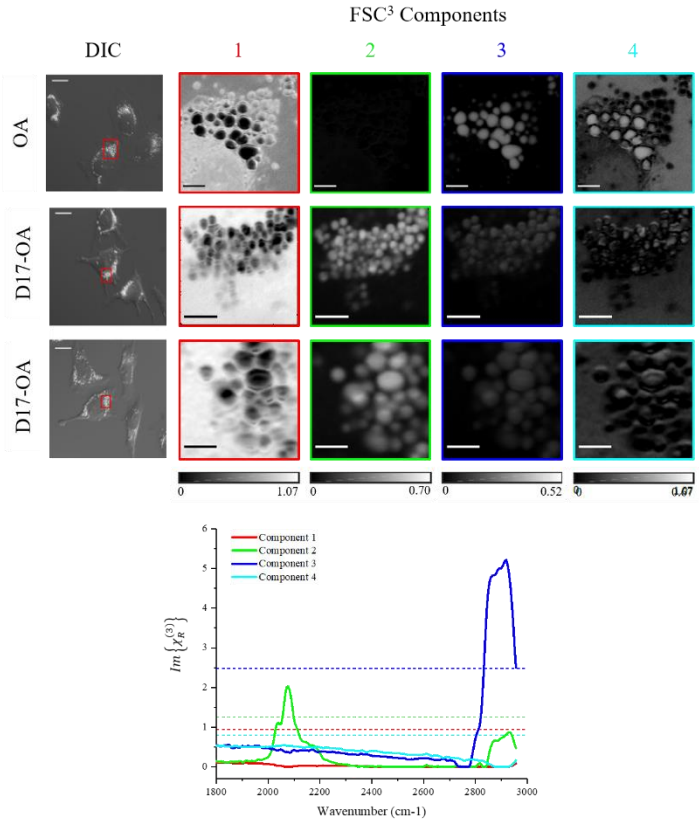
FSC3 Components
DIC
1
2
3
4
OA
D17-OA
D17-OA
0
1.07
0
0.70
0
0.52
Component 1
Component 2
Component 3
Component 4
Im{χR(3)}
Wavenumber (cm-1)

E

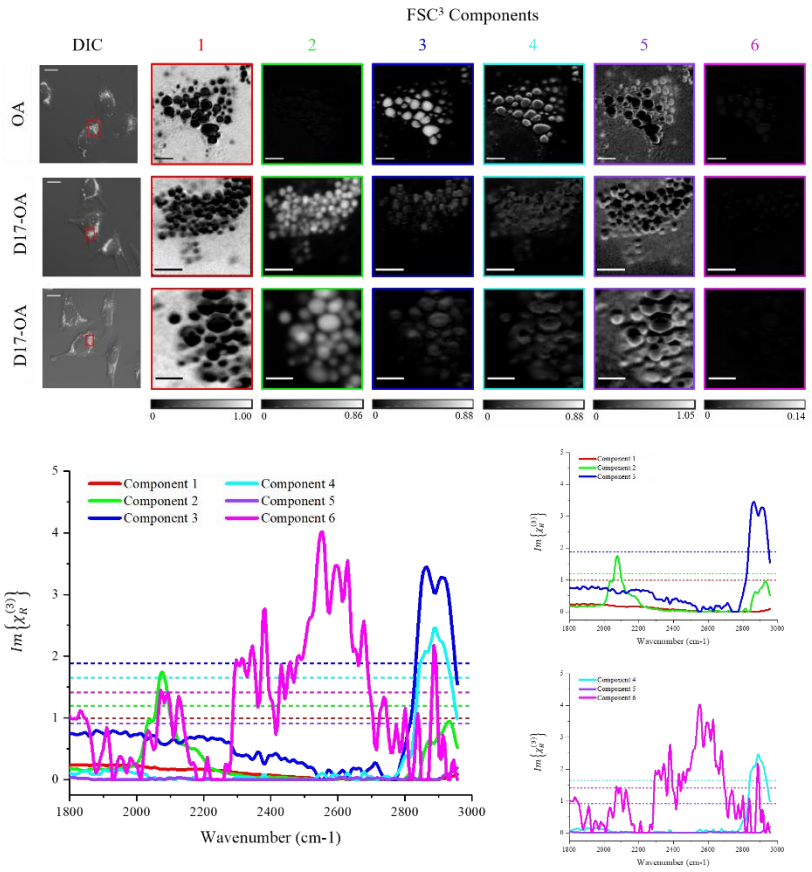
FSC³ Components
DIC
1
2
3
4
5
6
OA
D17-OA
D17-OA
0 1.00
0 0.86
0 0.88
0 0.88
0 1.05
0 0.14
Component 1
Component 2
Component 3
Component 4
Component 5
Component 6
$Im\{\chi_R^{(3)}\}$
Wavenumber (cm-1)
1800
2000
2200
2400
2600
2800
3000

F

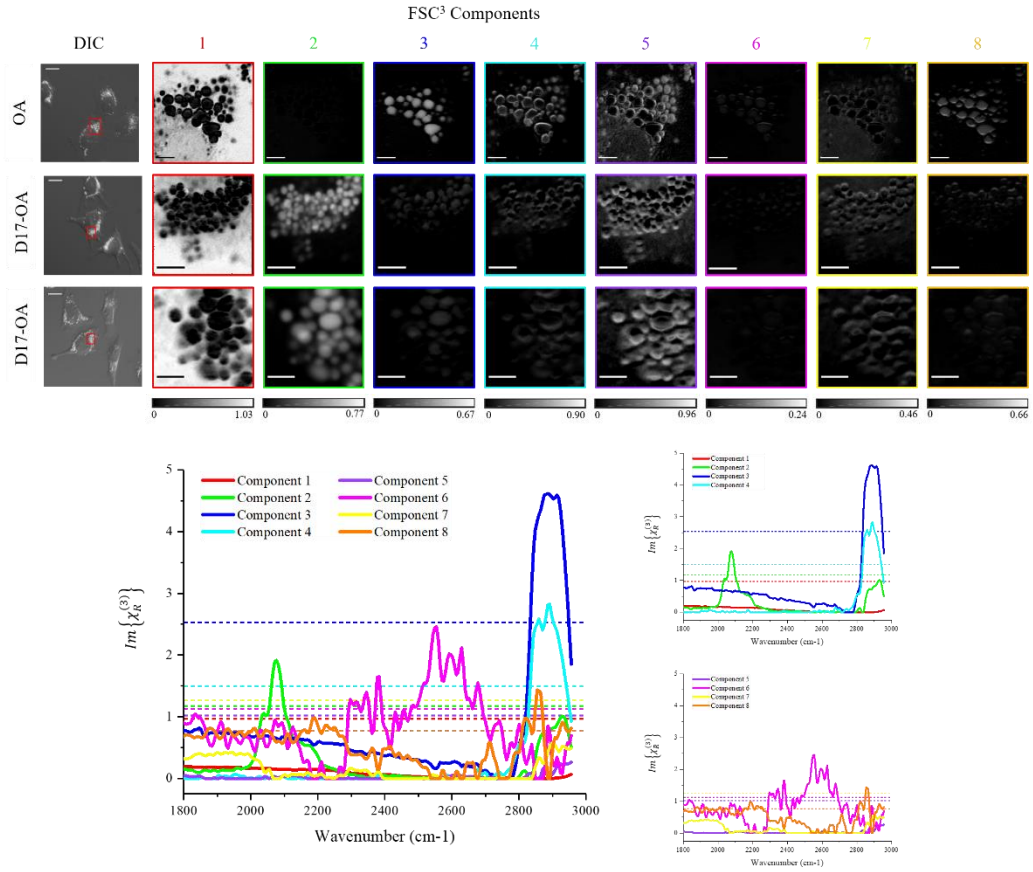
FSC³ Components
DIC
1
2
3
4
5
6
7
8
OA
D17-OA
D17-OA
0 1.03
0 0.77
0 0.67
0 0.90
0 0.96
0 0.24
0 0.46
0 0.66
Component 1
Component 2
Component 3
Component 4
Component 5
Component 6
Component 7
Component 8
$Im\{\chi_R^{(3)}\}$
Wavenumber (cm-1)
1800
2000
2200
2400
2600
2800
3000

G

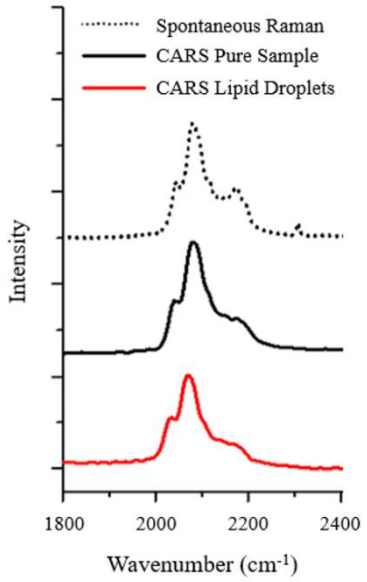

Figure 4.6 | Spatial and spectral outputs from unsupervised FSC^3, assessing its ability to identify and spatially resolve a CD-associated chemical component from a hyperspectral CARS dataset. FSC^3 results are shown when OA- and D17-OA-treated cells are analysed separately with three (A) and six (B) chemical components considered, and when OA- and D17-OA-treated cells are analysed together with three (C), four (D), six (E) and eight (F) components considered. A spectral range of 1800-3000 cm^{-1} is utilised, targeting the cell-silent region of the Raman spectrum, but enabling inclusion of both CD- and CH-associated peaks. Concentration maps are generated to identify and spatially resolve chemical components which are specified by their representative spectra showing the phase-retrieved imaginary part of the normalised CARS susceptibility $Im\left\{\chi_R^{(3)}\right\}$. Real parts are also shown as averages, represented by horizontal dashed lines. Within Figures A-F, components corresponding to water-based aqueous medium (Component 1), D17-OA (Component 2), and OA (Component 3) are consistently identified, whilst additional components either show variations of these three components (e.g. Component 3 in Figure 4.6B and Component 4 in Figures 4.6E and 4.6F) or background noise. Where six and eight components are considered, the retrieved spectra are also plotted on two separate graphs for clarity. Volume concentration ranges for spatially resolved images are shown on a grayscale and DIC images show whole cells and the lipid-rich regions selected for hyperspectral CARS acquisition. A comparison between the CD peak observed within the retrieved spectrum of the D17-OA component in Figure 4.6D, a single CARS spectrum acquired directly from a pure droplet of D17-OA, and the spontaneous Raman spectrum acquired from pure D17-OA in Figure 4.3 is also provided (G), showing conservation of spectral line-shape across the spectra. Scale bars show 20 μm in DIC images and 4 μm in FSC^3 images.

Figure 4.6A shows FSC^3 results following independent analysis of OA- and D17-OA-treated cells with three separate chemical components considered in the algorithm. Component 1 is comparable between the OA- and D17-OA-treated samples, showing CARS signal within the area surrounding lipid droplets, as well as no observable peaks within its retrieved spectrum over the acquired spectral range and is consequently considered to represent the aqueous medium surrounding the lipid droplets, comprised primarily of water. Vibrations of the O-H bonds that make up water molecules give a broad Raman peak from approximately 3200 cm^{-1} to 3600 cm^{-1}, outside of the investigated spectral range, hence explaining the absence of peaks from the retrieved spectrum for Component 1. Although the spatially resolved images of Component 2 show similar localisation of signal within lipid droplets, the retrieved spectra differ in their line-shape. The retrieved spectrum from the OA-treated cell shows a strong peak between 2800 cm^{-1} and 3000 cm^{-1}, which is attributed to stretching vibrations of the C-H bonds which are abundant within lipids, and consequently this component can be attributed to OA. The retrieved spectrum for Component 2 from the D17-OA-treated samples also shows a CH peak from 2800 cm^{-1} to 3000 cm^{-1}, although with a lower intensity, as well as a second peak at 2000-2200 cm^{-1}, which is attributed to vibrations of C-D bonds and is thus considered to represent D17-OA. The reduced CH peak intensity results from the reduced total number of C-H bonds in D17-OA compared to OA. Both of the retrieved spectra show similarities to the spontaneous Raman spectra shown in Figure 4.3. Component 3 appears to show some signal within the spatially resolved images from both groups of cells, but the associated spectra are noisy and lack clear spectral features. Consequently, this component is considered not to represent specific chemical groups but instead background noise.

Figure 4.6B also shows FSC^3 results following application to OA- and D17-OA-treated cells independently, but with consideration of six separate chemical components in the analysis algorithm. Components 1 and 2 once again represent the aqueous medium surrounding lipid droplets and the lipid within the droplets, respectively, displaying identical spatial signal and spectral line-shape to the corresponding components in Figure 4.6A. Component 3 also appears to correspond to lipid, with signal observed from droplets within the spatially resolved images from both OA- and D17-OA-treated cells, and a retrieved spectrum showing a CH peak in the OA-treated sample and both CH and CD peaks in the D17-OA-treated sample, although these peaks appear weaker than those observed for Component 2. Component 4 for the D17-OA-treated samples also appears to show a CH-associated peak, whilst the corresponding component for the OA-treated sample shows no spectral features. Component 5 from both OA- and D17-OA-treated samples also shows a CH-associated peak. Finally, Component 6 shows a noisy, featureless spectrum similar to that observed for Component 3 in Figure 4.6A, which is considered to

represent a background signal. Based on several of the components showing CH- or CD-associated peaks in their retrieved spectra, it appears that the FSC^3 algorithm has attempted to separate the lipid component identified in Figure 4.6A into multiple components to meet the selected criteria of six components, and consequently consideration of more components than is required does not appear to offer any additional benefit and may be counterintuitive, potentially compromising interpretation of data outputs. Thus, consideration of three separate components by the FSC^3 algorithm enables the chemical composition within the imaged fields of view to be well-represented.

Figures 4.6C-F show the spatial and spectral FSC^3 outputs when OA- and D17-OA-treated cells were analysed together, enabling direct comparison of chemical composition of the imaged lipid droplets. Figure 4.6C shows the FSC^3 results when three separate chemical components were considered in the analysis algorithm, with Component 1 once again showing signal from the water-based aqueous medium surrounding the droplets. As the OA- and D17-OA-treated cells are analysed together, components corresponding to both deuterated and non-deuterated lipid are given by Component 2 and 3, respectively. Component 2 shows CD- and CH-associated peaks within its retrieved spectrum located at 2000-2200 cm^{-1} and 2800-3000 cm^{-1}, respectively, analogous to the observed spectrum for the deuterated lipid component identified by FSC^3 in Figure 4.6A, where D17-OA-treated cells were analysed individually. Component 3 only shows a CH-associated peak at 2800-3000 cm^{-1} within its retrieved spectrum, as was observed for the lipid component from OA-treated cells in Figure 4.6A. Thus, when the OA- and D17-OA-treated cells are analysed together, separate components can be identified and spatially resolved, one of which is attributed to vibrations of carbon-deuterium bonds. Consideration of three separate chemical components within the FSC^3 algorithm was sufficient for identification of components corresponding to water, OA and D17-OA, however, signal from C-D bond resonance is observed from OA-treated cells. As cells do not endogenously produce molecules containing deuterium, CD-associated signal should not be observed from cells unless they are specifically treated with a deuterated molecule, thus the observed signal may be an artefact of the FSC^3 analysis, owing to consideration of too few components within the algorithm which limits its ability to separate chemical components of interest. Consequently, FSC^3 outputs with inclusion of more than three components within the data analysis were investigated.

Figure 4.6D shows the results of combined FSC^3 analysis of OA- and D17-OA-treated cells with four separate components considered. Components 1, 2 and 3 show spatial and spectral outputs which are comparable to those from the corresponding components observed in Figure 4.6C, displaying distribution of aqueous medium (water), D17-OA and OA, respectively. However, unlike the FSC^3 outputs shown in Figure 4.6C, signal corresponding to C-D bond

vibrations is not observed from lipid droplets of OA-treated cells, likely due to the inclusion of a fourth component which, despite showing some signal within its spatially resolved images, does not show spectral features within its retrieved spectrum and is thus considered to show a background signal which does not correspond to a particular chemical group. As this component appears to show signal within lipid droplets of the OA-treated sample, it is likely than when only three components were considered in the FSC^3 algorithm, signal from this component was incorporated into the D17-OA component, thus producing the observed signal within the CD-associated component in OA-treated cells in Figure 4.6C.

Figures 4.6E and 4.6F show the results of combined FSC^3 analysis of OA- and D17-OA-treated cells with consideration of six and eight separate chemical components, respectively. The spatial and spectral outputs of Components 1, 2 and 3 are preserved with consideration of six and eight components, showing water-based aqueous medium, D17-OA and OA, respectively, and CD-associated signal is not observed within lipid droplets of OA-treated cells. With consideration of both six and eight components, a further component showing a CH-associated peak within its retrieved spectrum is identified (Component 4), which shows observable signal within lipid droplets in the spatially resolved images. Consequently, FSC^3 has attempted to separate the OA component into multiple components in order to fulfil the six-component criteria, as was observed in Figure 4.6B, when six separate components were also considered in the FSC^3 algorithm. The additional components identified in Figures 4.6E and 4.6F do not show consistent localisation of signal within the spatial images or visible peaks within their retrieved spectra and are consequently attributed to background noise. Thus, consideration of more than four separate chemical components does not appear to provide additional chemical information, and separation of components of value into multiple components may limit interpretation of data outputs, consequently suggesting that the consideration of four separate chemical components is sufficient to well-represent the chemical composition within the imaged field of view.

Figure 4.6G shows comparison of CD peak line-shapes between the retrieved spectrum of the D17-OA component in Figure 4.6D, a single CARS spectrum acquired directly from a pure droplet of D17-OA, and the spontaneous Raman spectrum acquired from pure D17-OA in Figure 4.3. The CD peak from Figure 4.6D was selected as four components were determined to be the most suitable number considered in the FSC^3 algorithm, although the CD peak shape was maintained throughout Figures 4.6C-F. The line-shape of the CD-associated peak is well-conserved across the three spectra, illustrating the precision with which FSC^3 can identify a chemical component corresponding to a deuterium-labelled molecule. It has been previously described within this chapter that hyperspectral CARS has the advantage of highly accurate chemical specificity over single wavenumber CARS, and this is confirmed by the level of

similarity between the spectral output of FSC^3 and the CARS/Raman spectra acquired from pure D17-OA. Based on these results, spontaneous Raman spectra from pure materials will continue to be utilised to assist in the interpretation of hyperspectral CARS data and subsequent FSC^3 outputs in future chapters.

It has been shown that FSC^3 can be applied to hyperspectral CARS datasets not only to identify a chemical component corresponding to carbon-deuterium bond vibrations, but also to provide detailed chemical information about the deuterium-containing chemical groups and the type of molecule within which they are found. The Raman spectra acquired from each of the investigated fatty acids in Figure 4.3 showed variations in line-shapes of CD-associated peaks, and therefore D11-LA and D14-LNA were utilised to assess the ability of FSC^3 to distinguish between different deuterium-labelled fatty acids based on differences in CD peak shape. Figure 4.7 shows the outputs of unsupervised FSC^3 analysis applied to lipid droplets from HeLa cells treated with all three of the investigated fatty acids. The spatial and spectral FSC^3 outputs from OA- and D17-OA-treated cells in Figure 4.6D are reincluded in Figure 4.7 to enable direct comparison with results from samples treated with LA/D11-LA and LNA/D14-LNA. Cells treated with deuterated and non-deuterated isoforms of the same fatty acid were analysed together, enabling direct comparison of chemical composition of lipid droplets and identification of carbon-deuterium groups. The main spectral components of the XY images are identified and displayed as spatial concentration maps and representative spectra are retrieved over the range, 1800-3000 cm^{-1}, in order to include peaks corresponding to both carbon-deuterium and carbon-hydrogen bond vibrations. Based on the observed results in Figure 4.6, four separate chemical components were considered in the factorisation algorithm, which was considered the most suitable number to well-represent the lipid composition of the droplets within the field of view. DIC images were again acquired for initial visualisation of whole cells and selection of lipid-rich regions for hyperspectral CARS imaging.

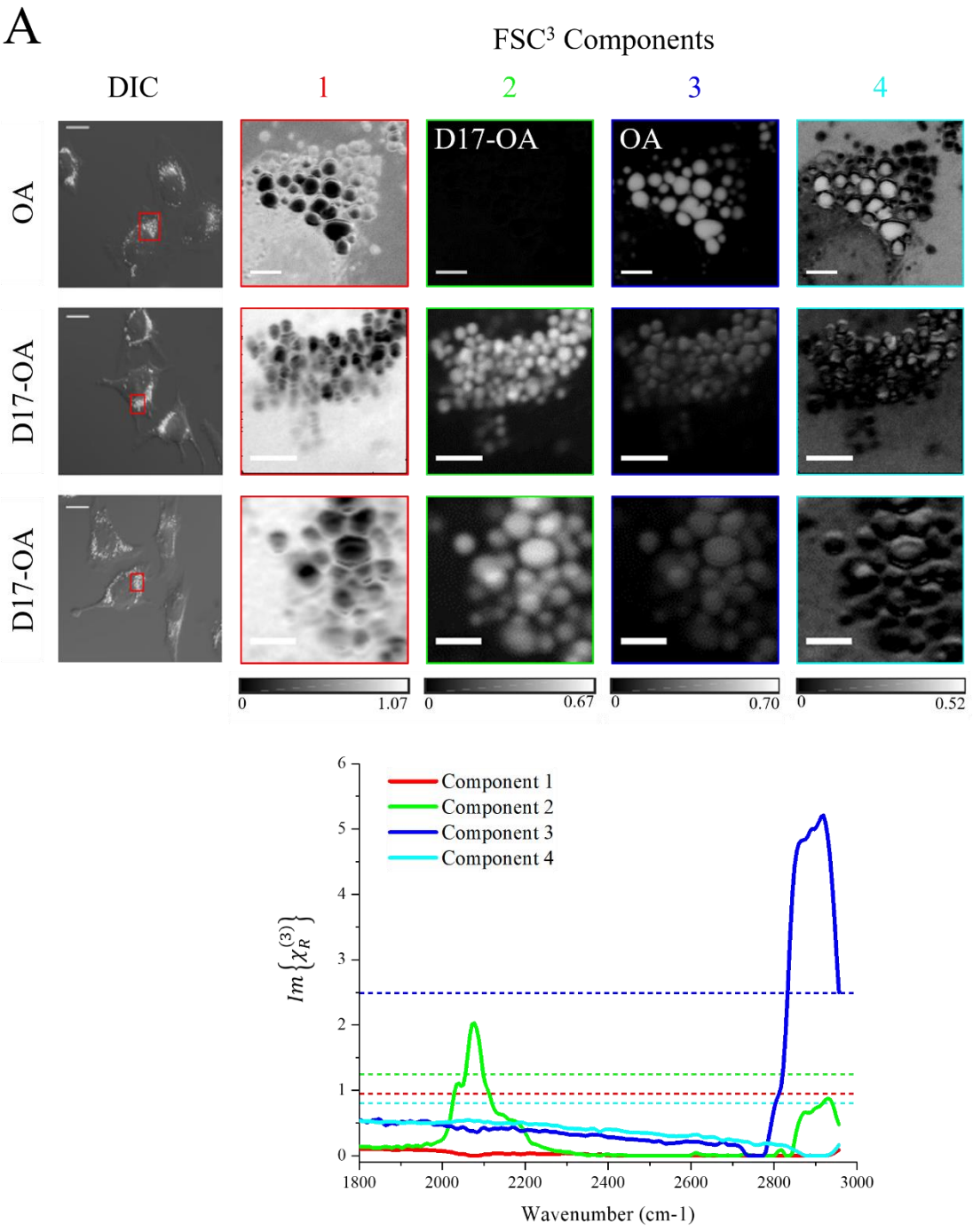
A
FSC3 Components
DIC
1
2
3
4
OA
D17-OA
D17-OA
D17-OA
OA
0
1.07
0
0.67
0
0.70
0
0.52
Component 1
Component 2
Component 3
Component 4
Im{χR(3)}
Wavenumber (cm-1)

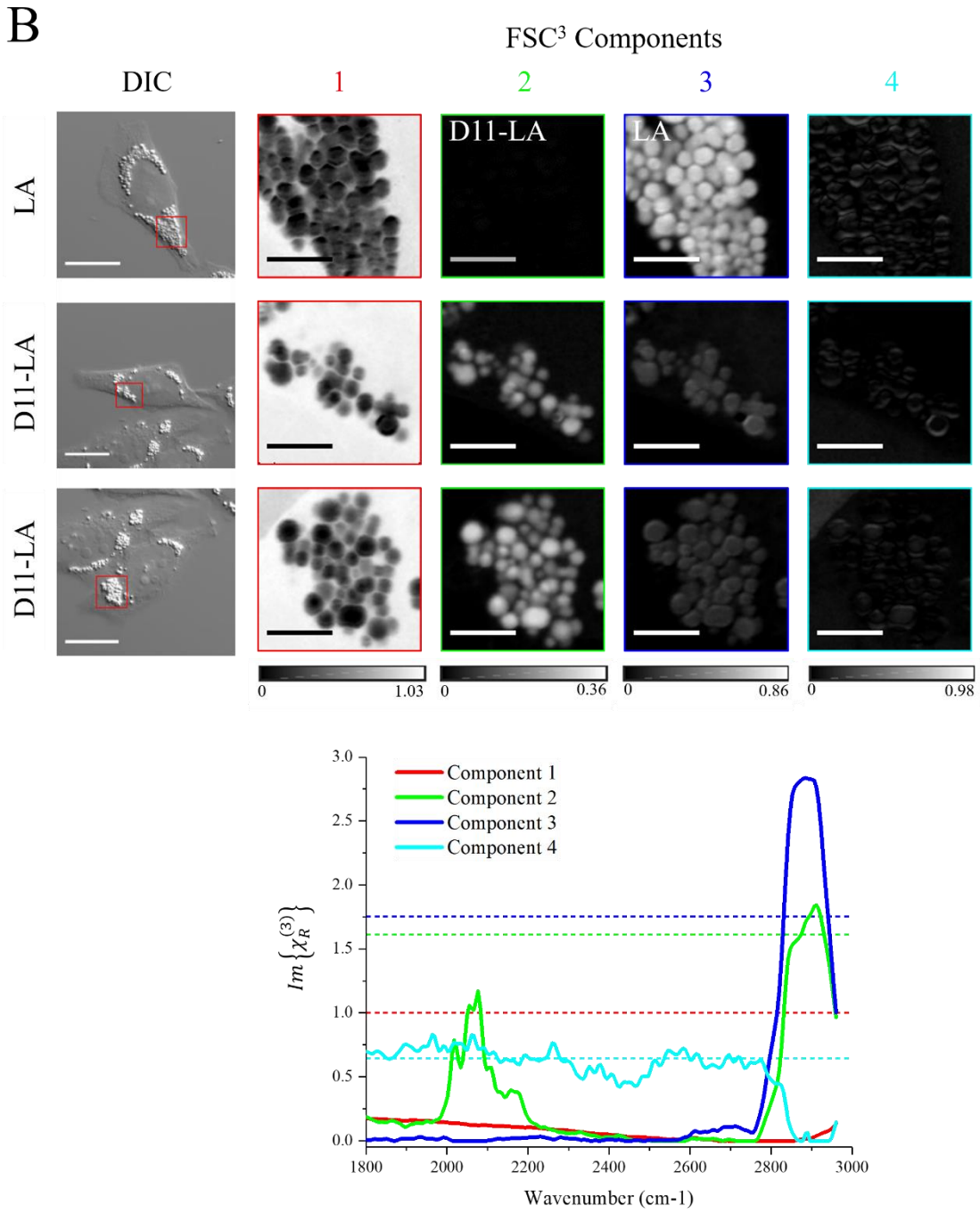
B
FSC³ Components
DIC
1
2
3
4
LA
D11-LA
D11-LA
D11-LA
LA
0
1.03
0
0.36
0
0.86
0
0.98
Component 1
Component 2
Component 3
Component 4
$Im\{\chi_R^{(3)}\}$
3.0
2.5
2.0
1.5
1.0
0.5
0.0
1800
2000
2200
2400
2600
2800
3000
Wavenumber (cm-1)

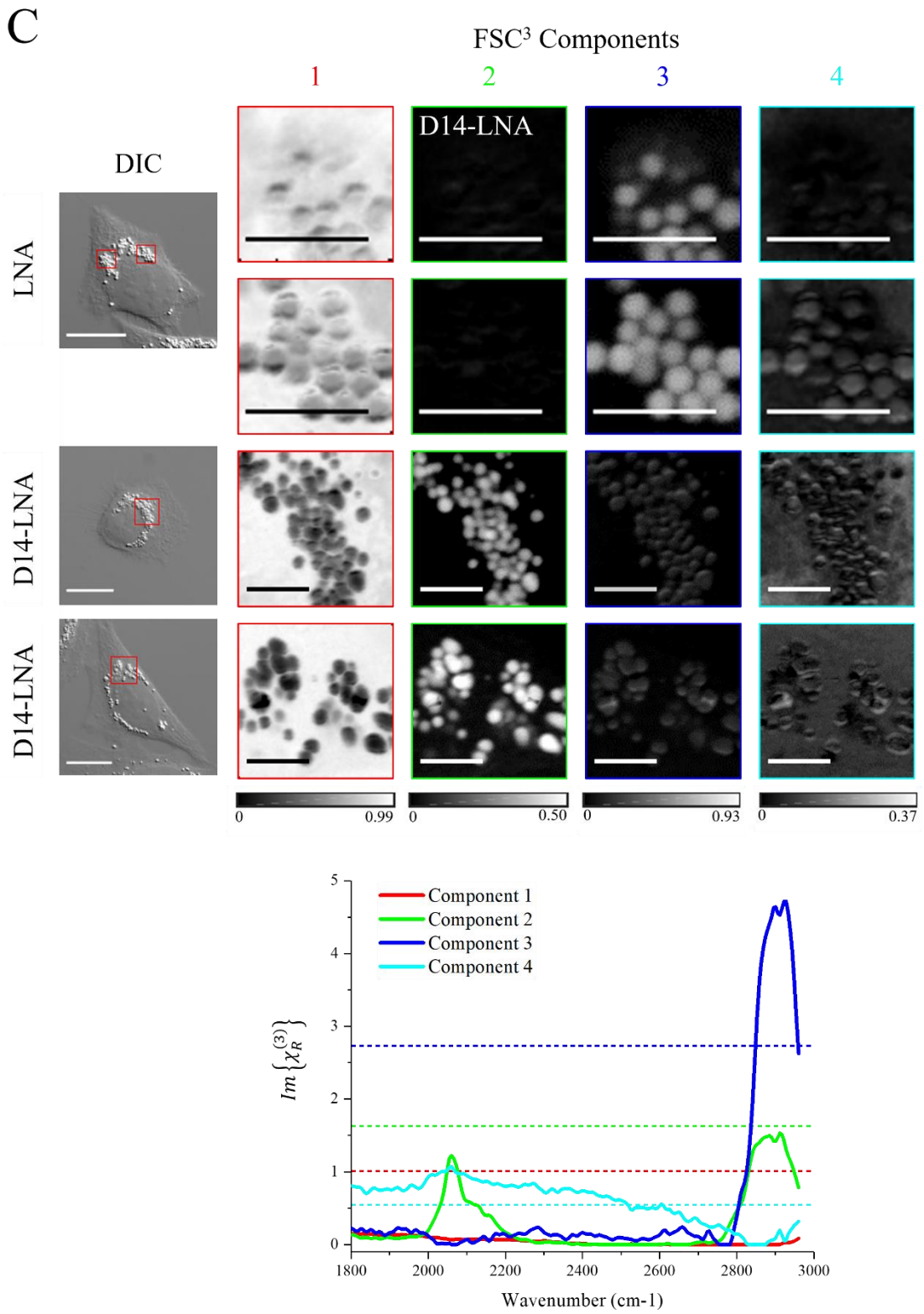
C
FSC3 Components
1
2
3
4
DIC
D14-LNA
LNA
D14-LNA
D14-LNA
0
0.99
0
0.50
0
0.93
0
0.37
Component 1
Component 2
Component 3
Component 4
$Im\{\chi_R^{(3)}\}$
Wavenumber (cm-1)

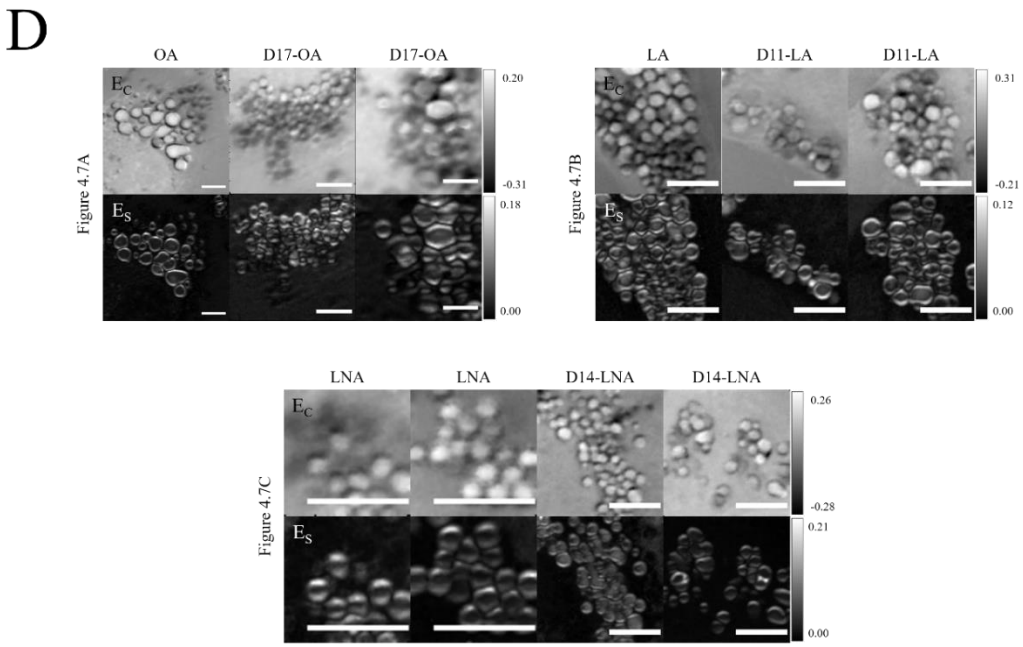

Figure 4.7 | Spatial and spectral outputs from unsupervised FSC^3 analysis of hyperspectral CARS datasets for deuterated fatty acid-treated HeLa cells, specifically targeted within the silent region of the Raman spectrum. The chemical composition of lipid droplets is directly compared between OA-treated and D17-OA-treated cells (A), LA-treated and D11-LA-treated cells (B), and LNA-treated and D14-LNA-treated cells (C). For each of the deuterated/non-deuterated pairings, concentration maps identify and spatially resolve four components which are chemically specified by their representative spectra showing the phase-retrieved imaginary part of the normalised CARS susceptibility $Im\left\{\chi_R^{(3)}\right\}$. Real parts are also shown as horizontal dashed lines. Components are identified corresponding to (primarily) water (Component 1), deuterated fatty acid (Component 2), and non-deuterated fatty acid (Component 3). Component 4 shows noisy, featureless spectra and is thus considered to represent background signal. Volume concentration ranges for spatially resolved images are shown on a grayscale. DIC images show whole cells and the lipid-rich regions selected for hyperspectral CARS acquisition. Scale bars show 20 μm in DIC images and 4 μm in FSC^3 images. The relative concentration (E_C) and spectral (E_S) error of the FSC^3 analysis in Figures A-C are shown in Figure D. Error values are given by a grayscale. Scale bars show 4 μm.

Figures 4.7A, 4.7B and 4.7C show direct comparison of chemical components between HeLa cells treated with OA and D17-OA (A), LA and D11-LA (B), and LNA and D14-LNA (C) through observation of spectral differences within the silent region of the Raman spectrum. For each of the deuterated/non-deuterated fatty acid pairings, the same chemical components are identified with respect to the spatially resolved images and the observed peaks within the silent region of the retrieved spectrum. Based on the localisation of signal within the spatially resolved images as well as the lack of observable peaks present in the retrieved spectrum over the measured wavenumber range, Component 1 is considered to represent the aqueous medium surrounding the lipid droplets, consisting primarily of water. Component 2 can be attributed to deuterated fatty acid due to localisation of signal within lipid droplets and the presence of a peak within the retrieved spectrum at 2000-2200 cm^{-1}, corresponding to C-D bond vibrations. Lipid droplets showing a deuterated fatty acid signal are only visible in the spatially resolved images acquired from the deuterated fatty acid-treated HeLa cells and are absent from cells fed with the non-deuterated isoform of each fatty acid. A peak at 2800-3000 cm^{-1} is also observed in the retrieved spectrum for Component 2, which corresponds to C-H bond vibrations. This peak arises as not every hydrogen within the investigated deuterated fatty acids is substituted for deuterium, and a portion of the acyl chain still contains C-H bonds. This peak is also present in the retrieved spectrum for Component 3 but at a higher intensity, and thus this component can be attributed to non-deuterated fatty acid based on localisation of signal to lipid droplets with an absence of a peak at ~ 2100 cm^{-1} within the retrieved spectrum. Although some signal is present within cytosolic droplets of deuterated fatty acid-treated cells for Component 3 due to the presence of C-H bonds and ongoing fatty acid synthesis, the observed spatially resolved signal and peak intensity are comparably larger in cells treated with non-deuterated fatty acid due to a larger total number of C-H bonds. The retrieved spectrum for Component 4 shows no distinguishable peaks within any of the deuterated/non-deuterated fatty acid pairings and appears noisy in Figures 4.7B and 4.7C. Furthermore, the spatially resolved images of Component 4 do not show consistent signal from a specific structure. Therefore, this component is considered to represent a background noise signal as oppose to a specific chemical group.

In agreement with observations from the spontaneous Raman spectra for each deuterated lipid shown in Figure 4.3, the retrieved spectra for D17-OA and D11-LA-associated components in Figures 4.7A and 4.7B, respectively, show a sub-peak at 2070 cm^{-1}, which is not present in the retrieved spectra for the D14-LNA component in Figure 4.7C. Therefore, we hypothesise that this sub-peak corresponds to the CD_3 group located at the 18^{th} position in the acyl chain of both D17-OA and D11-LA, which is absent from the D14-LNA structure. As the only chemical groups containing deuterium within each of the three deuterated fatty acids are C-D, CD_2 and CD_3, it is

likely that the other spectral features correspond to stretching vibrational modes of the C-D and CD_2 groups.

Figure 4.7D displays the factorisation errors from Figures 4.7A-C which are quantified by relative spectral error (E_S) and relative concentration error (E_C)[73]. E_S provides a measure of the residual generated when the phase-retrieved dataset is factorised as a product of a matrix of concentration and a non-negative matrix of spectra of chemical components, whilst $E_C = \left\{\left(\sum_{k=1}^{K} C_p^{\{k\}}\right) - 1\right\}$, where $C_p^{\{k\}}$ is the non-negative relative volume concentration of the k^{th} chemical component at voxel p. In Figure 4.7D, E_S shows a maximum relative value of approximately 20% across Figures 4.7A-C and a spatial localisation towards the edge of the lipid droplets. It is possible that these errors result from small movements of the sample during data acquisition although causes for this movement are unclear. E_C also shows the largest values at lipid droplet regions, possibly due to distortions of the excitation fields by the high spatial refraction index of the droplets[79,172]. The factorisation errors for each fatty acid also appear similar between deuterated and non-deuterated isoforms.

Interpretation of CH-associated peaks within the aforementioned hyperspectral datasets is made challenging by the upper limit of the intermediate filter located at approximately 3000 cm^{-1}, which distorts the spectral line-shape of the CH-associated peaks, preventing their attribution to chemical groups and limiting the quantitative capabilities of FSC^3. Consequently, hyperspectral CARS datasets were also acquired from the same samples over the spectral range, 2750 cm^{-1} to 3100 cm^{-1}, via a CH-stretch region-specific filter (Semrock FF01-562/40), enabling visualisation of spectral variations within the CH-stretch region of the Raman spectrum, corresponding to changes in chemical composition of lipid droplets. Figure 4.8 shows spatial and spectral outputs following application of FSC^3 to hyperspectral CARS datasets acquired within the CH-stretch region of the Raman spectrum. As in Figures 4.7, HeLa cells treated with deuterated and non-deuterated isoforms of the same fatty acid were analysed together, enabling direct comparison of lipid droplet composition. The lipid components of the XY images are once again identified and displayed as spatial concentration maps, with spectra for each component retrieved over the range, 2750 cm^{-1} to 3100 cm^{-1}, enabling visualisation of the CH-stretch peaks for each of the deuterated and non-deuterated lipids, which were obscured in Figure 4.7. Consideration of four separate chemical components within the factorisation algorithm once again enabled the lipid composition of the droplets within the field of view to be well-represented, and the identified components corresponding to water, deuterated lipid and non-deuterated lipid are shown in Figure 4.8. As before, DIC images were acquired for initial visualisation of whole cells and selection of lipid-rich regions for hyperspectral CARS imaging.

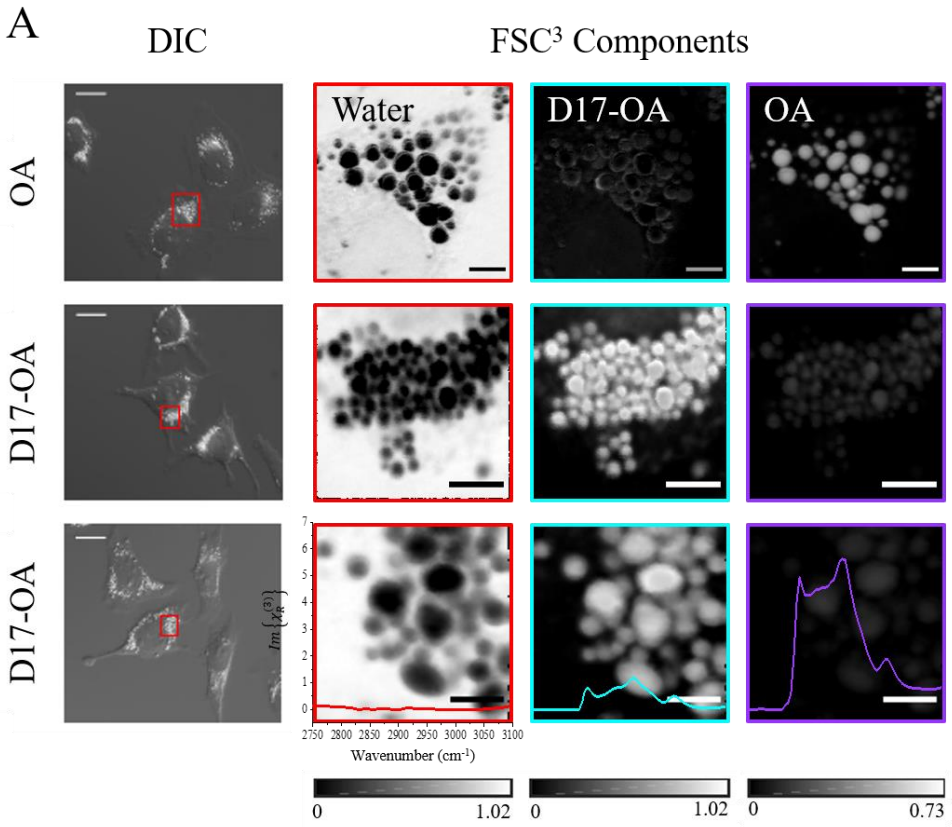
A
DIC
FSC3 Components
Water
D17-OA
OA
OA
D17-OA
D17-OA
Im{χR(3)}
2750 2800 2850 2900 2950 3000 3050 3100
Wavenumber (cm-1)
0
1.02
0
1.02
0
0.73

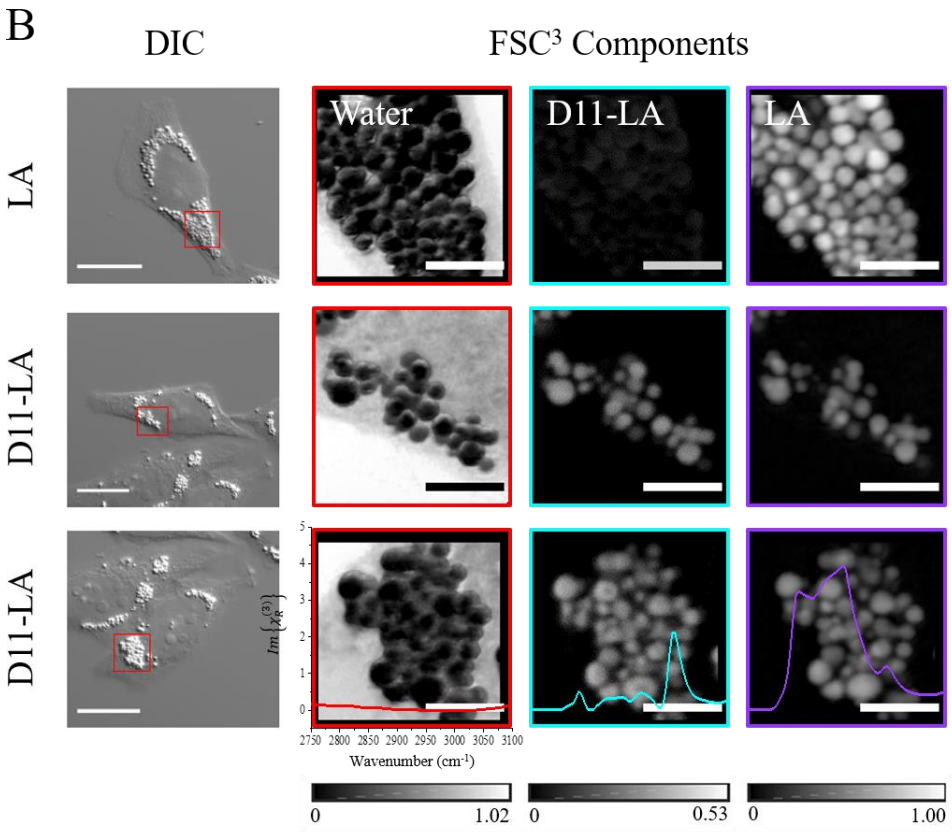
B
DIC
FSC3 Components
Water
D11-LA
LA
LA
D11-LA
D11-LA
Im{χR(3)}
2750 2800 2850 2900 2950 3000 3050 3100
Wavenumber (cm-1)
0
1.02
0
0.53
0
1.00

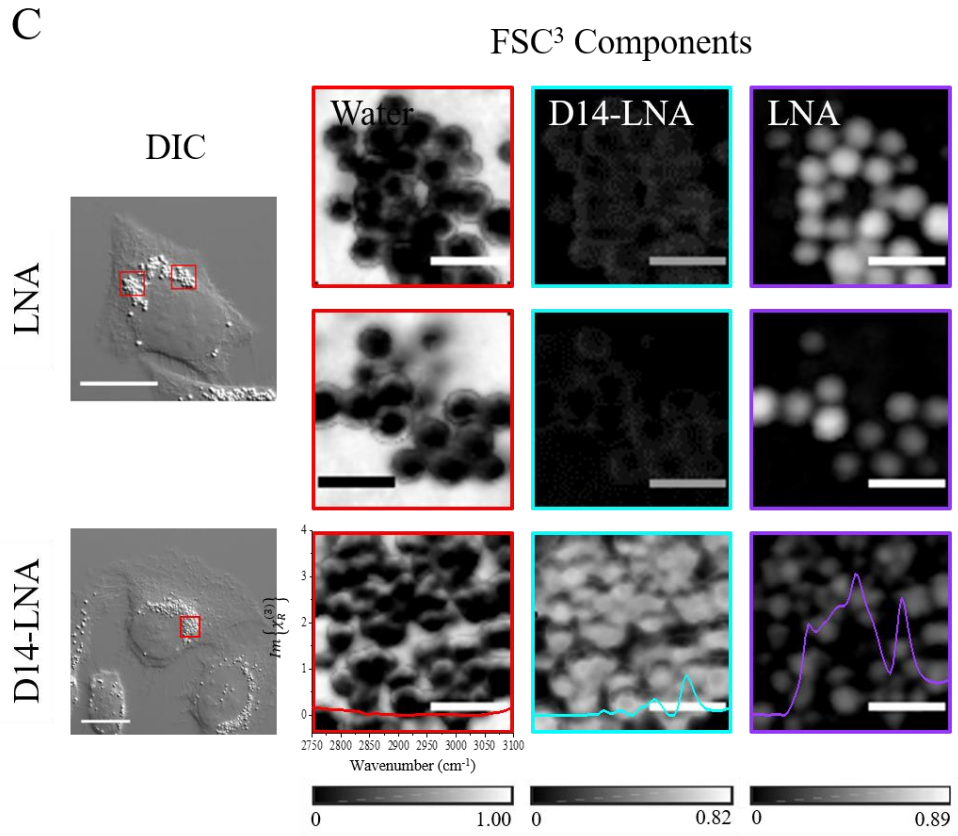
C
FSC3 Components
DIC
Water
D14-LNA
LNA
LNA
D14-LNA
Wavenumber (cm-1)
0
1.00
0
0.82
0
0.89

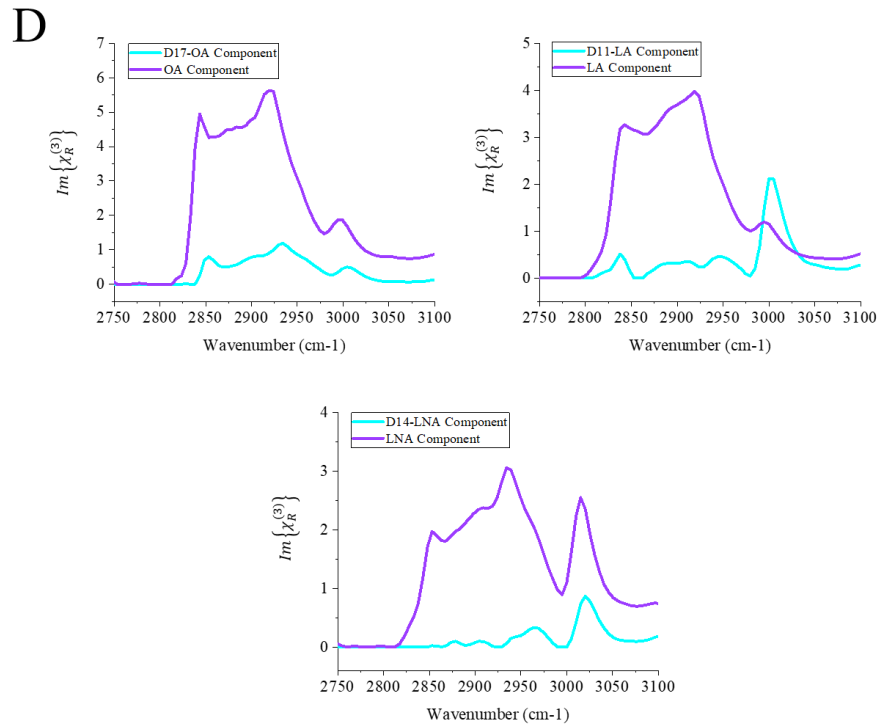
D
D17-OA Component
OA Component
D11-LA Component
LA Component
D14-LNA Component
LNA Component
Wavenumber (cm-1)

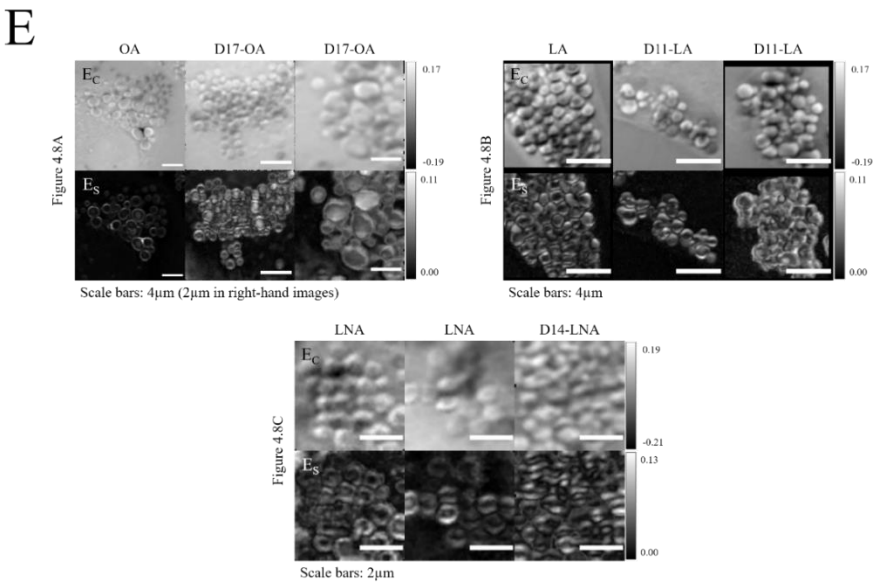

Figure 4.8 | Spatial and spectral FSC³ outputs following application to hyperspectral CARS datasets acquired within the CH-stretch region of the Raman spectrum for visualisation of spectral changes between identified deuterated and non-deuterated lipid components. Chemical components corresponding to water, deuterated lipid and non-deuterated lipid are identified and displayed as quantitative concentration maps for the pairings of OA- and D17-OA-treated HeLa cells (A), LA- and D11-LA-treated HeLa cells (B), and LNA- and D14-LNA-treated HeLa cells (C). For each component, representative spectra showing the phase-retrieved imaginary part of the normalised CARS susceptibility $Im\left\{\chi_R^{(3)}\right\}$ are shown as overlays and volume concentration ranges for spatial images are shown on a grayscale. Retrieved spectra for deuterated and non-deuterated components are also plotted together for comparison (D). DIC images show whole cells and the lipid-rich regions selected for hyperspectral CARS acquisition. Scale bars show 20 μm in all DIC images, 4 μm in FSC³ images in upper two rows of Figure A and all FSC³ images in Figure B, and 2 μm in FSC³ images in lower two rows of Figure A and all FSC³ images in Figure C. The relative concentration (E_C) and spectral (E_S) error of the FSC³ analysis in Figures A-C are shown in Figure E. Error values are given by a grayscale. Scale bars of error images match scale bars in Figures A-C.

Figures 4.8A, 4.8B and 4.8C show direct comparison of lipid components between HeLa cells treated with OA and D17-OA, LA and D11-LA, and LNA and D14-LNA, respectively, with images acquired from the same fields of view as for silent region analysis, with the exception of the D14-LNA-treated sample in Figure 4.8C. For each of the deuterated/non-deuterated fatty acid pairings, the same chemical components are identified, confirmed via both spatial and spectral FSC³ outputs. The component considered to represent the water-based aqueous media surrounding the droplets is shown, displaying CARS signal outside of the droplets and no peaks within the retrieved spectrum over the acquired range. Components corresponding to deuterated and non-deuterated lipid are also shown, with spatially resolved images displaying CARS signal

within droplets and typical lipid-associated Raman line-shapes observed within the CH-stretch region of the retrieved spectra. As in Figure 4.7, the deuterated lipid component (shown in cyan) only shows CARS signal within droplets of the deuterated lipid-treated cells, whilst signal corresponding to non-deuterated lipid (shown in purple) is present within droplets from all samples, although a reduced signal intensity can be seen in droplets of cells treated with each of the deuterated lipids compared to those treated with the respective non-deuterated isoforms. Whilst this difference in signal intensity could be observed in Figure 4.7, detailed information regarding how the different CH-related peaks are affected by changes in the overall quantities of C-H and C-D bonds within droplets was not available due to distortion of the spectral line-shape.

Figure 4.8D shows the retrieved spectra for both lipid components from Figures 4.8A, 4.8B and 4.8C, enabling comparison of spectral line-shape. CH-stretch peak positions appear to be maintained between lipid droplets from cells treated with each fatty acid isoform, with retrieved spectra showing a CH_2 symmetric stretch peak at ~ 2850 cm^{-1}, a CH_3 stretch / CH_2 asymmetric stretch peak at 2390 cm^{-1} and a =CH stretch peak at ~ 3010 cm^{-1}, which are comparable to the observed peaks within the acquired spontaneous Raman spectra shown in Figure 4.3. However, in both LA/D11-LA and LNA/D14-LNA samples, identification of some peaks is challenging due to low levels of signal.

It can be observed that changes in intensity are not consistent across all peaks within this region, with some peaks showing a more pronounced change than others. In the retrieved spectrum from lipid droplets of D17-OA-treated cells, peaks corresponding to CH_2 symmetric stretch, CH_3 stretch/CH_2 asymmetric stretch and =CH stretch show reduction by factors of 6.25, 4.7 and 3.5, respectively, compared to the retrieved spectrum from the non-deuterated lipid, indicating that the largest impact of deuterium incorporation is had on the CH_2 groups, and less of an effect is had on =CH groups. These differences in reduction can be explained by considering the molecular structure of D17-OA (see Section 3.1 of Chapter 3). Deuterium is not incorporated at either end of the C=C bond and thus resonance of =CH groups is not directly affected. Instead the observed changes in intensity must be due to indirect effects of deuterium present within the aliphatic chain of the fatty acid, hence the induced reduction is less pronounced than for the directly affected CH_2 and CH_3 groups. As previously mentioned, conservation of peak position is less clear in the retrieved spectra for LA/D11-LA and LNA/D14-LNA as some of the peaks are reduced to such an extent that they are no longer detectable. The retrieved spectrum from droplets of D11-LA-treated cells shows a CH_2 symmetric stretch peak just below 2850 cm^{-1}, which shows reduction by a factor of 6.4 from the corresponding LA component spectra, whilst the CH_3 stretch/CH_2 asymmetric stretch peak is difficult to identify, but appears to show reduction by a factor of around 8. In contrast to all of the other peaks observed for deuterated lipid components

in Figure 4.8, the =CH stretch peak within the D11-LA component spectrum shows an increase by a factor of 1.8, however, it is likely that this is due to an error in the LA sample as the =CH peak should be larger in the spectrum for the LA component compared to that of the OA component due to a higher degree of unsaturation, and yet when the retrieved spectra from each component are compared, the peaks are of a comparable size. Within the retrieved spectrum for the D14-LNA component, the CH_2 symmetric stretch peak is not visible due to the extent by which it has been reduced, the CH_3 stretch/CH_2 asymmetric stretch peak is reduced by a factor of 10, and the =CH stretch peak is reduced by a factor of 2.9, providing further evidence that deuterium incorporation has a larger impact on CH_2 and CH_3 vibrations than =CH vibrations.

Figure 4.8E shows the relative spectral error (E_S) and relative concentration error (E_C) for Figures 4.8A-D. E_S shows a maximum relative value of around 10% across the three datasets, and, as was observed in Figure 4.7D, the largest values are observed towards the outer edges of the lipid droplets. Large E_C values are observed within some of the lipid droplets, which may be due to excitation field distortion caused by the high spatial refraction index of the droplets[79,172], although this is less clear than for the cell-silent region datasets in Figure 4.7, with some droplets showing low E_C values. As in Figure 4.7, the factorisation errors for each fatty acid also appear similar between deuterated and non-deuterated isoforms.

4.5. Summary

In this chapter, the ability of an in-house-developed multimodal CARS microscopy system, along with its associated data processing and analysis procedures, to identify and spatially resolve a deuterium-labelled fatty acid within a cell has been assessed, determining whether incorporation of deuterium may present an effective labelling strategy which can be utilised to image exogenously applied molecules. Hyperspectral CARS datasets acquired from cytosolic lipid droplets in fatty acid- and deuterated fatty acid-fed HeLa cells have illustrated the capability of the novel data analysis algorithm, FSC^3, to identify a chemical component corresponding to carbon-deuterium bond vibrations and provide a quantitative assessment of intracellular distribution in a completely unsupervised manner. The retrieved chemical spectra for the deuterated fatty acid FSC^3 components acquired from intracellular droplets correspond well with the spontaneous Raman spectra acquired for pure preparations of the lipids, providing strong evidence for the accuracy with which carbon-deuterium bonds within the lipids can be identified and distinguished from the complex cellular background.

The observed results indicate potential for further application of this strategy, where deuterium can be incorporated into a variety of other molecules which are poorly compatible with fluorescence imaging for assessment of distribution, accumulation, turnover and metabolism. The high degree of contrast which can be achieved with only minimal structural change makes molecular labelling with deuterium an extremely appealing strategy. However, the combination of favourable chemical structure and the tendency to accumulate in concentrated droplets both contribute to the strong signal observed for the carbon-deuterium component within this chapter. Even though hardware optimisation and application of data processing procedures and FSC^3 analysis enable signal from carbon-deuterium bonds to be maximised, observation of other deuterium-labelled molecules may not be as straightforward, especially if the investigated molecule does not accumulate within a given area of a cell. As described in earlier chapters, CARS intensity scales non-linearly, and so a lower degree of accumulation can have drastic implications for the observed signal.

In principle, deuterated fatty acids have provided proof-of-concept evidence that the FSC^3 data analysis algorithm can be successfully applied to hyperspectral CARS datasets to identify and spatially resolve a chemical component corresponding to carbon-deuterium bonds within a molecule of interest. Thus, this imaging strategy will be investigated further to assess its potential as a research tool which can be employed to study distribution and metabolism of a variety of biological and chemical molecules.

5. DEUTERATED FATTY ACID VISUALISATION BY FSC^3 AS A TRANSFERABLE TOOL

5.1. Introduction

The proven compatibility of FSC^3 with deuterium-labelling of molecules provides a useful, transferable tool with potential applications across biology and biomedicine. As described in Chapter 1, isotopic substitution offers an effective labelling strategy which, when combined with Raman-based imaging techniques, can permit clear distinction of a molecule of interest from a mixed chemical background, whilst minimising potential structural perturbation. Through application of FSC^3, a deuterium-labelled molecule can be clearly visualised with quantitative spatial resolution, hence presenting a useful tool for studying various molecules within cells, especially those which show a tendency to accumulate to a high concentration within a given area, such as lipids localised within discrete droplets. Thus, the following chapter will further explore potential applications of this imaging strategy, once again utilising deuterated fatty acids based on the strong CARS signal that they generate, owing to their CH-rich aliphatic chains and strong tendency to accumulate within dense droplets.

Within this chapter, Sections 5.2 and 5.3 should be considered independent from one another and will each be preceded and succeeded by its own introduction and summary section, respectively. Section 5.2 will investigate the potential of FSC^3 for visualising lipid uptake, storage and turnover, providing information regarding the associated time-course for each process, as well as the homo- or heterogeneity of storage into cytosolic droplets. Ultimately, this section will assess the applicability of quantitative FSC^3 data analysis for studying such cellular processes, and once the principle is established, this will encourage use of deuterium-labelling with FSC^3 to study further biological molecules within cells. Section 5.3 will explore the utilisation of deuterium-labelled lipid storage within droplets for non-invasive visualisation and tracking of cells of interest within mixed populations. The principle of this will be assessed using two-dimensional cell populations, but its potential translation into three-dimensional spheroids and organoids may be of interest across a range of studies.

5.2. Part A: Hyperspectral CARS and FSC^3 data analysis for quantitative visualisation of deuterium-labelled lipid incorporation and turnover within cytosolic lipid droplets

5.2.1. Introduction

Cellular lipid dynamics have been extensively studied by Raman-based imaging techniques, including CARS[67], and deuterium-containing analogues of fatty acids have already been employed to investigate lipid uptake and storage[126–130]. Furthermore, FSC^3 has already been applied to biological samples to assess changes in lipid droplet composition[79,80]. However, to date, deuterium-labelling has not been combined with data analysis techniques, such as FSC^3, which can be applied to CARS data to maximise the chemical information obtained. Hence, FSC^3 is employed in this chapter to observe the uptake and storage of deuterium-labelled D11-LA into lipid droplets, as well as its corresponding turnover, and FSC^3 outputs are evaluated in the context of existing CARS studies which have observed deuterated fatty acids without supporting data analysis procedures, as well as recent SRS data, which may present more comparable outputs to those obtained from FSC^3.

As described in the previous chapter, the most efficient way for cells to store excess energy is as lipid, more specifically as dense droplets comprising a core of neutral lipids, such as triacylglycerols and sterol esters, surrounded by a monolayer of phospholipid[165]. These lipid droplets are formed in the endoplasmic reticulum (ER) membrane, and the most widely accepted model for their formation involves accumulation of neutral lipids between the bilayers of the ER membrane, followed by coalescence of the neutral lipids first into a lens, and then into a sphere, which becomes wrapped by the cytosolic phospholipid monolayer of the ER and the nascent lipid droplet buds off into the cytosol[173–175].

The ability of FSC^3 to quantitatively illustrate exchange of lipids within intracellular droplets has previously been shown through detection of spectral variations within the CH region of the Raman spectrum and via observation of changes in intensity within spatially resolved images[80]. FSC^3 was employed in a similar way to observe storage and turnover of deuterium-labelled lipids within droplets, with changes observed in spatial images and corresponding spectra acquired within both the CH-stretch and the cell-silent region of the Raman spectrum. The combination of spatial and spectral outputs from FSC^3 permitted quantitative assessment of the volume of CH- and CD-based lipids within droplets, thus providing information regarding the timescale over which deuterated and non-deuterated fatty acid was taken up and stored within

lipid droplets, and the rate at which the existing lipid was turned over. Furthermore, the observed changes in lipid droplet composition provided information regarding the nature of lipid turnover and metabolism within cells, more specifically whether the cell utilised lipid from its cytosolic droplets for metabolic processes, or whether it more readily utilised the available lipid supplemented within its growth media and instead preserved its energy reserves within cytosolic droplets.

5.2.2. Quantitative FSC^3 analysis of deuterium-labelled fatty acid uptake, storage and turnover within cytosolic droplets

As in the previous chapter, HeLa cells were subjected to an 18-hour starvation period followed by an 18-hour incubation with either D11-linoleic acid (D11-LA) or unlabelled linoleic acid (LA), providing adequate time for the deuterated or non-deuterated fatty acid to be taken up and stored within cytosolic lipid droplets. Up to this point, an 18-hour incubation had been chosen based on the presence of visible cytosolic droplets within cells at the end of this time-period, however, the visualisation of lipid uptake and storage within this chapter will provide a more definitive answer as to the necessary timescale. Following the 18-hour incubation period, cells were transferred to growth media supplemented with the alternative isoform of linoleic acid, i.e. cells previously incubated with LA were transferred to D11-LA-supplemented media (LA→D11-LA), whilst cells previously incubated with D11-LA were transferred to LA-supplemented media (D11-LA→LA). Multiple samples were prepared and PFA-fixed at different time-points over a 24-hour period, including 0 h samples from each treatment group which were fixed at the conclusion of the 18-hour incubation period, before hyperspectral CARS images were acquired and subsequent FSC^3 analysis was performed. Samples from each time-point were imaged under identical conditions to enable direct comparison.

Figure 5.1 shows the spatial and spectral outputs of FSC^3 analysis following its application to hyperspectral CARS images acquired from cells belonging to the LA→D11-LA treatment group. Samples were imaged at different time-points over a 24-hour period, and hyperspectral datasets were acquired over the spectral ranges, 1950-2300 cm^{-1} and 2750-3100 cm^{-1}, targeting CD- and CH-associated peaks, respectively. For each dataset, a single lipid droplet-containing field of view within a single cell was acquired from samples fixed at each experimental time-point and the experiment was only performed once. All fields of view were then analysed simultaneously by FSC^3 to identify the most common spectra across all time-points. As in Chapter 4, spectral processing of the acquired CARS spectra for each spatial point of the image was

required to generate Raman-like spectra which were linear in concentration of chemical components and thus enabled quantitative analysis to be conducted. Acquired DIC images are also displayed for each time-point showing whole cells and the lipid-rich regions imaged by hyperspectral CARS.

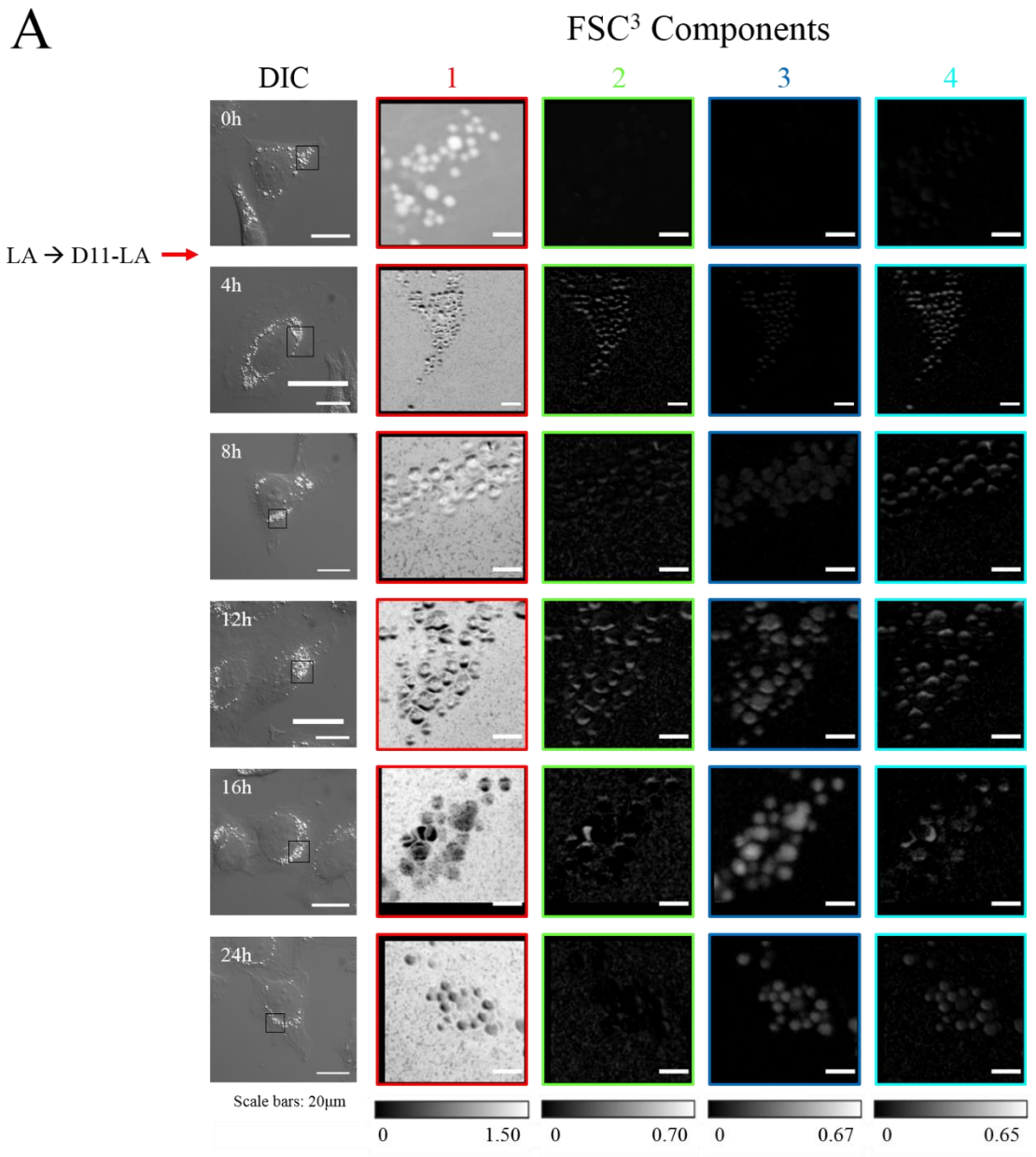
A
FSC3 Components
DIC
1
2
3
4
LA → D11-LA
0h
4h
8h
12h
16h
24h
Scale bars: 20µm
0
1.50
0
0.70
0
0.67
0
0.65

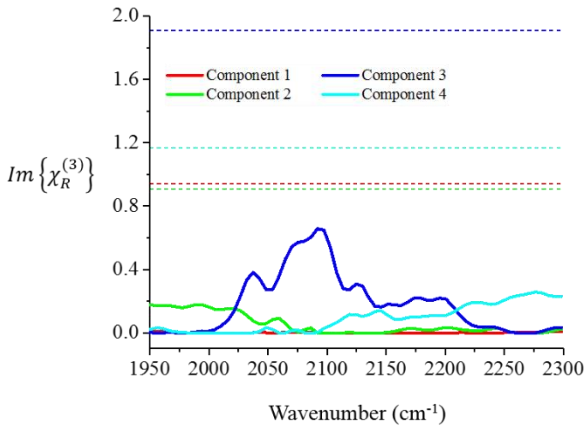
2.0
1.6
1.2
0.8
0.4
0.0
Component 1
Component 2
Component 3
Component 4
1950
2000
2050
2100
2150
2200
2250
2300
Wavenumber (cm-1)

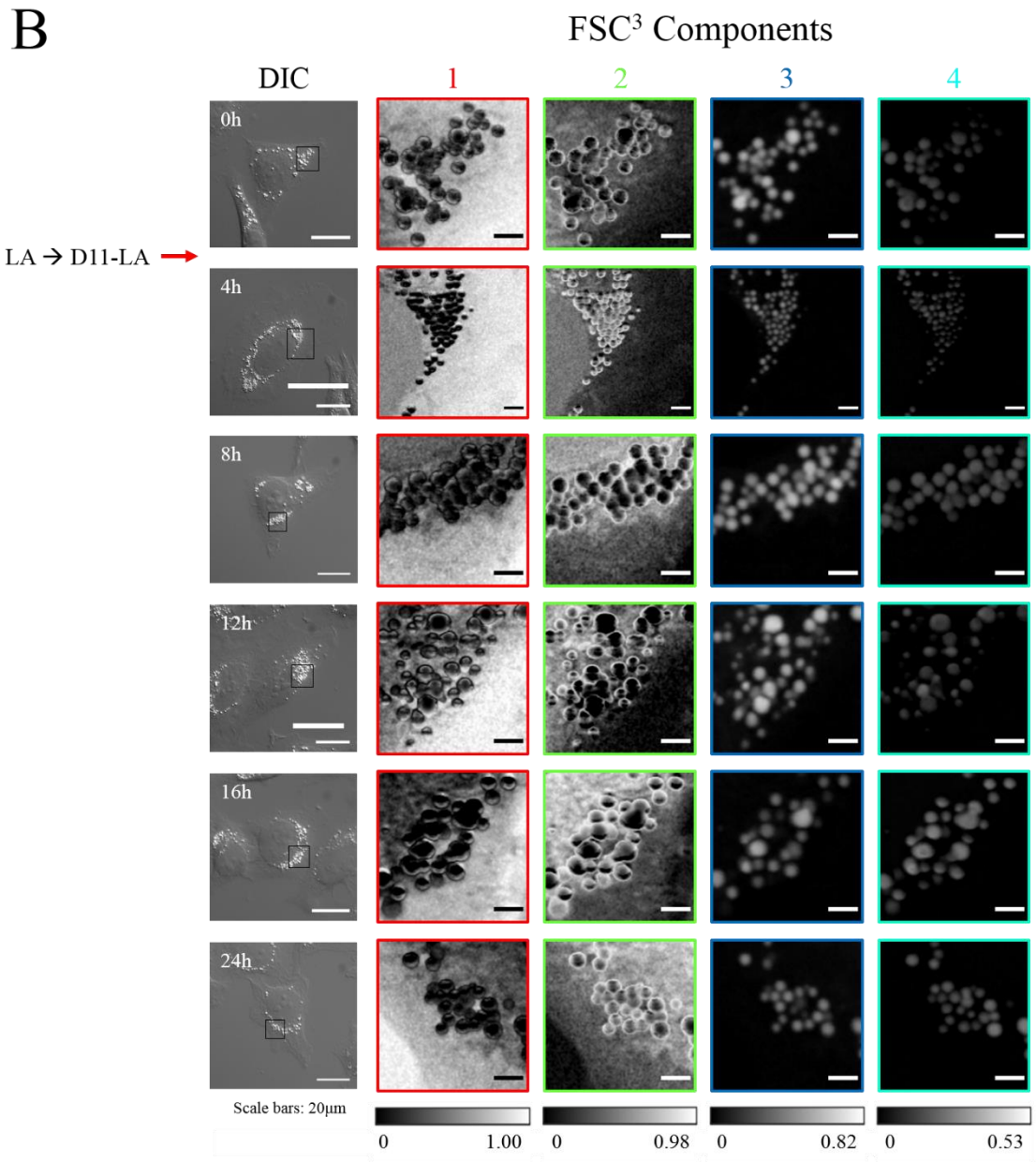
B
FSC3 Components
DIC
1
2
3
4
0h
4h
8h
12h
16h
24h
LA → D11-LA
Scale bars: 20µm
0
1.00
0
0.98
0
0.82
0
0.53
Component 1
Component 2
Component 3
Component 4
Im{χR(3)}
Wavenumber (cm-1)

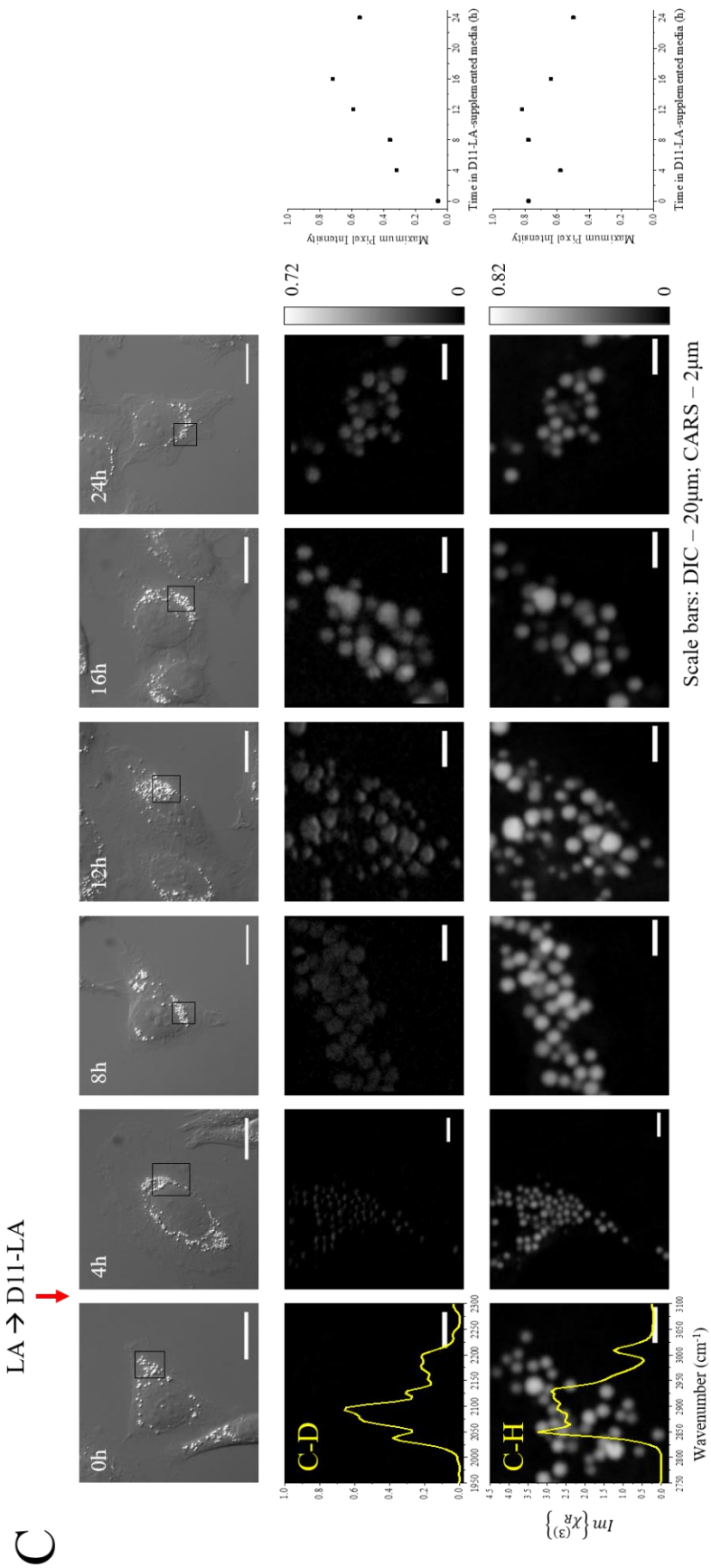
C
LA → D11-LA
0h
4h
8h
12h
16h
24h
C-D
C-H
0.72
0
0.82
0
Maximum Pixel Intensity
Time in D11-LA-supplemented media (h)
Scale bars: DIC – 20µm; CARS – 2µm
Wavenumber (cm-1)

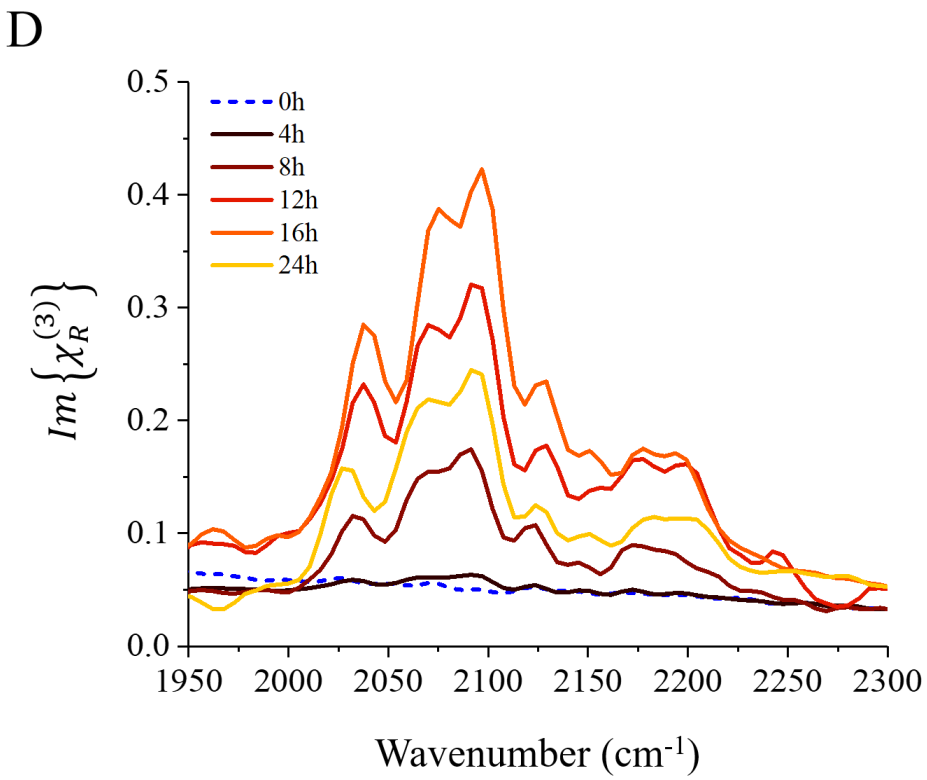

Figure 5.1 | FSC^3 analysis of D11-LA uptake and storage within cytosolic droplets. Cells from the LA→D11-LA treatment group were imaged by hyperspectral CARS over the spectral ranges, 1950-2300 cm^{-1} (A) and 2750-3100 cm^{-1} (B), targeting the CD- and CH-associated peaks, respectively. The hyperspectral datasets from all cells were analysed by FSC^3 simultaneously so that the most common spectra were identified across images from all time-points. The spatially resolved images for each component, along with the associated spectra showing the phase-retrieved imaginary part of the normalised CARS susceptibility $Im\left\{\chi_R^{(3)}\right\}$ are displayed. The corresponding real parts are shown as averages, indicated by horizontal dashed lines. Within the cell-silent region (1950-2300 cm^{-1}), a component corresponding to D11-LA was identified (Component 3), showing localisation of signal to droplets and a peak at ~ 2100 cm^{-1} corresponding to C-D bond vibrations within its retrieved spectrum. The other three components are considered to correspond to fluctuations in background signal, showing inconsistent spatial images and featureless spectra. Signal from the D11-LA component increases from 0 h to 16 h time-points, and then decreases slightly from the 16 h to 24 h time-points. Within the CH-stretch region, components corresponding to water (Component 1), protein (Component 2) and lipid (Components 3 and 4) are identified, based on localisation of signal and line-shapes of their retrieved spectra. The lipid components do not show clear differences in peak intensity between time-points. Component 3 from Figures 5.1A and 5.1B are combined in Figure 5.1C to give an overview of the observed changes in CD- and CH-based lipid concentrations, with the retrieved spectra shown as overlays. Concentration plots give the maximum intensity values from each image. Full volume concentration ranges across all images are given by the grayscale values. DIC images show whole cells and the droplet-containing regions selected for hyperspectral CARS acquisition. Scale bars show 20 μm in DIC images and 2 μm in FSC^3 images. Figure 5.1D shows a plot of the CD peaks when FSC^3 was applied to hyperspectral datasets from each time point individually.

Figure 5.1A shows the FSC^3 results when samples from all time-points were considered in the data analysis algorithm together, meaning that common spectra were identified across the samples and changes in deuterated lipid concentration could be assessed via differences in signal intensity from the droplets within each image. For each time-point, a single field of view was acquired from a single cell, thus retrieved spectra for each component are representative of the six time-points shown only. A narrow spectral range (1950-2300 cm^{-1}) within the cell-silent region was employed to specifically target the CD-associated peak. It was described in Chapter 4 that consideration of four separate chemical components could sufficiently represent the chemical data within the field of view, without separation of peaks of interest, which could be harmful to the interpretation of data. Thus, four chemical components were once again considered in the analysis algorithm. Due to the narrow spectral range utilised, as well as the acquisition being performed within the cell-silent region, the only meaningful component identified was Component 3 which could be considered to represent the deuterium-labelled lipid based on localisation of signal to droplets and a peak located at ~ 2100 cm^{-1} within its retrieved spectrum. The spectral line-shape was comparable to that observed for D11-LA when imaged by both spontaneous Raman and CARS within the previous chapter. The other three components did not show spectral features within the selected spectral range and are therefore considered to show fluctuations in background noise. The sample fixed at the 0h time-point showed no CARS signal corresponding to carbon-deuterium as it was not exposed to D11-LA and consequently possessed no deuterated lipid within its droplets. Over the subsequent 16 hours, an increase in the observed signal corresponding to CD resonances could be seen, indicating cellular uptake of the newly presented D11-LA from the growth media and subsequent storage within lipid droplets. However, from the 16 h to 24 h time-points, signal intensity from D11-LA appeared to reduce slightly, which may have been indicative of the cell depleting its growth media of deuterated lipid and beginning to replace the deuterated lipid in its droplets with endogenous non-deuterated lipid, however, a clear CD-associated signal was still observed.

Figure 5.1B also shows FSC^3 results where samples from all time-points are considered in the data analysis together, but over the spectral range, 2750-3100 cm^{-1}, targeting CH-associated bond vibrations. As in Figure 5.1A, a single field of view was acquired from a single cell for each time-point, thus retrieved spectra for each component are representative of only the six time-points shown. Four components were once again considered in the analysis algorithm. As the CH-stretch region of the Raman spectrum contained contributions from a wider variety of chemical groups than the cell-silent region, a higher number of meaningful components could be identified, hence components corresponding to aqueous media (water) (Component 1), protein with some lipid contribution (Component 2), and lipid (Component 3) were identified based on signal

localisation and peak positions within the retrieved component spectra. Differences in CARS signal intensity within the lipid component were considerably less clear between images acquired within the CH region of the Raman spectrum. This was likely due to CH groups being present within lipid droplets for the duration of the experiment, as both LA and D11-LA contained C-H bonds within their structure, and hence the signal did not change as dramatically as it did within the cell-silent region. In the previous chapter, the observed differences between the CH-related peaks for LA and D11-LA were less pronounced than those between the CD-related peaks, with the overall peak shape remaining similar and the main observable difference being the overall intensity of the peak, i.e. the total area covered by the peak. Consequently, it is possible that in this instance, FSC^3 was unable to distinguish between the small changes in peak intensity, unlike CD-related peaks which exhibited a much more pronounced change in peak intensity.

Figure 5.1C shows the spatially resolved images and retrieved spectra for the lipid components identified within the six imaged fields of view from both the cell-silent and CH-stretch regions of the Raman spectrum. As already described, the sample fixed at the 0h time-point showed no CARS signal corresponding to carbon-deuterium, as it was not exposed to D11-LA, and a strong CARS signal from carbon-hydrogen vibrations within LA, which had been taken up by cells and stored within cytosolic droplets over the prior 18-hour incubation period. Over the subsequent 16 hours, an increase in the observed signal corresponding to CD resonances was seen, indicating cellular uptake of the newly presented D11-LA from the growth media and subsequent storage within lipid droplets. However, from the 16h to 24h time-points, signal intensity from D11-LA appeared to reduce slightly, which may have been indicative of the cell depleting its growth media of deuterated lipid and beginning to replace the deuterated lipid in its droplets with endogenous non-deuterated lipid. These changes in deuterated lipid concentration are reflected in the corresponding plot, which shows the maximum intensity values for the spatial images acquired at each time-point, ranging from 0.06 to 0.72. Due to its comparable line-shape to spontaneous Raman spectra and a linear dependency on concentration of chemical components, the phase-retrieved imaginary part of the normalised CARS susceptibility $Im\left\{\chi_R^{(3)}\right\}$ can provide absolute concentrations of molecules per pixel. However, this requires acquisition of an equivalent reference spectrum from a pure sample of the investigated biological or chemical molecule at a known concentration. As reference spectra were not acquired from the cell-silent and CH-stretch regions of the D11-LA spectrum to accompany the data shown in Figure 5.1, determination of absolute volume concentrations per pixel was not possible. Comparison of the retrieved spectra for CD- and CH-based lipids in Figure 5.1C with equivalent reference spectra would have permitted determination of the maximum D11-LA concentration within the dataset (represented by a value of 1 in the concentration range). As the maximum concentration value for

the CD-associated signal was 0.72, pixels which only show signal corresponding to D11-LA, i.e. within droplets, will show 72% of the maximum concentration, and less signal will correspond to lower concentration. Thus, the maximum intensity values of 0.06 to 0.72 for CD-associated signal in Figure 5.1C correspond to 6% to 72% of the concentration represented by the retrieved spectrum shown for CD-associated signal, however, as discussed, acquisition of reference spectra would have permitted absolute determination of D11-LA concentration per pixel. The spatial images acquired within the CH-stretch region did not exhibit clear differences in intensity, and this was also apparent within the associated maximum intensity plot, where the concentration of CH-based lipid did not show a general increase or decrease over the 24-hour time-course, ranging between 0.5 (50%) to 0.82 (82%) with a peak concentration at the 12h time-point. Furthermore, small differences in signal intensity could be observed for different droplets within the spatial images, however these variations did not differ between silent and CH region images, and therefore did not appear to be suggestive of differences in CH- and CD-based lipid concentration or heterogeneity in the uptake and storage of deuterated lipid.

Figure 5.1D shows a plot of the CD-associated peaks from the single field of view at each time-point when analysed by FSC³ separately, providing the most common spectrum within each image individually. In agreement with the spatially resolved images, the signal corresponding to deuterium-labelled lipid increases from 0h to 16h, but then decreases slightly to 24h. However, the 4h time-point, which does not show a visible CD peak, does not appear to correlate with the spatial FSC³ outputs in Figure 5.1C, where signal is observed from lipid droplets and the associated plot suggests that it shows a similar concentration to the 8h time-point, although the cause of this discrepancy is unclear.

Figure 5.2 displays the FSC³ results following application to hyperspectral CARS images acquired from lipid droplet-containing regions of cells from the D11-LA→LA treatment group. Cells were once again imaged at different time-points over a 24-hour period, and hyperspectral datasets were acquired over the spectral ranges, 1950-2300 cm^{-1} and 2750-3100 cm^{-1}, targeting CD- and CH-associated peaks, respectively. For each dataset, a single lipid droplet-containing field of view within a single cell was acquired from samples fixed at each experimental time-point and the experiment was only performed once. As before, spectral processing of the acquired CARS spectra was performed to generate Raman-like spectra with a linear concentration of chemical components and DIC enabled selection of droplet-containing fields of view.

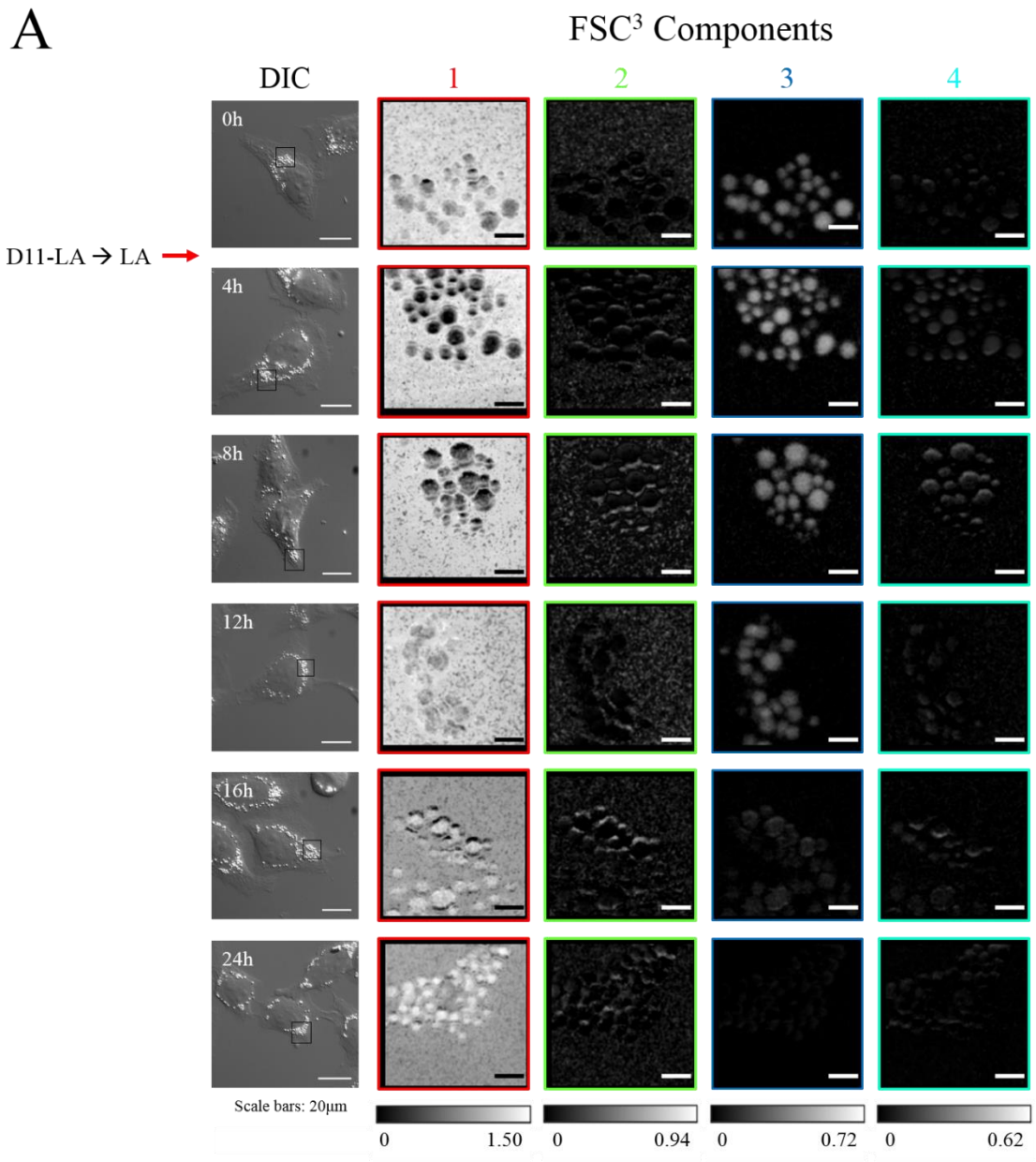
A
FSC3 Components
DIC
1
2
3
4
0h
4h
8h
12h
16h
24h
D11-LA → LA
Scale bars: 20µm
0
1.50
0
0.94
0
0.72
0
0.62

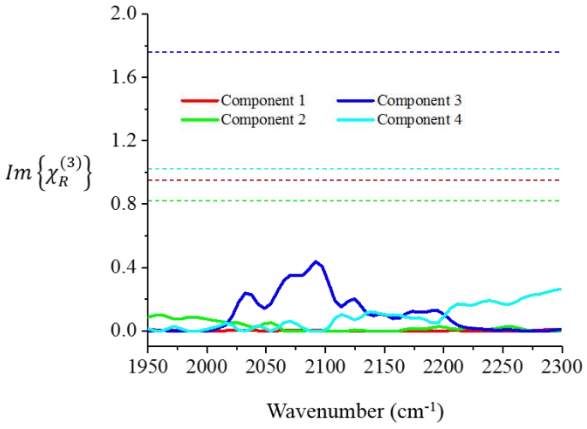
Component 1
Component 2
Component 3
Component 4
Im{χR(3)}
2.0
1.6
1.2
0.8
0.4
0.0
1950
2000
2050
2100
2150
2200
2250
2300
Wavenumber (cm-1)

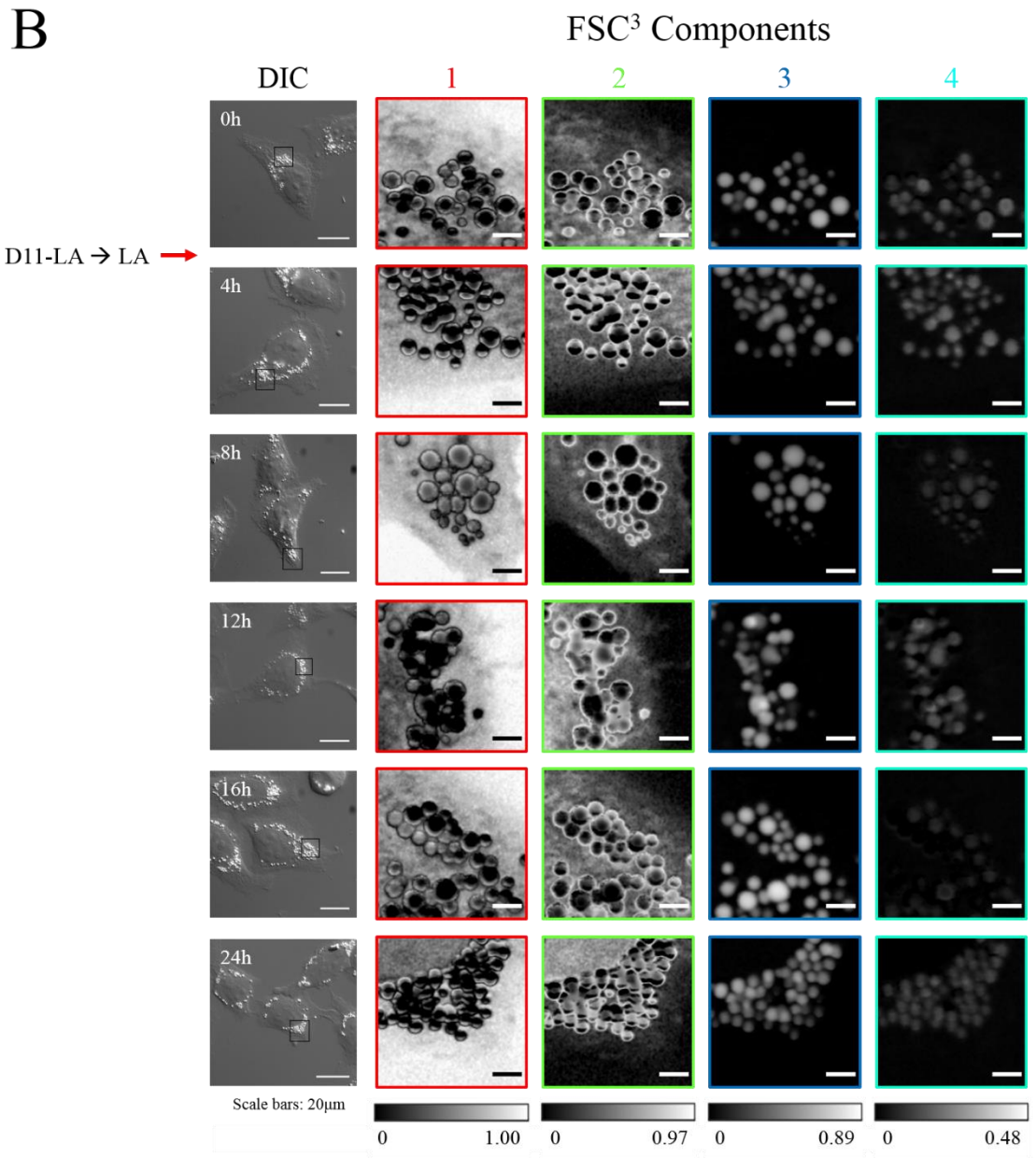
B
FSC3 Components
DIC
1
2
3
4
0h
4h
8h
12h
16h
24h
D11-LA → LA
Scale bars: 20μm
0
1.00
0
0.97
0
0.89
0
0.48

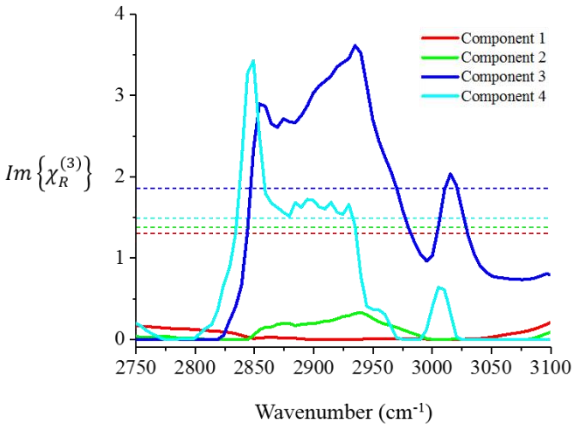
Component 1
Component 2
Component 3
Component 4
$Im\{\chi_R^{(3)}\}$
0
1
2
3
4
2750
2800
2850
2900
2950
3000
3050
3100
Wavenumber (cm-1)

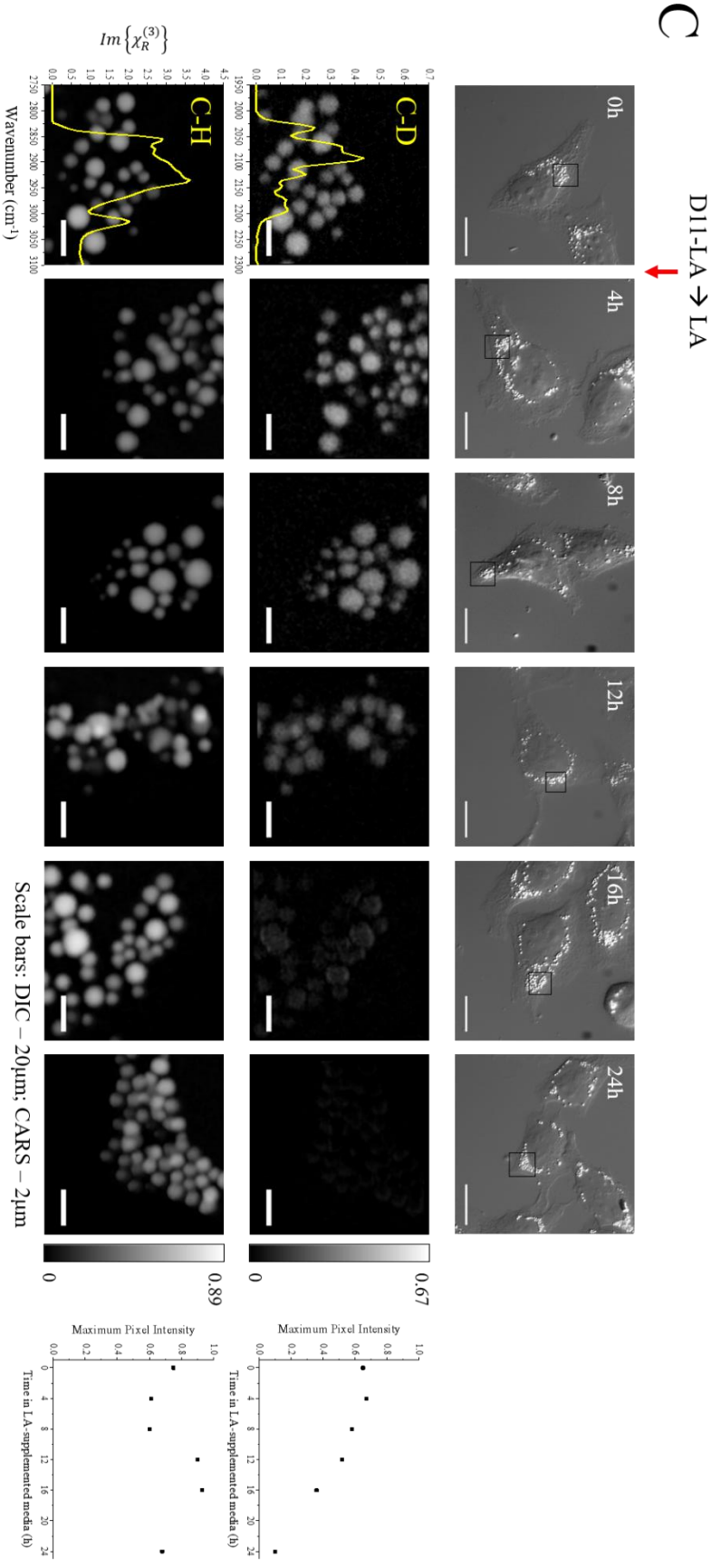
C
D11-LA → LA
0h
4h
8h
12h
16h
24h
C-D
C-H
$Im\{\chi_R^{(3)}\}$
Wavenumber (cm^{-1})
Scale bars: DIC – 20μm; CARS – 2μm
0
0.67
0
0.89
Maximum Pixel Intensity
Time in LA-supplemented media (h)
Maximum Pixel Intensity
Time in LA-supplemented media (h)

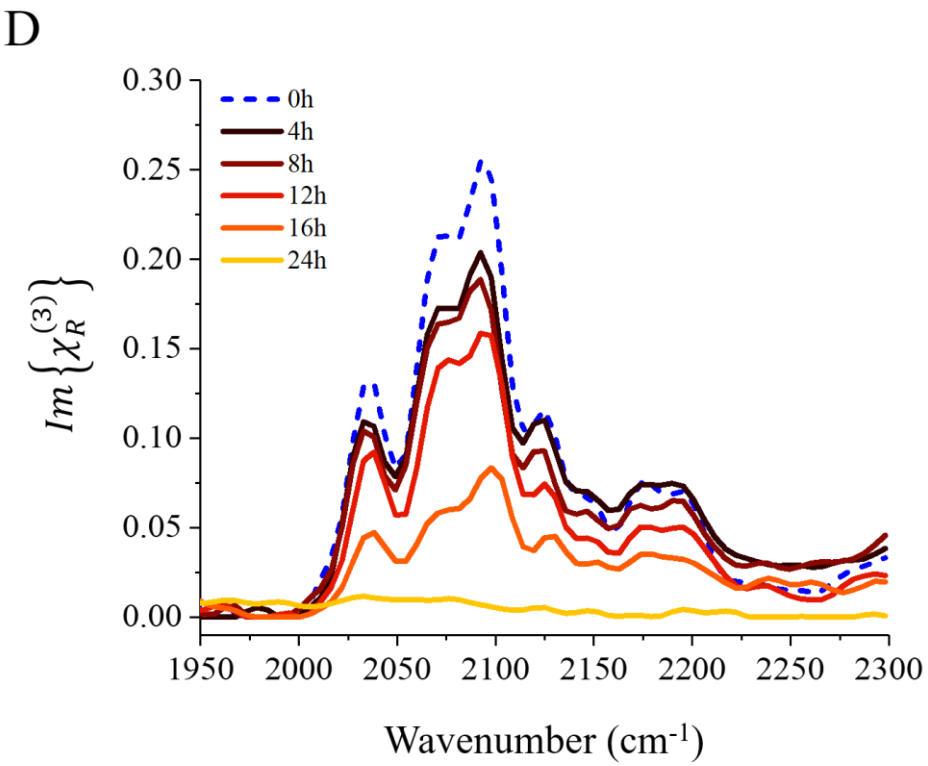

Figure 5.2 | FSC^3 analysis of D11-LA turnover from cytosolic droplets. Cells from the D11-LA→LA treatment group were imaged by hyperspectral CARS over the spectral ranges, 1950-2300 cm^{-1} (A) and 2750-3100 cm^{-1} (B), targeting the CD- and CH-associated peaks, respectively. The hyperspectral datasets from all cells were analysed by FSC^3 simultaneously so that the most common spectra were identified across images from all time-points. The spatially resolved images for each component, along with the associated spectra showing the phase-retrieved imaginary part of the normalised CARS susceptibility $Im\left\{\chi_R^{(3)}\right\}$ are displayed. The corresponding real parts are shown as averages, indicated by horizontal dashed lines. Within the cell-silent region (1950-2300 cm^{-1}), a component corresponding to D11-LA was identified (Component 3), showing localisation of signal to droplets and a peak at ~ 2100 cm^{-1} corresponding to C-D bond vibrations within its retrieved spectrum. The other three components are considered to correspond to fluctuations in background signal, showing inconsistent spatial images and featureless spectra. Signal from the D11-LA component decreases over the 24-hour time-period. Within the CH-stretch region, components corresponding to water (Component 1), protein (Component 2) and lipid (Components 3 and 4) are identified, based on localisation of signal and line-shapes of their retrieved spectra. The lipid components do not show clear differences in peak intensity between time-points. Component 3 from Figures 5.2A and 5.2B are combined in Figure 5.2C to give an overview of the observed changes in CD- and CH-based lipid concentrations, with retrieved spectra shown as overlays. Concentration plots give the maximum intensity values from each image. Full volume concentration ranges across all images are given by the grayscale values. DIC images show whole cells and the droplet-containing regions selected for hyperspectral CARS acquisition. Scale bars show 20 μm in DIC images and 2 μm in FSC^3 images. Figure 5.1D shows a plot of the CD peaks when FSC^3 was applied to hyperspectral datasets from each time point individually.

Figure 5.2A shows the spatial and spectral FSC^3 outputs when samples from all time-points were considered in the data analysis algorithm together, as in Figure 5.1A. The same spectral range of 1950-2300 cm^{-1} was utilised to target the CD-associated peak, four chemical components were once again considered in the analysis algorithm, and a single field of view was acquired from a single cell for each time-point, thus retrieved spectra for each component are again representative of only the six time-points shown. With the selected spectral range being located within the cell-silent region with no contributions from endogenous chemical groups, the only meaningful component was Component 3, which corresponded to D11-LA, showing signal localised to lipid droplets, and a CD-associated peak at ~ 2100 cm^{-1} within the retrieved spectrum. The other three components once again failed to show spectral features within the selected spectral range and were therefore considered to represent fluctuations in background noise. Contrary to the LA→D11-LA group, the 0h sample showed a strong CARS signal corresponding to carbon-deuterium bond vibrations, resulting from the uptake and storage of D11-LA over the 18-hour incubation period, and the lack of exposure to the LA-supplemented growth media, thus preventing turnover of deuterated lipid from droplets. A strong visible CARS signal corresponding to CD groups was maintained up to approximately 12 hours, after which the signal was seen to deplete, with little observable signal by the 24-hour time-point.

Figure 5.2B shows FSC^3 outputs from the six fields of view across all time-points following application of the algorithm to all samples simultaneously, as in Figure 5.2A. A spectral range of 2750-3100 cm^{-1} was employed to target vibrations of CH groups, and four components were considered in the analysis algorithm. Components were identified corresponding to aqueous media (water) (Component 1), protein with a small amount of lipid contribution (Component 2), lipid (Component 3), and another lipid component due heterogeneity in the retrieved spectra (Component 4). As in Figure 5.1B, changes in CARS intensity corresponding to CH-based lipids were not clear, with images at each time-point appearing similar over the full 24-hour time period. The reasoning of CH-associated signal being present throughout the 24-hour time-course, thus not producing as dramatic a change in signal compared to changes in the CD peak, was once again proposed.

Figure 5.2C shows the spatially resolved images and retrieved spectra for the lipid components identified within the six imaged fields of view from both the cell-silent and CH-stretch regions of the Raman spectrum. As shown by Figures 5.2A and 5.2B, the sample fixed at the 0h time-point showed the largest D11-LA signal, due to its exposure to D11-LA-supplemented media for the preceding 18-hour time-course, and lack of exposure to LA-supplemented media, thus not providing the cells with an opportunity to turn over the D11-LA from their cytosolic droplets. Over the following 24-hour period, cells showed a steady decrease in D11-LA

concentration (0.67 (67%) to 0.1 (10%), as indicated by the associated plot), as D11-LA was mobilised from their lipid droplets and replaced with the newly presented LA. By the 24-hour time-point, only a very small amount of D11-LA remained within droplets of cells. As described for Figure 5.1C above, determination of absolute volume concentrations per pixel was not possible as accompanying reference spectra were not acquired from the cell-silent and CH-stretch regions of the D11-LA spectrum. The lack of clear differences between signal intensity in images acquired at different time-points within the CH-stretch region was also observed in the associated plot, where the concentration of CH-based lipid did not show a general increase or decrease over the 24-hour time-course, ranging from 0.6 (60%) to 0.93 (93%) with a peak concentration at the 16h time-point. Similar to Figure 5.1C, some droplets appeared to differ in their intensity within the spatially resolved images, but these differences were apparent in images from both the cell-silent and the CH-stretch region, and were therefore not considered to represent variations in concentration of CD- and CH-based lipids. Instead, it was possible that other factors, such as z-plane, affected signal intensity from the lipid droplets. Figure 5.2D shows a plot of the CD-associated peaks corresponding to D11-LA from the single field of view for each time-point when FSC^3 analysis was applied to each sample individually. In agreement with the spatially resolved images displaying the D11-LA component, the intensity of the peak was seen to steadily decrease over the 24-hour period, until it could no longer be distinguished at the 24h time-point.

The results shown within Figures 5.1 and 5.2 indicated that some uptake of fatty acid into lipid droplets occurred as quickly as 4 hours, with observable signal for the CD-associated component in Figure 5.1A and 5.1C at the 4-hour time-point, and that uptake continued up to the 16-hour time-point. Between the 16- and 24-hour time-points, CARS signal intensity for CD-based lipid was seen to reduce, possibly due to depletion of deuterated lipid from the growth media and subsequent turnover of the deuterated lipid from droplets. However, the intensity of the observed CD-associated signal in Figure 5.2A and 5.2C was maintained at a similar level over an 8-hour period in absence of D11-LA, with a strong detectable signal still visible at 16 hours, hence it seemed unlikely that CD-associated signal should decrease from 16- to 24-hour time-points, even if D11-LA was completely depleted from the growth media. Based on continual accumulation of fatty acid within droplets over a 16-hour time period, and the observed reduction in CD signal between 16- and 24-hour time-points, an 18-hour incubation appeared to provide sufficient time for cells to take up and store lipids into droplets to roughly maximum concentration, thus providing justification for the incubation time employed throughout this thesis. Based on the observed uptake and depletion of D11-LA in Figures 5.1 and 5.2, respectively, it was apparent that cells readily used the lipids stored within their cytosolic droplets

for metabolic processes, as opposed to utilising the newly presented lipid and preserving the stored lipid within their droplets.

5.2.3. Part A summary

The above section evaluates the applicability of FSC^3 analysis for the investigation of lipid uptake, storage and turnover through use of deuterium as a non-perturbative labelling strategy, expanding on the proof-of-principle that was established within Chapter 4. Through utilisation of a deuterated isoform of linoleic acid (D11-LA), a FSC^3 component could be identified corresponding to C-D bond vibrations, enabling visualisation of uptake and storage of the fatty acid into cytosolic droplets, determined by an increase in CARS signal within spatially resolved images and emergence of a CD peak at ~ 2100 cm^{-1}, as well as its turnover from these droplets, giving a reduction in CARS intensity and gradual disappearance of the CD peak.

Whilst changes in CD-associated CARS intensity were clear between images acquired at different time-points, differences between CH-associated signal within the respective images were less distinguishable. This was considered to be due to CH groups being present within droplets throughout the experiment, with both LA and D11-LA containing C-H bonds within their chemical structures, hence giving a less dramatic change in CARS signal. The acquired Raman spectra for pure LA and D11-LA, which were discussed in Chapter 4, showed preservation of the CH-stretch peak shape, but D11-LA showed a reduced peak intensity. In contrast, the CD-associated peak which was present within the D11-LA spectrum was completely absent from that of LA. Therefore, the observed spectral differences between the two isoforms are more apparent within the cell-silent region compared to those within the CH-stretch region. Hence, whilst the total number of CH groups would have reduced over the 24-hour period due to incorporation of CD groups, because the CH bonds were never depleted to a low level, the change in CARS signal was not clear.

It may have been expected that when four components were considered in the algorithm, two lipid components would have been identified showing CH-stretch peaks with different intensities, i.e. a large CH peak corresponding to CH groups in LA, which may decrease over the time-course, and a smaller peak corresponding to CH groups in D11-LA, which may increase over the time-course. However, this was not observed, and although two separate lipid components were identified, neither of these components showed a large amount of variation between time-points. It is possible that because the retrieved spectra for each time-point were similar in both line-shape and intensity, the FSC^3 algorithm grouped them together into a single

lipid-associated component. It is likely that the use of a fully deuterated isoform of linoleic acid, with no C-H bonds remaining, would produce a clearer difference is CH-associated signal over the 24-hour time-period. As the molecule would be entirely deuterated, all CH groups within lipid droplets would be replaced with deuterium, and thus the CH-associated signal would be depleted further, generating clearer differences between images from each time-point.

Based on the data shown above, lipid droplet-associated storage and turnover appears consistent across all droplets within the imaged field of view, with droplets likely containing a combination of neutral lipids formed from the externally applied deuterium-labelled fatty acids and those formed endogenously by the cell. However, confirmation of this would require analysis of CH- and CD-based lipid concentration of each imaged droplet. Further investigation is thus warranted to completely eliminate the possibility of selective partitioning of different lipids into specific droplets. Co-treatment of cells with two different fatty acids would permit investigation into selective partitioning tendencies, assessing whether all droplets show a combination of both applied lipids, as suggested by the data described in section 5.2.2 above, or whether the different lipids undergo partitioning into lipid type-specific droplets. If selective partitioning of different lipids into specific droplets were to occur, this would likely take place within the ER during lipid droplets biogenesis. According to biophysical principles, low levels of neutral lipids can be stored within the bilayer of the ER membrane, but at high levels the neutral lipids undergo phase separation which is thought to lead to partitioning of the excess neutral lipid into an emerging droplet which then buds into the cytoplasm[176,177]. However, partitioning based on biophysical properties would not explain selective partitioning of different neutral lipids into specific droplets. Evidence has also been provided for controlled partitioning of lipids intended for storage from those intended for membrane biogenesis via activity of the phosphatidate phosphatase, Pah1, at the nuclear membrane[178], however it is unclear whether this enzyme could play a role in the partitioning of neutral lipids derived from different fatty acids into specific droplets.

In principle, the combination of deuterium-labelling and FSC³ data analysis is applicable to other biological molecules for the study of cellular uptake and turnover. However, as described frequently within this thesis, the accumulation of lipids within concentrated droplets generates a strong CARS signal. For other molecules, such as carbohydrates or amino acids, which show a more ubiquitous cellular distribution, detection of CARS signal above noise may present a significant challenge.

5.3. Part B: Deuterated lipid uptake combined with FSC^3 data analysis as a tool for tracking cell lines in a mixed population

5.3.1. Introduction

Based on the strong CARS signal generated within the cell-silent region of the Raman spectrum by cytosolic droplets containing deuterated lipid, the combination of deuterated lipid-treatment and FSC^3 analysis of chemical composition was explored as a method to distinguish between different subsets of cells within a mixed population. Depending on the timescale over which a CD-associated signal can be detected by FSC^3, this innovative labelling/imaging strategy may provide an effective non-invasive strategy for tracking cells of interest over time. The ability to visualise and track groups of cells over prolonged time periods is of importance within several areas of biomedicine, for example within cancer treatment, where observation of delivery of cell-based therapeutics (e.g. T-cells and stem cells) to tumour sites, as well as assessment of their differentiation and proliferation, is vital for improving understanding of cancer mechanisms and developing effective intervention strategies[179]. Fluorescence-based imaging has been employed to study T-cell migration to tumour sites[180,181], however, as described in Chapter 1, fluorescence imaging has many limitations, including structural perturbation, photobleaching and phototoxicity, and therefore, label-free cell tracking is an attractive prospect.

Given the ability of FSC^3 to provide a direct comparison of the chemical composition of biological samples, its potential application for identifying and separating cells from different sub-groups within a mixed population was explored by utilising the uptake and storage of deuterated fatty acids into cytosolic droplets within cells. Deuterated lipid is not endogenously produced by cells, and therefore its uptake and storage into cytosolic droplets can be exploited for non-invasively labelling, enabling cells to be tracked within a mixed population. The strong signal observed from lipid droplets, as well as the distinct differences between spectra acquired from droplets containing deuterated and non-deuterated lipid, makes them highly suitable structures for distinguishing between cells in a non-perturbative manner.

5.3.2. FSC^3 analysis for identification and tracking of a cell line of interest within a mixed population via deuterium-labelled lipid droplets

Figure 5.3 outlines the strategy employed to evaluate the ability of FSC^3 to identify cells of interest within a mixed population and track them over time. Acquired image data is also displayed, showing distinction of cells from one another within a mixed population based on differences in lipid droplet composition. Specifically, FSC^3 analysis is applied to hyperspectral CARS datasets acquired from lipid droplets of cells, with presence or absence of CD-associated CARS signal enabling assignment of cells to their original populations.

Two groups of HeLa cells were lipid starved before incubation with either LA or D11-LA for an 18-hour period, after which time cells were detached from their culture dishes via treatment with trypsin and combined to give a mixed population. After re-plating and a subsequent 8-hour incubation period, cells were PFA-fixed and cytosolic lipid droplets were imaged by hyperspectral CARS over the spectral range, 1800-3000 cm^{-1}, enabling inclusion of peaks from both the cell-silent and CH-stretch regions of the Raman spectrum. FSC^3 analysis was applied to generate spatial and spectral outputs, confirming presence or absence of CARS signal corresponding to carbon-deuterium bonds, thus enabling distinction between cells from each of the original populations. Initially, a fluorescently labelled form of dextran (AlexaFluor488-labelled dextran, Dex-488), was incorporated into one of the cell populations, in this case the population treated with LA (group b in Figure 5.3A), prior to its combining with the second population. This ensured efficient selection of fields of view containing cells from both of the original populations via fluorescence imaging, whilst also providing a reference for interpretation of the observed CARS data. Dextran was selected as a suitable fluorescent marker as it passes through the endosomal system and accumulates within lysosomes, which maintain their fluorescence following cell division.

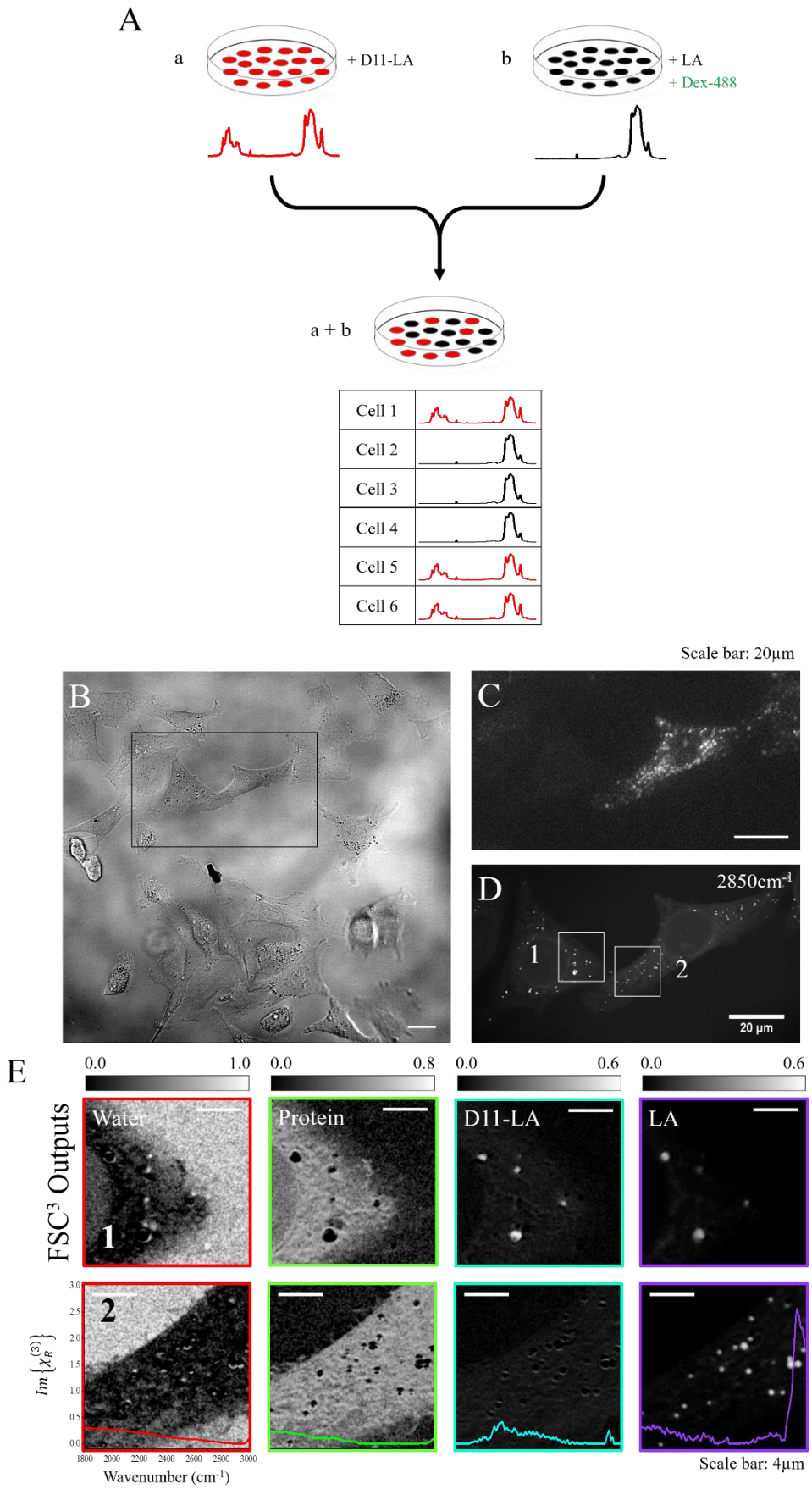
A
a
+ D11-LA
b
+ LA
+ Dex-488
a + b
Cell 1
Cell 2
Cell 3
Cell 4
Cell 5
Cell 6
Scale bar: 20µm
B
C
D
2850cm-1
1
2
20 µm
E
0.0
1.0
0.0
0.8
0.0
0.6
0.0
0.6
FSC3 Outputs
Water
Protein
D11-LA
LA
1
2
Im{χR(3)}
Wavenumber (cm-1)
Scale bar: 4µm

Figure 5.3 | Schematic overview of strategy for assessment of cell lineage tracking capabilities of FSC³ (A) and observed image data acquired from cells within a mixed population (B-E). Two populations of cells, a and b, are first incubated with D11-LA and LA, respectively, before cells are detached from culture dishes and combined to give a mixed population. By acquiring hyperspectral CARS datasets from lipid droplets of cells within the mixed population and applying FSC³ analysis, deuterated and non-deuterated lipid chemical components can be identified, and cells can be assigned to their original population (a or b) based on presence or absence of CD-associated CARS signal. AlexaFluor488-labelled dextran was incorporated into the LA-treated cell population for initial field of view selection and to provide further support for the observed CARS datasets. The brightfield image (B) shows a region of the mixed population of HeLa cells, from which two cells were selected for further imaging. The fluorescence image (C) confirms that the two cells originated from separate populations as signal is only observed within the right-hand cell, and not from the left-hand cell, and the CARS image acquired at 2850 cm^{-1} (D) confirms the presence of lipid droplets within both cells, which would serve as the target for subsequent hyperspectral CARS acquisition. Hyperspectral datasets were acquired from the fields of view indicated by white boxes over the spectral range, 1800-3000 cm^{-1}, and FSC³ was applied to identify and spatially resolve chemical components corresponding to water, protein, D11-LA and LA (E), confirmed by representative spectra showing the phase-retrieved imaginary part of the normalised CARS susceptibility $Im\left\{\chi_R^{(3)}\right\}$. Volume concentration ranges are shown on a grayscale. The presence of signal for the D11-LA component in the left-hand cell (Region 1), confirmed by presence of a small peak at ~ 2100 cm^{-1} in its retrieved spectrum, and the absence of such signal in the right-hand cell (Region 2) enables distinction between the two cells and assignment of each to its original population. The fluorescence image provides further confirmation of the FSC³ outputs. Scale bars show 20 μm in whole-cell images and 4 μm in FSC³ images.

Figures 5.3B to 5.3E show acquired images and FSC³ outputs from cells within a mixed population, enabling separation of cells from each of the original populations based on differences in lipid droplet composition. Figure 5.3B shows a region of the mixed population, from which two cells were selected for fluorescence and CARS imaging, the results of which are shown in Figures 5.3C and 5.3D, respectively. Fluorescent signal from Dex-488 was observed within the right-hand cell, confirming its origin from the LA-treated original group, whilst no comparable signal was seen within the left-hand cell, thus indicating its origin from the D11-LA-treated original group. The 2850 cm^{-1} CARS image confirms the presence of lipid droplets within both cells, which were imaged by hyperspectral CARS before subsequent FSC³ analysis was applied for assessment of chemical composition. The spatial and spectral outputs of FSC³ applied to hyperspectral CARS datasets acquired within the indicated fields of view are displayed in Figure 5.3E. A spectral range of 1800 cm^{-1} to 3000 cm^{-1} and consideration of six separate chemical components in the FSC³ algorithm enabled components corresponding to water, protein, D11-LA and LA to be identified and spatially resolved. The D11-LA component, which was identified based on the small CD-associated peak at ~ 2100 cm^{-1} in the retrieved spectrum, showed CARS signal within droplets of the left-hand cell (Cell 1), but not those of the right-hand cell (Cell 2), and could therefore be utilised to separate cells and assign them to their original populations. The

identification of D11-LA within droplets of the left-hand cell agreed with the observed absence of fluorescent signal in Figure 5.3C, both providing confirmation that the cell originated from the D11-LA-treated population (group b in Figure 5.3A). The observed results indicated the potential for labelling cells of interest with a deuterium-labelled lipid and then tracking those cells within a mixed population over time via hyperspectral CARS acquisition and FSC^3 analysis.

The combination of deuterium-labelling and FSC^3 analysis is intended to provide a non-invasive, label-free strategy for tracking cells within a mixed population, and thus incorporation of a fluorescent marker is somewhat contradictory. Consequently, the experiment was repeated without introducing the AlexaFluor488-labelled dextran into one of the cell populations, providing certainty that the observed results were due to differences in lipid concentrations only and were not influenced in any way by fluorescent label incorporation. As before, HeLa cells were first starved, and then treated with either LA or D11-LA, before combining to give a mixed population. Cell samples were fixed at 8- and 16-hour time-points following mixing of original populations, before CARS imaging of whole cells and acquisition of hyperspectral datasets from smaller lipid-rich regions of the cell was performed.

Initially, the capability of single wavenumber CARS was assessed for distinguishing between two investigated cells based on the presence or absence of signal corresponding to CD-associated signal, and the resulting images are shown in Figure 5.4. CARS images were acquired at 2850 cm^{-1}, the resonant frequency of C-H bonds, and 2170 cm^{-1}, the resonance frequency of C-D bonds. CH-associated signal was observed from lipid droplets of both cells due to both LA and D11-LA possessing C-H bonds within their chemical structures, whilst CD-associated signal was only present within lipid droplets from the lower cell (Cell b), and not from droplets within the upper cell (Cell a), thus permitting distinction between the two cells and allocation of each to their respective original populations. It could therefore be accepted that single wavenumber CARS was sufficient for separating cells at 8 hours post-mixing, however, the CARS intensity observed within the 2170 cm^{-1} image is weak compared to the observed intensity from the D11-LA component observed in Figure 5.3, as well as the CD-associated signal that was observed for deuterated lipid components within Chapter 4. Hence, hyperspectral CARS data was acquired from the same fields of view and FSC^3 data analysis was applied, the results of which are shown in Figure 5.5.

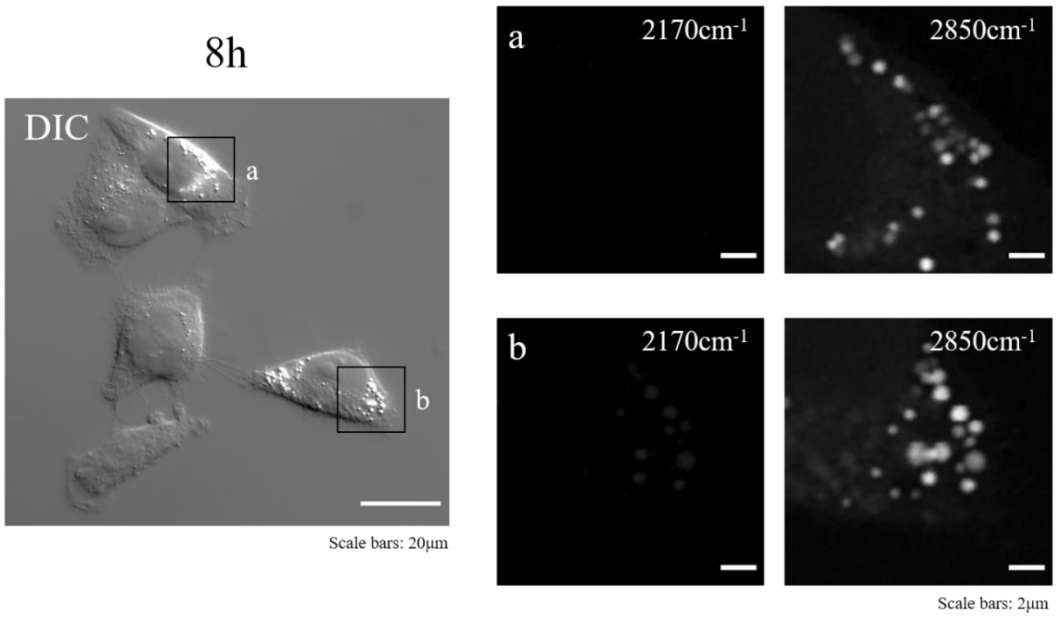

Figure 5.4 | Single wavenumber CARS images acquired from cytosolic lipid droplets of cells from the 8-hour post-mixing group at 2170 cm^{-1} and 2850 cm^{-1}, targeting vibrations of C-D and C-H bonds, respectively. DIC images show whole cells and the droplet-containing regions selected for CARS imaging. Scale bars show 20 μm in DIC images and 2 μm in CARS images.

Figure 5.5 shows the FSC^3 outputs from 8-hour samples following application to hyperspectral CARS data. As fluorescence imaging could not be used for initial selection of cells, CARS line-scans, where the Y axis is set to a single pixel and only the X axis is scanned as a single line, were acquired from lipid droplets within cells as a quick way of obtaining spectra for identification of cells possessing deuterated or non-deuterated lipid. Cells were thus selected from the mixed populations and hyperspectral CARS datasets were acquired from smaller lipid droplet-containing regions. Six separate chemical components were considered in the FSC^3 algorithm to well-represent the chemical composition within the field of view, generating concentration maps displaying the distribution of water (Component 1), protein (Components 2 and 3), LA (Component 4), D11-LA (Component 5) and an inhomogeneity in the lipid signal (Component 6), as shown in Figure 5.5A. Similar to Figure 5.4, the D11-LA component showed CARS signal within lipid droplets from the lower cell (Cell b) but not the upper cell (Cell a), enabling separation of cells and assignment to original populations, however, the observed D11-LA signal was clearer than for the single wavenumber CARS images, and a higher degree of chemical specificity was provided. Figure 5.5B showed only the water, LA and D11-LA components, which provided the necessary chemical information to distinguish between the two cells and assign them to their respective original populations.

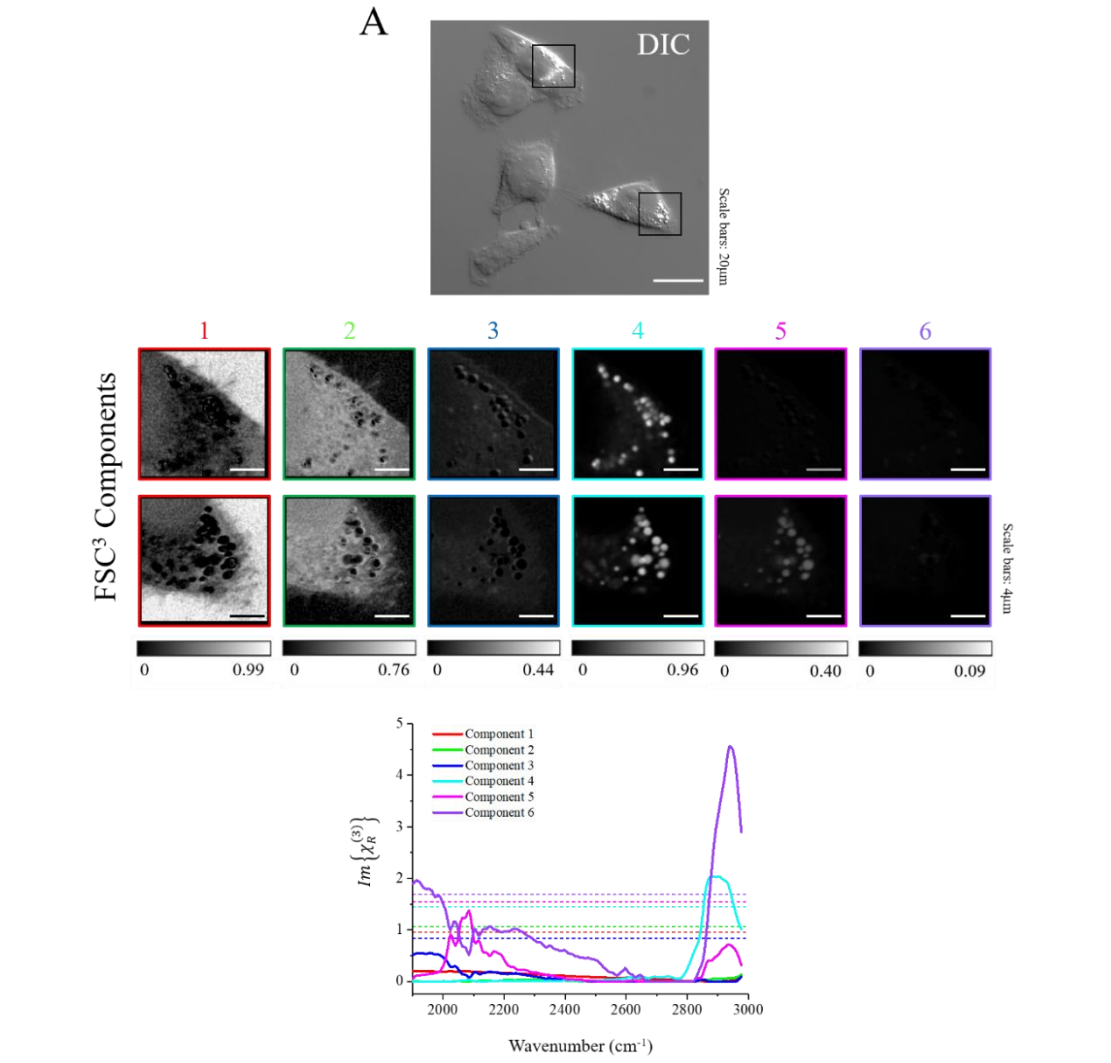
A
DIC
Scale bars: 20μm
1
2
3
4
5
6
FSC³ Components
Scale bars: 4μm
0 0.99
0 0.76
0 0.44
0 0.96
0 0.40
0 0.09
Component 1
Component 2
Component 3
Component 4
Component 5
Component 6
Im{χ_R^(3)}
Wavenumber (cm⁻¹)

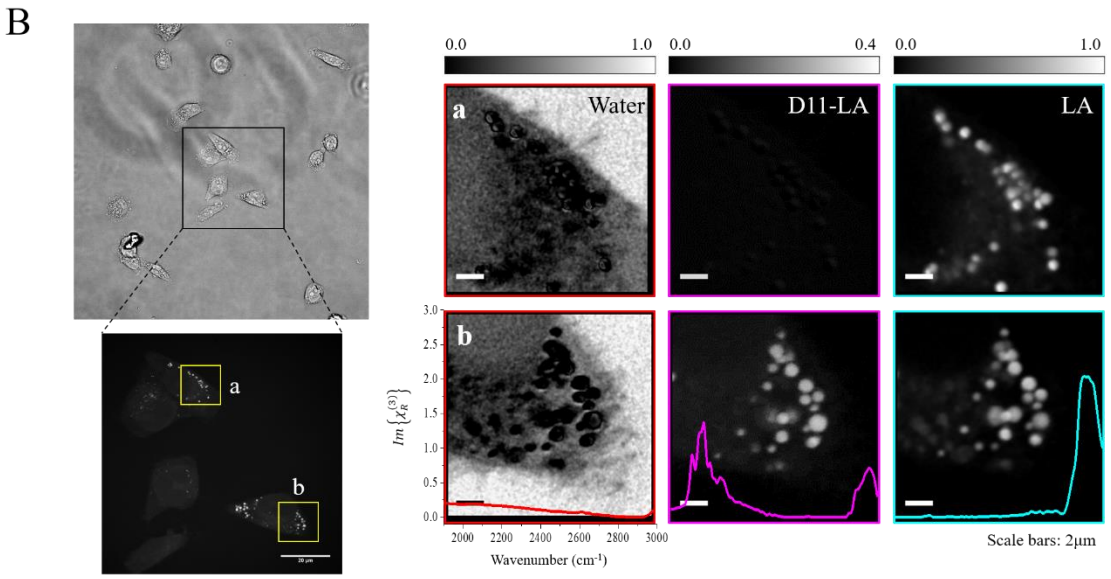
B
a
b
0.0 1.0
0.0 0.4
0.0 1.0
Water
D11-LA
LA
Im{χ_R^(3)}
Wavenumber (cm⁻¹)
Scale bars: 2μm

Figure 5.5 | Spatial and spectral FSC³ outputs from cells within a mixed population imaged at 8 hours post-mixing without incorporation of AlexaFluor488-labelled dextran. Hyperspectral CARS datasets were acquired from smaller lipid droplet-containing regions over the spectral range, 1800-3000 cm^{-1}, and FSC³ analysis was performed with consideration of six separate chemical components, producing concentration maps of water (Component 1), protein (Components 2 and 3), D11-LA (Component 5) and LA (Components 4 and 6) (A). The corresponding real parts of the retrieved spectra are shown as averages, indicated by horizontal dashed lines in Figure 5.5A. The chemical specificity of each chemical component is confirmed by retrieved spectra, showing the phase-retrieved imaginary part of the normalised CARS susceptibility $Im\left\{\chi_R^{(3)}\right\}$, and volume concentration ranges between both images for each component are shown on a grayscale. Figure 5.5B shows only the water, D11-LA and LA components for each cell. The presence of D11-LA signal in one cell and absence of such signal in the other cell confirms the capability of FSC³ to differentiate between cells in a mixed population based on lipid droplet composition. Scale bars show 20 μm in whole-cell images and 4 μm and 2 μm in FSC³ images in Figures 5.5A and 5.5B, respectively.

Single wavenumber CARS was once again employed to differentiate between two investigated cells based on the presence or absence of signal corresponding to CD-associated signal, and the resulting images are shown in Figure 5.6. CARS images were acquired at 2850 cm^{-1}, the resonant frequency of C-H bonds, and 2170 cm^{-1}, the resonance frequency of C-D bonds, from cells at 16 hours post-mixing. As in Figure 5.4, CH-associated signal was observed from lipid droplets of both cells due to both LA and D11-LA possessing C-H bonds within their chemical structures. CD-associated signal could be observed within lipid droplets from the upper cell (Cell a), and not from droplets within the lower cell (Cell b), thus permitting distinction between the two cells and allocation of each to their respective original populations, although the observed signal at 2170 cm^{-1} was extremely faint and unclear. Therefore, hyperspectral CARS data was acquired from the same fields of view and FSC³ data analysis was applied, the results of which are shown in Figure 5.7.

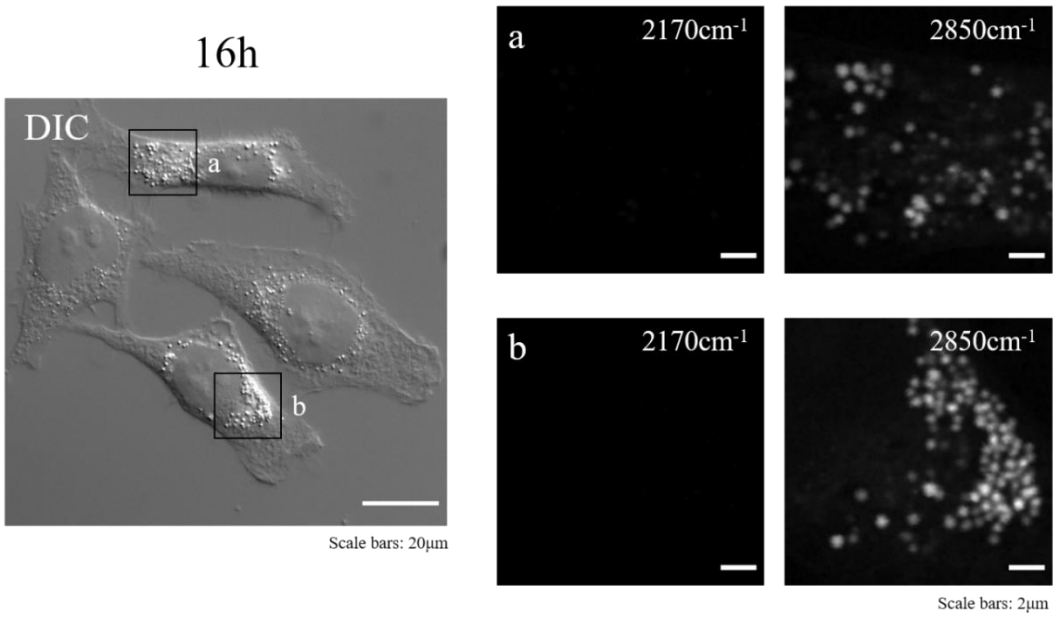

Figure 5.6 | Single wavenumber CARS images acquired from cytosolic lipid droplets of cells from the 16-hour post-mixing group at 2170 cm^{-1} and 2850 cm^{-1}, targeting vibrations of C-D and C-H bonds, respectively. DIC images show whole cells and the droplet-containing regions selected for CARS imaging. Scale bars show 20 μm in DIC images and 2 μm in CARS images.

Figure 5.7 shows the FSC^3 outputs from 16-hour samples following application to hyperspectral CARS data. Initial cell selection was performed by acquiring CARS line-scans, as described above, after which hyperspectral CARS datasets were acquired from lipid droplet-containing regions. Consideration of eight separate chemical components was required to obtain a component corresponding to C-D bond vibrations, and hence D11-LA. Concentration maps were generated displaying the distribution of water (Component 1), protein (Components 2, 3, 4 and 5), LA (Components 6 and 8) and D11-LA (Component 7), as shown in Figure 5.7A. The D11-LA component shows CARS signal within lipid droplets from the upper cell (Cell a) but not the lower cell (Cell b), enabling separation of cells and assignment to original populations. The observed D11-LA signal was considerably clearer than for the single wavenumber CARS images, and thus hyperspectral CARS and FSC^3 data analysis was considered a requirement for separation of cells at 16 hours post-mixing. Figure 5.7B shows only the water, LA and D11-LA components, which provided the necessary chemical information to distinguish between the two cells and assign each to their respective original populations.

Using the combination of hyperspectral CARS and FSC^3 data analysis, a clear distinction could be made between cells at both 8- and 16-hour time-points following mixing of cell populations based on lipid droplet composition, indicating that this strategy may be employed for

cell tracking over longer time periods. Furthermore, the absence of a fluorescence label provided certainty that the observed FSC^3 results were due to differences in lipid concentrations alone. However, a lower CARS signal was observed for the D11-LA component in the 16-hour dataset compared to the 8-hour dataset, indicating a reduction in the concentration of D11-LA present in lipid droplets. Earlier results in this chapter indicated that signal corresponding to carbon-deuterium resonances was detectable up to 16 hours, but by the 24-hour time-point only a very small CD signal could be observed, which may not be sufficient for distinguishing between cells, and hence, it is likely that over longer durations, the ability to separate cells based on D11-LA signal will be more difficult.

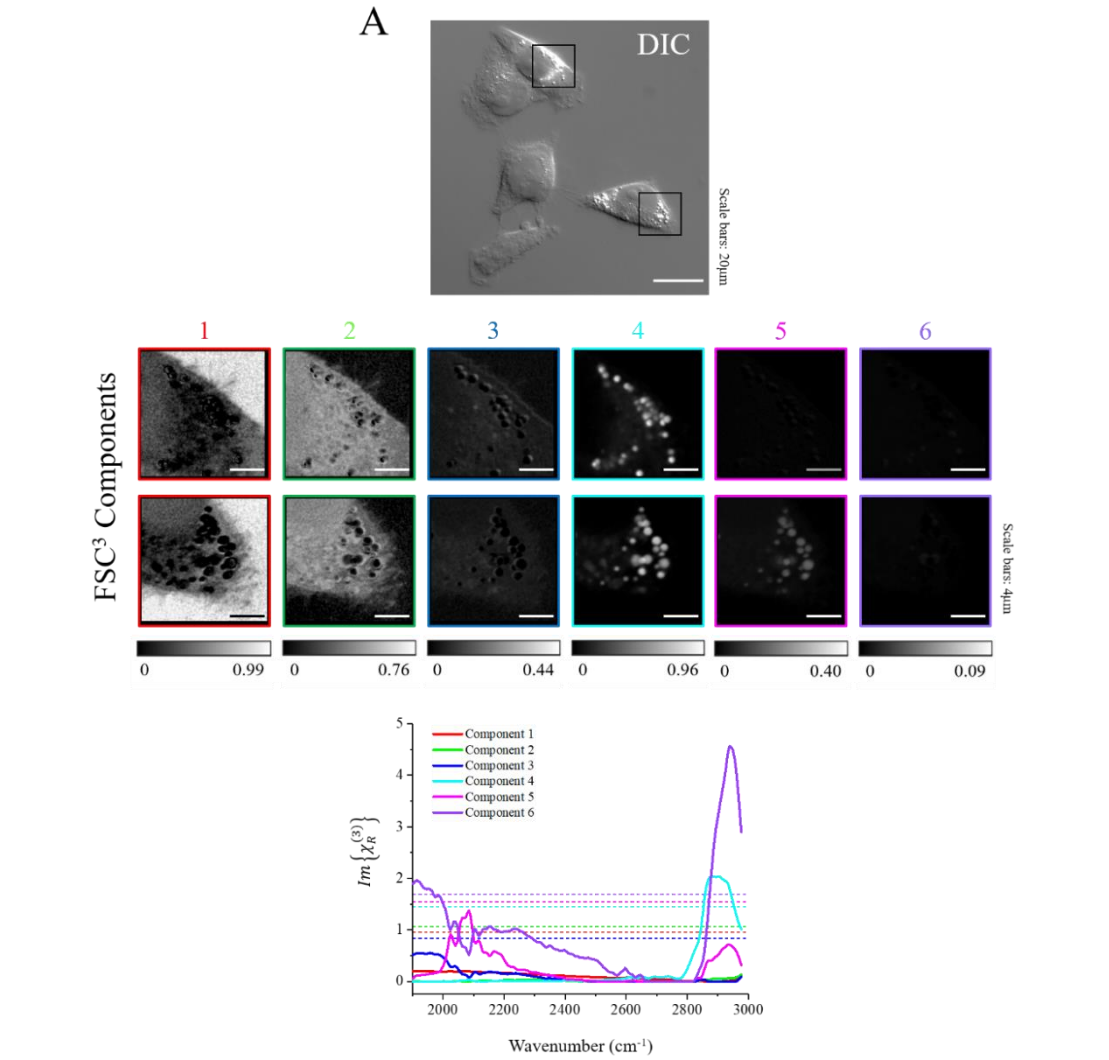
A
DIC
Scale bars: 20µm
1
2
3
4
5
6
FSC^3 Components
Scale bars: 4µm
0 0.99
0 0.76
0 0.44
0 0.96
0 0.40
0 0.09
Component 1
Component 2
Component 3
Component 4
Component 5
Component 6
$Im\{\chi_R^{(3)}\}$
Wavenumber (cm^{-1})
B
a
b
20 µm
0.0 1.0
0.0 0.3
0.0 0.9
Water
D11-LA
LA
Scale bars: 2µm
Wavenumber (cm^{-1})

Figure 5.7 | Spatial and spectral FSC³ outputs from cells within a mixed population imaged at 16 hours post-mixing without incorporation of AlexaFluor488-labelled dextran. Hyperspectral CARS datasets were acquired from smaller lipid droplet-containing regions over the spectral range, 1800-3000 cm^{-1}, and FSC³ analysis was performed with consideration of eight separate chemical components, producing concentration maps of water (Component 1), protein (Components 2-5), D11-LA (Component 7) and LA (Components 6 and 8) (A). The chemical specificity of each chemical component is confirmed by retrieved spectra, showing the phase-retrieved imaginary part of the normalised CARS susceptibility $Im\left\{\chi_R^{(3)}\right\}$, and volume concentration ranges between both images for each component are shown on a grayscale. The corresponding real parts of the retrieved spectra are shown as averages, indicated by horizontal dashed lines in Figure 5.7A. Figure 5.7B shows only the water, D11-LA and LA components for each cell. The presence of D11-LA signal in one cell and absence of such signal in the other cell confirms the capability of FSC³ to differentiate between cells in a mixed population based on lipid droplet composition. Scale bars show 20 μm in whole-cell images and 4 μm and 2 μm in FSC³ images in Figures 5.7A and 5.7B, respectively.

5.3.3. Part B summary

This section has proposed a strategy for non-invasive cell tracking, whereby cells are treated with deuterated fatty acid which is stored within cytosolic droplets. These droplets present imaging targets for hyperspectral CARS acquisition and subsequent FSC³ data analysis, which, based on the presence of carbon-deuterium signal, can be used to distinguish deuterated cells within a mixed population. The principle of this strategy has been proven over a 16-hour time-period, however, beyond this point it was unclear as to whether this technique will prove as effective. The results described in Part A of this chapter suggest not, showing almost complete depletion of CD-associated signal following a 24-hour period without exposure to deuterated fatty acid. However, in Part A, the cells were transferred to media supplemented with non-deuterated lipid, which may have induced turnover from lipid droplets and uptake of the new lipid. If cells were transferred into media which was not supplemented with lipid, as in Part B, the time for lipid turnover from droplets may be different. The combination of hyperspectral CARS acquisition and FSC³ analysis was shown to be necessary for separation of cells beyond 8 hours post-mixing as the single wavenumber CARS images could not achieve a comparable level of signal when targeting the C-D bond resonance.

Although this proof-of-principle study has been performed within two-dimensional cell cultures, it is possible that the strategy could be transferred to three-dimensional systems, such as spheroids or organoids, which comprise arrangements of multiple different cell types. Furthermore, there is potential for this strategy to be expanded so that multiple subsets of cells can be distinguished from other cells within a mixed population. This can be achieved through use of different deuterium-labelled fatty acids, which, as described in Chapter 4, show differences

in the line-shape of their associated CH-associated peak, but this will depend on the ability of FSC^3 to separate the CD-associated peaks based on only small spectral variations.

Ultimately, the applicability of this strategy will depend on the timescale over which the cells need to be tracked. T-cell migration studies typically take place over several days, which likely present timescales which are too long for droplet labelling with deuterated fatty acids to be effective. Lipids were utilised within this section due to their suitability for CARS imaging, however it is possible that other types of molecules may show a slower turnover and remain detectable within cells for longer time-periods. However, regardless of how long molecules take to be turned over, if the they cannot generate a sufficient CARS signal in the first place, then they will be unsuitable for utilisation within this strategy.

An alternative approach to extending the time over which lipids remain stored in cytosolic droplets may be to target the lipid mobilisation pathway, either through inhibition of lipolysis mediators or through synthesis of fatty acid derivatives which are not subjected to the same mobilisation procedures as naturally occurring fatty acids. Triacylglycerols stored within lipid droplets are mobilised sequentially by the lipases, adipose triglyceride lipase, hormone-sensitive lipase and monoacylglycerol lipase until glycerol and fatty acids remain, although all products of the triacylglycerol hydrolysis pathway are utilised by cells for metabolic functions, whilst the fate of the phospholipids that comprise the outer monolayer of the droplet is less well-understood[176,182].

Nicotinic acid is a well-described agonist of the lipolysis-regulating G-protein coupled receptor, GPR109A, and hence it is able to potently inhibit lipolysis of intracellular triacylglycerols[183,184]. Thus, it may be possible to utilise this chemical to preserve cytosolic lipid droplets for longer time periods, extending the duration for which cells can be distinguished from one another. As no endogenous lipids exist which undergo storage into cytosolic droplets but are not subsequently mobilised for metabolic purposes, structural modulation of fatty acids presents the only means by which long-term droplet preservation may be possible. For storage within droplets without subsequent mobilisation, the fatty acid derivative would need to undergo a structural change once stored within a lipid droplet to prevent it from being exported and degraded. To date, no such fatty acid derivative has been developed which can form triacylglycerols and accumulate within lipid droplets, and yet not be hydrolysed from the droplet core and degraded to diacylglycerols, monoacylglycerols, glycerol, and fatty acids, and thus, this concept is, at present, purely hypothetical.

6. VISUALISATION OF EXOGENOUSLY APPLIED SMALL MOLECULES BY HYPERSPECTRAL CARS AND FSC^3 DATA ANALYSIS

6.1. Introduction

As discussed in Chapter 1, the surge in interest in Raman-based imaging technologies over the past decade has been largely due to their label-free potential, being driven by detection of intracellular bond vibrations oppose to relying on incorporation of fluorescent markers for visualisation of molecules. Furthermore, the development of Raman-sensitive probes has provided an opportunity to improve chemical contrast and expand the chemical information obtained from samples, whilst introducing negligible structural change from the endogenous forms of the chemicals of interest. Consequently, the combination of Raman-based imaging and vibrational tag incorporation offers potential for improved imaging of small biological and chemical molecules which are perturbed by fluorescent labelling. Examples of such small molecules include lipids, which have been examined by CARS microscopy and subsequent FSC^3 data analysis in detail within Chapters 4 and 5, and small pharmacological molecules, whose cellular dynamics, such as the ability to traverse membranes and structures, can be largely altered with fluorescent label incorporation. Consequently, the following chapter will provide an assessment of the ability of FSC^3 to report intracellular distribution and accumulation of small therapeutic molecules when applied to hyperspectral CARS datasets.

An understanding of the uptake, distribution, accumulation, metabolism and turnover of small molecule compounds is a necessity in the drug development pipeline. Whilst potential therapeutics frequently fail as a result of poor cell membrane permeability, off-target activity, and inaccessibility of the disease target[185], the lack of information available within many existing cell- and animal-based studies makes precise determination of the underlying causes of failure extremely challenging. Mass spectrometry (MS) techniques, which are inherently label-free, are routinely employed to assess compound distributions within biological materials, with matrix-assisted laser desorption/ionisation (MALDI) and desorption electrospray ionisation (DESI) providing effective analysis of small molecule compound distribution at tissue level[186–189], however, these techniques do not display the lateral resolution required for subcellular imaging[190,191]. Time-of-flight secondary ion mass spectrometry (ToF-SIMS) has achieved subcellular resolution and has been employed to visualise small molecule compound accumulation within a single cell[192,193], although the investigated compound showed

advantageous properties, making it highly suited for the technique, and it is therefore unknown how effectively other less well-suited compounds can be visualised. As described in Chapter 1, fluorescence microscopy can be utilised to observe various biological and chemical molecules with subcellular resolution, but requires incorporation of a light-sensitive label to generate detectable signal, which can affect physical and chemical properties of small molecule compounds due to comparable sizes between small molecule compounds and fluorescent tags[11–14]. Thus, there is demand for spectroscopy or microscopy techniques which can be employed for visualisation of compounds with subcellular resolution in absence of a bulky fluorescent marker. Cellular distribution of some exogenously applied small molecule compounds have been successfully observed using spontaneous Raman imaging, for example, the alkyne group present within the chemical structure of erlotinib has enabled the compound to be visualised within cells, where it has been observed to accumulate in clusters at the cell membrane[98,132]. However, spontaneous Raman techniques suffer from a necessity for long integration times and high excitation powers, as discussed in Chapter 1, and thus coherent Raman scattering (CRS) approaches are becoming more favourable.

CARS microscopy presents a label-free technique which can provide images with subcellular resolution, whilst isotope-labelling with deuterium presents a labelling strategy which is not obstructive to the physical and chemical properties of the compound. It has been shown in Chapters 4 and 5 that FSC^3 data analysis can be applied to hyperspectral CARS data to identify and spatially resolve a chemical component corresponding to carbon-deuterium bond resonances. Thus, the combination of deuterium-labelling, hyperspectral CARS image acquisition and FSC^3 data analysis may present a strategy for observing small molecule compounds with subcellular resolution. In this chapter, it is investigated whether FSC^3 analysis can identify and spatially resolve a non-lipid-based biomolecule or small molecule compound within cells.

6.1.1. D5-L-tryptophan

L-tryptophan (Trp) is one of the eight essential amino acids which cannot be synthesised by the human body and must therefore be obtained via the diet[194,195]. Its main role is as a constituent of protein synthesis, but it is also involved in neurotransmitter regulation, acting as a precursor for synthesis of kynurenine and serotonin[196–198]. As proteins are found ubiquitously throughout cells, the distribution of L-tryptophan would be expected to be similar. Within this chapter, a deuterated isoform of L-tryptophan, D5-L-tryptophan (D5-Trp), is investigated, containing four carbon-deuterium bonds within its benzene ring and one within its pyrrole ring (see Section 3.2 of Chapter 3 for chemical structures). A large portion of the D5-Trp structure is

deuterated, but the CARS signal which the molecule generates will likely depend on how the compound accumulates due to the coherent nature of CARS.

6.1.2. D4-/D6-succinic acid

Succinic acid (SA) is a four-carbon dicarboxylic acid which is a major chemical component of the citric acid cycle and the electron transport chain, thus existing at high concentrations within mitochondria. However, SA has also been associated with the metabolism of branched-chain amino acids, haem synthesis and utilisation of ketone bodies, as well as being implicated in the mediation of the hypoxic response of cells[199] and is therefore likely to show a ubiquitous distribution throughout cells. In this chapter, two deuterium-labelled isoforms of SA are investigated; D4-succinic acid (D4-SA), which contains four carbon-deuterium bonds within its chemical structure, and D6-succinic acid (D6-SA), which contains four carbon-deuterium bonds and two oxygen-deuterium bonds, as shown in Section 3.2 of Chapter 3. In both of these deuterium-labelled isoforms of SA, the majority of the molecule is deuterated, which can provide a strong CARS signal provided the molecules show a degree of accumulation. If D4-SA and D6-SA fail to accumulate and show a ubiquitous distribution, then it is unlikely that sufficient CARS signal will be achieved to permit their visualisation.

6.1.3. Methyl-D3-triphenylphosphonium (D3-TPMP)

Methyltriphenylphosphonium (TPMP) is a cation which can permeate phospholipid bilayers and accumulate in negatively charged cellular compartments, such as the mitochondrial matrix, driven by its membrane potential, achieving increases in concentration of several hundredfold[200,201]. Thus, TPMP has been utilised for mitochondrial visualisation, delivery of therapeutic molecules, and measurement of membrane potential[202–207]. The tendency for TPMP to accumulate within mitochondria make it a well-suited molecule for imaging by CARS microscopy, which relies on coherent interference from large numbers of identical chemical bonds within the imaged focal volume. Furthermore, with *a priori* knowledge of the molecule's expected localisation site, an informed selection of the cellular field of view for imaging can be made. A deuterated isoform of TPMP is employed within this chapter, methyl-D3-triphenylphosphonium (D3-TPMP), which contains a single deuterated methyl group within its structure, as shown in Section 3.2 of Chapter 3. However, the deuterium-containing portion of the molecule consists of only three carbon-deuterium bonds, which may limit the CD-associated CARS signal generated.

6.1.4. Small molecule compounds

Initially, compounds for investigation were selected from a list of 17 deuterium-labelled compounds which had been synthesised on-site at GlaxoSmithKline. All compounds were reported to be > 99% pure. Based on the research conducted within this thesis comprising only a part of a larger network led by GSK to develop novel spectroscopy and microscopy techniques for improved understanding of pharmacokinetics and pharmacodynamics of various small molecule compounds, initial selection was based on previous analytical study of the compounds, specifically, whether the compounds were compatible with mass spectrometry. The ability to observe the same compounds with various techniques permits cross-correlation of results and systematic assessment of the effectiveness of each strategy. Existing literature which has observed deuterated biological and chemical molecules has indicated that CARS signal intensity scales with the number of C-D bonds present[125,133] and therefore compounds with a large number of C-D bonds were selected. A combination of aromatically and aliphatically labelled compounds were also selected to investigate the potential impact of CD label positioning on corresponding peak location and intensity.

Along with the chemical structure of the compounds, the accompanying data regarding compound permeability and uptake by cells was also considered, although some of this information was not available. As described in Chapters 4 and 5, one of the reasons lipids can be imaged so effectively by CARS microscopy is that they accumulate within discrete droplets within the cell cytoplasm, thus small molecule compounds which accumulate in a particular area within a cell will generate a stronger CARS signal than those which do not accumulate, and thus, compounds which were reported to show high permeability and cellular uptake were favoured over those which did not. Four compounds were thus selected for investigation by hyperspectral CARS microscopy and subsequent FSC^3 data analysis, assessing the ability of the imaging strategy to visualise deuterium-labelled small molecule compounds within a cell: D4-paracetamol (D4-Para); D8-histamine$_2$-receptor antagonist (D8-H_2Ri); D9-COX-2 inhibitor (D9-COX2i); and D7-human cytomegalovirus (HCMV) DNA synthesis inhibitor (D7-HCMVi). An overview of the chemical data for each of the compounds, along with their chemical structure, is provided in Section 3.2 of Chapter 3.

Paracetamol is a widely used analgesic and antipyretic, and whilst its mechanism of action has been disputed in the past, it is now accepted that it exerts its effects through inhibition of prostaglandin synthesis, resulting from the inhibition of cyclooxygenase-1 (COX-1) and cyclooxygenase-2 (COX-2) enzyme activity[208–210]. A deuterium-labelled isoform of paracetamol (D4-Para) is investigated within this chapter, which contains four carbon-deuterium bonds within

its aromatic ring structure. Histamine$_2$(H_2)-receptor antagonists are employed to inhibit histamine-mediated gastric acid secretion, thus permitting treatment of gastric acid-related conditions, including peptic ulcers and gastro-oesophageal reflux disease (GORD)[211,212]. Within this chapter, a deuterium-labelled H_2-receptor antagonist is investigated (D8-H_2Ri), which contains eight carbon-deuterium bonds arranged in an aromatic ring structure. Furthermore, an alkyne (C≡C) is present within the structure of D8-H2Ri, which, as described in Chapter 1, also gives a Raman peak within the cell-silent region of the Raman spectrum. Thus, it will be interesting to see if C-D bonds and C≡C bonds differ in the CARS signal they produce and the subsequent contrast they impart to D8-H2Ri. COX-2 inhibitors are non-steroidal anti-inflammatory drugs (NSAIDs), which show a similar mechanism of action to paracetamol, in that they inhibit COX-2 enzymes which in turn inhibits synthesis of prostaglandins from arachidonic acid. However, they are more frequently associated with gastrointestinal and renal toxicity, resulting from non-specific inhibition of COX-1 enzymes. A deuterium-labelled COX-2 inhibitor isoform, D9-COX2i, containing nine carbon-deuterium bonds with an aliphatic positioning, is investigated within this chapter. Information regarding cellular distribution of the aforementioned small molecule compounds or the location of their respective intracellular targets was limited within existing literature, preventing informed selection of the most appropriate field of view for CARS imaging.

D7-HCMVi is a deuterated isoform of a human cytomegalovirus (HCMV) DNA synthesis inhibitor. Inhibition of HCMV replication is achieved through inhibition of its protein kinase, UL97, which mediates phosphorylation of nuclear Lamin A/C and disperses the nuclear lamina of the host cell, thus, when UL97 is inhibited, the nuclear lamina is not dispersed and nuclear egress of newly formed HCMV virions is prevented[213,214]. Furthermore, UL97 inhibition reduces the efficiency of viral DNA synthesis and virion morphogenesis[215]. As the investigated cells within this chapter are uninfected, no HCMV is present to serve as the target site for D7-HCMVi, therefore hyperspectral CARS datasets were acquired from general cytoplasmic regions. D7-HCMVi contains seven carbon-deuterium bonds showing an aliphatic arrangement.

6.2. Raman characterisation of molecular compounds

As described in Chapter 4, Raman spectroscopy provides a reliable tool for characterisation of biological materials based on their chemical and physical properties. Thus, spontaneous Raman spectra were acquired from powder and aqueous preparations of each investigated chemical compound as a prerequisite to CARS data acquisition, providing a reference for identification and interpretation of vibrational peaks. As discussed in Chapter 2, molecular bonds are more difficult to assign in CARS spectra due to the interference between resonant and non-resonant terms of the susceptibility $\chi^{(3)}$ [106], and thus spectral processing steps are performed to address this difficulty by generating Raman-like spectra which are linear in concentration of chemical components and are comparable to acquired Raman reference spectra. Whilst both Trp and SA have been extensively studied by various analytical techniques, the other chemical compounds investigated in this chapter are not so well-characterised, and therefore peak positions corresponding to various chemical groups have not been defined.

Deuterium-labelling is once again employed within this chapter as a strategy to achieve contrast between a molecule of interest, in this case small biological and chemical compounds, and the mixed chemical background of a cell, and consequently peaks corresponding to the different vibrations of deuterium-containing chemical bonds are observed within the silent region of the Raman spectrum for each of the investigated molecules. The Raman reference spectra provide useful information for initial selection of the spectral range over which hyperspectral CARS data is acquired, as well as facilitating identification of peaks corresponding to genuine CARS signal from the investigated molecules, oppose to spectral fluctuations from background noise. The fatty acids studied in Chapters 4 and 5 were able to generate a large CARS signal within the silent region due to their repeating chains of carbon and deuterium, and so their identification above background noise was straightforward, however, as the compounds within this chapter do not possess such CARS-favourable molecular structures, it is unlikely that such a strong CARS signal will be observed, and thus differentiation between peaks corresponding to the investigated molecules and those from background noise will be more challenging. Moreover, accumulation of lipids within dense droplets further enhanced the generated CARS signal, and so a detectable CARS signal in this chapter will likely rely upon accumulation of the chemical compounds within a concentrated subcellular compartment.

Powder and aqueous samples consisted of powder preparations of each compound and 10µl droplets of compound/water solutions, respectively, mounted in air between a glass cover slip and a microscope slide via a 13 mm diameter, 0.12 mm thick imaging gasket (see Chapter 3). The acquired spontaneous Raman spectra for each of the investigated deuterated compounds are

displayed in Figures 6.1-6.4, and whilst Raman spectra for non-deuterated parent molecules are shown for Trp (Figure 6.1), SA (Figure 6.2) and TPMP (Figure 6.3), such spectra were not acquired for the other four compounds due to lack of availability (Figure 6.4).

6.2.1. L-tryptophan/D5-L-tryptophan

Acquired Raman spectra are shown for D5-Trp and its non-deuterated parent molecule in Figure 6.1 and attribution of each spectral peak to its associated chemical group is summarised in Table 6.1. L-tryptophan has been extensively studied by various analytical techniques, including Raman spectroscopy, and thus its vibrational peaks have been well-characterised[168,216].

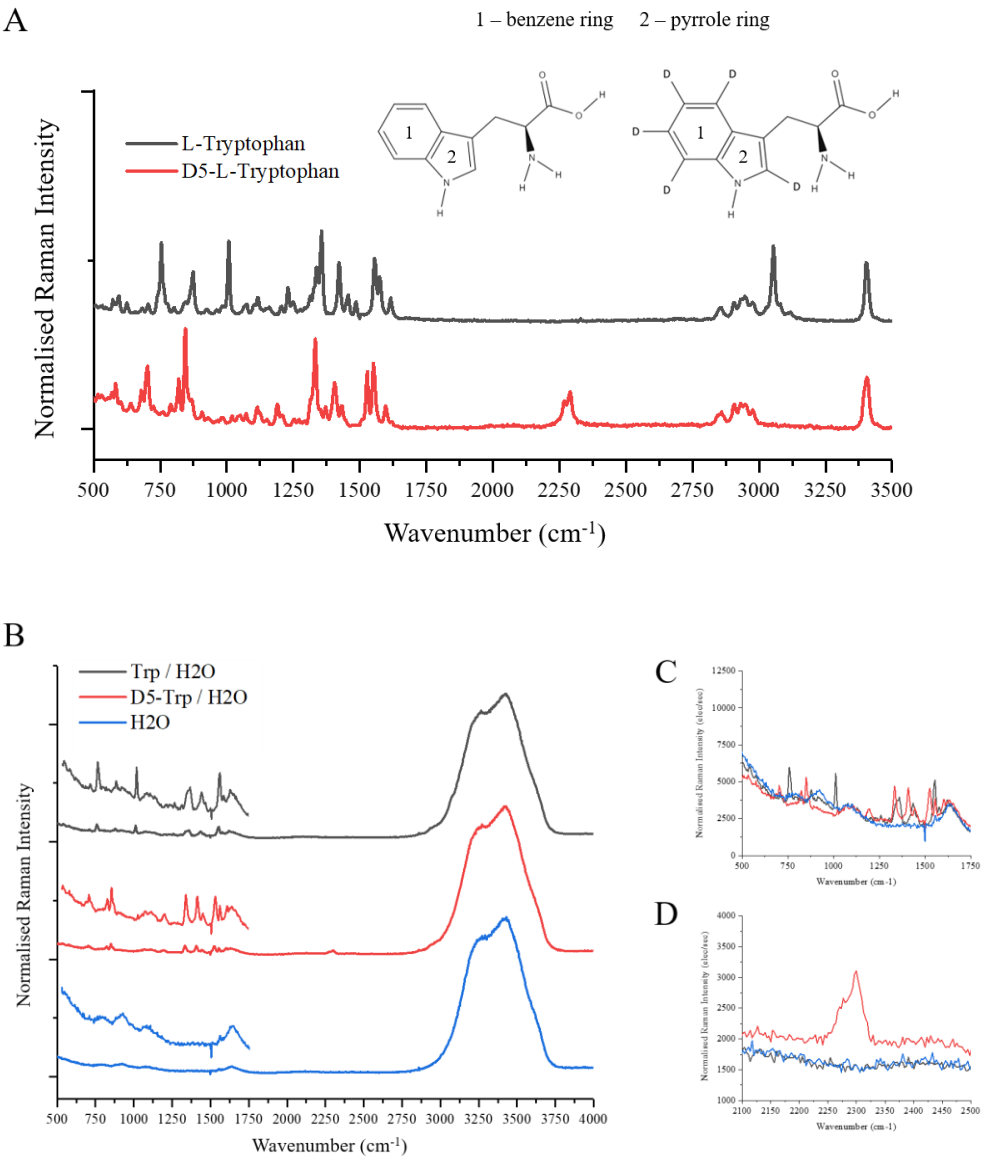

Figure 6.1 | Spontaneous Raman spectra for Trp and D5-Trp. Full spectra are shown with a spectral range of 500 cm^{-1} to 3500 cm^{-1} for molecules as powder preparations (A), and 500 cm^{-1} to 4000 cm^{-1} for molecules in 13 mg/ml solution with water (B), incorporating all three characteristic regions of the Raman spectrum, with spectra vertically shifted in respect to each other for clarity. The fingerprint region spectra from aqueous solutions are also shown with a different scale for improved visualisation of peaks. Spectra are also shown with reduced spectral ranges from 500 cm^{-1} to 1750 cm^{-1}, enabling direct comparison of peaks within the fingerprint region of the spectrum (C), and from 2100 cm^{-1} to 2500 cm^{-1}, centred around the carbon-deuterium-associated peak at ~ 2300 cm^{-1} within the silent region of the D5-Trp spectrum (D). Reduced spectra are transposed directly from the full spectra from the aqueous compound/water solutions but are not vertically shifted, enabling inclusion of Raman intensity values. Chemical structures of Trp and D5-Trp are also shown in Figure 6.1A.

Table 6.1 | Overview of Raman vibrational resonances for Trp with inclusion of peak positions within the silent region observed for D5-Trp. Adapted from ref [216].

Wavenumber (cm^{-1})	**Assignment**
574	β NH in pyrrole ring
596	β NH in pyrrole ring; β benzene ring; β pyrrole ring
755	θ benzene ring; θ pyrrole ring
875	α H in benzene and pyrrole rings
1010	θ benzene ring; θ pyrrole ring
1231	α H in benzene ring; γ H in pyrrole ring
1337	β CH; β H in CH_2
1355	ω CH_2; β CH
1423	ν benzene ring; ν pyrrole ring
1455	α CH_2
1483; 1557	ν benzene ring; ν pyrrole ring
1575	α NH_3^+
1617	ν_{as} CO_2^-
2268; 2290*	ν CD
2856; 2907	ν_s CH_2; ν CH
2933	ν_{as} CH_2
2951; 2979; 3030	ν_{as} H in benzene ring
3057	ν_s H in benzene ring
3080	ν_s NH_3^+ symmetrical stretch
3119	ν H in pyrrole ring
3409	ν NH in pyrrole ring

*observed as single peak at 2300 cm^{-1} in aqueous sample spectrum.

Symbols for vibrations: ν – stretching (further categorised into ν_s – symmetric stretch; ν_{as} – asymmetric stretch); β – bending/deformation (further categorised into ω – wagging; δ – twisting; γ – rocking); θ – ring breathing

Figure 6.1A shows full Raman spectra for powder preparations of Trp and D5-Trp. The fingerprint region is highly populated with resonances corresponding to bending, stretching and deformation vibrations within the pyrrole and benzene rings, whilst contributions from CH and CH_2 groups, as well as NH_3^+ and CO_2^- (as Trp exists in a zwitterionic state), also give rise to Raman peaks within this region (see Section 2.1 of Chapter 2 for overview of normal vibrational modes). The two high intensity peaks located at 755 cm^{-1} and 1010 cm^{-1} correspond to benzene and pyrrole ring breathing, whilst the prominent peak at 875 cm^{-1} corresponds to scissoring motions of the H atoms within both ring structures. The peaks at 1344 cm^{-1}, 1364 cm^{-1} and 1463 cm^{-1} correspond to bending within the aliphatic CH and CH_2 groups, whilst peaks at 1429 cm^{-1}, 1492 cm^{-1} and 1561 cm^{-1} correspond to stretching of the benzene and pyrrole rings. The peaks at 1581 cm^{-1} and 1622 cm^{-1} correspond to scissoring of NH_3^+ and asymmetric stretch of CO_2^-, respectively. Some variation is observed within the fingerprint region of the spectrum for D5-Trp as a result of hydrogen replacement with deuterium in both ring structures of the molecule, in particular, the peak at 1010 cm^{-1}, which corresponds to benzene and pyrrole ring breathing, is not present within the spectrum of D5-Trp, and changes in peak position are observed over the 500-1700 cm^{-1} spectral range, some more obvious than others. Given that deuterium is incorporated into the benzene and pyrrole ring structures of D5-Trp, the observed shifts in peak position primarily concern those corresponding to bond vibrations within these ring structures, hence the double peak at 1344 cm^{-1} and 1364 cm^{-1} does not change position between spectra for the deuterated and non-deuterated isoforms. Similarly, the peaks at 1581 cm^{-1} and 1622 cm^{-1} maintain their position as the chemical groups involved in the zwitterionic activity of (D5-)Trp are not subjected to deuterium incorporation.

The CH-stretch region of the Raman spectrum for Trp is not as populated as the fingerprint region, nor does it show the spectral overlap which was observed for the fatty acids in Chapter 4. The peaks from 2856 cm^{-1} to 2933 cm^{-1} correspond to stretching of aliphatic CH and CH_2 groups, whilst peaks from 2951 cm^{-1} to 3119 cm^{-1} correspond to stretching of H groups within the benzene and pyrrole ring structures, with the exception of the peak at 3080 cm^{-1}, which corresponds to symmetrical stretch of NH_3^+. The final peak at 3409 cm^{-1} corresponds to stretching of the NH group within the pyrrole ring. As in the fingerprint region, clear spectral differences can be observed between spectra for deuterated and non-deuterated isoforms of Trp. The peaks corresponding to H stretching within both ring structures are no longer present between 3030 cm^{-1} and 3119 cm^{-1} within the spectrum for D5-Trp and are instead down-shifted into the cell-silent region as a result of deuterium incorporation. The positions of the remaining peaks at 2856 cm^{-1}, 2907 cm^{-1}, 2933 cm^{-1}, 2951 cm^{-1}, 2979 cm^{-1} and 3409 cm^{-1} are well-preserved between spectra from both Trp isoforms. Like the vast majority of endogenous biological molecules, Trp does not

show any spectral peaks within the cell-silent region of its Raman spectrum, however, in contrast to this, D5-Trp exhibits two peaks at 2268 cm^{-1} and 2290 cm^{-1} within its silent region, corresponding to CD-associated vibrations, which are likely down-shifted from within the CH-stretch region, as suggested above. Consequently, it may be concluded that these two peaks correspond to stretching motions of deuterium within the benzene and pyrrole ring structures of Trp. As in previous chapters, these CD-associated peaks will provide the basis for studying the applicability of FSC^3 for visualisation of various deuterated molecules within cells, in this case the amino acid, Trp.

As cells would be exposed to the investigated deuterated compounds in an aqueous solution, Raman spectra were also acquired from each compound dissolved in water to observe whether peaks were still distinguishable above the signal given by water and whether their shape and/or position appeared different to those within the powder spectrum. Figures 6.1B-D show the acquired spontaneous Raman spectra from aqueous solutions of Trp and D5-Trp dissolved in water at maximum soluble concentration (13 mg/ml). A large peak corresponding to water between 3200 cm^{-1} and 3600 cm^{-1} is clearly visible within the full spectra from both isoforms of Trp, masking the CH-stretch peaks observed in the respective powder spectra, however spectral features can still be identified within the fingerprint and silent regions of the Raman spectrum, enabling distinction between spectra from each of the isoforms. Peaks from the fingerprint region are displayed more clearly in Figure 6.1C, where spectral differences between water, Trp and D5-Trp can be seen. The ring breathing peaks at 755 cm^{-1} and 1010 cm^{-1} can once again be observed within the spectrum for Trp but are absent from that of D5-Trp. The H scissoring peak at 875 cm^{-1}, the CH_2 wagging/CH bending peak at 1355 cm^{-1}, the ring stretching peak at 1557 cm^{-1}, the NH_3^+ scissoring peak at 1575 cm^{-1}, and the $CO2^-$ asymmetric stretch peak at 1617 cm^{-1} can also be distinguished from the underlying water spectrum and can all be observed at the same peak position as in the powder spectrum. Small changes in peak positions are once again observed between Trp and D5-Trp spectra within the fingerprint region as a result of selective replacement of hydrogen with deuterium. Figure 6.1D shows the observable CD-associated peak present within the silent region of the Raman spectrum for D5-Trp, which is absent from that of its non-deuterated parent molecule, appearing as a single peak at 2300 cm^{-1}, slightly altered from the double peak at 2268 cm^{-1} and 2290 cm^{-1} observed within the powder spectrum.

Overall, the peaks in the Raman spectra from both powder preparations and aqueous solutions of Trp and D5-Trp show consistency in their positioning and can be discriminated from the underlying water signal, in particular the CD-associated peak at approximately 2300 cm^{-1}, which will be utilised to achieve contrast between the molecule and the chemical background of a cell.

6.2.2. Succinic acid/D4-/D6-succinic acid

Figure 6.2 shows the acquired Raman spectra for SA, along with two of its deuterium-containing derivatives, D4-SA and D6-SA, and spectral peak attributions are once again summarised in the corresponding Table 6.2. The Raman spectrum given by SA has previously been characterised and peaks allocations have been reported[217,218].

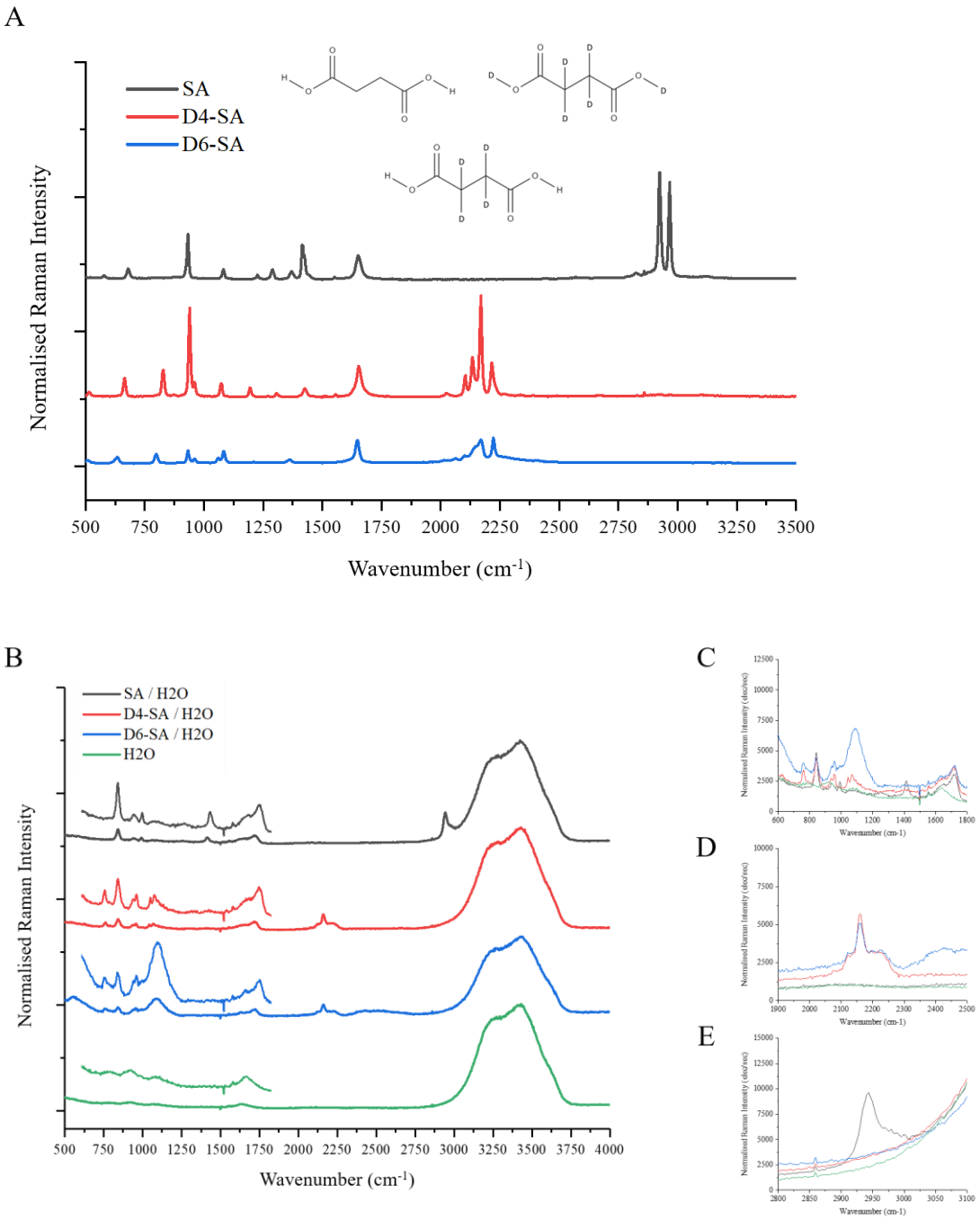

Figure 6.2 | Spontaneous Raman spectra for SA, D4-SA and D6-SA. Full spectra are shown with a spectral range of 500 cm^{-1} to 3500 cm^{-1}, for molecules as powder preparations (A), and 500 cm^{-1} to 4000 cm^{-1} for molecules in 76 mg/ml solution with water (B), incorporating all three characteristic regions of the Raman spectrum, with spectra vertically shifted in respect to each other for clarity. The fingerprint region spectra from aqueous solutions are also shown with a different scale for improved visualisation of peaks. Spectra are also shown with reduced spectral ranges from 600 cm^{-1} to 1800 cm^{-1}, enabling direct comparison of peaks within the fingerprint region of the spectrum (C), 1900 cm^{-1} to 2500 cm^{-1}, centred around the carbon-deuterium-associated peak at 2160 cm^{-1} within the silent region of the D4- and D6-SA spectra (D), and 2800 cm^{-1} to 3100 cm^{-1}, showing the CH-stretch peak at ~ 2940 cm^{-1} within the SA spectrum (E). Reduced spectra are transposed directly from the full spectra from the aqueous compound/water solutions but are not vertically shifted, enabling inclusion of Raman intensity values. Chemical structures for SA, D4-SA and D6-SA are also shown in Figure 6.2A.

Table 6.2 | Overview of Raman vibrational resonances for SA with inclusion of peak positions considered to correspond to CD-related resonances in D4-SA and D6-SA. Attributions of peaks showing altered positioning within aqueous solution spectra are given in brackets. Adapted from ref [217].

Wavenumber (cm^{-1})	**Assignment**
680	δ OC=O
797; 828 (760)	CD_2 resonance
932 (940)	δ OH…O
960; 1062 (956)	CD_2 resonance
1082	ν CC
1195	CD_2 resonance
1225 (992)	ω CH_2
1290	ν CO
1370 (1416)	ω CH_2
1417	δ OH…O
1652	ν C=O
2025; 2102; 2134; 2170; 2215 (2160)	ν CD
2924 (2940)	ν_s CH_2; ν CH
2966	ν_{as} CH_2

Symbols for vibrations: ν – stretching (further categorised into ν_s – symmetric stretch; ν_{as} – asymmetric stretch); β – bending/deformation (further categorised into ω – wagging; δ – twisting)

The full Raman spectra for powder preparations of SA, D4-SA and D6-SA are shown in Figure 6.2A. The fingerprint region shows two strong peaks at 932 cm^{-1} and 1417 cm^{-1}, which correspond to twisting of the OH…O groups at either end of the SA structure, as well as a prominent peak at 1652 cm^{-1}, corresponding to stretching of the C=O groups. Smaller peaks can be observed at 680 cm^{-1}, 1082 cm^{-1} and 1290 cm^{-1}, corresponding to twisting of the O-C=O groups, stretching of the C-C groups and stretching of the C-O groups, respectively, as well as at 1225 cm^{-1} and 1370 cm^{-1}, corresponding to wagging of the aliphatic CH_2 groups. Within the Raman spectra for D4-SA and D6-SA, some spectral differences can be observed from that of the non-deuterated parent molecule as a result of deuterium incorporation. The peak at 932 cm^{-1}, which corresponds to twisting of OH…O groups, appears to vary in signal intensity between the three spectra. For D6-SA, this is likely due to incorporation of deuterium into OH bonds which will affect vibrations of the OH…O chemical groups, although the reasoning behind the increased intensity observed within the D4-SA spectra is less clear, and most likely results from an indirect effect of deuterium incorporation within the aliphatic chain structure. The CH_2 wagging peaks at 1225 cm^{-1} and 1370 cm^{-1} are absent from the spectra of D4-SA and D6-SA due to replacement of hydrogen atoms with deuterium, and instead peaks are observed at 828 cm^{-1}, 960 cm^{-1} and 1195 cm^{-1} for D4-SA, and 797 cm^{-1}, 960 cm^{-1} and 1062 cm^{-1} for D6-SA, which likely correspond to CD_2-related resonances. The peak at 1417 cm^{-1}, corresponding to twisting motions of the OH…O groups, is also present within the spectrum for D4-SA, although showing a lower intensity than for SA, but is absent from the spectrum for D6-SA, due to deuterium incorporation within the OH bonds of the carboxylic acid groups at either end of the molecule, thus directly affecting vibrations of the OH…O groups. The peak at 1652 cm^{-1}, corresponding to C=O stretching, is maintained across the three Raman spectra as these bonds are not subjected to deuterium incorporation and therefore show the same vibrations within each of the three SA isoforms.

The CH-stretch region of the Raman spectrum for SA shows two strong peaks, one located at 2924 cm^{-1}, corresponding to symmetric stretching of CH_2 groups and stretching of CH bonds, and one located at 2966 cm^{-1}, corresponding to asymmetric stretching of CH_2 groups. In both deuterated isoforms of SA, these two peaks are not present, and the CH-stretch region is completely devoid of spectral peaks due to the absence of remaining C-H bonds within either molecule. Instead, spectral peaks are observed within the silent region for both D4-SA and D6-SA, having been down-shifted as a result of deuterium incorporation. Four peaks are present at 2102 cm^{-1}, 2134 cm^{-1}, 2170 cm^{-1} and 2215 cm^{-1} within the silent region of the D4-SA spectrum, which can be considered to correspond to stretching motions of the C-D bonds and CD_2 groups within its molecular structure. In the spectrum from D6-SA, the peak at 2217 cm^{-1} is clearly visible, but the other three peaks appear to merge together, making peak separation and

subsequent attribution difficult. Whether this is a result of broader peaks or reduced peak intensity is unclear. Furthermore, oxygen-deuterium bonds have been reported to give a broad Raman peak around 2489 cm^{-1} [219], however no spectral feature is observed at this wavenumber within the acquired D6-SA spectrum.

Figures 6.2B-E show acquired Raman spectra from aqueous solutions of SA and its D4- and D6-isoforms dissolved in water at maximum soluble concentration (76 mg/ml). A water peak is present between 3200 cm^{-1} and 3600 cm^{-1} within full spectra from all three isoforms of SA, although this does not mask the peak at ~ 2940 cm^{-1} within the SA spectrum (Figure 6.2E), as was the case for L-tryptophan. As no peak is visible to the left of this peak, it is assumed to correspond to CH_2 symmetric stretch/CH stretch, with the asymmetric CH_2 stretch peak masked by the water peak. Thus, it can be observed that the CH_2 symmetric stretch/CH stretch peak position is slightly altered from the powder SA sample, where the corresponding peak was located at 2924 cm^{-1}.

Peaks within the fingerprint region of the aqueous spectra can be visualised and compared in Figure 6.2C, many of which appear altered from those observed within the powder spectra, for example, whilst an OH…O twist peak can be seen at 940 cm^{-1} within spectra from all three dissolved molecules, the second OH…O peak, which was located at 1417 cm^{-1} in the powder spectra, is not observed within any of the aqueous spectra. The C=O stretch peak, which was located at 1652 cm^{-1} within the powder spectra, cannot be observed either, likely due to its tendency to react with water molecules. Similarly, the O-C=O twist peak, which was located at 682 cm^{-1}, and the C-O stretch peak, which was located at 1290 cm^{-1}, are not observed within the aqueous spectra for any of the investigated molecules. A strong peak is present within spectra from SA, D4-SA and D6-SA at 840 cm^{-1}, although it is unclear what this peak corresponds to as no peak was observed around this region in the powder spectrum, especially not one that was present in spectra from all three isoforms of the molecule. A large, broad peak can also be seen from 1030-1220 cm^{-1}, particularly prominent within the spectrum from D6-SA, but also noticeable within that of D4-SA, which is the result of signal interference from the glass of the cover slip. Despite the high variability in spectral features between powder and aqueous preparations of SA, D4-SA and D6-SA, differences in peak position can still be utilised to distinguish between deuterated and non-deuterated isoforms, for example, the aqueous spectrum of SA shows peaks at 992 cm^{-1} and 1416 cm^{-1}, which are not present within the aqueous spectra from D4-SA and D6-SA, and are therefore considered to correspond to CH_2 wagging. Conversely, the aqueous spectra of D4-SA and D6-SA show peaks at 760 cm^{-1} and 957 cm^{-1}, which are not observed within the SA spectrum, and are consequently attributed to CD_2-related resonances.

Figure 6.2D shows the observed CD-associated peak present within the silent region of the Raman spectrum for both D4-SA and D6-SA which is absent from the spectrum of their non-deuterated parent molecule. Spectra from D4-SA and D6-SA show identical peak-shapes centred at 2160 cm^{-1}, with shoulders either side of the main peak, appearing somewhat different to the multiple sharp peaks observed within the powder sample spectra. The largest peak in the powder sample spectra, which likely corresponds to the central peak within the aqueous spectra, was located at 2170 cm^{-1}, so a slight change in spectral position is observed. Overall, whilst consistency is not observed in peak positioning between powder and aqueous preparations of deuterated and non-deuterated SA isoforms within the fingerprint region, differences in peak positions enable discrimination of aqueous deuterated isoforms of SA from their non-deuterated parent molecule against the underlying water signal. Furthermore, the CD-associated peak within the silent region maintains its position relatively well and shows detectable signal above that given by water, and thus will be utilised to achieve contrast between the molecule and the chemical background of a cell.

6.2.3. TPMP/D3-TPMP

Figure 6.3 shows the acquired Raman spectra for D3-TPMP and its non-deuterated parent molecule, TPMP, with peak attributions summarised in Table 6.3. Unlike the previously discussed SA and Trp molecules, characterisation of TPMP is limited within existing literature, and therefore the peak attributions within this section are proposed based on a combination of reported Raman characterisation for similar molecules, as well as the observed spectral changes following deuterium incorporation within the TPMP structure. Furthermore, the chemical structure of the TPMP cation is simple, consisting of three phenyl rings and a methyl group attached to a phosphorus atom, making peak attribution more straightforward.

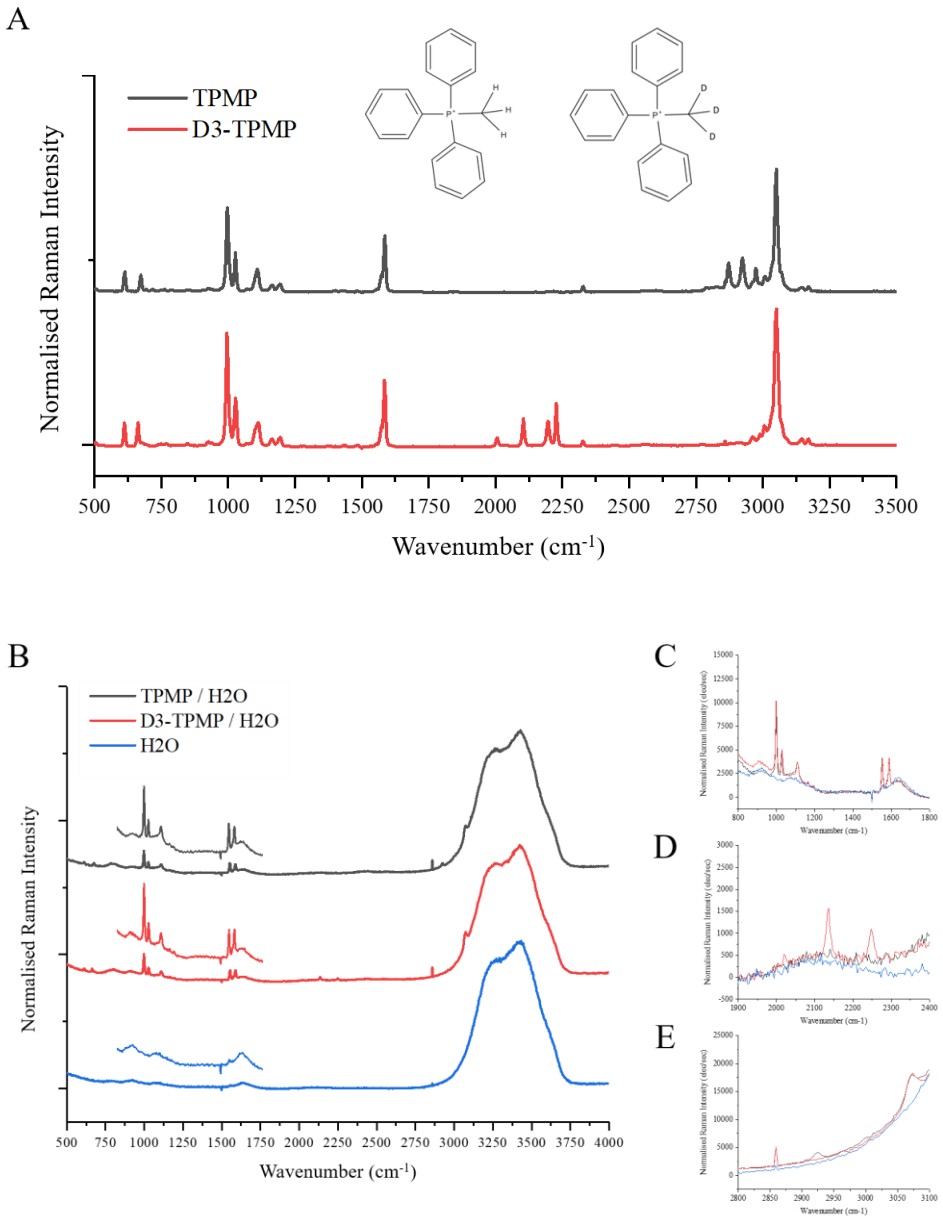

Figure 6.3 | Spontaneous Raman spectra for TPMP and D3-TPMP. Full spectra are shown with the spectral range, 500 cm^{-1} to 3500 cm^{-1} for molecules as powder preparations (A), and 500 cm^{-1} to 4000 cm^{-1} for molecules in 25 mg/ml solution with water (B), incorporating all three characteristic regions of the Raman spectrum, with spectra vertically shifted in respect to each other for clarity. The fingerprint region spectra from aqueous solutions are also shown with an alternative scale for improved visualisation of peaks. Spectra are also shown with reduced spectral ranges from 800 cm^{-1} to 1800 cm^{-1} (C), enabling direct comparison of peaks within the fingerprint region of the spectrum, 1900 cm^{-1} to 2400 cm^{-1} (D), centred around the carbon-deuterium-associated peaks at 2022 cm^{-1}, 2135 cm^{-1} and 2248 cm^{-1} within the silent region of the D3-TPMP spectrum, and 2800 cm^{-1} to 3100 cm^{-1} (E), showing the CH_3 stretch peak at ~ 2925 cm^{-1} within the TPMP spectrum and the peak corresponding to CH stretch within the phenyl rings at 3073 cm^{-1} in spectra from TPMP and D3-TPMP. Reduced spectra are transposed directly from the full spectra from the aqueous compound/water solutions but are not vertically shifted, enabling inclusion of Raman intensity values. Chemical structures for TPMP and D3-TPMP are also shown in Figure 6.3A.

Table 6.3 | Overview of Raman vibrational resonances for TPMP with inclusion of peak positions within silent region observed for D3-TPMP. Attributions of peaks showing altered positioning within aqueous solution spectra are given in brackets.

Wavenumber (cm^{-1})	**Assignment**
997	β CH in phenyl ring
1027	θ phenyl ring
1108	β CH in phenyl ring
1574 (1553); 1586	ν CC in phenyl ring
2006; 2104; 2197; 2227 (2022; 2135; 2248)	ν CD_3
2872; 2924; 2974	ν CH_3
3050 (3073)	ν CH in phenyl ring

Symbols for vibrations: ν – stretching; β – bending/deformation; θ – ring breathing

Raman spectra for powder preparations of TPMP and D3-TPMP are shown in Figure 6.3A. The fingerprint region of the Raman spectrum is dominated by peaks corresponding to resonances within the phenyl rings of TPMP, with the strongest peaks located at 997 cm^{-1}, 1027 cm^{-1} and 1586 cm^{-1}, corresponding to bending of C-H bonds within the phenyl ring structures, phenyl ring breathing and stretching of C-C bonds within the phenyl rings, respectively. As the phenyl ring groups in D3-TPMP are not subjected to deuterium incorporation, spectral peaks within the fingerprint region appear identical between the deuterated and non-deuterated TPMP isoforms.

The CH-stretch region of the TPMP spectrum shows four main peaks at 2872 cm^{-1}, 2924 cm^{-1}, 2974 cm^{-1} and 3050 cm^{-1}. The 3050 cm^{-1} peak has been widely reported within literature to represent CH stretching within aromatic structures and is consequently considered to correspond to stretching of the C-H bonds within the phenyl rings of TPMP, remaining unchanged between spectra for deuterated and non-deuterated isoforms of TPMP. The remaining three peaks within the CH-stretch region of the TPMP spectrum are absent from the respective spectrum from D3-TPMP and are therefore assumed to correspond to stretching of the methyl group, which undergoes deuterium incorporation in the D3-TPMP molecule, down-shifting the peaks into the silent region of the spectrum where they are observed at 2006 cm^{-1}, 2104 cm^{-1}, 2197 cm^{-1} and 2227 cm^{-1}. Hence, each of these peaks are assumed to correspond to stretching of the CD_3 group within D3-TPMP. As for the previously studied deuterium-labelled molecules, these CD-

associated peaks within the silent region of the Raman spectrum will be utilised for achieving contrast between D3-TPMP and the chemical background of a cell.

Figures 6.3B-E show acquired Raman spectra from aqueous solutions of TPMP and D3-TPMP dissolved at maximum soluble concentration (25 mg/ml). A water peak is observed between 3200 cm^{-1} and 3600 cm^{-1} within full spectra from solutions of both isoforms of TPMP, although CH-stretch region peaks are not completely obscured, as depicted in Figure 6.3E, with a CH_3 stretch peak visible within the TPMP spectrum at 2924 cm^{-1} and a CH stretch peak visible at 3073 cm^{-1} within spectra from both TPMP and D3-TPMP solutions. The position of these peaks is slightly altered from the powder sample spectra, with the CH stretch peak having shifted from 3050 cm^{-1} to 3073 cm^{-1}, and the peak at 2924 cm^{-1} being the only CH_3 stretch peak visible from the four that were observed within the TPMP spectrum in Figure 6.3A. It is unclear whether this peak represents only one of the CH_3 peaks from the TPMP powder spectrum or whether it is a combination of all three. Peaks within the fingerprint region of the spectra from aqueous preparations of TPMP and D3-TPMP can be visualised and compared in Figure 6.3C. In general, the positions of these peaks is well-maintained from the spectra acquired from the powder samples, with the only observable change in peak position being that of the CC stretch peak at 1553 cm^{-1}, which was observed at 1574 cm^{-1} in the powder spectra from both TPMP and D3-TPMP. The peaks corresponding to CH bending within the phenyl rings at 997 cm^{-1} and 1108 cm^{-1}, as well as those corresponding to phenyl ring breathing and CC stretch at 1027 cm^{-1} and 1586 cm^{-1}, respectively, do not show altered peak positioning between spectra from powder and aqueous samples of TPMP and D3-TPMP.

The observed peaks within the silent region of the acquired Raman spectra from the aqueous solutions of D3-TPMP, which are absent from the spectra of aqueous TPMP and water, are displayed in Figure 6.3D. Three peaks are visible above the underlying water signal within this region, located at 2022 cm^{-1}, 2135 cm^{-1} and 2248 cm^{-1}, which are considered to correspond to stretching of the CD_3 group within D3-TPMP. The positions of these peaks are altered from those observed within spectra from powder preparations of TPMP and D3-TPMP, and it is not clear which of the four peaks that were observed within the powder spectrum are visible here. Thus, the aqueous spectrum may provide a more informative reference for interpretation of CARS data in the next section based on the compound being administered to cells in an aqueous state. Overall, TPMP and D3-TPMP can still be distinguished from one another when in aqueous solution based on observable differences in peak positions resulting from hydrogen replacement with deuterium, and CD-associated peaks within the silent region of the acquired Raman spectrum can be clearly visualised above the underlying water signal.

A further point for consideration was whether the deuterium in the above described compounds could exchange with hydrogen in water molecules when dissolved in aqueous solution, potentially altering the deuterium-labelling of compounds prior to their exposure to cells. It has been previously reported that hydrogen and deuterium can exchange when amino acids and water are combined[220], and deuterium incorporation from deuterium oxide (D_2O) has become established as a technique for elucidating conformational properties of proteins owing to differences in hydrogen/deuterium exchange time[221]. Solvent-exposed peptides show markedly faster exchange times (minutes) compared to those buried within the interior of the protein structure (hours to days)[221].

To provide an indication of whether hydrogen/deuterium exchange occurred in the above described samples, a spectrum of the phase-retrieved imaginary part of the normalised CARS susceptibility $Im\left\{\chi_R^{(3)}\right\}$ was acquired from a pure D_2O sample, as shown in Figure 6.4. A broad CD-associated peak between 2200 cm^{-1} and 2800 cm^{-1} was generated by vibrations of oxygen-deuterium bonds. Therefore, if deuterium within the compounds was exchanging with hydrogen in water to generate D_2O, a peak would have been observed at ~ 2400 cm^{-1} in the acquired Raman spectra. Such peaks were not present in the Raman spectra in Figures 6.1-6.3, despite visible CD-associated peaks, suggesting that hydrogen/deuterium exchange between compounds and water was either not observed or only occurred at very low levels, failing to generate peaks within the acquired Raman spectra. Furthermore, the Raman spectra displayed in Figures 6.1-6.3 were acquired immediately following preparation of deuterated compound/water solutions, potentially not allowing sufficient time for all C-D bonds to exchange their deuterium with hydrogen in the water molecules.

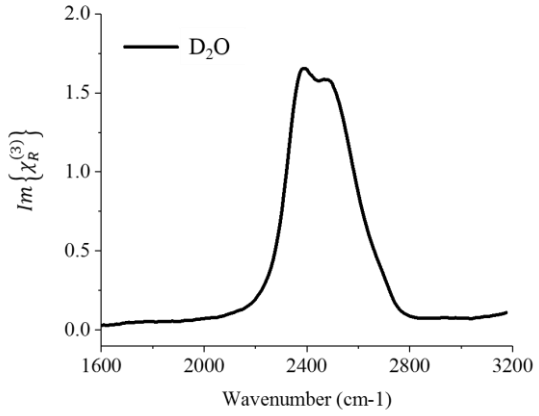

Figure 6.4 | Spectrum showing the phase-retrieved imaginary part of the normalised CARS susceptibility $Im\left\{\chi_R^{(3)}\right\}$ acquired from a pure D_2O sample over the spectral range, 1600-3200 cm^{-1} within the cell-silent region of the Raman spectrum.

Whilst it was preferential for the deuterium-labelled compounds to maintain their C-D bonds when dissolved in water, for the primary purpose of this project, which was to identify whether CARS microscopy and subsequent data analysis strategies could be employed to visualise deuterium-labelled molecules within cells, hydrogen/deuterium exchange should not have presented a major limitation to the investigation. Even if some deuterium was incorporated into water molecules, in theory, the generated D_2O should still have been taken up and metabolised by cells, hence the deuterium should still have been present intracellularly. When incubated in a high concentration D_2O solution, cells have been shown to incorporate deuterium into various metabolically active molecules, permitting detection of intracellular deuterium signal[219]. This would suggest that deuterium from D_2O taken up by cells is detectable but is more likely to relate to deuterium incorporated into other molecules rather than intracellular distribution of the D_2O molecules themselves. Thus, signal generated by D_2O molecules may show a different localisation to that expected from the deuterium-labelled biological and chemical compounds. This may be most evident for D3-TPMP, which readily targets to the mitochondrial matrix. If deuterium from the compound is exchanging with hydrogen in water, a more ubiquitous distribution of signal may be observed instead of the expected highly specific mitochondrial accumulation. Whilst hydrogen/deuterium exchange between D5-Trp and water may reduce the specificity of deuterium signal localisation to proteins exclusively, due to the involvement of proteins in various metabolic processes throughout different intracellular compartments, the ubiquitous localisation of the deuterium signal from D_2O may not be too dissimilar to that expected from D5-Trp. Similarly, due to its involvement in the citric acid cycle, D4-/D6-SA would be expected to show a wide distribution extending throughout the cell, likely comparable to that expected from D_2O.

6.2.4. Small molecule compounds

Figure 6.5 shows the acquired Raman spectra for four deuterium-labelled small molecule compounds and peak attributions are summarised in Tables 6.4 and 6.5. Unlike the other investigated molecules within this chapter, spectra were not acquired from non-deuterated isoforms of each compound. Furthermore, the maximum concentration at which the compounds could be dissolved in water was too low for the Raman signal generated by the compound to be detected above the underlying water signal, and consequently Raman spectra were not obtained from aqueous solutions of the deuterated compounds. Whilst the compounds could be dissolved at a higher concentration in a 50:50 mixture of water and methanol, which is how they are administered to cells (see Section 3.3.3 of Chapter 3 for overview of treatment protocol), the

Raman signal from methanol would likely obscure the observed spectral line-shape, compromising interpretation of data. However, based on the observed spectra from powder and aqueous preparations of D5-Trp, D4-/D6-SA and D3-TPMP, despite a small amount of variation being observed in CD-associated peaks between powder and aqueous samples, with multiple sharp peaks in the powder spectra being observed as broader single peaks in the aqueous spectra, the observed changes in peak position are not particularly large, and remain located within the same general area of the silent region between 2000 cm^{-1} and 2400 cm^{-1}. Consequently, the observed peak positions within the powder spectra will still be used as a reference for interpretation of CARS data in the next section.

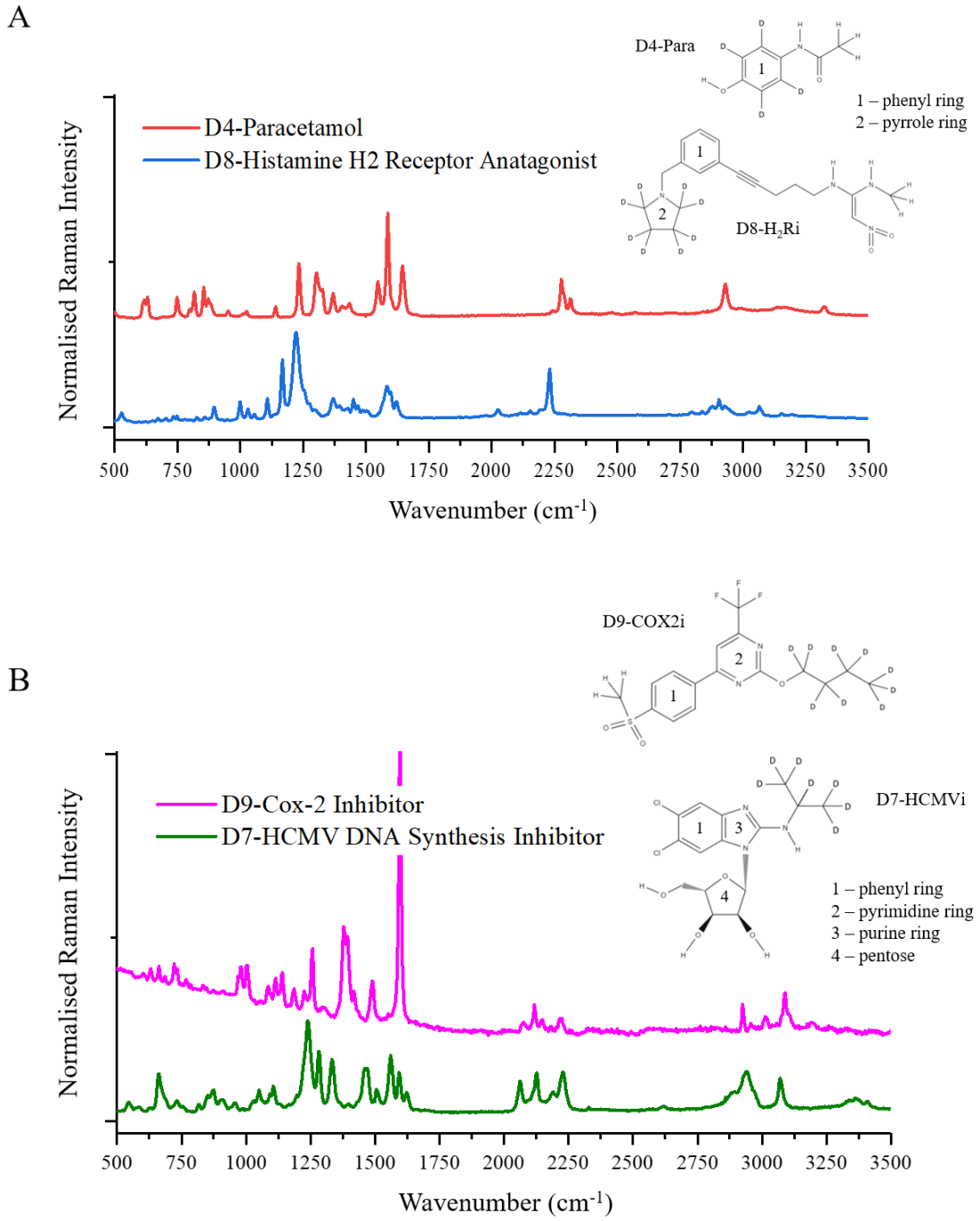

Figure 6.5 | Spontaneous Raman spectra for powder preparations of investigated deuterium-labelled small molecule compounds: D4-Para and D8-H_2Ri (A); and D9-COX2i and D7-HCMVi (B). Full spectra are shown with a spectral range of 500 cm^{-1} to 3500 cm^{-1}, incorporating all three characteristic regions of the Raman spectrum, with spectra vertically shifted in respect to each other for clarity. Chemical structures for each compound are also shown.

Table 6.4 | Overview of Raman vibrational resonances for D4-Para (A) and D8-H_2Ri (B). Peak attributions for D4-Para are based on those described for non-deuterated paracetamol in existing literature[222–225], whilst similar literature characterising peaks within the D8-H_2Ri spectra is not available, thus, attributions to vibrational modes are based on the peak allocations already discussed within this chapter, as well as reported Raman spectra for molecules with similar chemical structures within literature. If peak positions cannot be allocated to chemical groups based on existing evidence, they are considered to relate to CD-associated resonances, either directly or via an indirect effect on other molecular groups.

	Wavenumber (cm^{-1})	**Assignment**
A	617-629	CD resonance
	652-657*; 698*; 713*; 751*	β CH in phenyl ring*
	748	C-D resonance
	798	β C=O
	817	CD resonance
	854; 876	θ phenyl ring
	1233	γ phenyl ring; γ amide group; γ COH
	1303	CD resonance
	1324	β phenyl ring with β COH (amide III mode)
	1370	CD resonance
	1548	β NH coupled with ν CN (amide II mode)
	1586	ν CC in phenyl ring
	1646	ν C=O
	2244; 2278; 2314	ν CD
	2930	ν_s CH_3
	2987	ν_{as} CH_3
	3062*	ν CH in phenyl ring*
	3323	NH…O

*From literature, not present in D4-Para spectrum

B	999	θ phenyl ring
	1030; 1108	β CH in phenyl ring
	1167	CD resonance
	1221	ω CH_2
	1369	CD resonance

1583	ν CC in phenyl ring
1620	ν C=C
2026; 2153; 2194; 2231	ν CD; ν C≡C
2839	ν_s CH_2
2878	ν_{as} CH_2; ν CH_3
2905	ν_s CH_2; ν CH
2929	ν_{as} CH_2; ν CH_3
3065; 3154	ν CH in phenyl ring

Symbols for vibrations: ν – stretching (further categorised into ν_s – symmetric stretch; ν_{as} – asymmetric stretch); β – bending/deformation (further categorised into ω – wagging; δ – twisting; γ – rocking); θ – ring breathing

Table 6.5 | Overview of Raman vibrational resonances for D9-COX2i (A) and D7-HCMVi (B). As literature describing peak allocations for both compounds are not available, attributions to vibrational modes are based on the peak allocations already discussed within this chapter, as well as reported Raman spectra for molecules with similar chemical structures within literature. Peak attributions for CF and CF_3 groups within D9-COX2i were based on observed Raman spectra from fluoxetine[226]. Peak attributions for D7-HCMVi were based on the Raman spectra of ribose and purines due to structural similarities[168,227]. If peak positions cannot be allocated to chemical groups based on existing evidence, they are considered to relate to CD-associated resonances, either directly or via an indirect effect on other molecular groups.

	Wavenumber (cm^{-1})	**Assignment**
A	722; 732	CF_3-associated resonances; θ purine ring
	980; 1004	θ phenyl ring; ν CC in phenyl ring
	1087; 1113	β CH in phenyl ring
	1140	ν CF
	1186	γ CH_2 coupled with ν C=C in phenyl ring
	1227	ω CH_2
	1257	δ CH_2
	1380-1392	β CH_3
	1418	Pyrimidine ring-associated resonance
	1488	CD resonance
	1596	ν CC in phenyl ring
	2076; 2118; 2147; 2220	ν CD

2925	ν_{as} CH_2; ν CH_3
3012; 3089	ν C-H in phenyl ring

B	664	θ purine ring; ν CCl
	733	θ purine ring
	872	θ phenyl ring; ν CC; ν COC
	1050	β COH
	1106	ν_{as} COC
	1240	δ CH in pentose structure
	1282	δ CH_2 in pentose structure
	1333	ν CN; ν C-C in purine structure; ν CH
	1464	ν CN; β CH_2
	1561	ν CN
	1595: 1623	β NH; ν CN
	2063; 2126; 2191; 2228	ν CD
	2938	ν_{as} CH_2
	3071	ν CH in phenyl ring
	3364	ν OH
	3407	ν NH

Symbols for vibrations: ν – stretching (further categorised into ν_s – symmetric stretch; ν_{as} – asymmetric stretch); β – bending/deformation (further categorised into ω – wagging; δ – twisting; γ – rocking); θ – ring breathing

Figure 6.5A shows the acquired Raman spectra for D4-Para and D8-H_2Ri as powder preparations and peak attributions are discussed in Sections A and B of Table 6.4, respectively. Whilst a Raman spectrum was not acquired from the non-deuterated form of paracetamol, existing literature has reported its spectrum and characterised its main peaks[222–225], which are also included within Section A of Table 6.4 for comparison with the observed peaks within the D4-Para spectrum. Both deuterated and non-deuterated paracetamol isoforms show peaks at 798 cm^{-1}, 854 cm^{-1}, 876 cm^{-1}, 1233 cm^{-1}, 1324 cm^{-1}, 1586 cm^{-1} and 1646 cm^{-1} within the fingerprint region of the Raman spectrum. The peaks at 798 cm^{-1}, 1233 cm^{-1}, 1586 cm^{-1} and 1646 cm^{-1} correspond to

C=O bending, combined rocking of the phenyl ring, amide and C-OH groups, CC stretch within the phenyl ring, and C=O stretching, respectively, whilst the peaks at 854 cm^{-1} and 876 cm^{-1} are both considered to correspond to phenyl ring breathing modes. The peak at 1324 cm^{-1} is attributed to the amide III mode, which is produced by bending of the phenyl ring coupled with bending of the C-OH group, and similarly, the peak at 1548 cm^{-1} is attributed to the amide II mode, given by bending of NH coupled with stretching of CN. All of the aforementioned peaks remain unchanged between spectra from paracetamol and D4-Para as deuterium is incorporated within the phenyl ring structure only, and hence vibrations of each the groups discussed above are not altered by deuterium labelling. Within the Raman spectra shown in literature for non-deuterated paracetamol, a number of peaks are reported between 652 cm^{-1} and 751 cm^{-1} corresponding to bending motions of C-H bonds within the phenyl ring structure of paracetamol, however, in D4-Para the hydrogen atoms within these bonds are replaced with deuterium, and consequently these peaks are absent from its Raman spectrum. Instead, peaks corresponding to C-D bond vibrations are present, and thus, deuterium incorporation is considered to account for the peaks observed at 617-629 cm^{-1}, 748 cm^{-1}, 817 cm^{-1}, 1303 cm^{-1} and 1370 cm^{-1} within the D4-Para spectrum, if not corresponding directly to C-D bond vibrations then caused by the indirect effect of deuterium incorporation on other chemical groups within the paracetamol structure.

The CH-stretch region also shows some conservation of peak position between spectra from deuterated and non-deuterated isoforms of paracetamol. The strong peak present at 2930 cm^{-1} and the less pronounced, broad peak at 2987 cm^{-1} which corresponding to symmetric and asymmetric stretching of the methyl group, respectively, are not subjected to deuterium incorporation and thus peak positions are maintained within the D4-paracemtol spectrum. For the same reason, the peak at 3323 cm^{-1}, which relates to vibrations of the NH…O group, remains in the same position within acquired spectra from both paracetamol isoforms. Reported Raman spectra for non-deuterated paracetamol have shown a strong peak at 3062 cm^{-1}, corresponding to stretching of CH groups within the phenyl ring, however, replacement of hydrogen with deuterium induces a down-shift of this peak into the silent region of the D4-Para spectrum, and hence the 3062 cm^{-1} peak is not observed. Within the silent region of the D4-Para spectrum, three peaks are visible at 2244 cm^{-1}, 2278 cm^{-1} and 2314 cm^{-1}, which are all considered to correspond to stretching of C-D bonds within the phenyl ring structure and are consequently absent from the spectrum of non-deuterated paracetamol. These peaks will be utilised to achieve contrast between D4-Para and the chemical background of a cell, and the acquired Raman spectrum provides a reference for interpretation of CARS data in the following section, however, caution should be taken as the peak positions observed within the acquired spectrum from the deuterated compound

as a powder may not be identical to those observed within a spectrum from an aqueous solution of the compound, which is likely how the compound will exist in a cellular environment.

The remaining three compounds have not been characterised in their entirety in literature to date and consequently the peak attributions within the Raman spectra of the non-deuterated forms of each compound have not been reported. Therefore, assignment of spectral peaks to their corresponding vibrational modes for these compounds was based on the peak allocations already discussed within this chapter, as well as reported Raman spectra for molecules with similar chemical structures within literature. The lower spectrum in Figure 6.5A shows the acquired Raman spectrum for D8-H_2Ri as a powder preparation and peak attributions are discussed in Section B of Table 6.4. D8-H_2Ri shows peaks within its fingerprint region located at 999 cm^{-1}, corresponding to phenyl ring breathing; 1030 cm^{-1} and 1108 cm^{-1}, corresponding to bending of C-H bonds within the phenyl ring; 1221 cm^{-1}, corresponding to wagging motions of the CH_2 group; 1583 cm^{-1}, corresponding to stretching of C-C bonds; and 1620 cm^{-1}, corresponding to stretching of C=C bonds. The peaks at 1167 cm^{-1} and 1369 cm^{-1} are considered to correspond to CD-associated resonances as no non-deuterated chemical groups could be identified which showed Raman peaks at these positions. The CH-stretch region shows weak peaks corresponding to stretching motions of carbon-hydrogen-containing chemical groups within the D8-H_2Ri structure. Peaks are observed at 2839 cm^{-1}; 2878 cm^{-1}; 2905 cm^{-1}; and 2929 cm^{-1}, corresponding to symmetric CH_2 stretch; a combination of asymmetric CH_2 stretch and CH_3 stretch; a combination of symmetric stretch of CH_2 and CH stretch; and a combination of CH_2 asymmetric stretch and CH_3 stretch, respectively. Peaks at 3065 cm^{-1} and 3154 cm^{-1} correspond to stretching of C-H bonds within the phenyl ring structure. Within the silent region, peaks corresponding to stretching motions of CD and C≡C (alkyne) groups are observed at 2026 cm^{-1}; 2153 cm^{-1}; 2194 cm^{-1} and 2231 cm^{-1}, although determination of which peaks correspond to which group is unclear. Alkyne groups have been reported to give a Raman peak at ~ 2110 cm^{-1} [98,109,112], which would indicate that the peak at 2153 cm^{-1} may be most likely to correspond to C≡C stretch, however it has also been reported that alkyne groups give a larger Raman scattering cross-section than C-D bonds[19], and hence a larger peak intensity, indicating that the large peak at 2231 cm^{-1} is most likely to correspond to C≡C stretch. Regardless of whether it corresponds to CD or C≡C stretch, the peak at 2231 cm^{-1} should generate a strong CARS signal if targeted, potentially achieving contrast between D8-H_2Ri and the chemical background in which it is found.

Figure 6.5B shows the acquired Raman spectra for D9-COX2i and D7-HCMVi as powder preparations and peak attributions are summarised in Sections A and B of Table 6.5, respectively. Within its fingerprint region, D9-COX2i shows peaks at 722 cm^{-1} and 732 cm^{-1}, corresponding to resonances associated with the CF_3 group, as well as breathing modes of the purine ring structure.

Peaks at 980 cm^{-1} and 1004 cm^{-1} correspond to phenyl ring breathing and stretching of C-C bonds within the phenyl ring structure, whilst peaks at 1087 cm^{-1} and 1113 cm^{-1} correspond to bending of the C-H bonds in the phenyl ring. Further peaks are located at 1140 cm^{-1}; 1227 cm^{-1}; 1257 cm^{-1}; 1380-1392 cm^{-1}; and 1596 cm^{-1}, corresponding to CF stretching; CH_2 wagging; CH_2 twisting; CH_3 bending; and CC stretching within the phenyl ring. The peak at 1186 cm^{-1} corresponds to CH_2 rocking motions coupled with C=C stretching within the phenyl ring, and the peak at 1418 cm^{-1} corresponds to vibrations associated with the pyrimidine ring structure. The peak at 1488 cm^{-1} is considered to correspond to CD-associated resonances as no non-deuterated chemical groups could be identified which showed Raman peaks at this position. Within the CH-stretch region, peaks are observed at 2925 cm^{-1}, corresponding to asymmetric CH_2 stretch and CH_3 stretch, and at 3012 cm^{-1} and 3089 cm^{-1}, corresponding to stretching of C-H bonds within the phenyl ring. The silent region shows four peaks corresponding to stretching modes of CD groups, which will be used to achieve contrast between D9-COX2i within the next section.

The lower spectrum in Figure 6.5B shows the acquired Raman spectrum for D7-HCMVi as a powder preparation and peak attributions are summarised in Section B of Table 6.5. D7-HCMVi comprises a pentose region, which shows identical chemical structure to that of ribose, and a purine-like structure, which shows structural similarities to both adenosine and guanine. Consequently, the reported Raman spectra for each of these compounds were utilised for assignment of peaks within the D7-HCMVi spectrum to their corresponding bond vibrations[168,227]. Within the fingerprint region, peaks are observed at 664 cm^{-1}, corresponding to breathing modes of the purine ring structure (Ring 3 in Figure 6.5B) and CCl stretch; 733 cm^{-1}, also corresponding to purine ring breathing; and 872 cm^{-1}, corresponding to breathing modes of the phenyl ring (Ring 1 in Figure 6.5B) and stretching of CC and COC groups. Peaks are also observed at 1050 cm^{-1} and 1106 cm^{-1}, corresponding to bending of COH groups and asymmetric stretch of the COC group, respectively, and at 1240 cm^{-1} and 1282 cm^{-1}, corresponding to twisting motions of the C-H bonds and CH_2 groups within the pentose structure. The peak located at 1333 cm^{-1} is considered to correspond to stretching vibrations of C-N, C-H and C-C bonds within the purine ring structure (Ring 1 in Figure 6.5B), whilst the peak at 1464 cm^{-1} also corresponds to stretching of C-N bonds along with bending of CH_2 groups. The final three peaks within the fingerprint region are located at 1561 cm^{-1}, 1595 cm^{-1} and 1623 cm^{-1}, representing a combination of CN stretching and NH bending. The CH-stretch region of the D7-HCMVi spectrum shows peaks at 2938 cm^{-1}, 3071 cm^{-1}, 3364 cm^{-1} and 3407 cm^{-1}, corresponding to CH_2 asymmetric stretch and CH_3 stretch, CH stretch within the phenyl ring, OH stretch, and NH stretch, respectively. Peaks are also observed within the silent region at 2063 cm^{-1}, 2126 cm^{-1}, 2191 cm^{-1} and 2228 cm^{-1}, which are considered to correspond to stretching vibrations of the C-D bonds and CD_3 groups. Based on the observed

Raman spectra for D17-OA and D11-LA in Chapter 4, where the sub-peak at 2070 cm^{-1} was considered to correspond to CD_3 vibrations, the 2063 cm^{-1} peak within the D7-HCMVi spectrum is considered to correspond to stretching of CD_3 groups. These CD-associated peaks will be utilised in the next section to achieve contrast between D7-HCMVi and the chemical background of a cell.

Based on the observed CD-associated peak positions for each of the small molecule compounds described in the above section, the structural positioning of the deuterium labels within the compounds (aliphatic or aromatic) may affect the spectral positioning of associated Raman peaks. D4-Para, which possesses C-D bonds within aromatic ring structures, showed CD-associated peaks between 2244 cm^{-1} and 2314 cm^{-1}, whilst D9-COX2i and D7-HCMVi, which both show CD-labelling within aliphatic chain structures, showed CD-associated peaks between approximately 2070 cm^{-1} and 2225 cm^{-1}.

6.3. Hyperspectral CARS image acquisition and FSC^3 data analysis for identification of intracellular small molecule distribution

As already discussed in detail throughout this thesis, hyperspectral CARS microscopy can provide images with a high spatial resolution and chemical specificity[94], and through combination with data processing and analysis techniques, such as FSC^3, quantitative maps of chemical components can be generated[73,74]. The capability of this imaging strategy for identification of a deuterium-labelled molecule within a cell has already been demonstrated using deuterated fatty acids, where a strong signal corresponding to carbon-deuterium resonances was observed in both spatial and spectral outputs of FSC^3, enabling contrast against a mixed chemical background.

The ability of FSC^3 analysis to identify and spatially resolve a deuterium-labelled small molecule within a cell was assessed by once again utilising HeLa cells, which were exposed to each of the deuterated small molecules at different concentrations over various incubation times, before hyperspectral CARS datasets were acquired from cellular regions and FSC^3 was applied to generate maps of independently varying chemical components. The Raman spectra acquired from each investigated small molecule within the previous section of this chapter provide information about CD-associated peak positions within the cell-silent region, thus enabling informed selections of spectral ranges for hyperspectral CARS data acquisition. However, with

only a limited understanding of the attributions of CD-associated peaks within the cell-silent region, it is difficult to estimate how peak shapes and positions may change if the compound is metabolised by the cell, i.e. if metabolites present within cells do not show the same chemical structure as the compound which was initially applied. Therefore, the level of similarity between the component spectra retrieved by FSC^3 and the Raman spectra acquired from each of the compounds is unknown, however it is expected that all CD-associated resonances should give peaks within the cell-silent region of the Raman spectrum.

Hyperspectral CARS datasets were once again obtained through acquisition of XY images at different wavenumbers to give a spectrum for each pixel of the spatial image. These spectra were then processed to retrieve the imaginary part of the normalised CARS susceptibility, $Im\left\{\chi_R^{(3)}\right\}$, thus becoming linear in terms of concentration of chemical components, with a line-shape that was Raman-like, and hence more comparable to the acquired spectra in Section 6.2. FSC^3 could then be applied to the processed hyperspectral CARS datasets to generate concentration maps of independently varying chemical components in an unsupervised manner.

A mixture of individual and combined analysis is employed within this section, i.e. FSC^3 is either applied to a single deuterated compound-treated cell sample, identifying the most common spectra from the individual sample, or it is applied across multiple cell samples, some of which have received the deuterated compound, and some of which have not, hence identifying the most common spectra from all of the samples. As FSC^3 identifies the most common spectra from hyperspectral datasets in an unsupervised manner, it is possible that when treated and untreated controls are analysed together, a CD-associated component is less common than if the deuterated compound-treated cells are imaged independently. In previous chapters, FSC^3 has been used to directly compare cells treated with a deuterated or non-deuterated molecule (fatty acid), enabling distinction of a chemical component corresponding to C-D bond vibrations. Thus, FSC^3 is also applied to both deuterated compound-treated and untreated HeLa cells in a combined analysis, providing a direct comparison of the chemical composition of intracellular regions to identify a CD-associated component. A high number of chemical components (six to eight) are considered during FSC^3 data analysis within this section, in order to maximise the potential of distinguishing CD-associated signal above components attributed to background noise.

Generally, the wavenumber ranges over which the hyperspectral CARS images were acquired were selected based on the observed results from the spontaneous Raman characterisation in the previous section, primarily targeted within the silent region where contrast is most likely to be achieved, via use of the intermediate single-band filter, as described in detail in Section 3.6 of Chapter 3. However, for some of the small molecule compounds, the observed

CD-associated peak positions fell outside of the imaged spectral range, however, these datasets and associated FSC^3 outputs are still reported within this section, as the chemical information they provide may still be of value.

6.3.1. D5-L-tryptophan

The ability of FSC^3 to detect and spatially resolve D5-Trp within a cell was assessed by incubating HeLa cells with the deuterium-labelled molecule, which was first dissolved in water to give a homogenous solution, before it was combined with growth media to give a final concentration of 100 μM. Cells were exposed to D5-Trp for a 24-hour time-period, after which they were PFA-fixed and imaged by CARS microscopy. Hyperspectral datasets were acquired from cytoplasmic regions of cells and subsequent FSC^3 data analysis was applied. Figure 6.6 shows the spatially resolved images and retrieved spectra for eight independently varying chemical components following application of FSC^3 to a hyperspectral CARS dataset acquired from a single D5-Trp-treated cell. However, the spontaneous Raman spectrum for D5-Trp dissolved in water showed a peak at 2300 cm^{-1}, as described in Section 6.2, which lies outside of the targeted spectral range within Figure 6.6, therefore observation of signal corresponding to CD-associated bond resonances would not be expected in Figure 6.6. Selection of an incorrect spectral range arose as a result of the scaling of hyperspectral datasets which was performed during image analysis. When the intermediate filter (see Section 3.6 of Chapter 3 for details) was used on the CARS system, the reported wavenumbers within the imaging software were ~ 200 cm^{-1} higher than the actual wavenumber acquired, and thus, a range which was initially set to 2100-2400 cm^{-1} became 1900-2200 cm^{-1} following data analysis (see Appendix 1 for reacquired dataset with correct spectral range).

Whilst some variation in signal localisation is observed within the spatially resolved images, no distinguishable spectral features are present within the retrieved component spectra over the targeted spectral range. Some of the components appear to show signal localised within the cell (Components 4, 5, 6 and 8), although without features within the retrieved spectra it is difficult to determine whether this signal corresponds to intracellular molecules or background noise. Based on signal observed at the edge of the cell, it is also possible that some of these components, e.g. Components 3-6, show artefacts caused by sample movement during image acquisition. Thus, a chemical component corresponding to resonances of C-D bonds was not identified, the most likely cause of which is that the CD-associated peak lies outside of the imaged spectral range.

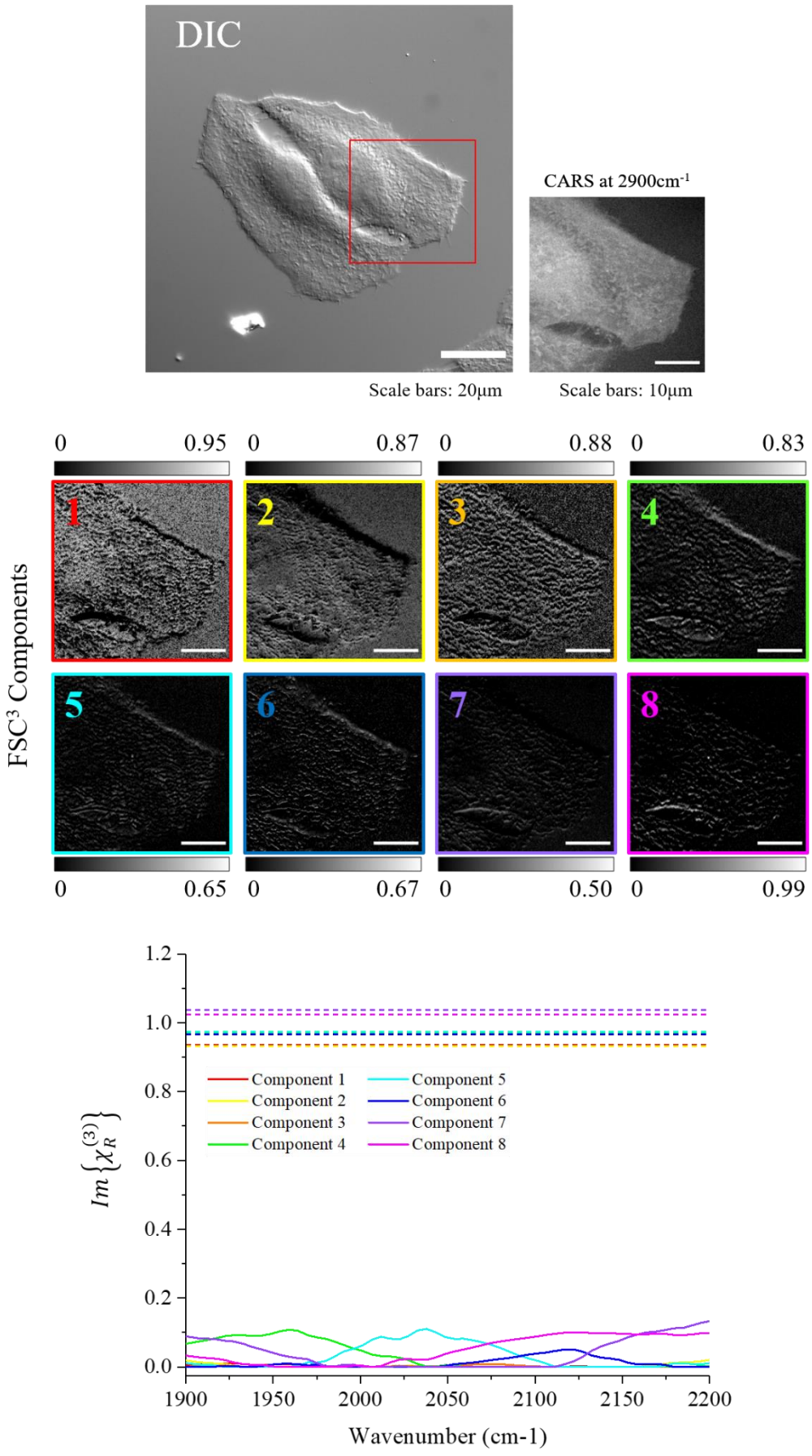
DIC
CARS at 2900cm-1
Scale bars: 20µm
Scale bars: 10µm
FSC3 Components
0
0.95
0.87
0.88
0.83
1
2
3
4
5
6
7
8
0.65
0.67
0.50
0.99
Component 1
Component 2
Component 3
Component 4
Component 5
Component 6
Component 7
Component 8
Wavenumber (cm-1)

Figure 6.6 | Spatial and spectral outputs of FSC^3 following its application to a hyperspectral CARS dataset acquired from an individual HeLa cell treated with 100 μM D5-Trp for 24 hours. A spectral range of 1900-2200 cm^{-1} is utilised. Eight separate chemical components are identified, and their distribution is shown within the spatially resolved images. The associated spectra show the phase-retrieved imaginary part of the normalised CARS susceptibility $Im\left\{\chi_R^{(3)}\right\}$ and the corresponding real parts are shown as averages, indicated by horizontal dashed lines. CARS signal does not appear to show specific localisation to cellular structures within the spatial images, and the retrieved spectra do not show spectral features over the imaged wavenumber range, thus the spatially resolved images appear to show only background noise. Volume concentration ranges for each component are given by the grayscale values. DIC was utilised for initial selection of cells, and the single wavenumber CARS image shows cellular structure based on protein signal. Scale bars show 20 μm in DIC images and 10 μm in CARS images.

6.3.2. D6-succinic acid

D6-SA was also investigated to assess the ability of FSC^3 to detect and spatially resolve a deuterium-labelled small molecule within a cell. HeLa cells were incubated with D6-SA, which was first dissolved in water to give a homogenous solution and then combined with growth media to give a final concentration of 100 μM, for a 24-hour time-period, after which they were PFA-fixed and imaged by CARS microscopy. The most likely cellular region for D6-SA to be present at a high concentration is the mitochondria, based on its role within the citric acid cycle and electron transport chain, therefore hyperspectral CARS datasets were acquired from cytoplasmic regions of cells before FSC^3 data analysis was applied. Figure 6.7 shows the spatially resolved images and retrieved spectra for eight independently varying chemical components following application of FSC^3 to a hyperspectral CARS dataset acquired from a single D6-SA-treated cell. A spectral range of 1900 cm^{-1} to 2400 cm^{-1} is targeted based on the observed CD peak position of 2160 cm^{-1} within the Raman spectrum for D6-SA dissolved in water.

Figure 6.7 displays the spatial and spectral FSC^3 outputs following application to a single D6-SA-treated cell over the spectral range, 1900-2400 cm^{-1}, within the cell-silent region of the Raman spectrum, specifically targeting the CD-associated peak at 2160 cm^{-1}. Components 1 and 7 show extracellular localisation of signal and no spectral features over the imaged spectral range and are thus likely to correspond to the aqueous media surrounding cells, primarily consisting of water. Components 2, 6 and 8 appear to show localisation of signal inside the cell, and therefore are likely to correspond to intracellular molecules, however their retrieved spectra do not show spectral features over the imaged wavenumber range, and consequently attribution to specific chemical groups is challenging. The remaining components do not show region-specific localisation of signal, with signal observed both inside and outside of the cell, nor do they show

spectral features within their associated spectra, and hence these components are considered to either aqueous media/water or background noise.

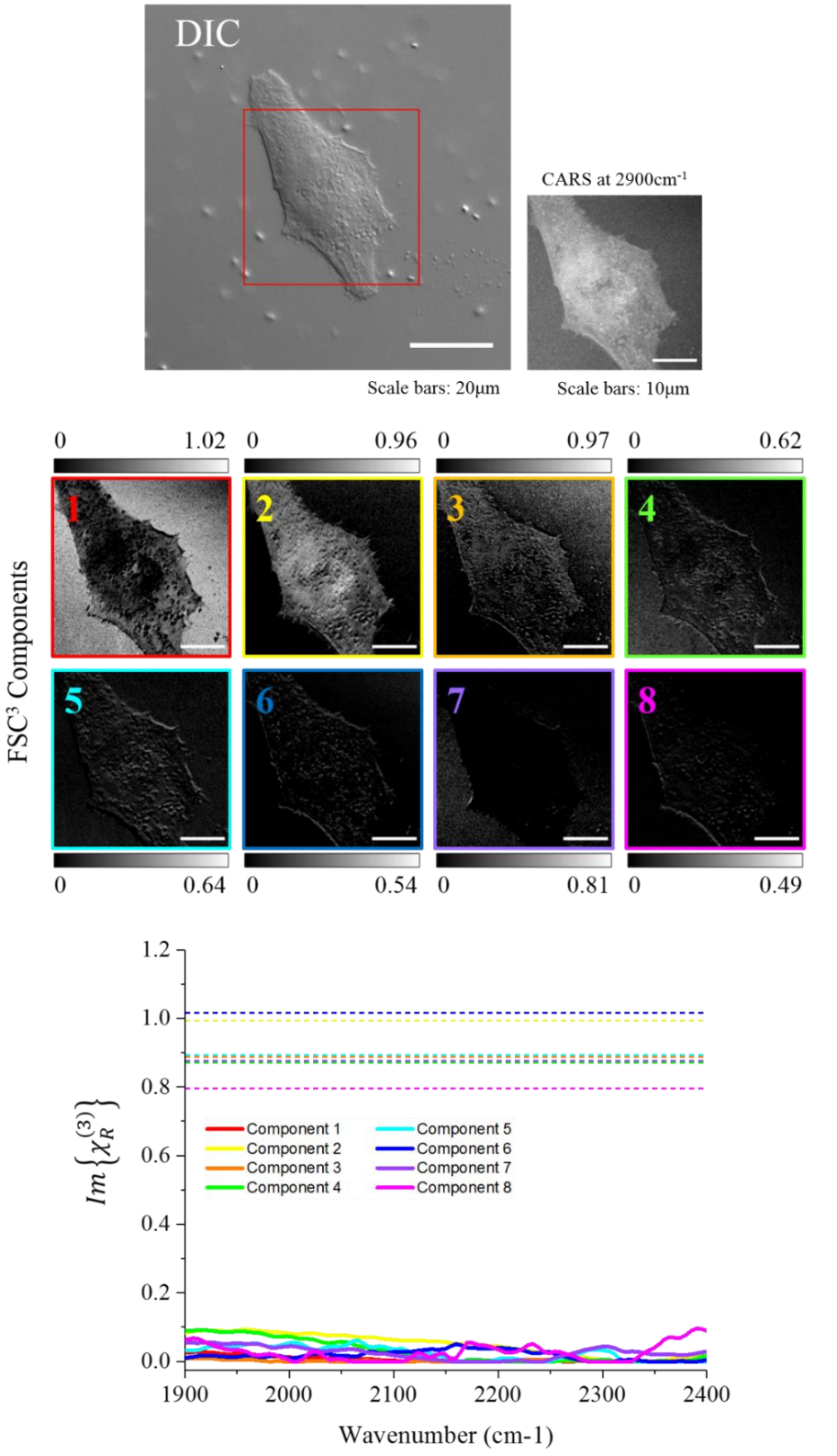

Figure 6.7 | Spatial and spectral outputs of FSC³ following its application to a hyperspectral CARS dataset acquired from an individual HeLa cell treated with 100 μM D6-SA for 24 hours. A spectral range of 1900-2400 cm^{-1} is utilised. Eight separate chemical components are identified, and their distribution is shown within the spatially resolved images. The associated spectra show the phase-retrieved imaginary part of the normalised CARS susceptibility $Im\left\{\chi_R^{(3)}\right\}$ and the corresponding real parts are shown as averages, indicated by horizontal dashed lines. Components 1 and 7 show extracellular localisation of signal, and are thus likely to correspond to water, whilst Components 2, 6 and 8 show localisation of signal inside the cell, and therefore are likely to correspond to intracellular molecules, however none of the retrieved spectra show spectral features over the target wavenumber range, and thus attribution to specific chemical groups is challenging. Components 3, 4 and 5 do not show localisation of signal to specific structures, with signal observed both inside and outside of the cell, nor do they show spectral features within their associated spectra, and hence these components are considered to represent either aqueous media (water) or background noise. Volume concentration ranges for each component are given by the grayscale values. DIC was utilised for initial selection of cells, and the single wavenumber CARS image shows cellular structure based on protein signal. Scale bars show 20 μm in DIC images and 10 μm in CARS images.

Consequently, FSC³ was not able to identify a chemical component corresponding to C-D bond vibrations, and hence D6-SA. This may have been due to the ubiquitous distribution of the molecule throughout the cell, hence limiting the coherent CARS signal which could be achieved and preventing generation of detectable signal above noise. Alternatively, the molecule may not have been present within cells at the time of imaging, which could have related to turnover of the molecule within the 24-hour time-period or due to membrane permeabilisation during PFA-fixation and subsequent loss of the molecule from cells, the latter of which would warrant study of live cells.

A further explanation for the inability of hyperspectral CARS and FSC³ data analysis to observe deuterium-labelled isoforms of SA within cells may relate to the metabolic fate of the deuterium atoms within the D4- and D6-SA structures. Figure 6.8 shows the specific citric acid cycle reactions which are likely responsible for the degradation of D4-/D6-SA and hence may provide additional information regarding possible localisation sites for CD-associated signal. If in the above described example D6-SA was incorporated into the citric acid cycle, the deuterium-labelled molecule would have initially been converted to fumaric acid and, consequently, two of its deuterium atoms would have rapidly been incorporated into $FADH_2$, hence giving deuterated $FADD_2$. The deuterium-labelled fumaric acid would then have been converted to malic acid via addition of water, although the two deuterium atoms would have been expected to remain within the malic acid structure. The deuterium-labelled malic acid would then have been converted to oxaloacetic acid and another of the deuterium atoms would have been lost from the molecule, giving either deuterated NADD and H^+, or a D^+ cation and non-deuterated NADH. Thus, in only

three citric acid cycle reactions, three deuterium atoms would have been metabolised from the original D6-SA molecule and passed to the electron transport chain at the inner mitochondrial membrane. The remaining deuterium atom would likely have remained within the citric acid cycle components until it was also incorporated into $FADH_2$/NADH or released as D^+ at a later stage. It can therefore be concluded that deuterium-labelled SA would have been rapidly metabolised by cells following uptake. As cells in Figure 6.7 were incubated with D6-SA, oppose to D4-SA, the deuterium bound to oxygen would have remained present throughout the reaction pathway shown in Figure 6.8A, and, based on their positioning, would likely have remained within the structure of the various citric acid cycle intermediates up to the isocitric acid formation stage. As the two reactions which succeed isocitric acid formation involve generation of NADH, H^+ and CO_2, either one or both of the oxygen-bound deuterium atoms would likely have been metabolised at this stage of the citric acid cycle, as illustrated in Figure 6.8B. The liberated deuterium would likely have either been incorporated into NADH or released as a D^+ cation, as in the reactions described in Figure 6.8A.

Thus, it is possible that most, if not all, of the deuterium atoms were metabolised from D6-SA in a single turn of the citric acid cycle and incorporated into the electron transport chain intermediates, $FADH_2$ and NADH. As the electron transport chain functions to pump protons across the inner mitochondrial membrane and into the intermembrane space to drive ATP production and cellular respiration, the intermembrane space of mitochondria presents the most likely accumulation site for deuterium. However, assuming that metabolism and turnover of deuterium from D6-SA is very rapid, it is unlikely that large volumes of deuterium remained within the mitochondrial intermembrane space within cells at the conclusion of the 24-hour timescale employed in the above described example, and hence sufficient CARS signal could not be generated for identification of CD-associated signal.

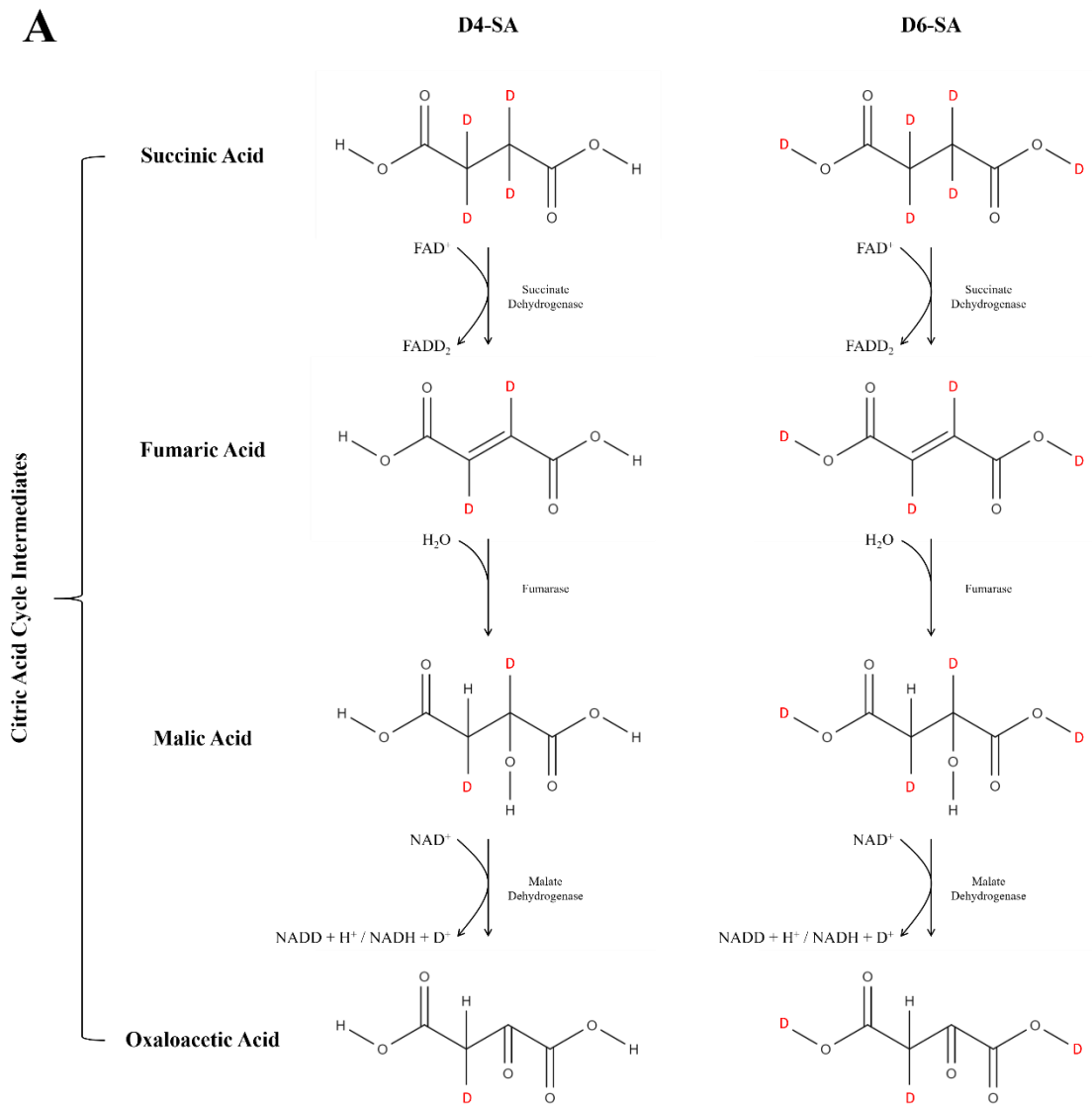
A
D4-SA
D6-SA
Citric Acid Cycle Intermediates
Succinic Acid
FAD+
FADD2
Succinate Dehydrogenase
Fumaric Acid
H2O
Fumarase
Malic Acid
NAD+
NADD + H+ / NADH + D+
Malate Dehydrogenase
Oxaloacetic Acid

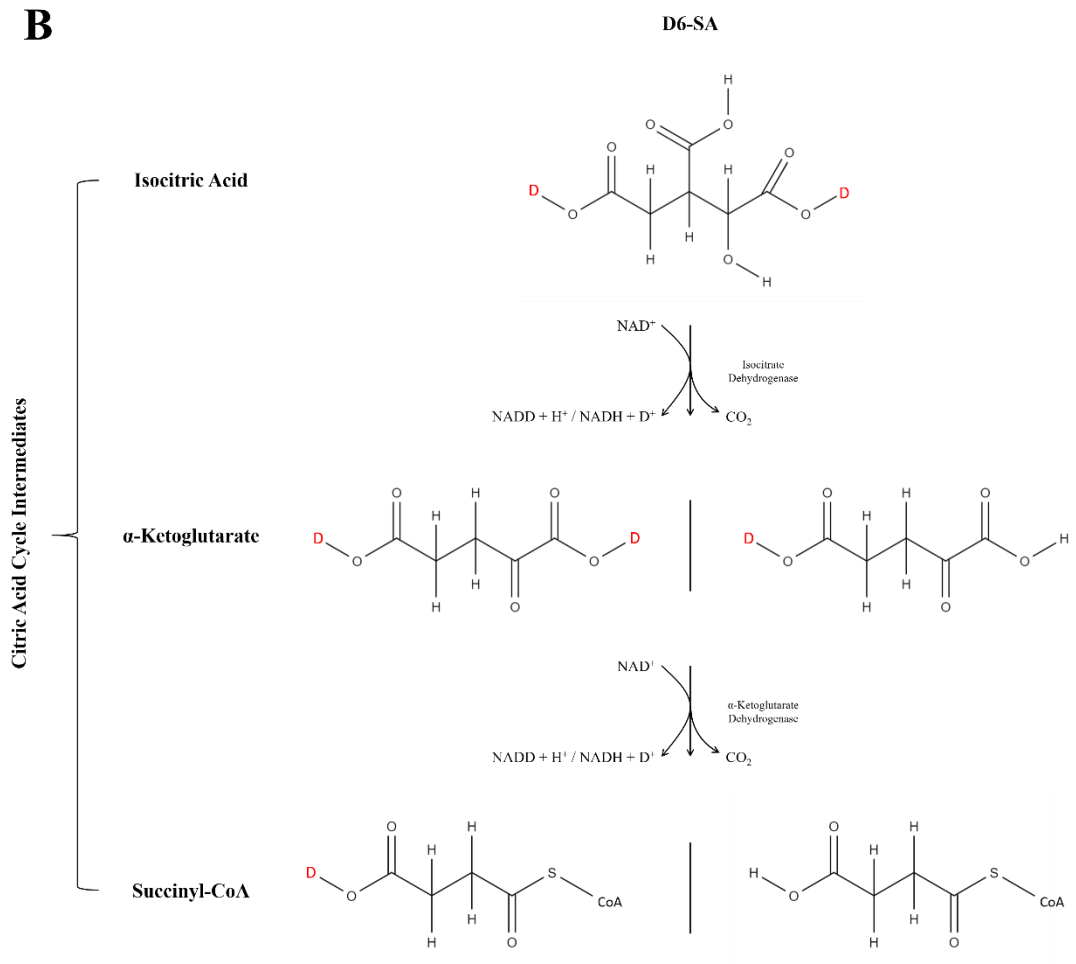

Figure 6.8 | Illustration of the fate of deuterium atoms during cellular metabolism of D4-/D6-SA. At various stages of the citric acid cycle, deuterium is removed from the reaction intermediate and combined with FAD^+ or NAD^+ to give deuterated $FADD_2$, deuterated NADD or a D^+ cation. D4-SA loses most of its deuterium atoms within the four reactions which generate oxaloacetic acid (A), whilst deuterium bound to oxygen in D6-SA is preserved until the release of CO_2 in later citric acid reactions (B). The two possible isoforms of α-ketoglutarate and succinyl-CoA, dependent on where CO_2 is removed from, are shown. Deuterium atoms are represented by 'D' and shown in red. MolView was used as a molecule editor to generate the two-dimensional representations.

6.3.3. D3-TPMP

As previously discussed, the ability of cationic TPMP to accumulate up to 1000-fold within the negatively charged mitochondrial matrix[200,201] makes it a well-suited molecule for imaging by CARS microscopy, which relies on coherent interference from large numbers of identical chemical bonds within the imaged focal volume. Hence, the deuterated isoform of TPMP, D3-TPMP, was investigated to assess the ability of hyperspectral CARS and subsequent FSC^3 data analysis to identify and spatially resolve a chemical component corresponding to a deuterium-labelled small molecule compound within a cell. With the *a priori* knowledge that D3-TPMP will accumulate within mitochondria, fields of view for CARS imaging were selected based on the presence of these cellular organelles. Although the tendency for D3-TPMP to accumulate within mitochondria is highly beneficial for generation of coherent signal, the ability to visualise the small molecule compound within cells may be limited by the small number of C-D bonds that constitute the deuterium label (a single CD_3 group). This was reflected by the weak CD-associated peaks within the Raman spectrum acquired from D3-TPMP dissolved in water.

To determine the concentration at which the deuterium-labelled compound should be administered to cells, fluorescence analysis was performed to observe changes in mitochondrial structure over a 24-hour time period with different concentrations of D3-TPMP dissolved in water, the results of which are displayed in Figure 6.9. A GFP-labelled viral construct (CellLight™ Mitochondria-GFP) (Invitrogen, UK) was utilised, which permits targeting of GFP to mitochondria through the E1 alpha pyruvate dehydrogenase leader sequence, efficiently labelling the cellular structures. Samples were PFA-fixed at the conclusion of a 24-hour incubation period, and images were acquired using a widefield fluorescence microscope at 10x magnification (see Section 3.4 of Chapter 3 for overview of fluorescence imaging set-up). Cells treated with 0.01 mM D3-TPMP showed a mitochondrial morphology which was comparable to that observed within untreated control cells, whilst cells exposed to 0.05 mM and 0.1 mM concentrations of D3-TPMP showed alterations in mitochondria structure, indicating poor cell health. Consequently, a concentration of 10 μM was selected for cell treatment.

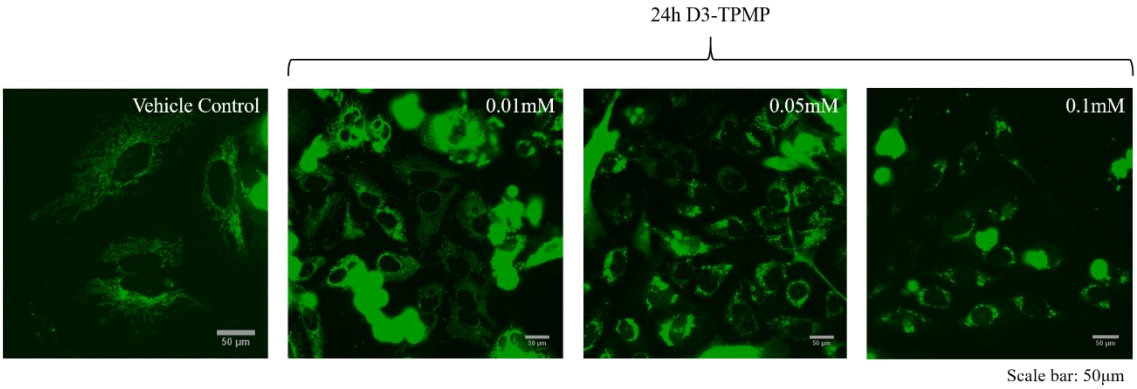

Figure 6.9 | Fluorescence images showing HeLa cells treated with different concentrations of D3-TPMP and the CellLight™ Mitochondria-GFP reagent for a 24-hour incubation period, permitting visualisation of induced structural changes to mitochondria, providing the basis for selection of the most suitable compound concentration for subsequent experiments. Images were acquired at 100x with scale bars showing 50 μm.

Figures 6.10 and 6.11 show the spatial and spectral outputs of FSC^3 analysis applied to hyperspectral CARS datasets acquired from intracellular regions of D3-TPMP-treated HeLa cells over the ranges, 1600-3000 cm^{-1} and 1600-2600 cm^{-1}, respectively, once again assessing the ability of FSC^3 analysis to identify a deuterium-labelled small molecule within a cell. HeLa cells were incubated in media supplemented with 10 μM D3-TPMP for 24 hours, before PFA-fixation and subsequent CARS imaging was performed. The compound was initially dissolved in water to give a homogenous solution, which was then added to growth media at a final concentration of 10 μM. A second set of HeLa cells was treated with non-deuterated TPMP at a concentration of 10 μM for 24 hours for direct comparison with the D3-TPMP-treated cells, and a set of control cells were incubated in media containing water only (vehicle controls).

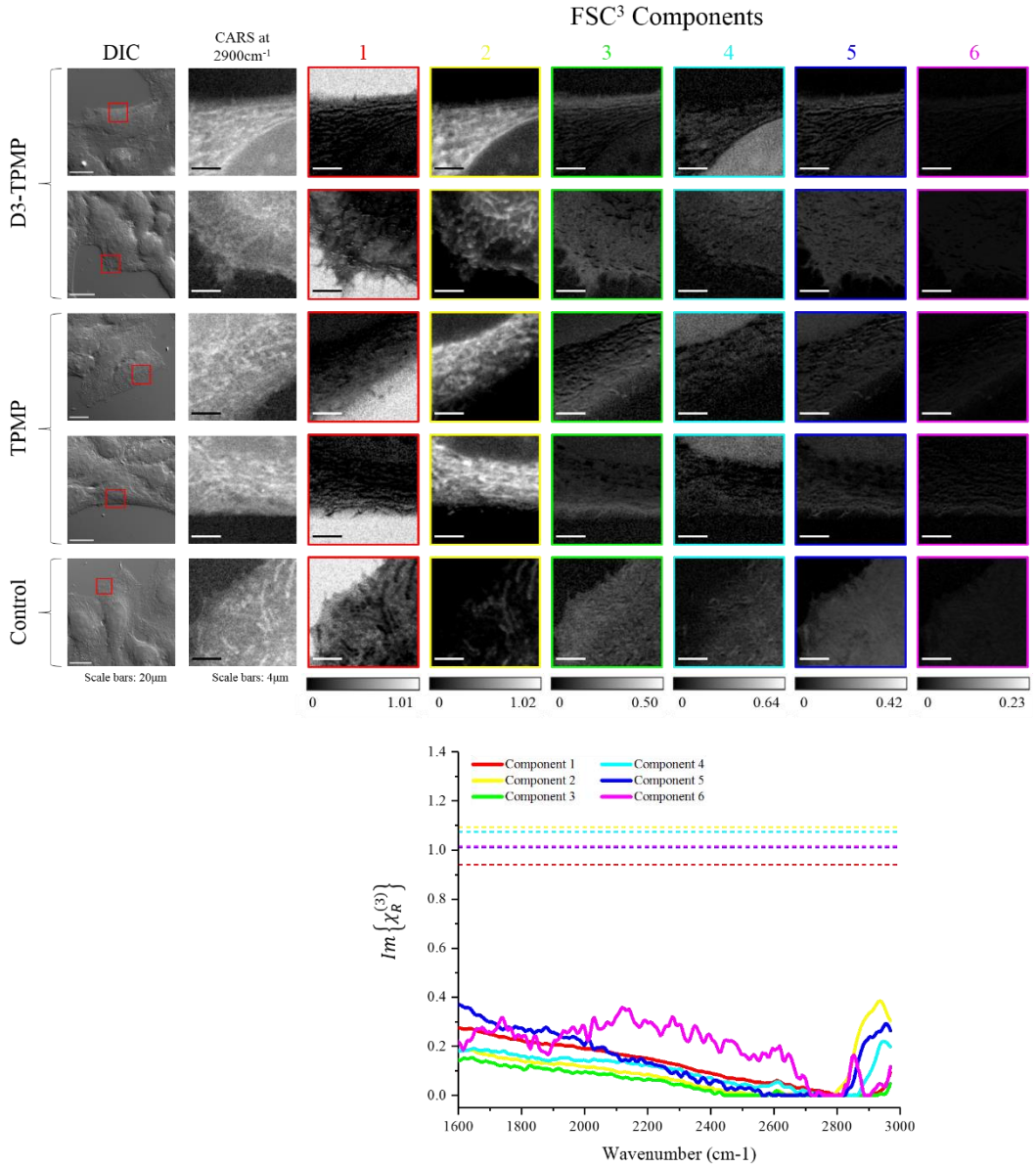

Figure 6.10 | Spatial and spectral FSC^3 outputs following application to hyperspectral CARS datasets acquired from cytoplasmic regions of HeLa cells treated with 10 μM TPMP, 10 μM D3-TPMP or vehicle control for 24 hours. A spectral range of 1600-3000 cm^{-1} is utilised and the spatially resolved images for each component, along with the associated spectra showing the phase-retrieved imaginary part of the normalised CARS susceptibility $Im\left\{\chi_R^{(3)}\right\}$ are displayed. The corresponding real parts are shown as averages, indicated by horizontal dashed lines. Chemical components are identified corresponding to water (Component 1), a combination of protein and lipid (Components 2 and 5), and nucleic acid (Component 4), based on the localisation of signal within the spatially resolved images and line-shapes of the retrieved spectra. Components 3 and 6 either show inhomogeneities in the water signal or background noise. Full volume concentration ranges for each component across all images are given by the grayscale values. DIC images show whole cells and the cytoplasmic regions selected for hyperspectral CARS acquisition, and single wavenumber CARS images provided initial confirmation of presence of mitochondria within fields of view. Scale bars show 20 μm in DIC images and 4 μm in FSC^3 images.

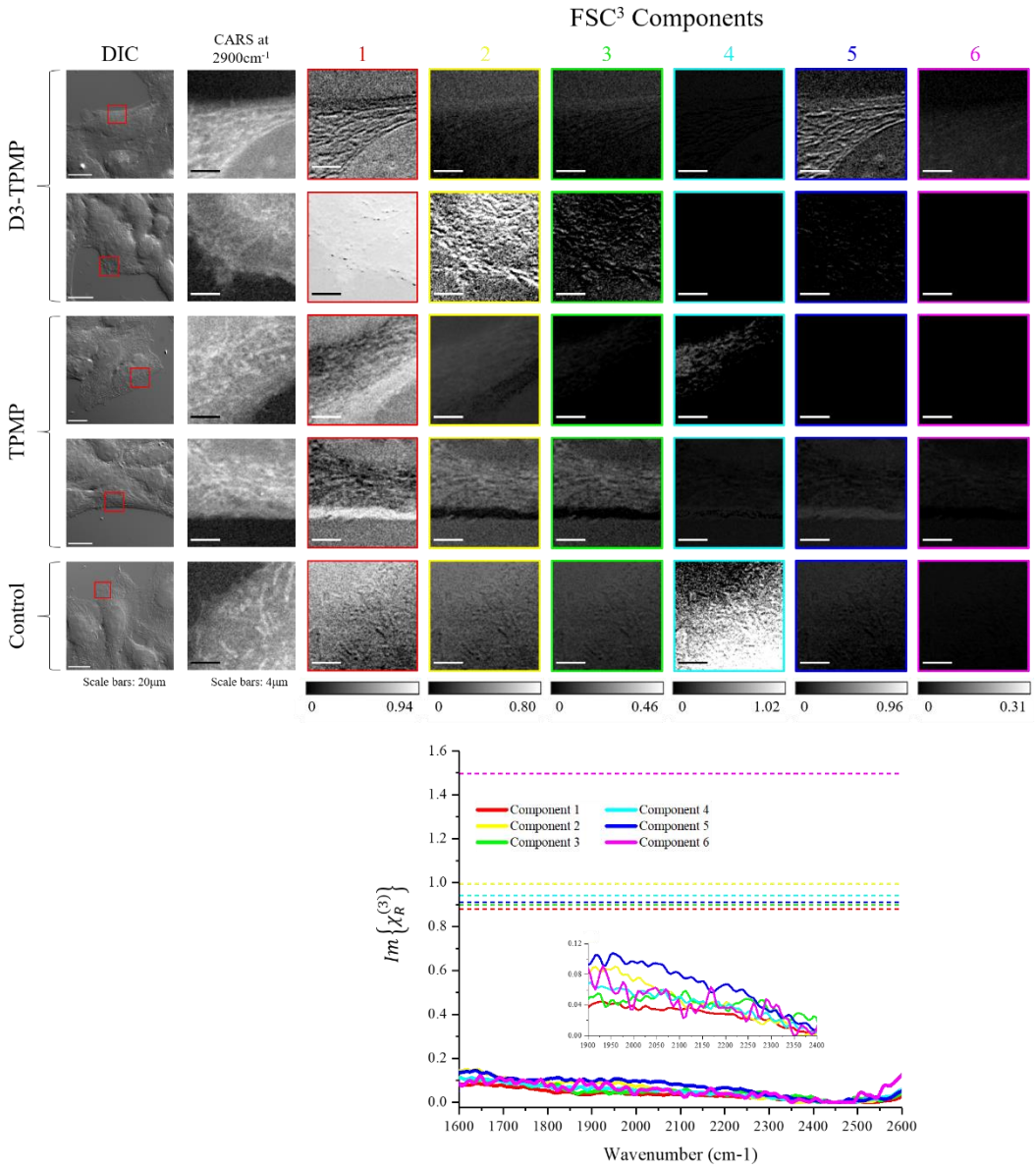

Figure 6.11 | Spatial and spectral FSC^3 outputs following application to hyperspectral CARS datasets acquired from cytoplasmic regions of HeLa cells treated with 10 μM TPMP, 10 μM D3-TPMP or vehicle control for 24 hours. A spectral range of 1600-2600 cm^{-1} is utilised to remove the lipid and protein contribution, and the spatially resolved images for each component, along with the associated spectra showing the phase-retrieved imaginary part of the normalised CARS susceptibility $Im\left\{\chi_R^{(3)}\right\}$ are displayed. The corresponding real parts are shown as averages, indicated by horizontal dashed lines. Whilst the spatially resolved images appear to show localisation of signal to cellular structures, the associated spectra fail to show any spectral features over the employed wavenumber range and hence components can only be attributed to fluctuations in background noise. Full volume concentration ranges for each component across all images are given by the grayscale values. DIC images show whole cells and the cytoplasmic regions selected for hyperspectral CARS acquisition, and single wavenumber CARS images provided initial confirmation of presence of mitochondria within fields of view. Scale bars show 20 μm in DIC images and 4 μm in FSC^3 images.

Figure 6.10 shows the spatially resolved FSC^3 images following application to hyperspectral datasets acquired from D3-TPMP-treated cells over the spectral range, 1600-3000 cm^{-1}. Associated spectra showing the phase-retrieved imaginary part of the normalised CARS susceptibility $Im\left\{\chi_R^{(3)}\right\}$ are also shown for each identified component. Hyperspectral data from TPMP-treated cells and untreated controls are also included in the FSC^3 analysis, permitting direct comparison between the three sets of cells. As in Part A of Chapter 5, FSC^3 analysis was applied to all samples simultaneously, thus identifying the most common spectra across all images. The cell-silent region of the Raman spectrum is once again targeted in the hope that CD-associated peaks (identified at 2022 cm^{-1}, 2135 cm^{-1} and 2248 cm^{-1} in the aqueous Raman spectrum in the previous section) can provide contrast against the chemical background of the cell. Six separate chemical components were considered in the FSC^3 algorithm. Fields of view containing mitochondria, the assumed localisation site of D3-TPMP, were initially identified through acquisition of CARS images at 2900 cm^{-1}, generating signal from protein-rich structures.

Hyperspectral datasets were acquired over the spectral range, 1600-3000 cm^{-1} to incorporate CH-stretch region resonances, providing further confirmation of the presence of mitochondria within the imaged fields of view via the identified Component 2, the associated spectrum of which shows a peak from 2800-3000 cm^{-1} owing to signal from both lipid and protein. Component 4 shows nucleic acids, with signal observed from the nuclear region of the cells. However, as discussed in Chapter 4, the spectral shape of these peaks is obscured by the upper limit of the employed intermediate filter, which specifically targets the cell-silent region of the spectrum. Component 1 can be attributed to water based on localisation of signal within the spatially resolved image and absence of peaks from its retrieved spectrum, whilst Component 5 is also likely to correspond to a combination of lipid and protein, owing to the peak observed between 2800 cm^{-1} and 3000 cm^{-1}. The remaining two components are more difficult to assign based on an absence of peaks from their retrieved spectra and a ubiquitous localisation of signal throughout the imaged intracellular regions and therefore may either represent water within the cells or simply background noise. Despite identification of chemical groups based on lipid, protein and water peaks, no signal is observed corresponding to carbon-deuterium resonances, owing to a lack of visible peaks between 2000 cm^{-1} and 2300 cm^{-1} within the retrieved spectra. Furthermore, no clear differences were observed between cells treated with D3-TPMP, TPMP and untreated controls.

Figure 6.11 shows FSC^3 outputs following its application to the same hyperspectral CARS datasets but performed over a reduced spectral range (1600-2600 cm^{-1}), removing resonances from lipids and proteins and specifically targeting those associated with vibrations of

carbon-deuterium bonds. Six chemical components are once again considered in the FSC^3 algorithm. Although some of the spatially resolved images appear to show localisation of signal to specific cellular regions, in particular Component 5 in the upper D3-TPMP-treated sample and Component 4 in the upper TPMP sample, the corresponding spectra for each component fail to show observable peaks above noise levels over the imaged spectral range, and consequently the observed variations in CARS signal are considered to correspond to fluctuations in the background signal. Furthermore, consistency is not observed between components from the two D3-TPMP-treated samples or the two TPMP-treated samples, which would be expected if any genuine signal was present corresponding to C-D bonds within the deuterium-labelled small molecule compound. The spectral range was not reduced further due to the inability of the FSC^3 algorithm to identify at least three separate chemical components.

A possible reason for the inability of FSC^3 to discriminate a chemical component corresponding to carbon-deuterium bond vibrations is loss of the compound from cells as a result of the fixation process, in which paraformaldehyde is known to cause transient permeabilization of the plasma membrane. Consequently, hyperspectral CARS datasets were acquired from HeLa cells which were prepared in the same way as the fixed samples in the previous section, including an incubation time of 24 hours, but were subsequently imaged live. The corresponding FSC^3 results, following application to hyperspectral CARS datasets, are displayed in Figures 6.12 and 6.13. CARS microscopy has become established as an effective technique for imaging live cells, with much faster acquisition times than spontaneous Raman techniques, however the time requirement for generation of hyperspectral CARS datasets still produces challenges when imaging live cell samples. One such difficulty is the necessity for keeping samples at ~ 37°C to ensure survival, which can cause fluctuations in z-position over longer time periods. Given that acquisition of a single hyperspectral CARS dataset with 15 μm x 15 μm images over the spectral range, 1600-3000 cm^{-1} (281 5 cm^{-1} steps), as in Figures 6.10, typically takes 25-30 mins, z-drift can alter sample position by a considerable amount, dramatically affecting the outputs of FSC^3 analysis. To avoid this difficulty, hyperspectral CARS datasets were acquired without heating the stage, overcoming the z-drift problem, but at the expense of cell health. As a result, cells developed signs of necrosis, with vacuole-like features forming within the cell cytoplasm, as observed by both DIC and CARS. Despite this, the hyperspectral CARS datasets were still analysed by FSC^3 to assess whether D3-TPMP could be visualised within the live cells.

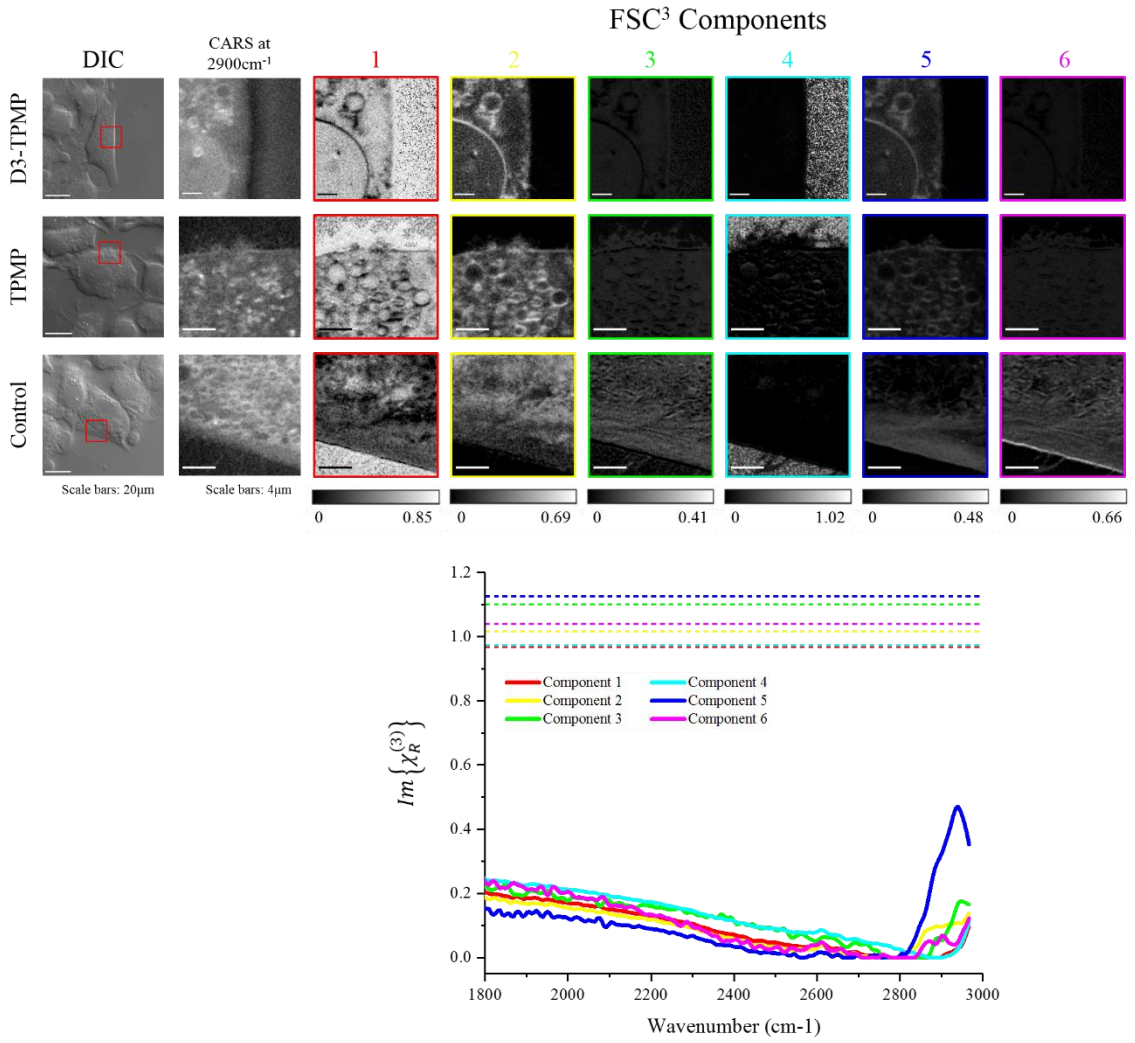

Figure 6.12 | Spatial and spectral FSC^3 outputs following application to hyperspectral CARS datasets acquired from cytoplasmic regions of live HeLa cells treated with 10 μM TPMP, 10 μM D3-TPMP or vehicle control for 24 hours. A spectral range of 1800-3000 cm^{-1} is utilised and the spatially resolved images for each component, along with the associated spectra showing the phase-retrieved imaginary part of the normalised CARS susceptibility $Im\left\{\chi_R^{(3)}\right\}$ are displayed. The corresponding real parts are shown as averages, indicated by horizontal dashed lines. Chemical components are identified corresponding to water (Components 1 and 4), combinations of protein and lipid (Components 2, 3 and 5), based on the localisation of signal within the spatially resolved images and line-shapes of the retrieved spectra. Components 6 is considered to show a combination of lipid and intracellular aqueous media. Full volume concentration ranges for each component across all images are given by the grayscale values. DIC images show whole cells and the cytoplasmic regions selected for hyperspectral CARS acquisition, and single wavenumber CARS images indicate the presence of cellular features within fields of view. Scale bars show 20 μm in DIC images and 4 μm in FSC^3 images.

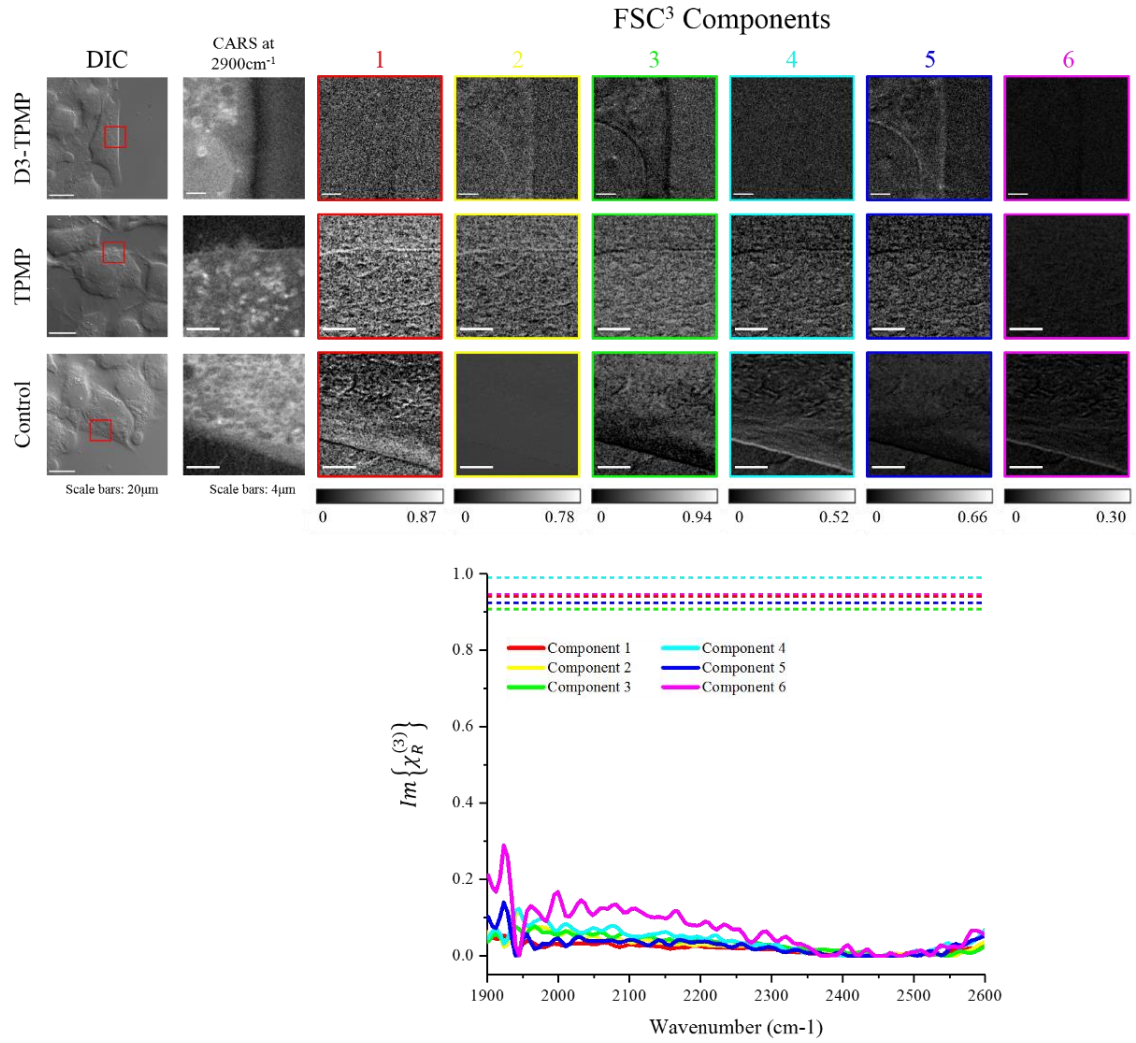

Figure 6.13 | Spatial and spectral FSC^3 outputs following application to hyperspectral CARS datasets acquired from cytoplasmic regions of live HeLa cells treated with 10 μM TPMP, 10 μM D3-TPMP or vehicle control for 24 hours. A spectral range of 1900-2600 cm^{-1} is utilised to remove the lipid and protein contribution, and the spatially resolved images for each component, along with the associated spectra showing the phase-retrieved imaginary part of the normalised CARS susceptibility $Im\left\{\chi_R^{(3)}\right\}$ are displayed. The corresponding real parts are shown as averages, indicated by horizontal dashed lines. Whilst the spatially resolved images appear to show some localisation of signal, e.g. at the plasma membrane and nuclear envelope, the corresponding retrieved spectra fail to show any spectral features over the employed wavenumber range, hence components can only be attributed to fluctuations in background noise. Full volume concentration ranges for each component across all images are given by the grayscale values. DIC images show whole cells and the cytoplasmic regions selected for hyperspectral CARS acquisition, and single wavenumber CARS images indicate the presence of cellular features within fields of view. Scale bars show 20 μm in DIC images and 4 μm in FSC^3 images.

Figure 6.12 shows the FSC^3 outputs following application to hyperspectral datasets acquired from live HeLa cells incubated with either D3-TPMP, TPMP or water (vehicle control) for a 24-hour time period. The hyperspectral data was acquired over the spectral range, 1800-3000 cm^{-1}, incorporating peaks within the CH-stretch region, which enabled visualisation of intracellular structures via signal from lipid and protein, and six separate chemical components were considered in the analysis algorithm. Components are identified corresponding to water (Components 1 and 4), owing to localisation of signal outside of the cells and retrieved spectrum showing no spectral features over the targeted spectral range, and combinations of lipid and protein (Components 2, 3 and 5), based on observed signal from intracellular structures and a peak at ~ 2850-3000 cm^{-1}. Component 6 shows weak signal inside the cell and a retrieved spectrum which follows the same line-shape as Component 4, increasing at ~ 3000 cm^{-1}, hence this component is considered to represent aqueous medium within the cell, containing very small amounts of other biological molecules. None of the component spectra show spectral peaks between 2000 cm^{-1} and 2300 cm^{-1}, indicating that no CD-associated signal is detected. The poor health of the cells may have contributed to loss of the compound from cytoplasmic regions.

As lipid/protein signal appears to dominate the identified components, the same hyperspectral datasets were reanalysed by FSC^3 over a reduced spectral range (1900-2600 cm^{-1}), removing peaks from the CH-stretch region of the Raman spectrum and enabling identification of components based exclusively on spectral line-shapes observed within the cell-silent region. The respective FSC^3 outputs are shown in Figure 6.13, with six components once again considered in the analysis algorithm. As was observed for the fixed samples in Figure 6.11, variation in CARS signal is observed within the spatially resolved images, e.g. at the plasma membrane and nuclear envelope, however the retrieved spectra fail to show distinguishable peaks above noise, and consequently the observed differences within the spatial images can only be attributed to background noise fluctuations. The observed variations in spectral line-shape at the lower wavenumber end of the acquired range are an artefact of the data analysis procedure. A different sample preparation method is thus required to avoid the observed problems with poor cell health, improving the potential for observation of D3-TPMP within live cells.

Another possible reason for the lack of observed CD-associated signal is that the compound is taken up and excreted from the cell within the 24-hour incubation period, meaning that by the time the cells are either fixed or imaged live, the compound is no longer present within the cells. Consequently, the above experiment was repeated but with cells exposed to the compound for only 3 hours prior to imaging. The resulting spatial and spectral FSC^3 outputs are displayed in Figure 6.14. Cells were once again imaged live without the use of a stage heater,

causing the cells to develop vacuole-like structures, indicating sub-optimal health, however these cellular changes were not observed to the same extent as in Figures 6.12 and 6.13.

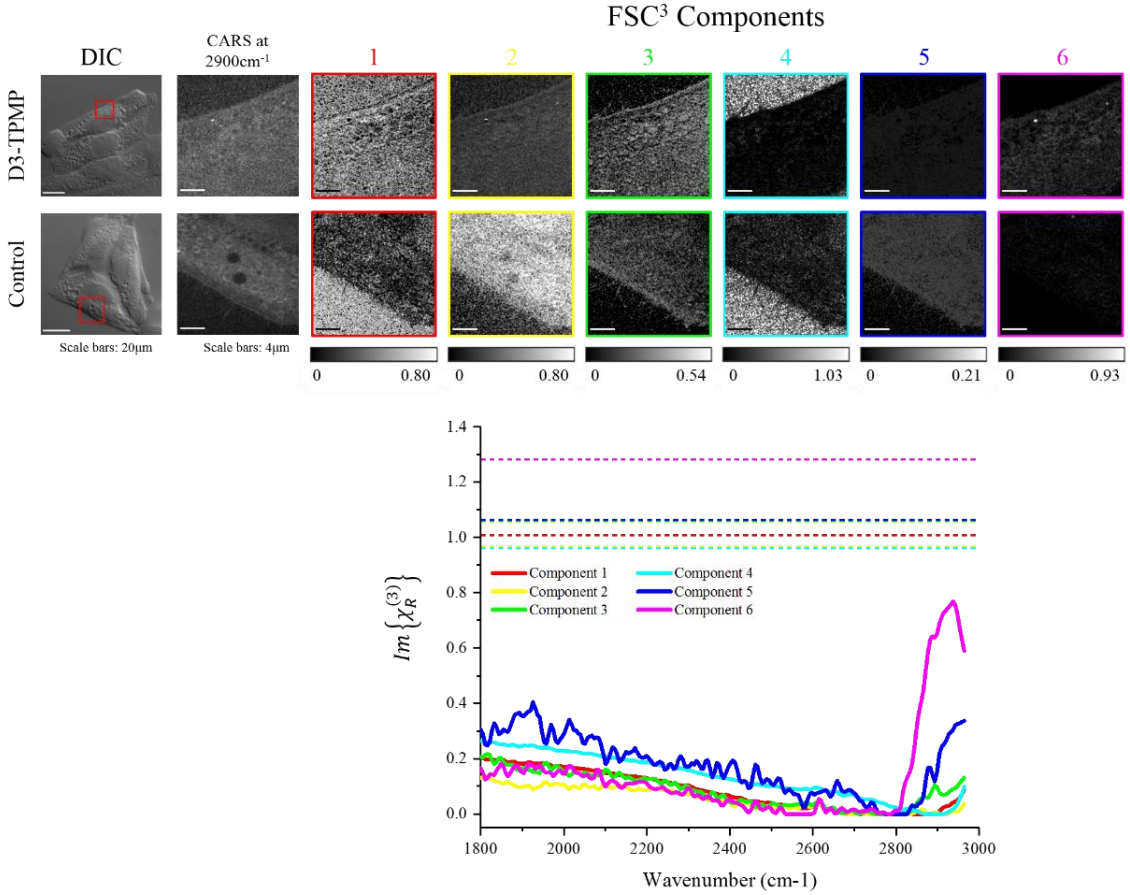

Figure 6.14 | Spatial and spectral FSC^3 outputs following application to hyperspectral CARS datasets acquired from cytoplasmic regions of live HeLa cells treated with 10 μM D3-TPMP or vehicle control for 3 hours. A spectral range of 1800-3000 cm^{-1} is utilised and the spatially resolved images for each component, along with the associated spectra showing the phase-retrieved imaginary part of the normalised CARS susceptibility $Im\left\{\chi_R^{(3)}\right\}$ are displayed. The corresponding real parts are shown as averages, indicated by horizontal dashed lines. Chemical components are identified corresponding to water (Components 1 and 4) and combinations of protein and lipid (Components 3, 5 and 6), based on the localisation of signal within the spatially resolved images and line-shapes of the retrieved spectra. Component 2 shows spatial signal within the cells but no features within its retrieved spectrum, and consequently it can either represent water within cells or background noise. Full volume concentration ranges for each component across all images are given by the grayscale values. DIC images show whole cells and the cytoplasmic regions selected for hyperspectral CARS acquisition, and single wavenumber CARS images indicate the presence of cellular features within fields of view. Scale bars show 20 μm in DIC images and 4 μm in FSC^3 images.

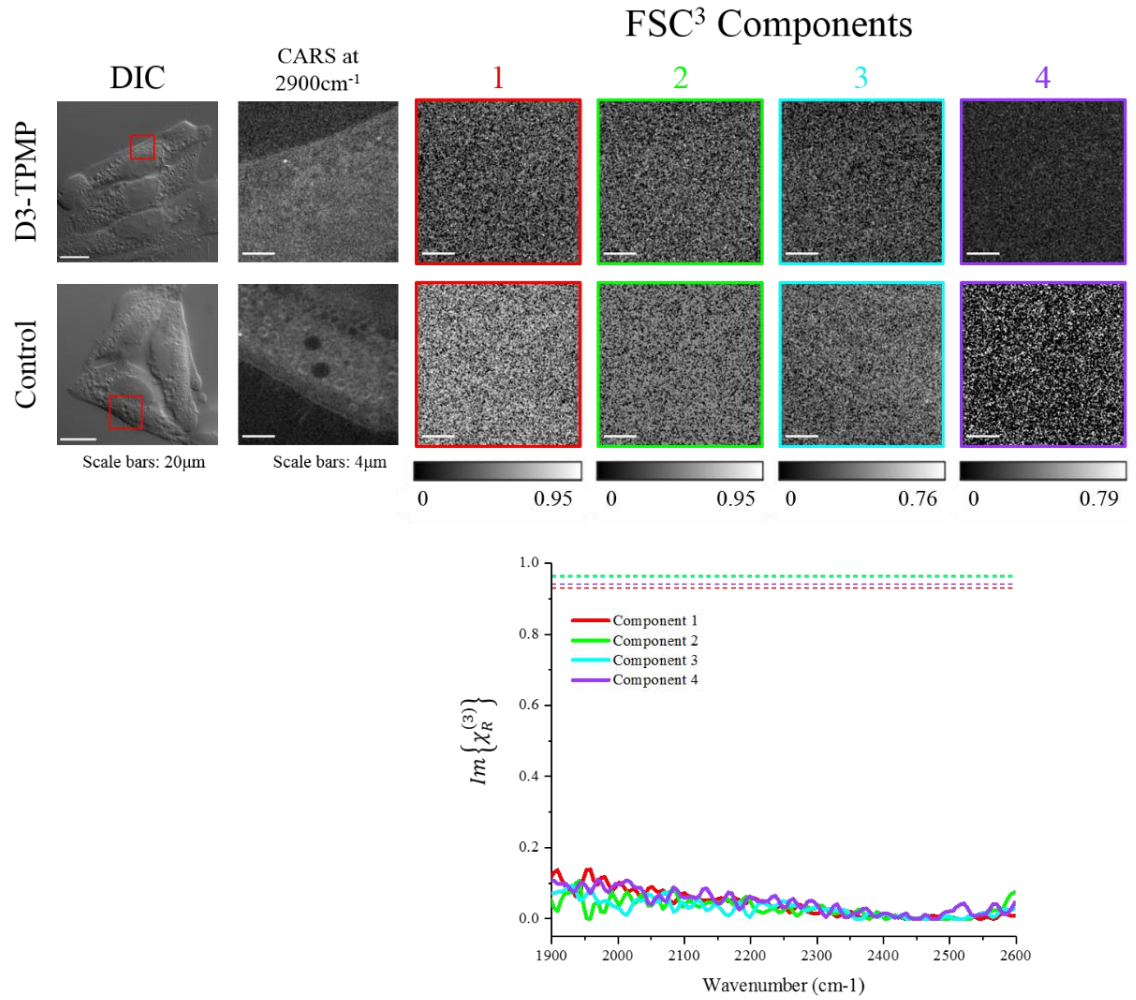

Figure 6.15 | Spatial and spectral FSC^3 outputs following application to hyperspectral CARS datasets acquired from cytoplasmic regions of live HeLa cells treated with 10 μM D3-TPMP or vehicle control for 3 hours. A spectral range of 1900-2600 cm^{-1} is utilised to remove the lipid and protein contribution, and the spatially resolved images for each component, along with the associated spectra showing the phase-retrieved imaginary part of the normalised CARS susceptibility $Im\left\{\chi_R^{(3)}\right\}$ are displayed. The corresponding real parts are shown as averages, indicated by horizontal dashed lines. Four chemical components were considered in the analysis algorithm, however none of the components shown spatial or spectral features, and thus only background noise is observed. Full volume concentration ranges for each component across all images are given by the grayscale values. DIC images show whole cells and the cytoplasmic regions selected for hyperspectral CARS acquisition, and single wavenumber CARS images indicate the presence of cellular features within fields of view. Scale bars show 20 μm in DIC images and 4 μm in FSC^3 images.

Figures 6.14 shows the results of FSC^3 analysis following its application to hyperspectral CARS datasets acquired from D3-TPMP-treated HeLa cells and vehicle control cells over the spectral range, 1800-3000 cm^{-1}, targeting the cell-silent region of the spectrum, but also incorporating CH-stretch peaks. Six chemical components were once again considered in the analysis algorithm, enabling spatial resolution of water (Components 1 and 4) and combinations of lipid and protein (Components 3, 5 and 6). The assignment of Component 2 is less clear, but it likely corresponds to either a water signal within the cells or simply background noise, owing to observed spatially resolved signal within cells but no spectral features over the targeted wavenumber range. Once again, peaks are not visible between 2000 cm^{-1} and 2300 cm^{-1} within the retrieved spectra from any of the identified components, suggesting that no CD-associated signal is detected. Figure 6.15 shows the FSC^3 outputs following application to hyperspectral CARS datasets acquired from the same fields of view, but over the reduced spectral range, 1900-2600 cm^{-1}, removing CH-stretch peaks from the analysis, thus enabling identification of chemical components based on spectral variations within the cell-silent region. However, even with only four chemical components considered, no spatial or spectral features were observed within the utilised spectral range.

This section has shown little success in observing D3-TPMP within cells, despite its known tendency to accumulate to a high concentration within the mitochondrial matrix, which is highly advantageous for CARS due to the large number of bonds which can be included within the focal volume, enhancing the coherent signal. The strong signal observed from lipid, protein and nucleic acid suggested that the imaging hardware was configured correctly, and the observation of intracellular structures within both single wavenumber CARS images and the hyperspectral datasets which extended to 3000 cm^{-1} indicated that a suitable field of view was utilised. Therefore, the only possible explanations for the complete absence of CD-associated signal are that the label is not large enough (only a single CD_3 group) or the compound is no longer present within cells by the time of imaging.

6.3.4. D4-paracetamol

The ability of FSC^3 to detect and spatially resolve D4-Para within a cell was assessed by incubating HeLa cells with the deuterium-labelled small molecule compound, which was first dissolved in a 50:50 solution of methanol/water to give a homogenous solution, before it was combined with growth media to give a final concentration of 100 μM. Cells were exposed to D4-Para for a 24-hour time-period, after which they were PFA-fixed and imaged by CARS microscopy. As the most likely intracellular region for D4-Para to accumulate was unknown, hyperspectral CARS datasets were acquired from the whole cell before FSC^3 data analysis was applied. However, the spontaneous Raman spectrum acquired from a powder preparation of D4-Para (discussed in Section 6.2) showed CD-associated peaks at 2244 cm^{-1}, 2278 cm^{-1}, 2314 cm^{-1}, all of which lie outside of the targeted spectral range of 1900-2200 cm^{-1}. Therefore, observation of signal corresponding to CD-associated bond resonances would not be expected. As previously described for Figure 6.6, incorrect spectral range selection arose as a result of the scaling of hyperspectral datasets performed during image analysis. When the intermediate filter was used, the wavenumbers reported within the imaging software were around 200 cm^{-1} higher than the actual wavenumber acquired, and thus, a range which was initially set to 2100-2400 cm^{-1} became 1900-2200 cm^{-1} following data analysis (see Appendix 2 for reacquired dataset with correct spectral range).

Figure 6.16 shows the spatially resolved images and retrieved spectra for eight independently varying chemical components following application of FSC^3 to a hyperspectral CARS dataset acquired from a single D4-Para-treated cell over the spectral range, 1900-2200 cm^{-1}. Components 2 and 3 show localisation of signal inside the cell, and are likely to correspond to resonances from intracellular molecules, however the retrieved spectra from each of these components fail to shown spectral features, and thus attribution to specific chemical groups is challenging. Components 4, 5 and 6 show extracellular localisation of signal and retrieved spectra absent of features, and are thus likely to correspond to aqueous media, consisting primarily of water. As Component 1 shows ubiquitous signal throughout the image, it is considered to represent either aqueous media (water) or a background signal. Components 7 and 8 show a weak spatially resolved signal and noisy spectra and are thus considered to correspond to background noise. Consequently, FSC^3 is not able to identify a chemical component corresponding to C-D bond vibrations, and hence D4-Para, the most likely cause of which is that the CD-associated peaks lie outside of the imaged spectral range.

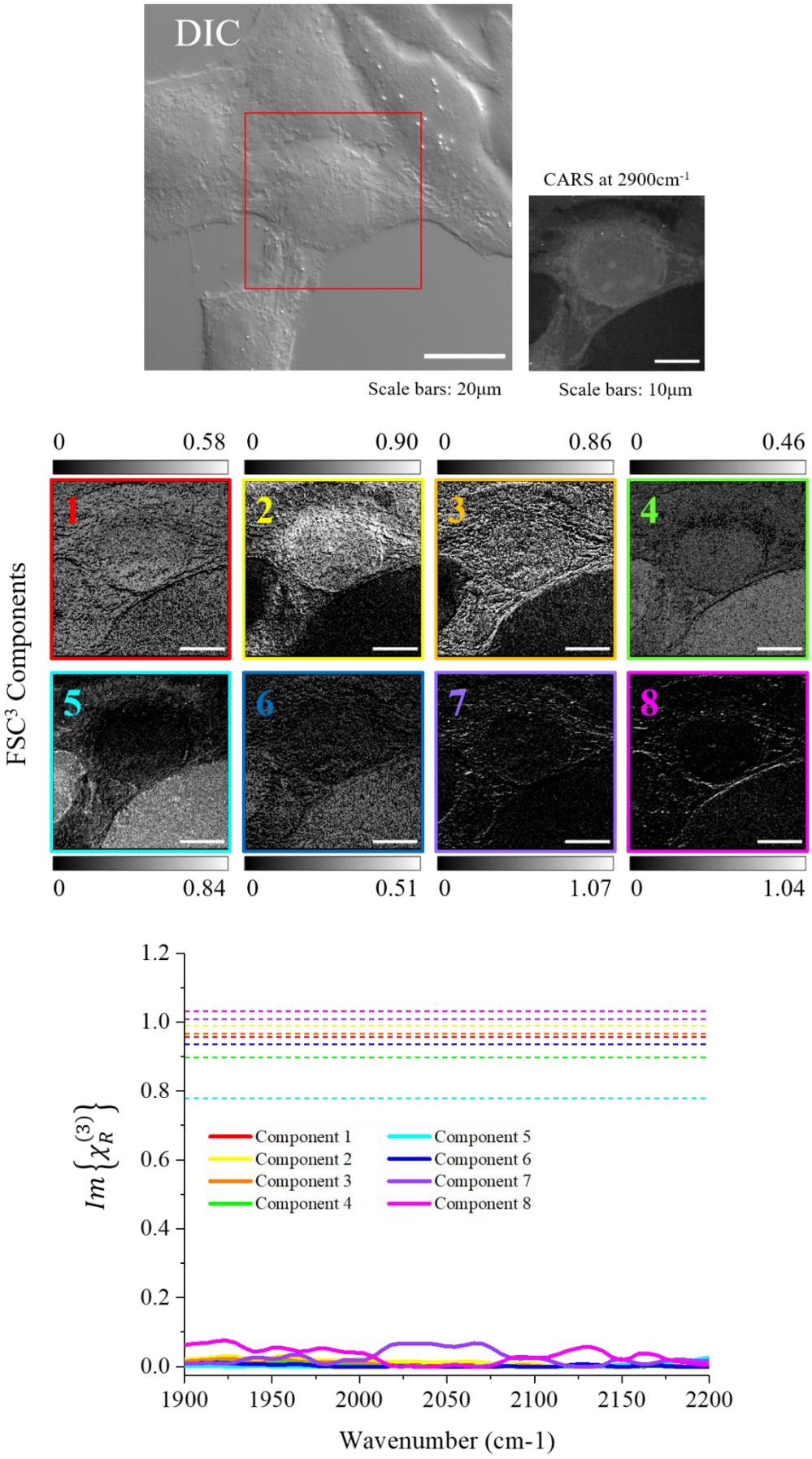
DIC
CARS at 2900cm-1
Scale bars: 20µm
Scale bars: 10µm
FSC3 Components
0
0.58
0.90
0.86
0.46
1
2
3
4
5
6
7
8
0.84
0.51
1.07
1.04
1.2
1.0
0.8
0.6
0.4
0.2
0.0
Component 1
Component 2
Component 3
Component 4
Component 5
Component 6
Component 7
Component 8
1900
1950
2000
2050
2100
2150
2200
Wavenumber (cm-1)

Figure 6.16 | Spatial and spectral outputs of FSC³ following its application to a hyperspectral CARS dataset acquired from an individual HeLa cell treated with 100 μM D4-Para for 24 hours. A spectral range of 1900-2200 cm^{-1} is utilised. Eight separate chemical components are identified, and their distribution is shown within the spatially resolved images. The associated spectra show the phase-retrieved imaginary part of the normalised CARS susceptibility $Im\left\{\chi_R^{(3)}\right\}$ and the corresponding real parts are shown as averages, indicated by horizontal dashed lines. Components 2 and 3 show intracellular localisation of signal and are likely to correspond to resonances of intracellular molecules, whilst Components 4, 5 and 6 show extracellular signal, and are thus likely to correspond to water, however, the retrieved spectra fail to show spectral features and therefore it is difficult to assign the observed signal to specific chemical groups. As Component 1 shows ubiquitous signal throughout the image, it is considered to represent either aqueous media (water) or a background signal. Components 7 and 8 show weak spatially resolved signal and noisy spectra and are thus considered to correspond to background noise. Volume concentration ranges for each component are given by the grayscale values. DIC was utilised for initial selection of cells, and the single wavenumber CARS image shows cellular structure based on protein signal. Scale bars show 20 μm in DIC images and 10 μm in CARS images.

6.3.5. D8-histamine$_2$ receptor antagonist

The ability of FSC³ to detect and spatially resolve D8-H_2Ri within a cell was assessed by incubating HeLa cells with a high concentration of the deuterium-labelled small molecule compound. D8-H_2Ri was first dissolved in a 50:50 solution of water/methanol to give a homogenous solution, before it was combined with growth media to give a final concentration of 0.5 mM. Cells were exposed to D8-H_2Ri for a 24-hour time-period, after which they were PFA-fixed and imaged by CARS microscopy. As with D4-Para and D9-COX2i, *a priori* information regarding potential intracellular accumulations sites was limited for D8-H_2Ri, thus hyperspectral CARS datasets were acquired from cytoplasmic regions of cells before FSC³ data analysis was applied. The spontaneous Raman spectrum for a powder preparation of D8-H_2Ri showed a strong peak at 2231 cm^{-1}, which was attributed to either C-D or C≡C stretching, thus a spectral range of 1800-2600 cm^{-1} was targeted.

Figure 6.17 shows the spatial and spectral outputs of FSC³ analysis applied to hyperspectral CARS datasets acquired from intracellular regions of a D8-H_2Ri-treated HeLa cell and a vehicle control cell which was exposed to 50:50 water/methanol for 24 hours. FSC³ was applied to hyperspectral data from both samples simultaneously, permitting identification of the most common spectra from both datasets. Component 1 shows spatially resolved CARS signal outside of the cells and shows no spectral features over the targeted spectral range, therefore, it is considered to correspond to aqueous media (water). The other components show differences between the D8-H_2Ri-treated cell and the vehicle control cell, with Components 2 and 3 showing signal localised within the control cell but not the compound-treated cell, whilst Components 4, 5 and 6 show signal localised within the compound-treated cell but not the control cell. It is

possible that these components correspond to vibrations of molecules within the studied cells, however, retrieved spectra from all of these components fail to show spectral features, and therefore assignment to specific chemical groups is difficult. It is also possible that these components simply show fluctuations in background noise. Despite observed differences between the compound-treated and untreated cell, a component corresponding to CD-associated resonances was not identified, and thus D8-H_2Ri was not visualised within a cell. As previously discussed within this section, the inability to differentiate a CD-associated chemical component may result from a ubiquitous distribution of the compound, hence limiting the coherently generating signal, or from the compound no longer being present within the cell at the time of imaging either due to turnover by the cell or permeabilisation of the plasma membrane, e.g. during fixation, and consequent loss of compound from the cell.

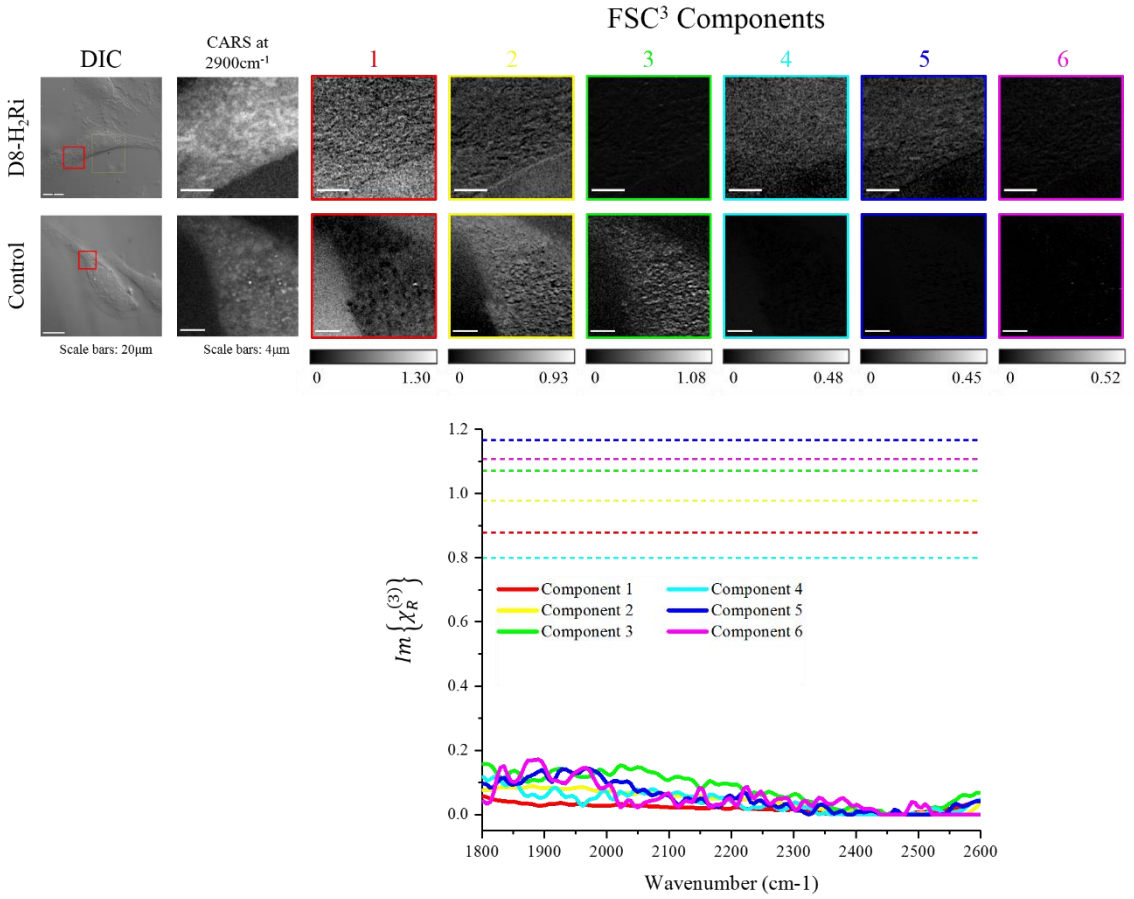

Figure 6.17 | Spatial and spectral FSC^3 outputs following application to hyperspectral CARS datasets acquired from cytoplasmic regions of HeLa cells which were exposed to 0.5 mM D8-H_2Ri or a 50:50 water/methanol solution (vehicle control) for 24 hours. A spectral range of 1800-2600 cm^{-1} is utilised, and the spatially resolved images for each component, along with the associated spectra showing the phase-retrieved imaginary part of the normalised CARS susceptibility $Im\left\{\chi_R^{(3)}\right\}$ are displayed. The corresponding real parts are shown as averages, indicated by horizontal dashed lines. Component 1 shows signal outside of the cell and a retrieved spectrum will no spectral features and is therefore considered to correspond to water. Components 2 and 3 show spatially resolved signal within the control cell but not the D8H2Ri-treated cell, whilst Components 4, 5 and 6 show signal within compound-treated cells but not control cells. It is possible that these components correspond to resonances of molecules, however the retrieved spectra from each of the components fail to show spectral features and therefore it is difficult to assign signal to specific chemical groups. Alternatively, these components may shown background noise. Full volume concentration ranges for each component across all images are given by the grayscale values. DIC images show whole cells and the cytoplasmic regions selected for hyperspectral CARS acquisition, and single wavenumber CARS images enable identification of cellular features within fields of view. Scale bars show 20 μm in DIC images and 4 μm in FSC^3 images.

6.3.6. D9-COX-2 inhibitor

D9-COX2i was also investigated to assess the ability of FSC^3 to detect and spatially resolve a deuterium-labelled small molecule within a cell. HeLa cells were incubated with D9-COX2i, which was first dissolved in water to give a homogenous solution and then combined with growth media to give a final concentration of 100 μM, for a 24-hour time-period, after which they were PFA-fixed and imaged by CARS microscopy. Hyperspectral CARS datasets were acquired from cytoplasmic regions before FSC^3 data analysis was applied. The spontaneous Raman spectrum acquired from D9-COX2i in powder form showed CD-associated peaks at 2076 cm^{-1}, 2118 cm^{-1}, 2147 cm^{-1} and 2220 cm^{-1}, as shown in Section 6.2, and thus a spectral range of 1800-3000 cm^{-1} was selected, covering the cell-silent region.

Figure 6.18 shows the spatially resolved images and retrieved spectra for eight independently varying chemical components following application of FSC^3 to a hyperspectral CARS dataset acquired from a single D9-COX2i-treated cell. Component 7 shows CARS signal localised extracellularly and a retrieved spectrum with no spectral features, and is therefore considered to represent aqueous media, comprising mainly water. Component 6 shows intracellular signal localisation and a peak between 2900 cm^{-1} and 3000 cm^{-1} in its retrieved spectrum and is therefore considered to correspond to resonance of protein molecules. Components 2, 5 and 8 also show signal within the cell, but fail to show spectral features within their retrieved spectra, therefore these components are considered to show aqueous media (water) present inside the cell. Components 1, 3 and 4 show signal both intracellular and extracellular

signal and no spectral features within their associated spectra, therefore these components may also represent aqueous media (water) which is present both inside and outside of the cell, or they may show contributions from background noise. The spatial images of Components 1 and 3 show a gradient in signal in the vertical direction, which suggests an artefact in either data acquisition, e.g. a change in z-position across the sample due to incorrect laser scanning or sample not being mounted flat, or in the data analysis process. Consequently, FSC^3 is once again unable to identify a chemical component corresponding to C-D bond vibrations, and hence D9-COX2i.

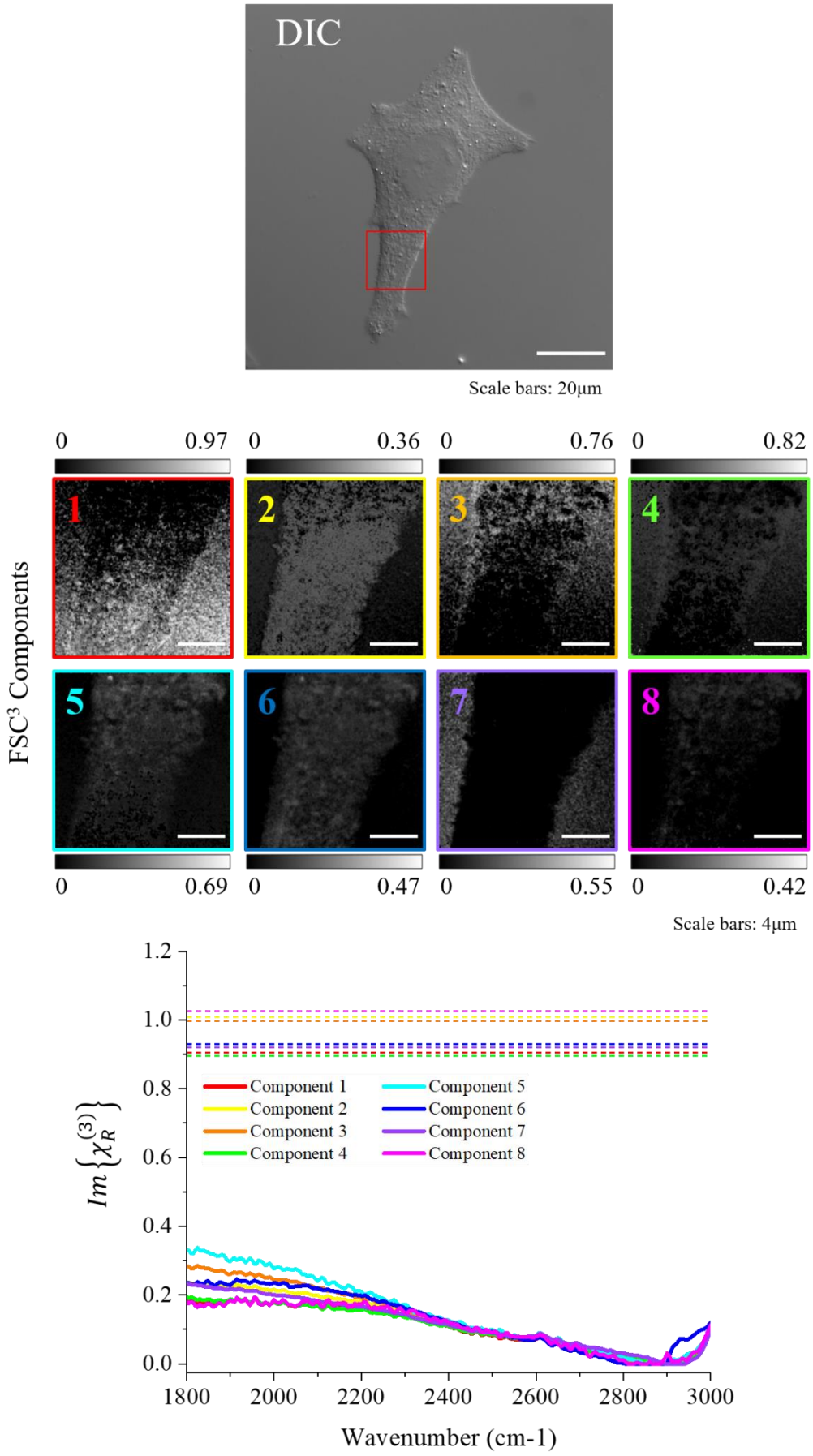
DIC
Scale bars: 20μm
FSC^3 Components
0
0.97
0.36
0.76
0.82
1
2
3
4
5
6
7
8
0.69
0.47
0.55
0.42
Scale bars: 4μm
$Im\{\chi_R^{(3)}\}$
Component 1
Component 2
Component 3
Component 4
Component 5
Component 6
Component 7
Component 8
Wavenumber (cm-1)

Figure 6.18 | Spatial and spectral FSC³ outputs following application to hyperspectral CARS datasets acquired from cytoplasmic regions of HeLa cells which were exposed to 100 μM D9-COX2i or a 50:50 water/methanol solution (vehicle control) for 24 hours over a spectral range of 1800-3000 cm^{-1}. Eight separate chemical components are identified, and their distribution is shown within the spatially resolved images. The associated spectra show the phase-retrieved imaginary part of the normalised CARS susceptibility $Im\left\{\chi_R^{(3)}\right\}$ and the corresponding real parts are shown as averages, indicated by horizontal dashed lines. Component 7 corresponds to aqueous media (water), with an extracellularly localised signal and a lack of spectral features within its retrieved spectrum. Component 6 corresponds to a combination protein, with an intracellularly localised signal and a peak at 2900-3000 cm^{-1}. Components 2, 5 and 8 are considered to correspond to aqueous media (water) inside the cell, showing an intracellular localisation of signal but no spectral features within their retrieved spectra. Components 1, 3 and 4 either show aqueous media (water) both inside and outside of the cell or background noise, based on signal observed both intracellularly and extracellularly and retrieved spectra showing no spectral features over the selected wavenumber range. Components 1 and 3 show a gradient in signal in the vertical direction, suggesting an artefact in either data acquisition or data analysis. Volume concentration ranges for each component are given by the grayscale values. DIC was utilised for initial selection of cells, and the single wavenumber CARS image shows cellular structure based on protein signal. Scale bars show 20 μm in DIC images and 10 μm in CARS images.

6.3.7. D7-HCMV DNA synthesis inhibitor

D7-HCMVi was also investigated to assess the ability of FSC³ to detect and spatially resolve a deuterium-labelled small molecule within a cell. HeLa cells were incubated with D7-HCMVi, which was first dissolved in a 50:50 solution of water/methanol to give a homogenous solution and then combined with growth media to give a final concentration of 100 μM, for a 24-hour time-period, after which they were PFA-fixed and imaged by CARS microscopy. As described in Section 6.1 of this chapter, D7-HCMVi targets the HCMV protein kinase, UL97. As the cells utilised within this chapter were uninfected, the target site of D7-HCMVi was not present, and thus general cytoplasmic regions of D7-HCMVi-treated cells were imaged by hyperspectral CARS, before subsequent FSC³ data analysis was applied for visualisation of distribution and identification any potential accumulation sites.

Figure 6.19 shows the spatial and spectral outputs of FSC³ analysis applied to hyperspectral CARS datasets acquired from a D7-HCMVi-treated HeLa cell and a vehicle control cell which was exposed to 50:50 water/methanol for 24 hours. FSC³ was applied to hyperspectral data from both samples simultaneously, permitting identification of the most common spectra across both datasets. The spontaneous Raman spectrum from a powder preparation of D7-HCMVi showed CD-associated peaks at 2063 cm^{-1}, 2126 cm^{-1}, 2191 cm^{-1} and 2228 cm^{-1}, thus a spectral range of 1800-2400 cm^{-1} was targeted. Component 1 shows a ubiquitous signal across its spatial images and no spectral features within its retrieved spectrum; thus, it is considered to correspond to either aqueous medium (water) present both intracellularly and extracellularly, or background

signal. A similar localisation of signal is observed within the spatial images for Components 2 and 6, which differ between the D7-HCMVi-treated and vehicle control samples. For the compound-treated sample, signal is observed ubiquitously, with a higher signal intensity observed extracellularly, whilst for the control sample, signal is observed from the nuclear membrane. The retrieved spectra for both components fail to show spectral features over the targeted wavenumber range, and therefore attribution of these components to groups is challenging. Component 3 shows similar intracellular signal localisation between the two cells, which may relate to resonances of molecules, however, the absence of spectral features within the associated spectra prevent chemical assignment. Components 4 and 5 show differences in signal localisation between the D7-HCMVi-treated cell and the vehicle control cell, with both components showing intracellular signal from the compound-treated cell, whilst for the control cell, Component 4 shows signal at the nuclear membrane and Component 5 shows a very weak intracellular signal. As with the other components, a lack of spectral features over the targeted spectral range prevents assignment of these components to specific chemical groups. Overall, this dataset shows no consistency in localisation of CARS signal between the samples, indicated by the spatially resolved images. The clear differences between components suggest that the identified spectra are unique to each sample, which would not be the case if specific chemical groups showing typical spectra were observed. Hence, it is possible that the displayed components simply relate to background signal.

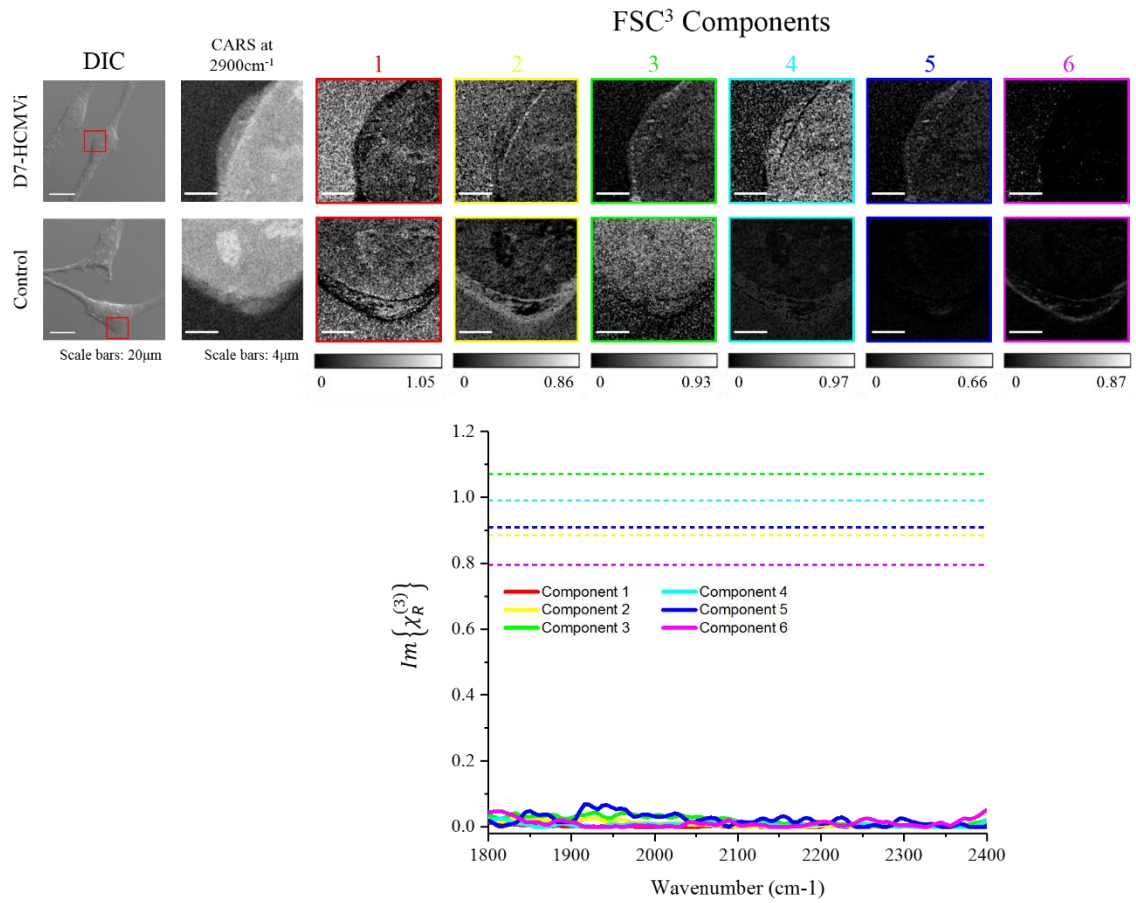

Figure 6.19 | Spatial and spectral FSC^3 outputs following application to hyperspectral CARS datasets acquired from perinuclear regions of HeLa cells which were exposed to 100 μM D7-HCMVi or a 50:50 water/methanol solution (vehicle control) for 24 hours. A spectral range of 1800-2400 cm^{-1} is utilised, and the spatially resolved images for each component, along with the associated spectra showing the phase-retrieved imaginary part of the normalised CARS susceptibility $Im\left\{\chi_R^{(3)}\right\}$ are displayed. The corresponding real parts are shown as averages, indicated by horizontal dashed lines. Component 1 shows a ubiquitous signal across its spatial images and no spectral features within its retrieved spectrum, thus it is considered to correspond to either aqueous medium (water) present both intracellularly and extracellularly, or background signal. The remaining components differ in their localisation of signal between the samples, and their retrieved spectra show no spectral features, hence they are considered to correspond to fluctuations in background signal. Full volume concentration ranges for each component across both samples are given by the grayscale values. DIC images show whole cells and the cytoplasmic regions selected for hyperspectral CARS acquisition, and single wavenumber CARS images enable identification of cellular features within fields of view. Scale bars show 20 μm in DIC images and 4 μm in FSC^3 images.

Figures 6.20 and 6.21 show the results of FSC^3 analysis of HeLa cells treated with D7-HCMVi, assessing the capability of the unsupervised algorithm to detect CARS signal corresponding to carbon-deuterium bond vibrations, thus enabling identification of the deuterium-labelled compound within a cell. HeLa cells were incubated in media supplemented with D7-HCMVi at a concentration of 100 μM for a total of 144 hours. The compound was initially dissolved in a 50:50 mixture of methanol and water to give a homogenous solution, which was then added to growth media at a final concentration of 100 μM. Cells were incubated in the compound-supplemented media for 96 hours, at which point the existing media was replaced with fresh compound-supplemented media at the same concentration. Cells remained in this media for a further 96 hours, before undergoing PFA-fixation and subsequent imaging by CARS microscopy. Vehicle control cells were incubated in media supplemented with the 50:50 mixture of methanol and water. CARS datasets were acquired from intracellular regions of compound-treated and untreated cells, as indicated by single wavenumber CARS images acquired at 2900 cm^{-1} showing whole cells, at two different Z-planes.

Figure 6.20 displays the spatially resolved FSC^3 images following application of the analysis algorithm to hyperspectral CARS datasets acquired within the cell-silent region of the Raman spectrum. The associated spectra for each identified component showing the phase-retrieved imaginary part of the normalised CARS susceptibility $Im\left\{\chi_R^{(3)}\right\}$ are also shown. The chemical composition within the selected field of view is assessed over the wavenumber range, 1600-2600 cm^{-1}, specifically targeted around the observed spectral peaks at 2063 cm^{-1}, 2126 cm^{-1} and 2228 cm^{-1} within the acquired spontaneous Raman spectrum in the previous section, providing direct comparison between D7-HCMVi-treated and vehicle control cells. The FSC^3 algorithm was run multiple times considering increasing numbers of components until spatial and spectral features were identified, which in this case required consideration of six independent components. Whilst one of the z-planes imaged from each field of view showed no clear spatial features within the displayed images in Figure 6.20, likely due to the focal point set above the cell oppose to inside it, the retrieved images in the other plane show signal at the nuclear envelope in some of the identified components. Importantly, differences in observed signal are apparent between components from the D7-HCMVi-treated cell and the vehicle control cell. In particular, Component 4 shows signal from the nuclear envelope region in the untreated cell, which is not observed from the corresponding region of the compound-treated cell, and Component 5 shows signal from the nuclear envelope region in the treated cell, which is absent from the untreated cell. In Component 4 from the compound-treated cell and Component 5 from the untreated cell, the nuclear envelope region shows a lower signal than the rest of the retrieved spatial image, appearing as a darker band. This occurs due to the nature of the FSC^3 algorithm, in which the sum

of the intensities of a single pixel across the spatial images from each component equals 1, meaning that a large observed signal in pixels of one component may cause the corresponding pixels to show a low intensity in another component. Component 6 also shows a difference in the observed signal within the nuclear envelope region between the compound-treated and vehicle control cell, though less clear than Components 4 and 5, whilst no such signal is observed within the remaining components, and differences are not observed between the D7-HCMVi-treated and vehicle control cell. Based on the ubiquitous distribution of signal within Components 1, 2 and 3, they are considered to show a background signal.

The associated spectra for each identified component, acquired within the cell-silent region of the Raman spectrum, are also shown in Figure 6.20, and retrieved spectra for Components 4 and 5 are also displayed separately for improved visualisation of spectral line-shapes. Only Component 5 shows features above background noise within its retrieved spectrum, possessing a visible peak at 2108 cm^{-1}, which is considered to correspond to CD-resonances based on the known absence of endogenous cell signal within the acquired spectral range. Whilst the spontaneous Raman spectrum acquired from the compound in powder preparation showed three CD-related peaks at 2063 cm^{-1}, 2126 cm^{-1} and 2228 cm^{-1}, as shown in Figure 6.5, a respective spectrum was not acquired from an aqueous sample of the compound, and consequently, it is not certain how similar the CD-associated peaks will appear in an aqueous environment. For the deuterium-labelled molecules described earlier in this chapter, multiple sharp peaks within the silent region of the powder Raman spectrum were often observed as single broader peaks within the respective spectra from aqueous solutions, and consequently this may account for the single peak observed within the retrieved spectrum.

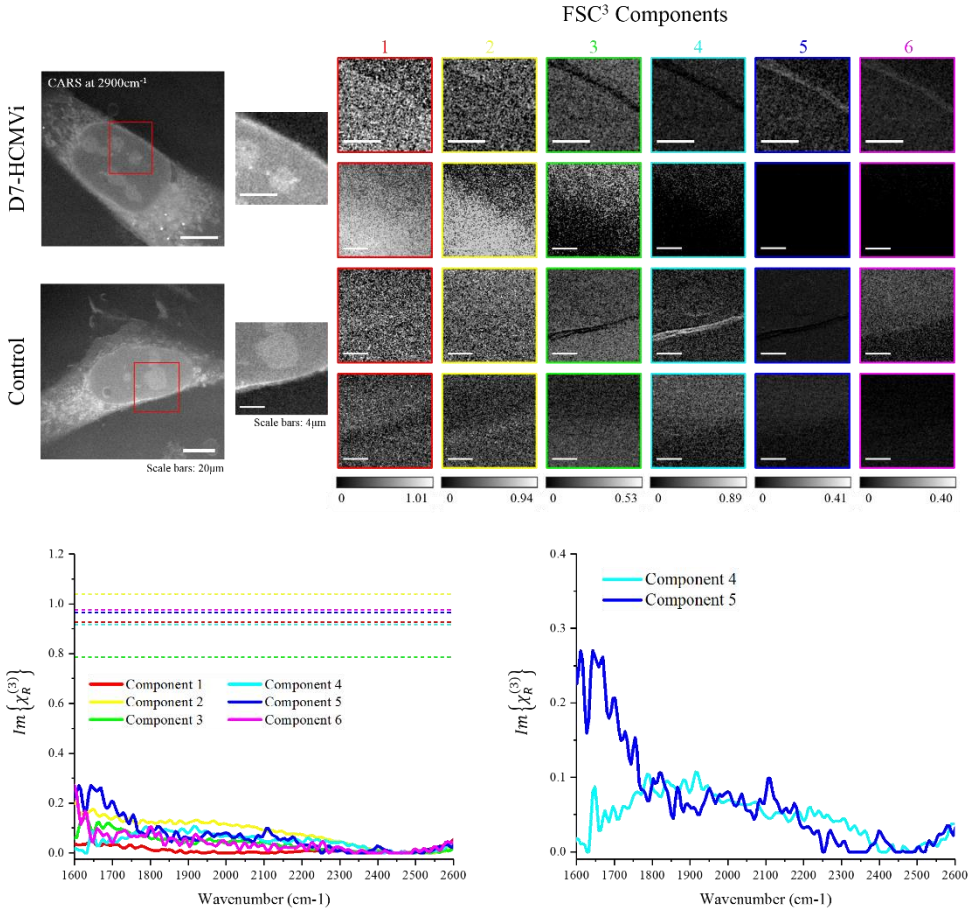

Figure 6.20 | Spatial and spectral FSC^3 outputs following application to hyperspectral CARS datasets acquired from perinuclear regions of HeLa cells which were exposed to 100 μM D7-HCMVi or a 50:50 water/methanol solution (vehicle control) for a total of 144 hours. A spectral range of 1600-2600 cm^{-1} is utilised, and the spatially resolved images for each component, along with the associated spectra showing the phase-retrieved imaginary part of the normalised CARS susceptibility $Im\left\{\chi_R^{(3)}\right\}$ are displayed. The corresponding real parts are shown as averages, indicated by horizontal dashed lines. Component 4 shows signal from the nuclear envelope region of the vehicle control cell, which is not observed from the corresponding region of the compound-treated cell, but its retrieved spectrum does not show any features, and thus attribution of the component to a specific chemical group is difficult. Component 5 shows signal from the nuclear envelope region in the D7-HCMVi-treated cell, which is absent from the vehicle control cell, and its retrieved spectrum shows a peak at ~ 2100 cm^{-1}. Thus, it is possible that this component corresponds to C-D bond vibrations, and consequently D7-HCMVi. The retrieved spectra from Components 4 and 5 are also plotted separately to the other retrieved spectra for clearer visualisation of line-shape (C). Component 6 also shows signal from the nuclear membrane region in the compound-treated cell but not the vehicle control cell but doesn't show a peak within its retrieved spectrum. Components 1, 2 and 3 show ubiquitous distribution of signal within their spatially resolved images and no spectral features within their retrieved spectra, hence they are considered to correspond to background noise. Full volume concentration ranges for each component across both samples are given by the grayscale values. DIC images show whole cells and the cytoplasmic regions selected for hyperspectral CARS acquisition, and single wavenumber CARS images enable identification of cellular features within fields of view. Scale bars show 20 μm in DIC images and 4 μm in FSC^3 images.

Figure 6.21 shows spatial and spectral FSC^3 outputs from the same hyperspectral CARS datasets, but over the reduced spectral range, 1900-2400 cm^{-1}, tightly focussed around the 2108 cm^{-1} peak observed in Figure 6.20, aiming to improve spectral resolution and further confirm the legitimacy of the peak above noise. Six separate chemical components were again considered in the FSC^3 algorithm, enabling identification of components showing spatially resolved features. Figure 6.21 shows the spatially resolved images from FSC^3 analysis and, as observed in the images in Figure 6.20, one of the z-planes shows no clear spatial features whilst the other shows signal within nuclear envelope regions, which again differ between the compound-treated and untreated cell. Components 3 and 4 show signal at the nuclear envelope in untreated samples, but not in the corresponding regions from cells treated with the compound, whilst Components 5 and 6 show signal at the nuclear envelope in compound-treated cells, whilst no comparable signal is observed in the respective components from untreated cells. The associated spectra for each of the components are also displayed in Figure 6.21 over the reduced spectral range, 1900-2400 cm^{-1}. Of the retrieved spectra from Components 5 and 6, which showed signal at the nuclear envelope of compound-treated cells, only that of Component 6 shows spectral features which may correspond to CD-associated resonances, with an observable peak at 2130 cm^{-1}, whilst the retrieved spectra from each of the other components fail to clearly identify spectral features above noise. The position of the peak within the Component 6 spectrum is slightly altered from its observed position in the retrieved spectrum for Component 5 in Figure 6.20, although the reasoning behind this is unclear. Furthermore, the observed fluctuations in intensity of spectra between 1900 cm^{-1} and approximately 2000 cm^{-1} are likely artefacts of the post-acquisition spectral processing procedures which are performed to give Raman-like spectra, as they are present in spectra from several of the components and were not present at this region in the retrieved spectra shown in Figure 6.20. Figure 6.21 also shows the retrieved spectrum for Component 6 plotted independently with the spontaneous Raman spectrum acquired from the compound in powder preparation overlaid, illustrating the similar positioning of the observed peak at 2130 cm^{-1} within the retrieved spectrum from Component 6 with the central CD-associated Raman peak at 2126 cm^{-1} within the powder Raman spectrum.

Based on the presence of a visible peak within the corresponding retrieved spectrum from the cell-silent region of the Raman spectrum, at a comparable position to that observed within the respective Raman spectrum, it is proposed that FSC^3 has successfully identified a chemical component corresponding to carbon-deuterium bond resonances at the nuclear envelope region, representing the exogenously applied D7-HCMVi. The presence of signal at the nuclear envelope region in absence of the deuterium-labelled compound suggests that FSC^3 has identified a component corresponding to an endogenous molecule located at the nuclear envelope of the cell,

despite not showing spectral features within the targeted wavenumber range. Thus, the identified component corresponding to the deuterium-labelled compound is considered to represent a combination of an endogenous molecule located at the nuclear envelope and D7-HCMVi within the same region, oppose to showing the deuterium-labelled compound alone. However, it cannot be overlooked that the intensity of the peak observed within the retrieved spectrum for Component 6 is very weak, with the other components which are considered to represent background noise showing similar intensities, and therefore the possibility that we may simply be observing a fluctuation in background noise cannot be ruled out.

Importantly, the results described in Figures 6.20 and 6.21 consist of preliminary data acquired from a single sample (n=1). When the experiment was later repeated, a potential CD-associated component similar to Components 5 and 6 in Figures 6.20 and 6.21, respectively, was not observed. It is unclear whether this was due to insufficient signal generation from D7-HCMVi in the repeat sample, or whether it implies that the observed spectral features within the cell-silent region in Figures 6.20 and 6.21 do not correspond to CD-associated signal. The difficulty in observing intracellular CARS signal following exposure of a second sample to D7-HCMVi can likely be attributed to the same factors as proposed for the other molecules investigated within this chapter, namely, a lack of accumulation of the molecule within a concentrated area or a deuterium label comprised of too few deuterium-containing bonds, both of which limit the coherent CARS signal generated. However, the reasoning as to why one sample would generate intracellular CD-associated signal whilst a second would not is more challenging to determine. As sample preparation and experimental procedures for the repeat sample were identical to those performed for the above described sample, the observed differences in results may be a result of heterogeneity between cells and associated variability in uptake, storage and turnover of biological and chemical molecules. Thus, further repeats of the experiment, with analysis of multiple cells from different sample sets will be required to provide definitive evidence that hyperspectral CARS and FSC^3 analysis can be successfully employed to observe D7-HCMVi within cells.

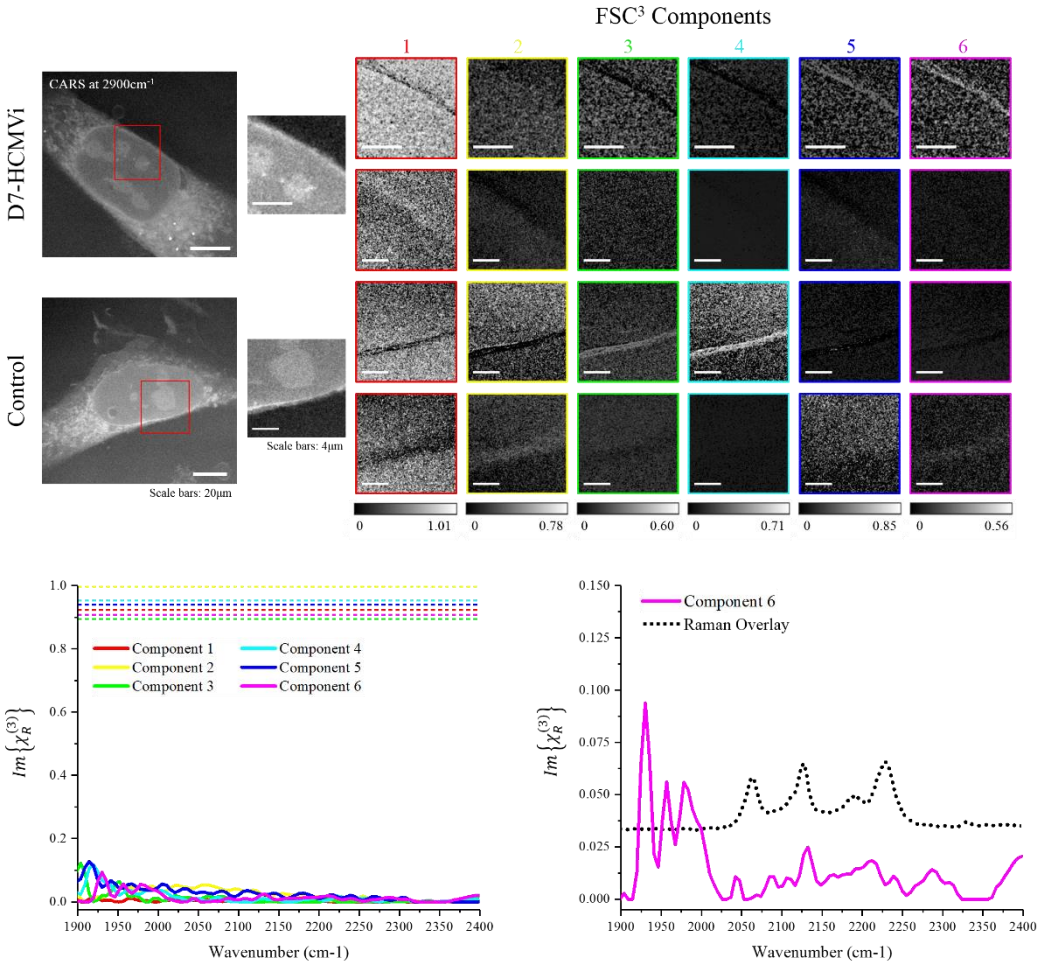

Figure 6.21 | Spatial and spectral FSC^3 outputs following application to hyperspectral CARS datasets acquired from perinuclear regions of HeLa cells which were exposed to 100 μM D7-HCMVi or a 50:50 water/methanol solution (vehicle control) for a total of 144 hours. A spectral range of 1900-2400 cm^{-1} is utilised, and the spatially resolved images for each component, along with the associated spectra showing the phase-retrieved imaginary part of the normalised CARS susceptibility $Im\left\{\chi_R^{(3)}\right\}$ are displayed. The corresponding real parts are shown as averages, indicated by horizontal dashed lines. Components 3 and 4 show signal from the nuclear envelope region of the vehicle control cell, which is not observed from the corresponding region of the compound-treated cell, but neither component shows spectral features within its retrieved spectra. Components 5 and 6 show signal from the nuclear envelope region in the D7-HCMVi-treated cell, which is absent from the vehicle control cell, and whilst the retrieved spectrum for Component 5 fails to show spectral features, the associated spectrum for Component 6 shows a peak at ~2130 cm^{-1}. The retrieved spectrum from Component 6 is also plotted individually with the CD-associated Raman peaks from D7-HCMVi in powder form (see Section 6.2) overlaid (C). Thus, it is possible that this component corresponds to C-D bond vibrations, and consequently D7-HCMVi. Components 1 and 2 show ubiquitous distribution of signal within their spatially resolved images and no spectral features within their retrieved spectra, hence they are considered to correspond to background noise. Full volume concentration ranges for each component across both samples are given by the grayscale values. DIC images show whole cells and the cytoplasmic regions selected for hyperspectral CARS acquisition, and single wavenumber CARS images enable identification of cellular features within fields of view. Scale bars show 20 μm in DIC images and 4 μm in FSC^3 images.

6.4. Summary

Within this chapter, the ability of FSC^3 data analysis to identify deuterium-labelled non-lipid-based biological molecules and small molecule compounds from hyperspectral CARS datasets has been assessed. A range of molecules were investigated which varied in their chemical structures, involvement in cellular processes and intracellular accumulation tendencies, whilst also presenting a range of different deuterium labelling configurations. Spontaneous Raman spectra were initially acquired from powder preparations of each molecule, as well as aqueous solutions of D5-Trp, D6-SA and D3-TPMP in water, providing information about their physical and chemical properties, importantly identifying the positions of CD-associated peaks within the silent region of the spectrum, which enabled informed selections of spectral ranges for hyperspectral CARS acquisition in following sections. Some of the compounds showed slight alterations in peak position when dissolved in an aqueous solution with water, for example, D5-Trp showed two CD peaks at 2268 cm^{-1} and 2290 cm^{-1} when imaged as a powder preparation, but only a single CD peak positioned at 2300 cm^{-1} when dissolved in water. It is possible that these changes in peak position result from interactions between the investigated molecules and water, or the underlying water signal may interfere with the spectrum from the investigated molecules, hence giving spectral alterations. As the molecules would be administered to cells dissolved in an aqueous solution, the corresponding spectra from dissolved molecules potentially provide a more representative reference for interpretation of hyperspectral CARS datasets in the subsequent sections. However, in general, the CD-associated peaks positions did not show a large amount of change, indicating that spectra from both powder and aqueous forms of the compounds provide useful information. This was important as Raman spectra were not acquired from aqueous preparations of D4-Para, D8-H2Ri, D9-COX2i and D7-HCMVi, and thus the spectra acquired from powder preparations were used for reference.

Hyperspectral datasets were acquired from cellular regions of deuterium-labelled compound-treated cells and FSC^3 data analysis was applied to identify and spatially resolve chemical components, which could be identified based on their retrieved spectra showing the phase-retrieved imaginary part of the CARS susceptibility. Generally, FSC^3 struggled to identify a chemical component corresponding to carbon-deuterium bond vibrations, and hence was unable to permit visualisation of the deuterium-labelled biological molecules and small molecule compounds within cells. D5-Trp and D4-Para both showed CD-associated peaks within their spontaneous Raman spectra that lay outside of the spectral range over which hyperspectral datasets were acquired and therefore, unsurprisingly, FSC^3 could not identify a chemical component corresponding to C-D bond vibrations from cells treated with either molecule. D6-SA

could also not be identified from hyperspectral datasets acquired from cytoplasmic regions of cells. Due to its involvement in the citric acid cycle and electron transport chain, it was hypothesised that D6-SA would be most abundant within mitochondria, however, in reality, the molecule was likely distributed throughout the whole cell, and this may have limited the CARS signal that could be generated. The molecule itself was fully deuterated, so the overall number of C-D bonds would not have been a limiting factor. Another consideration is the rate at which D6-SA is turned over by cells. Based on its metabolic function, D6-SA may be turned over rapidly and thus 24 hours may have presented too long an incubation period, as cells may have already turned over the deuterated carbohydrate by the time cells were fixed. D9-COX2i also failed to show detectable signal corresponding to C-D bond vibrations within the cell-silent region. Prior knowledge of the likely accumulation tendencies of D9-COX2i were limited and therefore a general cytoplasmic region was imaged. The inability to observe this deuterium-labelled compound may have been due to a ubiquitous distribution. The above samples were imaged individually, i.e. FSC^3 was applied to a small molecule compound-treated cell independently, identifying the most common spectra within the cell. Analysis of a larger number of deuterated compound-treated cells, as opposed to only a single cell, may have maximised the likelihood of identifying a CD-associated component, as the CD spectrum would have become more common across the samples, compared to the highly variable fluctuations in background noise.

The remaining three deuterium-labelled small molecule compounds, D8-H_2Ri, D7-HCMVi and D3-TPMP were analysed in combination with vehicle control cells, which received the equivalent volume of the solvent in which the compounds were dissolved (50:50 water/methanol for D8-H_2Ri and D7-HCMVi, water only for D3-TPMP). This permitted identification of the most common from both compound-treated and control cells, providing a direct comparison of chemical composition, however, it was possible that this made the CD spectra less common across the samples and therefore less likely to be identified by FSC^3. D8-H_2Ri could not be identified within cells, with the same possible reasoning as the previously described small molecule compounds – lack of accumulation or turnover before fixation. D3-TPMP was proposed as a highly suitable small molecule compound for CARS imaging based on its strong tendency to accumulate within mitochondria, which would maximise the coherent signal generated, however, FSC^3 analysis was unable to identify a chemical component corresponding to C-D bond vibrations. Mitochondria were initially visualised via their strong CARS signal from protein/lipid combinations, confirming that the optimal fields of view were selected and the CARS system was operating correctly. A possible limiting factor in the detection of C-D bond resonances is that the deuterium label comprises only a single CD_3 group within the D3-TPMP structure, as reflected by the low intensity of the peak observed in the spontaneous

Raman spectrum from D3-TPMP dissolved in water. Another potential reason for the lack of signal, which can be considered for all of the aforementioned small molecule compounds within this section, is loss of the deuterium-labelled compound from cells as a result of the transient permeabilisation of the plasma membrane associated with PFA-fixation. Hence, D3-TPMP-treated cells were also imaged live, however, due to not utilising a stage heater to prevent sample drift over the required acquisition time for hyperspectral CARS data generation, cells showed poor health and alterations in intracellular structure, and as a result, D3-TPMP may still have been lost from cells. Furthermore, to address the issue of possible turnover of the deuterated compound within the incubation time, HeLa cells were again imaged live following a 3h exposure to D3-TPMP, however, a CD-associated signal could still not be identified by FSC^3.

D7-HCMVi was the only deuterium-labelled small molecule compound to show any signs of intracellular visualisation by FSC^3 analysis. Despite cells which were exposed to D7-HCMVi for a 24-hour time-period showing no CD-associated signal, preliminary data from cells incubated with the compound for 144 hours showed a chemical component with a peak at ~ 2100 cm^{-1} within its retrieved spectrum. The spatially resolved image accompanying this spectrum showed CARS signal within a nuclear envelope region of the cell in D7-HCMVi-treated samples but not vehicle controls. Further investigation of this region via FSC^3 analysis performed over a reduced spectral range showed a CD-associated peak at 2130 cm^{-1}, which aligned with one of the peaks within the spontaneous Raman spectrum from a powder preparation of D7-HCMVi. However, it cannot be overlooked that the observed signal for the identified CD-associated component in the FSC^3 analysis is very weak, with intensities comparable to those observed for other small molecules described within the section, which were considered to represent featureless, background noise. Hence, there is still a possibility that this peak may simply be a variation in the background noise signal. Furthermore, it is unclear as to why only a single peak was observed in the retrieved spectrum for the identified FSC^3 component, as opposed to the four that were observed in the Raman spectrum from D7-HCMVi in powder form, although a number of potential explanations could be suggested. Firstly, a spontaneous Raman spectrum was not acquired from an aqueous solution of D7-HCMVi and thus it is not known whether alterations in peak position would have been observed, as they were for some of the other investigated molecules. Merging of CD-associated Raman peaks has been observed for D5-Trp and D4-/D6-SA when dissolved in water, hence this may also be observed for D7-HCMVi, explaining why only a single peak was observed. Secondly, FSC^3 may have separated out the CD peaks into multiple components and the other peaks may have not been identified, or thirdly, the compound may have been metabolised by cells, and the resulting metabolites which were detected by hyperspectral CARS and FSC^3 may have shown peaks that varied from those shown by pure D7-

HCMVi. It should also not be overlooked that these results consisted of preliminary data only, and a repeat of the experiment failed to generate comparable results. Thus, further analysis of multiple cells from various sample sets is necessary to conclusively prove or disprove the ability of hyperspectral CARS and FSC^3 data analysis to visualise D7-HCVi within cells.

Overall, although FSC^3 analysis has shown signs of being able to identify and spatially resolve a chemical compound corresponding to D7-HCMVi, in general, the ability of FSC^3 data analysis to visualise a deuterium-labelled small molecule compound within a cell has not been proven.

7. INVESTIGATION INTO NONLINEAR IMAGING CAPABILITIES ACROSS THREE GSK-ASSOCIATED SYSTEMS

7.1. Introduction

Development of state-of-the-art imaging systems is being driven by ongoing work within research institutes, and the emerging technologies are being implemented within the industrial environment, where the decision often needs to be made as to whether there is more benefit in collaborating with an academic partner or investing in commercially available systems. In light of this, this chapter describes the evaluation of nonlinear imaging capabilities of three GSK-associated imaging systems, two of which were developed in academic centres at Cardiff University and the Beckman Institute, University of Illinois Urbana-Champaign (UIUC), and hence featured multimodal capabilities to maximise the data outputs from investigated samples, whilst the other system was commercially available from Leica and was capable of hyperspectral CARS and SRS, as well as TPF, whilst being accessible to all users. Furthermore, by assessing the potential for identifying signal from a deuterium label across multiple systems, the transferability of the technology was also evaluated. The Cardiff system featured hardware optimisation which permitted strong signal generation within the cell-silent region, however neither of the other investigated systems had been optimised specifically for imaging within this region, and hence it would be interesting to observe whether substantial signal could still be generated.

7.1.1. Beckman Institute, University of Illinois Urbana-Champaign

Within the GSK Centre for Optical Molecular Imaging (COMI) at the Beckman Institute, UIUC, two custom-built imaging systems were utilised, the first of which was a multimodal system set up for label-free imaging of live samples, whilst the second was an exclusively nonlinear system, showing CARS and SRS capabilities. In the first system, single wavenumber CARS was implemented specifically to image lipids (targeted at 2850 cm^{-1}), and the focus was on combining CARS with other imaging modalities to provide comprehensive chemical assessment of a range of cell and tissue samples. The layout of this system can be found in ref [228–231]. A tuneable Ti:Sa laser (Mai Tai HP, Spectra Physics) provided 100 fs pulses with a bandwidth of 10 nm at a centre wavelength of 730-1000 nm, permitting extensive multimodal capabilities,

including two-photon excitation (2PE/TPF), three-photon excitation (3PE), SHG, THG, FLIM and CARS (detected in epi direction). However, based on the type of samples being investigated and the time constraint of this aspect of the project, only CARS and FLIM were employed. The excitation wavelength for FLIM was 730 nm, and signal was detected by a 16-channel PMT spectrometer (PML-16-C; Becker-Hickl, Berlin, Germany). Subsequent analysis was performed using SPCImage software (Becker-Hickl). The biexponential fluorescence decay model was fit to the recorded dataset at each pixel to acquire the four following parameters: total FLIM intensity; fluorescence lifetime of protein bound NADH; fluorescence lifetime of free NADH; and mean fluorescence lifetime.

Conversely, the second system provided both CARS and SRS modalities extending over the full spectral range, and ongoing developments aimed to progress the technologies within the system to permit hyperspectral imaging, although over a narrower spectral bandwidth compared to that utilised within the Cardiff system. However, this system was still in the early stages of development, and thus the primary focus was upon efficient signal generation and, for CARS, non-resonant background minimisation. Consequently, the system was not yet in a position to generate advanced hyperspectral CARS datasets with the same level of chemical information as the Cardiff system, however the potential for hyperspectral CARS and SRS was proven. An attractive feature of this COMI system was the ability to acquire CARS and SRS on the same system with the requirement of only minor adjustments.

7.1.2. Leica TCS SP8 CARS microscope (GlaxoSmithKline)

A commercially available CARS/SRS microscope was purchased from Leica (Leica TCS SP8 CARS microscope) which could generate high resolution, hyperspectral CARS and SRS images. Unlike the custom-built systems that have been developed at both Cardiff University and within the COMI at the Beckman Institute, which required a detailed understanding of the involved optical processes and hence trained personnel to operate them, this system was designed to provide a resource which was not limited to users with a vibrational imaging background. However, the inability to modify the internal optics limited the freedom with which the system could be expanded with further modalities incorporated (in addition to CARS, SRS and TPF which the system offered).

7.1.3. Sample set

To conduct the cross-site analysis, a set of biological samples was prepared which well-reflected the capabilities of the multimodal imaging capabilities of the system in Cardiff University's School of Biosciences. As described in Chapters 4 and 5 of this thesis, deuterium-labelled lipids could be effectively imaged by CARS, and therefore provided a suitable proof-of-concept molecule to assess the ability of each system for visualising a deuterated molecule within a cell. However, as observed in Chapter 6, deuterium-labelled compounds could not be imaged with the same effectiveness, and difficulty in achieving sufficient CARS signal above noise was apparent. Therefore, cells samples treated with deuterated small molecule compounds were also included in the sample set, investigating whether other systems with slightly different configurations and modalities may show greater success in visualising deuterium-labelled small molecule compounds. Specifically, three compounds were selected: D7-HCMVi, based on the observed chemical component considered to correspond to C-D bond vibrations (as discussed in Section 6.3.7 of Chapter 6); D8-H_2Ri, based on the presence of both C-D bonds and a C≡C bond within its structure and the large peak observed within the silent region of its spontaneous Raman spectrum; and D3-TPMP, based on its reported mitochondrial accumulation. Lipid-treated samples were prepared using the same method that was employed within Chapters 4 and 5, as outlined in Section 3.3.2 of Chapter 3. HeLa cells were initially depleted of their lipid droplets for 18 hours before treatment with either deuterated or non-deuterated fatty acid for a further 18 hour, followed by PFA-fixation. As in Chapter 4, OA-, D17-OA-, LA-, D11-LA-, LNA- and D14-LNA-treated samples were prepared. Compound-treated samples were prepared using the same method that was employed within Chapter 6, as outlined in Section 3.3.3 of Chapter 3. D7-HCMVi-, D8-H_2Ri- and D3-TPMP-treated cells were incubated with the deuterium-labelled compound for 24 hours, after which time they were PFA-fixed. In addition to this, live cells were also utilised for multimodal imaging, which were cultured and treated with deuterium-labelled compounds on-site using the same methods described in Sections 3.3.1 and 3.3.3 in Chapter 3.

7.2. Deuterium-labelled fatty acids

For assessment of the COMI capabilities for observing deuterated fatty acids within cells, the CARS/SRS system was utilised. Figure 7.1 provides an overview of the early-stage imaging capabilities of the custom-built CARS/SRS system within the COMI at the Beckman Institute. Single wavenumber CARS images were acquired from PFA-fixed, D11-LA-treated HeLa cells at 2125 cm^{-1} and 2850 cm^{-1}, targeting C-D and C-H bonds, respectively. A similar single

wavenumber CARS image acquired from PFA-fixed, D11-LA-treated HeLa cells at 2850 cm^{-1} using the Cardiff system was included for comparison. As described in Chapter 4, due to D11-LA not showing a fully deuterated structure, signal was present within both cell-silent and CH-stretch regions of the Raman spectrum, hence lipid droplets could be observed in images acquired at both wavenumbers using the COMI system. This indicated that deuterium-labelled droplets could be visualised within cells through single wavenumber CARS. Comparison between the single wavenumber CARS images acquired using the Cardiff system and the COMI system showed comparable signal intensity, although the Cardiff system was able to achieve a higher spatial resolution. The possibility of hyperspectral CARS and SRS was also shown, with spectra acquired from a pure droplet of D11-LA, however, implementation of this modality involved the manual changing of the target wavenumber. Further development of this system will enable this to become automated, speeding up the process greatly, thus enabling more spectral steps to be included, which will improve the spectral resolution. As observed within Chapter 4, spectra which are retrieved through FSC^3 analysis show comparable line-shapes to spontaneous Raman spectra, however the SRS spectrum shown in Figure 7.1, which should give a spectral shape similar to that of the Raman spectrum, failed to identify the sub-peaks that were visible within the spontaneous Raman spectrum, although both SRS and spontaneous Raman peaks are centred at the same wavenumber. The spectrum produced by hyperspectral CARS showed a distorted peak shape compared to that of SRS and spontaneous Raman due to a lack of available spectral processing procedures to suppress the non-resonant contribution. Therefore, application of FSC^3 analysis to hyperspectral CARS datasets acquired using COMI system may be possible.

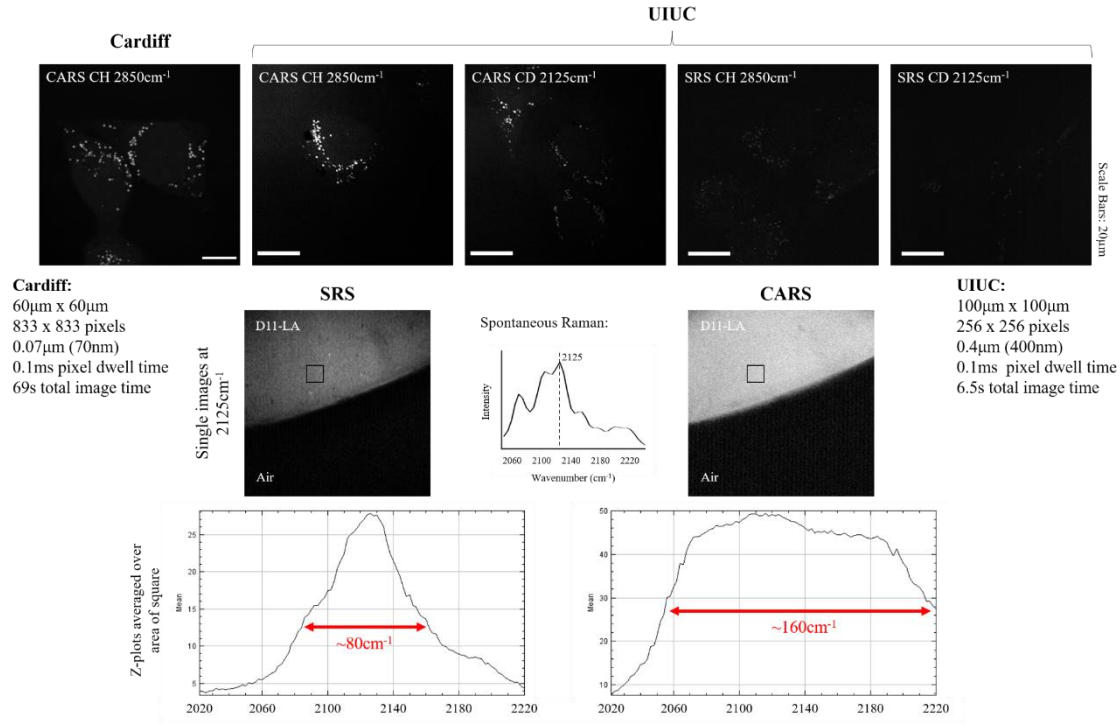

Figure 7.1 | Overview of CARS and SRS imaging capabilities of the COMI system for imaging D11-LA-treated HeLa cells. Single wavenumber CARS and SRS images are shown at 2125 cm^{-1} and 2850 cm^{-1}, targeting C-D and C-H bond vibrations, respectively. A similar single wavenumber CARS image acquired at 2850 cm^{-1} is shown as a comparison. Evidence for hyperspectral CARS and SRS capabilities is also shown with spectra obtained from a droplet of pure D11-LA, and a spontaneous Raman spectrum over the same wavenumber range is shown for comparison of line-shape. Scale bars in single wavenumber CARS images show 20 μm.

Figure 7.2 shows the hyperspectral CARS and SRS datasets acquired from HeLa cells treated with OA, D17-OA, LA, D11-LA, LNA and D14-LNA. Like the Cardiff system, the Leica TCS SP8 microscope provided broadband hyperspectral capabilities, permitting image acquisition over the full range of the Raman spectrum. For observation of both cell-silent and CH-stretch regions by CARS, a single filter was employed, which permitted imaging from 2000 cm^{-1} to 3200 cm^{-1}, incorporating both CD- and CH-associated peaks, whilst SRS permitted imaging over the entire range of Raman spectrum. However, to prevent excessively long integration times, hyperspectral images were acquired over narrower spectral ranges, targeted around the CD and CH peaks. The imaging configuration settings for acquisition of the data displayed in Figure 7.2 are shown in Table 7.1. For CD peak targeting, a spectral range of 835-855 nm (1999-2279 cm^{-1}) was utilised for both CARS and SRS imaging, and for CH peak targeting, the spectral ranges, 780-810 nm (2648-3123 cm^{-1}) and 780-800 nm (2803-3123 cm^{-1}) were utilised for CARS and

SRS imaging, respectively. CARS spatial images are shown at 2100 cm^{-1} and 2850 cm^{-1}, displaying CD- and CH-associated signal, respectively, whilst SRS spatial images are shown at ~ 2120 cm^{-1} and 2865 cm^{-1}, also displaying signal from C-D and C-H bond vibrations, respectively. CARS and SRS spectra for the full imaged spectral range were obtained from lipid droplet regions of the cells, as indicated in the zoomed images.

Signal from C-H bonds was clearly visualised within spatial images from all samples imaged using both CARS and SRS. The corresponding spectra within the CARS images showed distorted line-shapes due to contribution from the non-resonant part of the CARS susceptibility, hence there was a necessity for development of spectral processing methods to generate more Raman-like spectra, which would enhance interpretation of the hyperspectral CARS data. As SRS signal does not contain a non-resonant contribution, the spectral line-shapes appeared comparable to those of spontaneous Raman. The absence of non-resonant background could be observed in the spatially resolved SRS images, which showed a much higher contrast between lipid droplets and the rest of the image compared to the spatially resolved CARS images. Differences in peak shape were observed for droplets within each of the deuterated and non-deuterated fatty acid-treated cells. For all three fatty acids, both CARS and SRS spectra showed a reduced intensity for the deuterated fatty acid-treated cells owing to a reduced total number of C-H bonds as a result of deuterium incorporation. Furthermore, as the degree of unsaturation increased, the intensity of the peak at ~ 3010 cm^{-1} was seen to increase due to its attribution to stretching of =CH bonds, and this can be observed in both CARS and SRS data.

Signal from C-D bonds was less clear in both CARS and SRS images. By CARS, lipid droplets from cells treated with D17-OA and D14-LNA could be visualised, and this was reflected by differences in the shapes of their corresponding spectra compared to those from cells treated with the equivalent non-deuterated fatty acid isoforms. In contrast, such signal was not observed within the 2100 cm^{-1} image from D11-LA-treated cells, and no spectral differences were observed between its CARS spectra and that from LA-treated cells. Similar to the CH-associated peaks, the identified spectral features in the spectra from D17-OA- and D14-LNA-containing lipid droplets show distorted line-shapes due to a non-resonant background contribution, which limits interpretation of the data. This is limited further by the positioning of the lower limit of the filter at ~ 2000 cm^{-1}, which is very close to the position of the CD-associated peak. Within hyperspectral SRS, the CD-associated peaks for each of the deuterium-labelled fatty acids are much clearer as the spectral range is not confined to the limitations of the same filter, and the background levels are much lower. This is also reflected in the spatially resolved images, which all show visible CD-associated signal at ~ 2120 cm^{-1}. In chapter 4, the ability of the Cardiff system to identify differences in the CD peak shape was described, where a sub-peak was visible to the left of the

main peak in retrieved spectra for D17-OA and D11-LA chemical components, but was absent from the corresponding spectra for a D14-LNA component. This variation in CD peak shape can also be observed within the SRS spectra from the cell-silent region in Figure 7.2, indicative of the high spectral resolution offered by the Leica system.

A

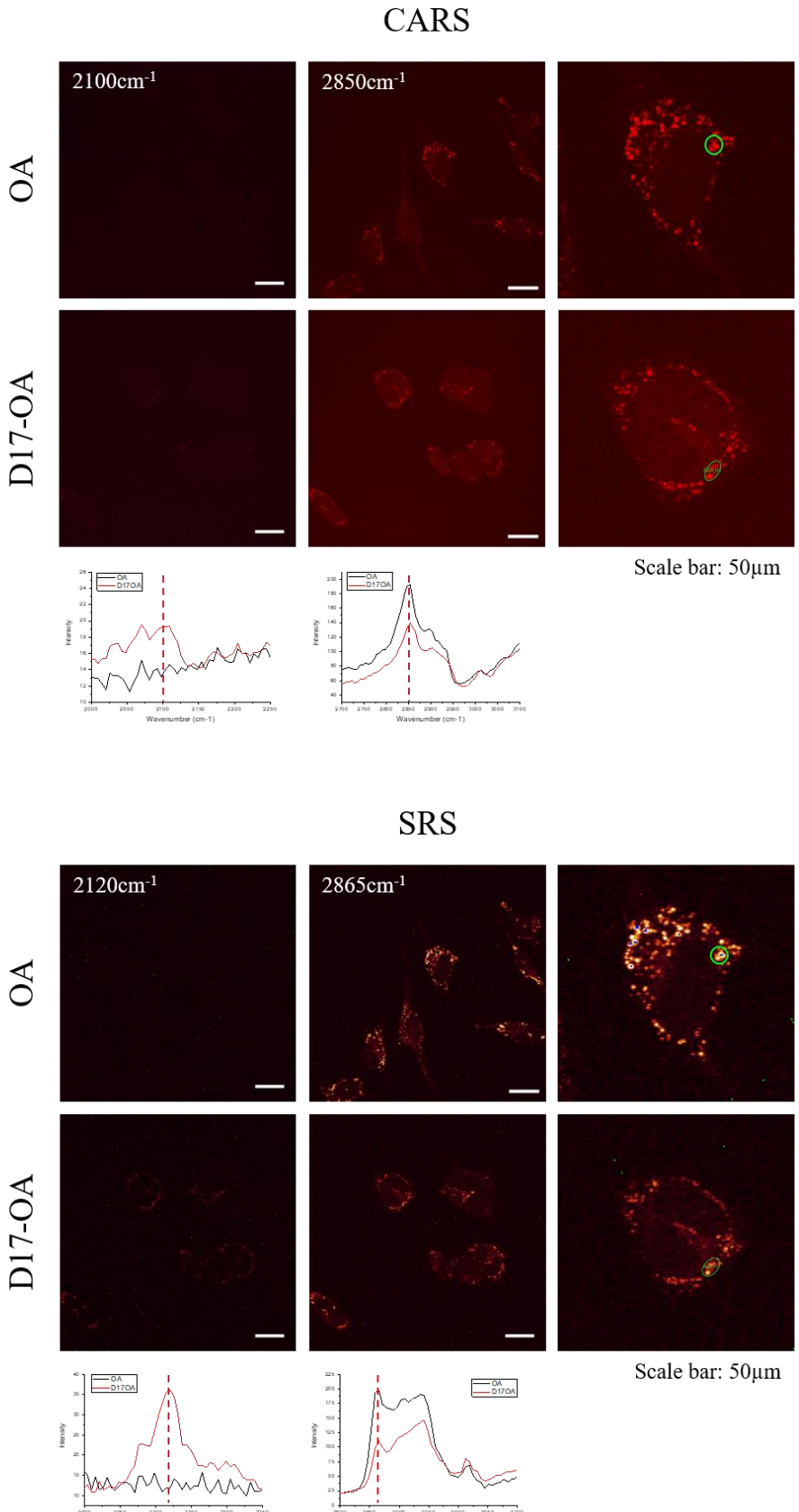
CARS
2100cm-1
2850cm-1
OA
D17-OA
Scale bar: 50µm
SRS
2120cm-1
2865cm-1
OA
D17-OA
Scale bar: 50µm

B

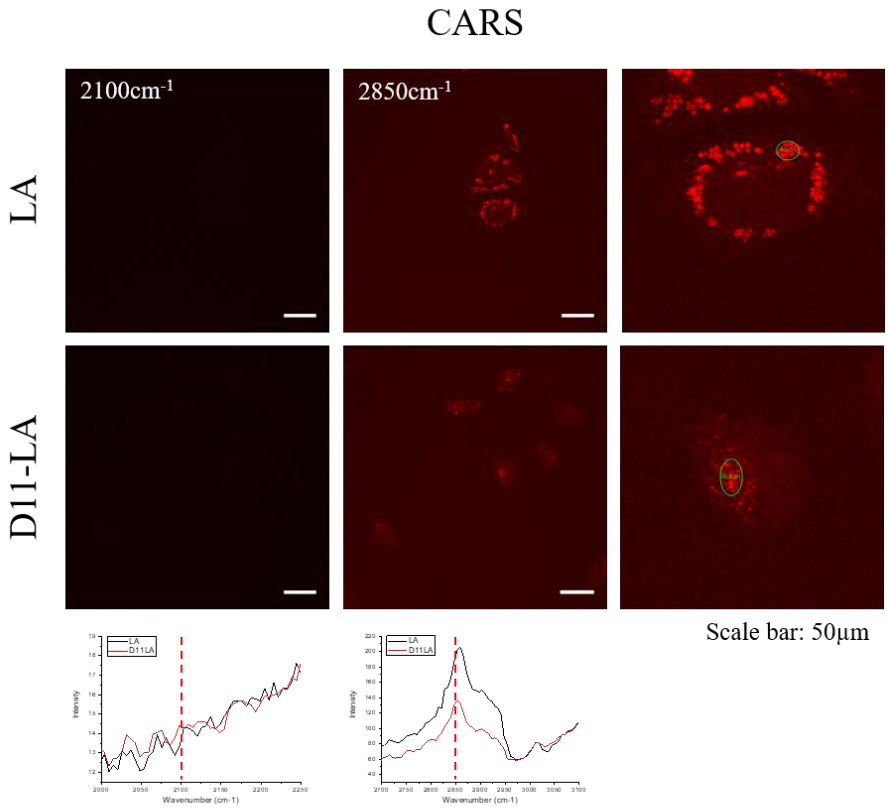
CARS
2100cm-1
2850cm-1
LA
D11-LA
Scale bar: 50µm
LA
D11LA
Intensity
Wavenumber (cm-1)
SRS
2125cm-1
2865cm-1
LA
D11-LA
Scale bar: 50µm
LA
D11LA
Intensity
Wavenumber (cm-1)

C

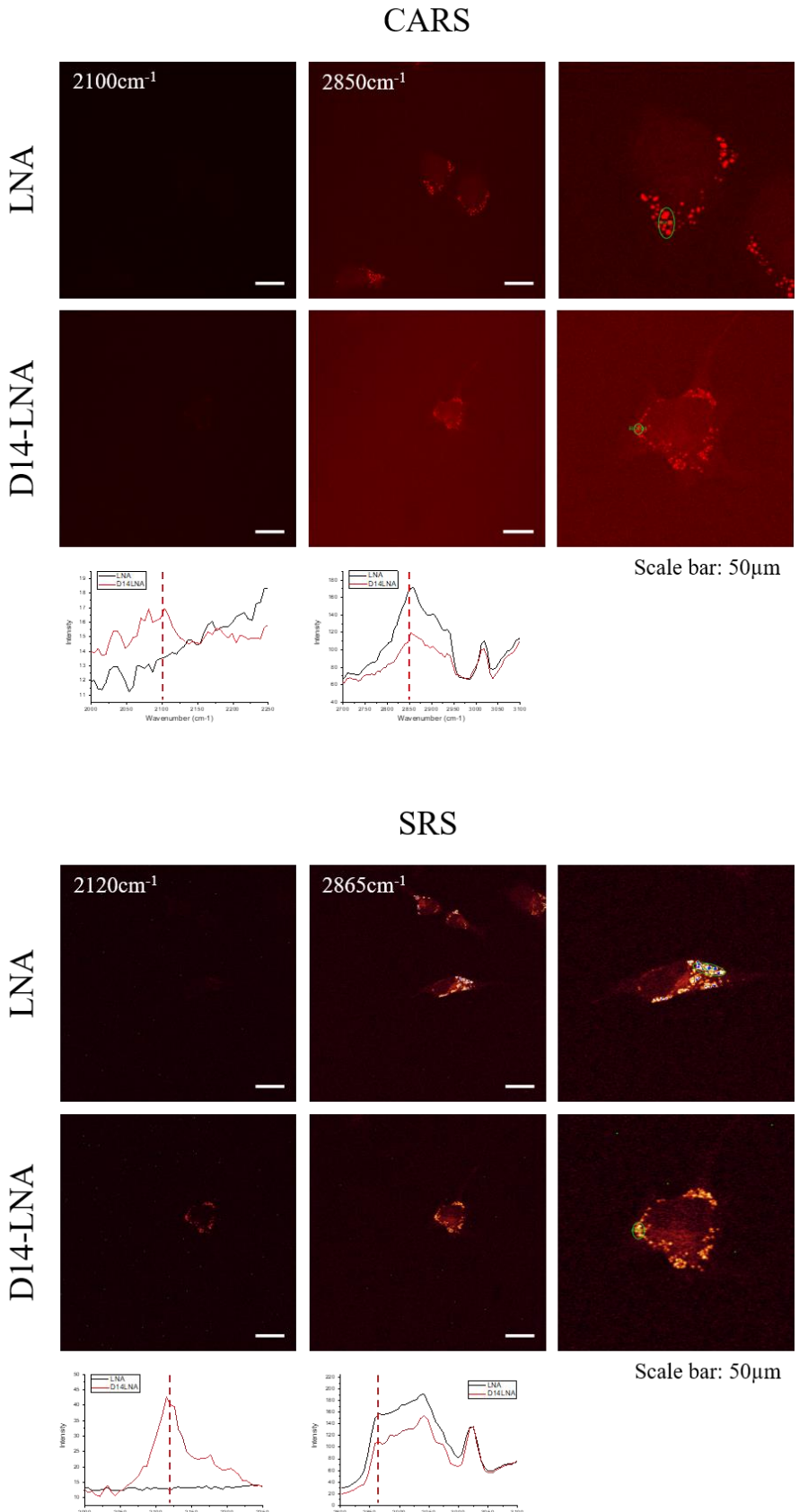
CARS
2100cm-1
2850cm-1
LNA
D14-LNA
Scale bar: 50μm
LNA
D14LNA
Intensity
Wavenumber (cm-1)
SRS
2120cm-1
2865cm-1
LNA
D14-LNA
Scale bar: 50μm
LNA
D14LNA
Intensity
Wavenumber (cm-1)

Figure 7.2 | Hyperspectral CARS and SRS imaging of OA- and D17-OA-treated HeLa cells (A), LA- and D11-LA-treated HeLa cells (B) and LNA- and D14-LNA-treated HeLa cells (C) by the Leica TCS SP8 CARS microscope. Spatial images are shown at CD-associated resonances (2100 cm^{-1} for CARS; ~ 2120 cm^{-1} for SRS) and CH-associated resonances (2850 cm^{-1} for CARS; 2865 cm^{-1} for SRS). Associated spectra for the full hyperspectral range (2000-2250 cm^{-1} for CD; 2800-3100 cm^{-1} for CH) are obtained from lipid droplet regions of cells, indicated in zoomed images. Scale bars shown 50 μm.

Table 7.1 | Configuration settings used for acquisition of CARS and SRS images in Figure 7.2.

	CARS	**SRS**
Image size	232.5 x 232.5 μm 512 x 512 pixels	
Pixel dwell time	1.2 μs	
No. of frame averages	1	8
Pump wavelength	CH: 780-810 nm 2648-3123 cm^{-1} CD: 835-855 nm 1999-2279 cm^{-1}	CH: 780-800 nm 2803-3123 cm^{-1} CD: 835-855 nm 1999-2279 cm^{-1}
Pump power	0.3 W	0.15 W
Stokes wavelength	1031.2 nm	
Stokes power	0.3 W	
Total acquisition time	CH: 15 mins CD: 9 mins	CH: 18 mins CD: 17 mins

7.3. Deuterium-labelled small molecule compounds

For assessment of the COMI capabilities for investigating deuterium-labelled small molecule compounds within cells, the multimodal system was employed. Along with assessing the ability of the system to identify deuterium-labelled compounds within cells, the potential application of the multimodal capabilities of the system were also explored. Specifically, FLIM was utilised in combination with single wavenumber CARS, targeting both C-H and C-D bond vibrations. FLIM, like CARS, is a label-free imaging technique which provides information about the metabolic activity of cells through comparison of the amounts of protein-bound and free NADH, determined by their different fluorescence lifetimes, as described in Chapter 1. Hence, if CARS could be used to visualise distribution or accumulation of a small molecule compound within a cell, FLIM could provide complimentary information regarding the resulting metabolic implications. Figure 7.3 shows multimodal CARS and FLIM images acquired from live HeLa cells treated with non-deuterated TPMP, D3-TPMP, D7-HCMVi and D8-H_2Ri and untreated controls. The datasets shown in Figure 7.3A and 7.3B were acquired independently from one another, and therefore the intensities of the treated and untreated cells within the same dataset are relative to each other. Images in Figure 7.3A should consequently be considered separately to those in Figure 7.3B. Single wavenumber CARS images are provided targeting both CD- and CH-associated resonances.

Figure 7.3A shows the multimodal CARS/FLIM data acquired from TPMP- and D3-TPMP-treated live cells, as well as untreated control cells. Within the CD-targeted images, some signal can be observed, however this is likely to correspond to non-resonant background. In the lower image, some features are visible, however they can also be seen at identical positions within both the CH-targeted CARS image and the FLIM images, and thus, the signal is considered to correspond to an artefact of the sample. The CH-targeted CARS images show the intracellular distribution of lipid droplets. The total number of droplets appears to be increased within the two small molecule compound-treated samples compared to the control cells, which may be indicative of a cellular response to deuterated and non-deuterated isoforms of TPMP. Generally, the FLIM images show reduced lifetimes in the compound-treated cells compared to the control cells, indicated by a darker blue colour. This suggests that more free NADH is present, which may indicate less mitochondrial activity.

Figure 7.3B shows multimodal CARS/FLIM data acquired from D7-HCMVi- and D8-H_2Ri-treated live cells, as well as untreated control cells. CARS images targeting both C-D and C-H bonds fail to show genuine signal, and instead appear to show interference with the glass of the coverslip, which may be a result of either incorrect z-positioning or too high a gain setting on

the PMT. In contrast to the FLIM images shown in Figure 7.3A, the images in Figure 7.3B show increased fluorescence lifetime within compound-treated cells, indicated by a stronger red colour, which may suggest more bound NADH within mitochondrial regions, and hence increased metabolic activity in response to the compounds.

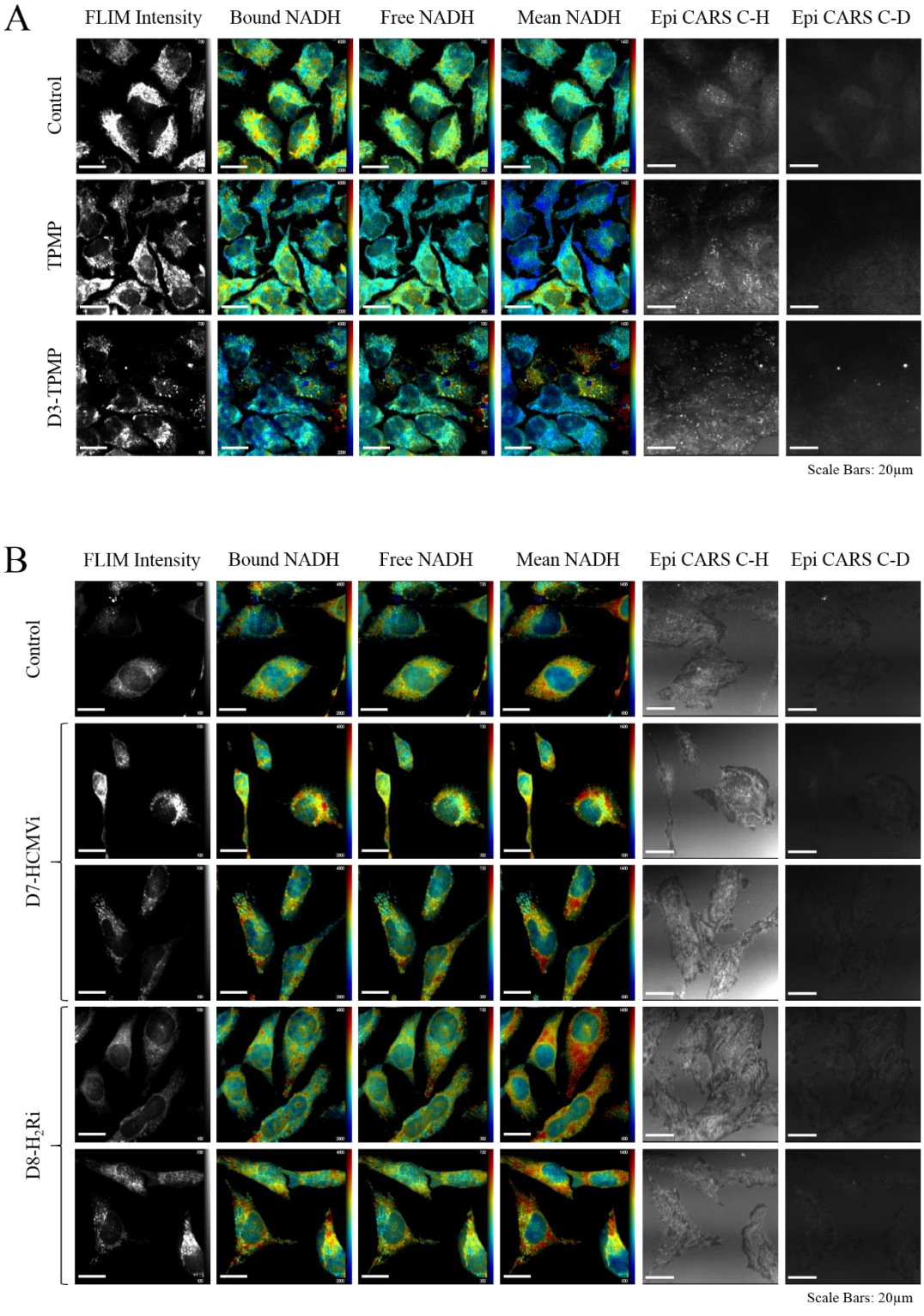

Figure 7.3 | Multimodal CARS and FLIM datasets acquired from TPMP/D3-TPMP-treated live HeLa cells and corresponding untreated controls (A), and D7-HCMVi- and D8-H2Ri-treated live HeLa cells and corresponding untreated controls (B). Intensities are relative to samples within each dataset, and therefore should be considered separately. Four FLIM parameters are shown: total FLIM intensity; fluorescence lifetime of protein bound NADH; fluorescence lifetime of free NADH and mean fluorescence lifetime. Epi-detected CARS images targeted at C-D and C-H bonds are also shown. Scale bars show 20 μm.

7.4. Summary

Table 7.2 summarises the nonlinear and multimodal capabilities of each system, as well as the deuterium-labelled molecules which have been investigated with each. All three systems can achieve single wavenumber and hyperspectral CARS and SRS, however the COMI system is still in its early stages of development and therefore cannot currently achieve the same level of spectral resolution as the other two systems. Furthermore, the deuterium-labelled fatty acids could be visualised using all three systems, hence confirming its transferability. The CARS capabilities shown by both the COMI system and the Leica system are limited by the fact that there are no associated spectral processing or data analysis procedures in place which can convert the distorted spectra into more Raman-like spectra, hence limiting interpretation and preventing quantitative imaging. However, the FSC^3 data analysis algorithm, which has been described and demonstrated extensively throughout this thesis, has been developed as a transferable tool which can be applied to any hyperspectral dataset, that is, a series of XY images acquired at regular intervals over a range of wavenumbers. Thus, application of the image analysis methodology to hyperspectral data acquired from both the COMI system and the Leica system should be possible, and hence this is an area which warrants further exploration in order to maximise the combined outputs across the multiple imaging systems. The FSC^3 analysis algorithm is compatible with a range of file types, including .tif files, which are a common format by which image data is stored across a variety of hardware systems. Both the COMI and Leica system can generate data outputs with the .tif file type, thus, software compatibility should not present an obstacle to the transferability of FSC^3. With regards to image acquisition, single spectra from both water and glass should be acquired with the same hardware settings and a water/glass spectrum should be generated for use at the CARS ratio calculation stage of HIA analysis (see Section 3.7.3 of Chapter 3 for HIA overview). Imaged fields of view should contain an extracellular region with water/imaging solution only from which the CARS ratio can be calculated.

The SRS outputs of the Leica system are comparable to the CARS outputs from the Cardiff system. This indicates that by applying spectral processing procedures and FSC^3 analysis to hyperspectral CARS datasets, the Cardiff system can achieve outputs providing an equal level

of spatial resolution and chemical specificity to SRS, which has become a more favoured nonlinear methodology in recent years. The Leica system has not been designed for targeted imaging within the cell-silent region, with the lower limit of the CH-stretch filter and the upper limit of the fingerprint region filter located at 2000 cm^{-1}, close to the location of the CD-associated peak. This limits the interpretation of CARS data, but as SRS does not require use of these filters, it can still be employed for effective cell-silent region imaging.

FLIM provides an interesting modality which is not offered by the Cardiff system. Clear differences were visible between compound-treated cells and untreated cells, with TPMP and D3-TPMP inducing a reduction in metabolic activity, given by an increase in signal corresponding to free NADH, whilst D7-HCMVi and D8-H2Ri caused an increase in metabolic activity. Support for the observed FLIM results for TPMP- and D3-TPMP-treated cells is provided in literature, where TPMP has been shown to inhibit the citric acid cycle enzyme, 2-oxologlutarate dehydrogenase[201], which provides a plausible explanation for the reduced metabolic function within treated cells. Whilst such convincing evidence does not exist to support the observed results for D7-HCMVi- and D8-H2Ri-treated cells, it can be considered that the cells increase their metabolic rate as a compensatory mechanism in response to these small molecule compounds. However, the sole purpose of this limited study was to evaluate the cross-compatibility of imaging techniques and not a detailed investigation into the effects of the deuterium-labelled compounds on metabolism.

Overall, each of these systems shows advantages over the others. The Leica system offers user-friendly imaging and does not require specialist training, but this comes at the expense of multimodal capabilities. In comparison, the range of modalities offered by the COMI system surpasses both the Cardiff and Leica systems, however for specific nonlinear-based imaging the Cardiff system appears to provide superior data outputs.

Table 7.2 | Summary of nonlinear and multimodal capabilities of each of the three systems with inclusion of successfully imaged deuterium-labelled molecules by each.

		Cardiff	**COMI**	**GSK**
Spontaneous Raman		✓	✓	×
Single Wavenumber CARS	CH	✓	✓	✓
	CD	✓	✓	✓
Hyperspectral CARS	CH	✓	✓*	✓
	CD	✓	✓*	✓
Single Wavenumber SRS	CH	✓	✓	✓
	CD	✓	✓	✓
Hyperspectral SRS	CH	✓	✓*	✓
	CD	✓	✓*	✓
Data Analysis		FSC^3 – quantitative spatial and spectral output	Non-quantitative spatial and spectral output, but compatible with FSC^3	Non-quantitative spatial and spectral output
Multimodal Capabilities	CARS	✓	✓	✓
	SRS	✓	✓	✓
	Raman	✓	×	×
	2PE	✓	✓	✓
	3PE	×	✓	×
	SHG	✓	✓	×
	THG	×	✓	×
	DIC	✓	×	×
	FLIM	×	✓	×
Deuterated Fatty Acids		✓	✓	✓
Deuterated Small Molecule Compounds		?	×	×

*Modality present but further optimisation required

8. CONCLUSIONS AND PERSPECTIVES

The main aim of the research described within this thesis was to evaluate the potential application of hyperspectral CARS and subsequent data analysis for intracellular visualisation of biological and chemical molecules isotopically labelled with deuterium. A novel data analysis algorithm, referred to as Factorisation into Susceptibilities and Concentrations of Chemical Components (FSC^3), has been utilised to generate quantitative concentration maps of chemical components in an unsupervised and unbiased manner. Deuterium-labelling is compatible with CARS imaging of biological samples due to carbon-deuterium bonds showing vibrational peaks within the "cell-silent" region of the Raman spectrum, so-called because it is devoid of spectral contributions from endogenous biological molecules. Thus, peaks located within this spectral region can be targeted using Raman-based techniques to generate chemical contrast against the mixed chemical background of a cell. This thesis has provided an investigation into the compatibility of deuterium-labelling with FSC^3 data analysis for observation of a range of biological and chemical molecules, assessing intracellular distribution, accumulation and turnover.

8.1. Quantitative visualisation of an isotope-labelled molecule from hyperspectral CARS datasets using FSC^3 data analysis

Deuterium-labelled fatty acids were initially utilised in a series of proof-of-concept experiments to confirm the ability of FSC^3 to identify and distinguish a chemical component corresponding to carbon-deuterium bond vibrations. Hence, following application of FSC^3 analysis to hyperspectral CARS datasets, deuterium-labelled fatty acids could be observed within cytosolic droplets. Chemical specificity for the identified CD-associated component was provided by its associated spectrum which showed the phase-retrieved imaginary part of the CARS susceptibility. When hyperspectral CARS datasets were acquired from lipid droplets of cells treated with different deuterium-labelled fatty acids, it was shown that FSC^3 retrieved slightly different spectra within the cell-silent region for components corresponding to each deuterated lipid. Based on these differences in CD-associated peak shape, deductions could be made regarding chemical attributions of the sub-peaks. Some of the most recent developments in vibrational tag development have focussed on developing probes which permit multiplex labelling within the cell-silent region of the Raman spectrum. If the chemical properties underlying observed CD-associated Raman peaks are understood, this permits informed selection of which molecular groups within a molecule to deuterate, which can provide an initial platform

for multiplex deuterium-based imaging. The ability to identify differences within retrieved silent region spectra also indicates the possibility of separating deuterium-labelled molecules based on variations in their CD peak shape. Whilst the allocated timescale for this project did not permit extensive investigation into this area, the potential of FSC^3 to differentiate between different deuterium-labelled molecules based on variations within the cell-silent region is interesting and warrants further exploration, with some potential applications discussed later within this chapter. Much of the recent research into nonlinear optical imaging of lipids[110,116,131,232] has favoured SRS methodologies over CARS due to the absence of a non-resonant contribution within its generated signal, which has been shown to give images with improved spatial resolution and spectra which show line-shapes comparable to Raman spectra with linear concentrations of chemical components. However, the steps which are taken to process the hyperspectral CARS datasets prior to FSC^3 analysis permit removal of the non-resonant component of the CARS signal, and hence the spatial and spectral outputs of FSC^3 are comparable to images and spectra acquired by hyperspectral SRS techniques. Thus, when combined with post-acquisition processing and FSC^3 data analysis, CARS becomes an equally attractive technique to SRS due to its simpler configuration and consequent compatibility with many multimodal systems, such as the one utilised within this thesis, whilst still providing high resolution images with suppressed non-resonant background.

When imaging deuterated fatty acid-containing lipid droplets within cells, a spectral range was utilised where both CD- and CH-associated bond vibrations were included, thus permitting the relationship between the CD and CH peaks to be directly observed. However, as none of the investigated deuterium-labelled fatty acids showed fully deuterated structures, with each showing portions where C-H bonds remained, a CH-associated peak was always present within the retrieved spectrum of the deuterated lipid component. If cells were treated with a fully deuterated fatty acid, in which no C-H bonds remained, FSC^3 should identify a deuterated fatty acid component which does not show a CH-associated peak, thus giving a purely CD-based signal. The potential utilisation of such molecules may also provide interesting follow-up experiments to some of the results described within this thesis, which will be discussed later in this concluding chapter. These results indicated the potential for further application of this approach to other deuterium-labelled molecules, however, the CARS-favourable characteristics shown by the investigated deuterated fatty acids permitted generation of strong CARS signal. It was proposed that the translation of this imaging approach to observation of other deuterium-labelled molecules would be more challenging, based on the assumption that the number of C-D bonds comprising the deuterium label would be considerably less than observed for the deuterated

fatty acids, and that the molecules may not show the same level of accumulation as the fatty acid isoforms, hence generating less CARS signal.

8.2. Hyperspectral CARS and FSC^3 data analysis for quantitative visualisation of deuterium-labelled lipid incorporation and turnover within cytosolic lipid droplets

With the proven ability of FSC^3 to identify and spatially resolve a chemical component from a hyperspectral CARS dataset corresponding to deuterated fatty acid, the potential application of this strategy for quantitative illustration of lipid exchange within intracellular droplets was explored. Through analysis of lipid droplet composition, specifically the concentrations of CD- and CH-based fatty acids, uptake, storage and turnover could be assessed. The changes in deuterated fatty acid concentration could be visualised clearly, with increases and decreases in component signal intensity (spatial and spectral) indicating storage and turnover, respectively, thus providing information about the associated timescales for these processes. The change in non-deuterated lipid concentration was less clear, the reason for which was thought to relate to the continued presence of CH-associated signal within the imaged lipid droplets over the time-course of the experiment, owing to the only partially deuterated fatty acid structures. Consequently, the change in CH-associated signal intensity was not as dramatic and hence less clear. As introduced in the previous paragraph, the use of a fully deuterated fatty acid isoform would likely address this issue, permitting clearer visualisation of changes in non-deuterated lipid concentration through depletion of the CH-associated signal following treatment of cells with the fully deuterated fatty acid. Whilst the observed changes in CARS signal intensity within the spatial outputs of FSC^3 appeared to show homogenous changes in CD-lipid concentration within droplets between time-points, analysis of individual lipid droplets would be required to confirm this. By assessing specific concentrations of CD- and CH-based lipid within each droplet, the homo- or heterogeneity of lipid uptake and storage could be confirmed quantitatively, and this could be taken further by comparing the identified homo- or heterogeneity between multiple cells, revealing information regarding uptake and turnover across a cell population.

These experiments also addressed the question of whether cells more readily mobilise lipid from their cytosolic droplets for metabolic purposes, or whether they instead utilise externally available lipid (within their growth media) and preserve their droplets. The observed turnover of deuterated lipid from cytosolic droplets over the course of the experiment provided evidence for the former, suggesting that cells do not favour preservation of lipid within their

droplet-based stores and this lipid is readily mobilised. Whilst turnover of deuterated lipid from droplets could be visualised by changes in CD-associated signal intensity, further information regarding the fate of the mobilised deuterated lipid was not obtained. To investigate this, hyperspectral CARS datasets could be acquired from larger fields of view, extending beyond the lipid droplets and incorporating other structures which may provide targets for the mobilised lipid, e.g. plasma membranes. Whilst the results that have been observed here are comparable to those that have been described in recent literature[124,129,131], many recent studies which have utilised deuterium-labelling to observe fatty acid uptake and turnover have done so in live cells. Consequently, another potential follow-up experiment could involve observing fatty acid uptake and turnover in a single live cell, which could be tracked over the full experiment duration, enabling it to be relocated and reimaged at each consecutive time-point. As eluded to in the previous section, a large number of recent studies have employed SRS imaging to observe lipid uptake into (and turnover from) lipid droplets[129,131], the results of which are comparable to the processed and analysed CARS data shown within Chapter 5. Ultimately, these experiments confirmed the applicability of deuterium labelling and quantitative FSC^3 data analysis for observation of lipid uptake, storage and turnover, encouraging the application of this strategy for the observation of other biological molecules. However, as discussed earlier in this chapter, lipids provide the gold-standard for CARS imaging in terms of signal generation, and thus, visualisation of other molecules, such as amino acids or monosaccharides, may prove challenging as they are likely to show a more ubiquitous distribution, hence limiting the coherent CARS signal generated.

8.3. Deuterated lipid uptake combined with FSC^3 data analysis as a tool for tracking cell lines in a mixed population

The ability of FSC^3 to spatially resolve deuterated fatty acids within cells was also applied as a non-invasive cell labelling and tracking strategy, which could permit the visualisation of cells of interest within a mixed population based the presence of deuterium-labelled lipid within its droplets. The principle behind this strategy was proven by treating two sets of cells with deuterated and non-deuterated lipid, before combining the cells to give a mixed population. Application of FSC^3 to hyperspectral datasets acquired from lipid droplets determined presence or absence of CD-associated signal, which was used to distinguish between cells from each original group. Consequently, as deuterated molecules are not naturally synthesised, the treatment of an investigated set of cells with deuterium-labelled lipid prior to their introduction into a mixed cell population will permit their differentiation from all other cells, which may show value in the

analysis of tissue composition or cell migration studies. The necessity for hyperspectral CARS imaging and subsequent FSC^3 data analysis to distinguish deuterated lipid-treated cells within a mixed population was apparent at the 16-hour time-point, where single wavenumber CARS images acquired at 2150 cm^{-1} failed to show CD-associated signal within intracellular lipid droplets, whilst the spatial outputs of FSC^3 clearly showed CD-associated signal within the same field of view.

In this example, both sets of cells were treated with lipid, hence stimulating lipid droplet formation and providing identifiable imaging targets. In a scenario where only the cells of interest are treated with lipid, it could be argued that the large number of lipid droplets alone may suffice for identification of the cells of interest within a mixed population. However, unlike deuterated lipids, non-deuterated lipids are naturally synthesised by cells, and the number of lipid droplets can show considerable variation between cells, hence limiting the ease with which investigated cells could be identified from others based on a high number of lipid droplets alone. Furthermore, this strategy could be expanded to observe multiple cell groups of interest within a mixed population. The ability of FSC^3 to identify separate chemical components for different deuterium-labelled fatty acids based on variations in CD peak shape would expand the number of cell subsets which could be identified and tracked simultaneously, progressing towards a multiplex approach.

However, a major deciding factor in assessment of the effectiveness of this non-invasive cell lineage tracking approach is the timescale over which it can employed, dictated by the duration for which deuterium-labelled fatty acid remains within lipid droplets and hence the time period over which a chemical component corresponding to deuterated fatty acid can be resolved by FSC^3. Cells from each of the initial populations could be successfully distinguished from one another over a 16-hour time period, however, based on the observed results from the lipid uptake/turnover experiments, sufficient CD-associated signal is not likely to be achieved beyond this time-point, therefore suggesting that over longer timescales, this approach will be limited. It is possible that the use of fully deuterated fatty acids could extend the time duration for which CD signal can be resolved, with a greater number of C-D bonds initially present and thus a higher intensity CD peak. Furthermore, different cell types and deuterated fatty acids may present different time-courses over which CD-associated signal can be effectively detected. A previous study which utilised fully deuterated isoforms of palmitic and oleic acid observed that macrophages continue to take up fatty acid over a 36-hour time period[124]. Another consideration which was not investigated extensively due to the time-constraints of the project was the potential of lipid transfer between cells, which could limit the effectiveness with which this non-invasive cell tracking approach can be employed. Within the aforementioned experiments, observed cells which were not exposed to deuterium-labelled fatty acid-supplemented media did not show signal

within the CD-associated FSC^3 component, however the small number of cells which were imaged may not be representative of the entire population, which warrants further studies to investigate the possibility of lipid transfer between cells.

Whilst this proof-of-principle study was performed in a two-dimensional cell culture, this strategy could be transferred to three-dimensional systems, such as spheroids or organoids[233], which comprise arrangements of multiple different cell types, providing a more representative model of the environment is which this approach may be of interest. Ultimately, whilst the principle of this imaging strategy has been proven, its applicability will depend on the timescale over which the cells need to be tracked. T-cell migration presents an area where this approach may be show potential, however the necessary timescales (often several days) are likely too long for droplet labelling with deuterated fatty acids to be effective. Fatty acids were utilised in this study due to their suitability for CARS imaging, however it is possible that other types of molecules may show a slower turnover and remain detectable within cells for longer time-periods. Dextran is an example of a molecule which remains within cells for long periods of time and is not lost during cell division due its passage through the endosomal system and consequent accumulation within lysosomes. For these reasons, dextran was initially utilised within the cell tracking experiments to give fluorescence images which ensured efficient selection of suitable fields of view and provided support for the observed FSC^3 results. Owing to its slow cellular turnover time and lysosomal accumulation, a deuterium-labelled isoform of dextran may provide an effective molecule for non-invasive cell labelling and tracking within mixed populations.

8.4. Visualisation of exogenously applied small molecules by hyperspectral CARS and FSC^3 data analysis

The ability of FSC^3 to observe non-lipid-based deuterium-labelled molecules within cells was investigated using a combination of biological molecules and chemical compounds, which showed varied structural arrangements of deuterium-containing groups and intracellular accumulation tendencies. Generally, FSC^3 data analysis showed limited success in identifying the investigated biological molecules and small molecule compounds when applied to hyperspectral CARS data, with only one of the investigated small molecule compounds showing any signs of signal generated by its CD label. Several suggestions as to the underlying causes of the lack of observable CD-associated signal has been proposed. Firstly, it is possible that the molecules distribute ubiquitously throughout the cell, giving a small number of identical bonds within the imaged focal volume, hence limiting the coherent signal generated. Secondly, the number of C-

D bonds that comprise the deuterium label within the molecular structure of the compounds may be too low. It is known that increasing the number of C-D bonds in a molecule increases the generated CARS signal[125,133], and hence some of the investigated molecules within this thesis may not have shown an adequate number of C-D bonds to give sufficient signal-to-noise. Thirdly, the investigated small molecule compound may have no longer been present within cells at the point of image acquisition, which may result from turnover of the compound by the cell within the employed incubation times, or from the transient plasma membrane permeabilisation that is often observed during PFA-fixation, which would warrant live cell imaging, however the long acquisition times required for hyperspectral CARS acquisition give rise to difficulties, such as cells moving and z-drift in response to stage heating.

D3-TPMP was studied the most extensively of all the investigated small molecule compounds, based on its reported dramatic accumulation within the mitochondrial matrix, which it was hypothesised would assist in the generation of a strong CARS signal. Acquired spontaneous Raman spectra from both powder and aqueous preparations of the compound enabled selection of a suitable spectral range for hyperspectral CARS acquisition, targeted around observed CD-associated peaks within the silent region, and visualisation of mitochondria via their strong protein/lipid signal ensured a suitable field of view was selected. However, despite the selection of optimal imaging conditions, CD-associated signal was not identified following FSC^3 analysis of hyperspectral datasets. To address some of the considerations outlined above, live cells were utilised as well as shorter incubation times, however, neither of these considerations permitted generation of CD-associated signal. However, as a stage was not utilised in order to avoid problems with sample drift over the required acquisition time for hyperspectral CARS data generation, cells showed poor health and alterations in intracellular structure, and as a result, D3-TPMP may still have been lost from cells prior to imaging. Consequently, the investigation of live cells needs to be re-explored, with emphasis on maintaining cell health whilst preventing associated problems with long image acquisition times. This may involve reducing the spectral range over which hyperspectral data is acquired, focusing more specifically around the CD-associated peaks, to reduce the overall imaging time, preventing associated issues such as cells moving etc., and permitting optimal conditions for live cell imaging. However, even with optimal live imaging conditions and the most appropriate incubation time, the ability to spatially resolve D3-TPMP within cells may still be limited by its deuterium label consisting of only a single deuterated methyl group, hence the only way to overcome this sensitivity problem may be to synthesise a fully deuterated isoform of TPMP. It is also possible that the CD_3 group was rapidly cleaved from D3-TPMP and used by the cell for metabolism, thus preventing deuterium from accumulating within the mitochondrial matrix as expected. Hyperspectral CARS imaging of the

same cell sample both before and after D3-TPMP-treatment may have revealed differences in CD-associated signal owing to incorporation of deuterium into other cellular regions following metabolism. However, unless the metabolised deuterium accumulated within a concentrated area, the likelihood of being able to visualise the deuterium-labelled compound above background noise would still be low.

Following its application to hyperspectral CARS data acquired from cytoplasmic regions of D7-HCMVi-treated cells, FSC^3 was able to identify a component showing a peak at ~ 2100 cm^{-1}, which was considered to correspond to CD-associated signal and hence the deuterated molecule. Justification for attribution of this peak to C-D bond resonances was provided by reducing the spectral range to target the ~ 2100 cm^{-1} peak specifically, which identified a peak at 2130 cm^{-1}, consistent with one of the peaks within the spontaneous Raman spectrum for D7-HCMVi, as described in Section 6.4 of Chapter 6. The respective spatially resolved image for this component showed CARS signal localised to the nuclear envelope region of the cell. This is interesting as the reported mechanism of action for the non-deuterated form of this small molecule compound involves inhibition of the HCMV protein kinase, UL97, which acts at the nuclear envelope to permit egress of the newly formed virions. However, the cells investigated within Chapter 6 of this thesis were uninfected, and hence the proposed target of D7-HCMVi was not present. In absence of a target, it is unclear where the deuterium-labelled compound would likely distribute within the cell, however, observed signal at the nuclear envelope could indicate an unintended target of the compound. One of the main driving forces behind the development of techniques to observe small molecule compound distribution in cells is to identify any off-target accumulation which may relate to cell toxicity, and it is possible in this example that off-target binding to an endogenous protein found in mammalian cells is being observed. Alternatively, based on HCMV DNA replication taking place within host cell nuclei, the compound may have been designed in such a way that it targets the cell nucleus, with a structure similar to that of a nucleotide, hence permitting the compound to exert its antiviral effects, although literature is not available that confirms this. An obvious follow-up experiment would involve investigation of whether D7-HCMVi can be observed in HCMV-infected cells, where the intended target is present, which would enable comparison between the observed D7-HCMVi signal localisation within infected and uninfected cells. However, due to the time-requirements and necessary experimental conditions for handling live or attenuated viruses, these extended investigations fell outside of the allocated timescale of this project.

On reflection of the data reported within Chapter 6, exploration of different analytical approaches may have provided further supporting data to conclusively prove or disprove the ability of hyperspectral CARS combined with FSC^3 analysis to visualise deuterium-labelled

compounds within cells. Additional information for each investigated biological and chemical molecule may have permitted a more informed decision to be made regarding initial deuterium-labelled molecule selection, prioritising those which were most likely to generate a strong intracellular CARS signal. Knowledge of the half-life of the molecules would have provided an indication of time durations over which molecules are likely to remain within cells, enabling prioritisation of molecules which are not metabolised and turned over rapidly. Similarly, exploration of *in silico* strategies, such as fragment-based drug design, to determine binding properties between each compound and its associated receptor may have revealed additional information regarding potential distribution and accumulation sites, as well as compound turnover times. Spontaneous Raman spectra were only acquired from aqueous solutions of D5-Trp, D4-/D6-SA and D3-TPMP, and only at their maximum soluble concentration. Acquisition of Raman spectra from aqueous solutions over a range of concentrations would have enabled identification of the minimum concentrations at which CD-associated signal could be distinguished above noise for each of the deuterium-labelled compounds, thus determining the concentration to which the molecules would need to accumulate within cells for visualisation.

Whilst many of the imaging techniques described throughout this thesis aim to minimise the detrimental impact on the health of the investigated cells, more invasive analytical techniques could have been employed to provide confirmation of presence or absence of the deuterium-labelled compounds within cells following CARS imaging. As cells were imaged by CARS alone, it was difficult to determine whether the deuterium-labelled compounds were present within cells at the time of imaging but not detectable, either due to low concentrations or ubiquitous intracellular distribution, or whether the compounds were excreted from cells prior to imaging as a result of rapid turnover or transient permeabilisation during fixation. Homogenisation of cells and subsequent analysis of cell lysates may have determined intracellular presence or absence of compound. High-performance liquid chromatography (HPLC) has been employed to effectively assess intracellular concentrations of therapeutic compounds within cells isolated from human and animal blood in preclinical pharmacokinetic studies[234,235], and the technique has more recently been coupled with mass spectrometry in liquid chromatography-mass spectrometry (LC-MS/MS)-based assays, which offer enhanced sensitivity compared to HPLC alone[236–238]. Thus, application of such techniques for analysis of the cell samples described within Chapter 6 may have provided confirmation of whether deuterium-labelled compounds were present within cells following CARS imaging. In particular, if mitochondria could be isolated from D3-TPMP-treated cells and analysed using the above-mentioned techniques, it may have been possible to determine presence or absence of the deuterium-labelled compound with a higher sensitivity than that offered by CARS. Alternatively, the remaining media in which the cells were incubated could

have been analysed to quantify the amount of compound either not taken up by cells or excreted from cells prior to imaging, which would have limited the detectable intracellular CD-associated signal. Through generation of standard curves using aqueous solutions of the deuterium-labelled compounds, intracellular and extracellular concentrations of compounds could have been calculated, providing supporting information to accompany the generated CARS data. Time-of-flight secondary ion mass spectrometry (ToF-SIMS) was also discussed within Chapter 6 as a technique able to achieve subcellular resolution imaging of compound accumulation within intact, unlabelled cells[192,193]. Thus, it would have been interesting to have imaged an equivalent set of deuterium-labelled compound-treated cells by ToF-SIMS had the timescale of the project allowed. Overall, the above described analytical techniques may have provided confirmation of whether or not the deuterium-labelled compound was present within cells at the time of imaging, thus providing further explanation as to why CD-associated signal was not observed for the majority of the investigated deuterium-labelled molecules. Presence of the investigated molecule within cells at the time of imaging would have provided conclusive evidence that CARS imaging combined with FSC^3 data analysis does not present an effective strategy for observing deuterium-labelled molecules within cells.

It has recently emerged that alkyne tags may provide an alternative to deuterium labels, which offer a large Raman cross-section but are slightly more perturbative to small molecule structure. Furthermore, some small molecule compounds have been reported with endogenous alkynes present within their chemical structure, e.g. erlotinib[98,132], which permits their intracellular observation in an unaltered form. D8-H_2Ri also possesses an alkyne group within its structure, and therefore enabled assessment of the ability of FSC^3 analysis to observe alkynes, in addition to deuterium. However, FSC^3 was not able to distinguish this small molecule compound within a cell, indicating that alkyne-labelled small molecule compounds may also show limited applicability to FSC^3 analysis, although further investigation of this molecule is certainly warranted.

8.5. Investigation into nonlinear imaging capabilities across three GSK-associated systems

A common set of samples were utilised to assess the nonlinear capabilities of three GSK-associated systems, two of which (Cardiff University and the COMI at the Beckman Institute) are custom-built and implement various modalities, whilst the other (Leica TCS SP8 CARS microscope) is a commercially available system which is intended to be accessible to all users,

but is consequently limited in its multimodal capabilities. Both CARS and SRS data was obtained using the COMI and Leica systems. The acquired CARS data from both systems was limited by a lack of spectral processing capabilities, hence images showed reduced spatial resolution compared to those acquired by SRS, and spectral outputs were distorted from their respective Raman spectra. The custom-built system which is utilised at Cardiff University benefits from advanced data processing and analysis methodologies, which effectively generate Raman-like spectra for each spatial point of a hyperspectral image. Subsequently, the unsupervised and unbiased FSC^3 algorithm can be applied to generate quantitative maps of concentrations of chemical components. The resulting spatially resolved images and associated retrieved spectra are comparable to the corresponding outputs from hyperspectral SRS, as indicated by the results acquired from deuterium-labelled fatty acid-treated cells using the Leica system.

The combination of FLIM with CARS is potentially a very interesting prospect as small molecule compound accumulation and cellular toxicity are commonly associated, thus changes in the metabolic activity of cells may provide an indication of cell health, even when structural alterations are not clearly observed. Whilst this modality is not offered by the Cardiff system, and so this potentially interesting area could not be investigated further, with the suggestion that there may be value in incorporating FLIM as a multimodal technique, this may be something that could be investigated in the future.

8.6. Outlook

This thesis has provided a large volume of information which can be used to assess the capabilities of the application of FSC^3 data analysis to hyperspectral CARS datasets for observing a wide range of deuterium-labelled biological and chemical molecules. Whilst the multimodal system has proven extremely effective at imaging deuterium-labelled lipids, which has enabled exploration of further potential areas for application, it has shown considerably less success when imaging non-lipid-based biological and chemical compounds. The overall aim of this project was to investigate and assess the ability of CARS to observe deuterium-labelled small molecules within cells, and on the whole, the technique has not proved especially effective. This raises two fundamental questions: i) Is CARS the most suitable technique for observing isotope-labelled molecules within cells; and ii) Is deuterium the most suitable labelling strategy for intracellular visualisation of small molecules?

It can be hypothesised that SRS presents a more effective imaging strategy than CARS as it does not show a non-resonant background signal, hence giving improved spatial resolution

and, when utilised in hyperspectral implementations, spectra which show a line-shape comparable to spontaneous Raman spectra with a linear concentration dependency, i.e. SRS signal directly proportional to concentration. However, the custom-built CARS system that has been employed throughout this project is supported by advanced data processing strategies, which permit retrieval of the imaginary part of the resonant CARS susceptibility, hence the non-resonant background is suppressed, providing images with high spatial resolution and spectra which are Raman-like and linear in their concentrations of chemical components, both of which are comparable to the observed outputs of SRS. Consequently, the CARS microscopy employed throughout this project should be no less-suited to intracellular imaging of deuterium-labelled molecules than comparable SRS microscopy. This has been illustrated within Chapter 7, which has provided a direct comparison between the outputs generated by combined hyperspectral CARS and FSC^3 data analysis, and those produced by hyperspectral SRS, the results of which showed comparable spatial images and corresponding spectra.

Recent literature has proposed that alkynes may present a more effective alternative to deuterium based on the stronger Raman signal that they generate. Furthermore, manipulation of these tags has permitted the precise positioning of the alkyne-associated peak within the cell-silent region, enabling multiplex imaging[135]. In the context of the deuterium-labelled small molecules investigated within this project, which showed only a small number of C-D bonds, an alkyne group may provide a considerably stronger signal, however, if compared to a fully deuterated small molecule, the potential increase in signal provided by the alkyne may not be as pronounced, and hence may not warrant the higher degree of associated structural change. It should also be noted that one of the investigated molecules, D8-H_2Ri, contained an alkyne group within its structure, and yet FSC^3 still failed to identify and spatially resolve it within a cell.

To summarise, both the CARS system and its supporting data processing and analysis methodologies which have been utilised throughout this project should offer comparable imaging capabilities to SRS imaging, and the signal generated by deuterium is likely limited by a low number of C-D bonds incorporated within the investigated molecules or a lack of accumulation, neither of which would be addressed through use an alkyne tag. Hence, the most likely solution to the low sensitivity problem may lie in the use of fully deuterated isoforms of small molecule compounds. Alternatively, this strategy may only be applicable to compounds which accumulate to a high concentration, and thus may serve as a selective oppose to a general imaging strategy. The overall aim of this project was to assess the capabilities of CARS microscopy for observing deuterium-labelled molecules in cells. A large amount of data has been provided in an attempt to answer this question and the observed results suggest that, in short, if a biomolecule or small molecule compound shows a high number of C-D bonds within its structure and it accumulates

strongly within a specific cellular compartment then CARS will likely be able to distinguish the molecule effectively. However, if both of these criteria are not met, then the system will more than likely fail to generate CD-associated signal. Thus, the potential success of this imaging strategy will depend on the molecule being investigated.

BIBLIOGRAPHY

1. Gershell, L. J. & Atkins, J. H. A brief history of novel drug discovery technologies. *Nat. Rev. Drug Discov.* **2**, 321–327 (2003).

2. Rajendran, L., Knölker, H. J. & Simons, K. Subcellular targeting strategies for drug design and delivery. *Nat. Rev. Drug Discov.* **9**, 29–42 (2010).

3. Simon, G. M., Niphakis, M. J. & Cravatt, B. F. Determining target engagement in living systems. *Nat. Chem. Biol.* **9**, 200–205 (2013).

4. Stewart, M. P. *et al.* In vitro and ex vivo strategies for intracellular delivery. *Nature* **538**, 183–192 (2016).

5. Lin, A. *et al.* Off-target toxicity is a common mechanism of action of cancer drugs undergoing clinical trials. *Sci. Transl. Med.* **11**, 1–18 (2019).

6. Shtengel, G. *et al.* Interferometric fluorescent super-resolution microscopy resolves 3D cellular ultrastructure Understanding molecular-scale architecture of cells requires determination of 3D locations of specific proteins with accuracy match-ing their nanometer-length sca. *Proc. Natl. Acad. Sci.* **106**, 3125–3130 (2009).

7. Schermelleh, L., Heintzmann, R. & Leonhardt, H. A guide to super-resolution fluorescence microscopy. *J. Cell Biol.* **190**, 165–175 (2010).

8. Sahl, S. J., Hell, S. W. & Jakobs, S. Fluorescence nanoscopy in cell biology. *Nat. Rev. Mol. Cell Biol.* **18**, 685–701 (2017).

9. Watson, P., Jones, A. T. & Stephens, D. J. Intracellular trafficking pathways and drug delivery: Fluorescence imaging of living and fixed cells. *Advanced Drug Delivery Reviews* **57**, 43–61 (2005).

10. Giepmans, B. N. G., Adams, S. R., Ellisman, M. H. & Tsien, R. Y. The fluorescent toolbox for assessing protein location and function. *Science (80-.).* **312**, 217–224 (2006).

11. Theillet, F.-X. *et al.* Physicochemical Properties of Cells and Their Effects on Intrinsically Disordered Proteins (IDPs). *Chem. Rev.* **114**, 6661–6714 (2014).

12. Hann, M. M., Leach, A. R. & Harper, G. Molecular Complexity and Its Impact on the Probability of Finding Leads for Drug Discovery. *J. Chem. Inf. Comput. Sci.* **41**, 856–864 (2001).

13. Bemis, G. W. & Murcko, M. A. The properties of known drugs. 1. Molecular frameworks. *J. Med. Chem.* **39**, 2887–2893 (1996).

14. Yin, L. *et al.* How does fluorescent labeling affect the binding kinetics of proteins with intact cells? *Biosens. Bioelectron.* **66**, 412–416 (2015).

15. Fukumoto, S. & Fujimoto, T. Deformation of lipid droplets in fixed samples. *Histochem. Cell Biol.* **118**, 423–428 (2002).

16. Nan, X., Cheng, J.-X. & Xie, X. S. Vibrational imaging of lipid droplets in live fibroblast cells with coherent anti-Stokes Raman scattering microscopy. *J. Lipid Res.* **44**, 2202–2208 (2003).

17. Ohsaki, Y., Shinohara, Y., Suzuki, M. & Fujimoto, T. A pitfall in using BODIPY dyes to label lipid droplets for fluorescence microscopy. *Histochem. Cell Biol.* **133**, 477–480 (2010).

18. Huang, K. & Martí, A. A. Recent trends in molecular beacon design and applications. *Anal. Bioanal. Chem.* **402**, 3091–3102 (2012).

19. Yamakoshi, H. *et al.* Alkyne-tag Raman imaging for visualization of mobile small molecules in live cells. *J. Am. Chem. Soc.* **134**, 20681–20689 (2012).

20. Wright, A., Bubb, W. A., Hawkins, C. L. & Davies, M. J. Singlet Oxygen–mediated Protein Oxidation: Evidence for the Formation of Reactive Side Chain Peroxides on Tyrosine Residues¶. *Photochem. Photobiol.* **76**, 35–46 (2002).

21. Bartosz, G. Oxidative stress in plants. *Acta Physiol. Plant.* **19**, 47–64 (1997).

22. Foyer, C. H., Lelandais, M. & Kunert, K. J. Photooxidative Stress in Plants. *Physiol Plant* **92**, 696–717 (1994).

23. Bernas, T., Zarebski, M., Cook, R. R. & Dobrucki, J. W. Minimizing photobleaching during confocal microscopy of fluorescent probes bound to chromatin: role of anoxia and photon flux. *J. Microsc.* **215**, 281–296 (2004).

24. Song, L., Varma, C. A., Verhoeven, J. W. & Tanke, H. J. Influence of the triplet excited state on the photobleaching kinetics of fluorescein in microscopy. *Biophys. J.* **70**, 2959–2968 (1996).

25. Song, L., van Gijlswijk, R. P. M., Young, I. T. & Tanke, H. J. Influence of fluorochrome labeling density on the photobleaching kinetics of fluorescein in microscopy. *Cytometry*

27, 213–223 (1997).

26. Vrouenraets, M. B., Visser, G. W., Snow, G. B. & van Dongen, G. A. Basic principles, applications in oncology and improved selectivity of photodynamic therapy. *Anticancer Res.* **23**, 505–522 (2003).

27. Dixit, R. & Cyr, R. Cell damage and reactive oxygen species production induced by fluorescence microscopy: effect on mitosis and guidelines for non-invasive fluorescence microscopy. *Plant J.* **36**, 280–290 (2003).

28. Martin, R. M., Leonhardt, H. & Cardoso, M. C. DNA labeling in living cells. *Cytom. Part A* **67**, 45–52 (2005).

29. Hsi, R. A., Rosenthal, D. I. & Glatstein, E. Photodynamic Therapy in the Treatment of Cancer. *Drugs* **57**, 725–734 (1999).

30. Hoebe, R. A. *et al.* Controlled light-exposure microscopy reduces photobleaching and phototoxicity in fluorescence live-cell imaging. *Nat. Biotechnol.* **25**, 249–253 (2007).

31. Magidson, V. & Alexey, K. Circumventing photodamage in live-cell microscopy. *Methods Cell Biol.* **114**, 545–560 (2013).

32. Hadjantonakis, A. K., MacMaster, S. & Nagy, A. Embryonic stem cells and mice expressing different GFP variants for multiple non-invasive reporter usage within a single animal. *BMC Biotechnol.* **2**, 1–9 (2002).

33. Xiang, A. P. *et al.* Extensive contribution of embryonic stem cells to the development of an evolutionarily divergent host. *Hum. Mol. Genet.* **17**, 27–37 (2008).

34. Strack, R. L. *et al.* A noncytotoxic DsRed variant for whole-cell labeling. *Nat. Methods* **5**, 955–957 (2008).

35. Zhou, J., Lin, J., Zhou, C., Deng, X. & Xia, B. Cytotoxicity of red fluorescent protein DsRed is associated with the suppression of Bcl-xL translation. *FEBS Lett.* **585**, 821–827 (2011).

36. Liu, H. S., Jan, M. S., Chou, C. K., Chen, P. H. & Ke, N. J. Is green fluorescent protein toxic to the living cells? *Biochem. Biophys. Res. Commun.* **260**, 712–717 (1999).

37. Taghizadeh, R. R. & Sherley, J. L. CFP and YFP, but Not GFP, Provide Stable Fluorescent Marking of Rat Hepatic Adult Stem Cells. *J. Biomed. Biotechnol.* **2008**, 1–9 (2008).

38. Bulina, M. E. *et al.* A genetically encoded photosensitizer. *Nat. Biotechnol.* **24**, 95–99

(2006).

39. Pletnev, S. *et al.* Structural Basis for Phototoxicity of the Genetically Encoded Photosensitizer KillerRed. *J. Biol. Chem.* **284**, 32028–32039 (2009).

40. Ansari, A. M. *et al.* Cellular GFP Toxicity and Immunogenicity: Potential Confounders in in Vivo Cell Tracking Experiments. *Stem Cell Rev. Reports* **12**, 553–559 (2016).

41. Li, Z.-H., Peng, J. & Chen, H.-L. Bioconjugated Quantum Dots as Fluorescent Probes for Biomedical Imaging. *J. Nanosci. Nanotechnol.* **11**, 7521–7536 (2011).

42. Shao, L., Gao, Y. & Yan, F. Semiconductor Quantum Dots for Biomedicial Applications. *Sensors* **11**, 11736–11751 (2011).

43. Jensen, E. C. Use of Fluorescent Probes: Their Effect on Cell Biology and Limitations. *Anat. Rec.* **295**, 2031–2036 (2012).

44. Lakowicz, J. R., Szmacinski, H., Nowaczyk, K. & Johnson, M. L. Fluorescence lifetime imaging of free and protein-bound NADH. *Proc. Natl. Acad. Sci. U. S. A.* **89**, 1271–1275 (1992).

45. Drozdowicz-Tomsia, K. *et al.* Multiphoton fluorescence lifetime imaging microscopy reveals free-to-bound NADH ratio changes associated with metabolic inhibition. *J. Biomed. Opt.* **19**, 086016 (2014).

46. Becker, W. Fluorescence lifetime imaging - techniques and applications. *J. Microsc.* **247**, 119–136 (2012).

47. Evers, M. *et al.* Enhanced quantification of metabolic activity for individual adipocytes by label-free FLIM. *Sci. Rep.* **8**, 1–14 (2018).

48. Huang, D. *et al.* Optical Coherence Tomography. *Science (80-.).* **254**, 1178–1181 (1991).

49. Pope, I., Langbein, W., Borri, P. & Watson, P. Live Cell Imaging with Chemical Specificity Using Dual Frequency CARS Microscopy. *Methods Enzymol.* **504**, 273–291 (2012).

50. Smith, R., Wright, K. L. & Ashton, L. Raman spectroscopy: An evolving technique for live cell studies. *Analyst* **141**, 3590–3600 (2016).

51. Cricenti, A. *et al.* Chemically resolved imaging of biological cells and thin films by infrared scanning near-field optical microscopy. *Biophys. J.* **85**, 2705–2710 (2003).

52. Turrell, G. & Corset, J. *Raman Microscopy: Developments and Applications.* (1996).

53. Liu, M. & Barth, A. Mapping interactions between the Ca2+-ATPase and its substrate ATP with infrared spectroscopy. *J. Biol. Chem.* **278**, 10112–10118 (2003).

54. Rahmelow, K. & Hübner, W. Infrared spectroscopy in aqueous solution: Difficulties and accuracy of water subtraction. *Appl. Spectrosc.* **51**, 160–170 (1997).

55. Raichlin, Y., Millo, A. & Katzir, A. Investigations of the Structure of Water Using Mid-IR Fiberoptic Evanescent Wave Spectroscopy. *Phys. Rev. Lett.* **93**, 185703 (2004).

56. Sabbatini, S., Conti, C., Orilisi, G. & Giorgini, E. Infrared spectroscopy as a new tool for studying single living cells: Is there a niche? *Biomed. Spectrosc. Imaging* **6**, 85–99 (2017).

57. Sijtsema, N. M., Wouters, S. D., De Grauw, C. J., Otto, C. & Greve, J. Confocal direct imaging Raman microscope: Design and applications in biology. *Appl. Spectrosc.* **52**, 348–355 (1998).

58. Stiles, P. L., Dieringer, J. A., Shah, N. C. & Van Duyne, R. P. Surface-enhanced Raman spectroscopy. *Annu. Rev. Anal. Chem.* **1**, 601–626 (2008).

59. Campagnola, P. J. & Loew, L. M. Second-harmonic imaging microscopy for visualizing biomolecular arrays in cells, tissues and organisms. *Nat. Biotechnol.* **21**, 1356–1360 (2003).

60. Campagnola, P. Seocnd harmonic generation imaging microscopy: Applications to diseases diagnostics. *Anal. Chem.* **83**, 3224–3231 (2011).

61. Bueno, J. M., Ávila, F. J. & Artal, P. Comparison of second harmonic microscopy images of collagen-based ocular tissues with 800 and 1045 nm. *Biomed. Opt. Express* **8**, 5065–5074 (2017).

62. Mostaço-Guidolin, L., Rosin, N. & Hackett, T.-L. Imaging Collagen in Scar Tissue: Developments in Second Harmonic Generation Microscopy for Biomedical Applications. *Int. J. Mol. Sci.* **18**, 1772 (2017).

63. Barad, Y., Eisenberg, H., Horowitz, M. & Silberberg, Y. Nonlinear scanning laser microscopy by third harmonic generation. *Appl. Phys. Lett.* **70**, 922–924 (1997).

64. Débarre, D. *et al*. Imaging lipid bodies in cells and tissues using third-harmonic generation microscopy. *Nat. Methods* **3**, 47–53 (2006).

65. Adur, J., Carvalho, H. F., Cesar, C. L. & Casco, V. H. Nonlinear microscopy techniques: Principles and biomedical applications. in *Microscopy and Analysis* 121–149 (InTech,

2016). doi:10.5772/57353

66. Enejder, A., Heinrich, C., Brackmann, C., Bernet, S. & Ritsch-Marte, M. Coherent anti-Stokes Raman scattering microscopy. in *Biomedical Imaging: Principles and Applications* (ed. Salzer, R.) 304–330 (2012). doi:10.1002/9781118271933

67. Zumbusch, A., Langbein, W. & Borri, P. Nonlinear vibrational microscopy applied to lipid biology. *Progress in Lipid Research* **52**, 615–632 (2013).

68. Maker, P. D. & Terhune, R. W. Study of optical effects due to an induced polarization third order in the electric field strength. *Phys. Rev.* **137**, A801–A818 (1965).

69. Zheltikov, A. M. Coherent anti-stokes Raman scattering: From proof-of-the-principle experiments to femtosecond CARS and higher order wave-mixing generalizations. *J. Raman Spectrosc.* **31**, 653–667 (2000).

70. Zumbusch, A., Holtom, G. R. & Xie, X. S. Three-dimensional vibrational imaging by coherent anti-stokes raman scattering. *Phys. Rev. Lett.* **82**, 4142–4145 (1999).

71. Ichimura, T., Hayazawa, N., Hashimoto, M., Inouye, Y. & Kawata, S. Tip-enhanced coherent anti-Stokes Raman scattering for vibrational nanoimaging. *Phys. Rev. Lett.* **92**, 20–23 (2004).

72. Cheng, J.-X., Book, L. D. & Xie, X. S. Polarization coherent anti-Stokes Raman scattering microscopy. *Opt. Express* **26**, 1341–1343 (2001).

73. Masia, F., Glen, A., Stephens, P., Borri, P. & Langbein, W. Quantitative chemical imaging and unsupervised analysis using hyperspectral coherent anti-stokes Raman scattering microscopy. *Anal. Chem.* **85**, 10820–10828 (2013).

74. Masia, F., Karuna, A., Borri, P. & Langbein, W. Hyperspectral image analysis for CARS, SRS, and Raman data. *J. Raman Spectrosc.* **46**, 727–734 (2015).

75. Karuna, A. *et al.* Label-Free Volumetric Quantitative Imaging of the Human Somatic Cell Division by Hyperspectral Coherent Anti-Stokes Raman Scattering. *Anal. Chem.* **91**, 2813–2821 (2019).

76. Potma, E. O., Boeij, W. P. De, Haastert, P. J. M. Van & Wiersma, D. A. Real-time visualisation of intracellular hydrodynamics in single living cells. *Proc. Natl. Acad. Sci.* **98**, 1577–1582 (2001).

77. Cheng, J., Pautot, S., Weitz, D. A. & Xie, X. S. Ordering of water molecules between

phospholipid bilayers visualized by coherent anti-Stokes Raman scattering microscopy. *Proc. Natl. Acad. Sci.* **100**, 9826–9830 (2003).

78. Yu, Y. C., Sohma, Y., Takimoto, S., Miyauchi, T. & Yasui, M. Direct visualization and quantitative analysis of water diffusion in complex biological tissues using CARS microscopy. *Sci. Rep.* **3**, 1–11 (2013).

79. Di Napoli, C. *et al.* Hyperspectral and differential CARS microscopy for quantitative chemical imaging in human adipocytes. *Biomed. Opt. Express* **5**, 1378 (2014).

80. Di Napoli, C. *et al.* Quantitative Spatiotemporal Chemical Profiling of Individual Lipid Droplets by Hyperspectral CARS Microscopy in Living Human Adipose-Derived Stem Cells. *Anal. Chem.* **88**, 3677–3685 (2016).

81. Bradley, J. *et al.* Quantitative imaging of lipids in live mouse oocytes and early embryos using CARS microscopy. *Development* **143**, 2238–2247 (2016).

82. Lyn, R. K., Kennedy, D. C., Stolow, A., Ridsdale, A. & Pezacki, J. P. Dynamics of lipid droplets induced by the hepatitis C virus core protein. *Biochem. Biophys. Res. Commun.* **399**, 518–524 (2010).

83. Day, J. P. R., Rago, G., Domke, K. F., Velikov, K. P. & Bonn, M. Label-free imaging of lipophillic bioactive molecules during lipid digestion by multiplex coherent anti-Stokes Raman scattering microscopy. *J. Am. Chem. Soc.* **132**, 8433–8439 (2010).

84. Paar, M. *et al.* Remodeling of lipid droplets during lipolysis and growth in adipocytes. *J. Biol. Chem.* **287**, 11164–11173 (2012).

85. Le, T. T., Yue, S. & Cheng, J. X. Shedding new light on lipid biology with coherent anti-Stokes Raman scattering microscopy. *J. Lipid Res.* **51**, 3091–3102 (2010).

86. Hartshorn, C. M. *et al.* Multicomponent chemical imaging of pharmaceutical solid dosage forms with broadband CARS microscopy. *Anal. Chem.* **85**, 8102–8111 (2013).

87. Fussell, A. L., Grasmeijer, F., Frijlink, H. W., De Boer, A. H. & Offerhaus, H. L. CARS microscopy as a tool for studying the distribution of micronised drugs in adhesive mixtures for inhalation. *J. Raman Spectrosc.* **45**, 495–500 (2014).

88. Kang, E. *et al.* In situ visualization of paclitaxel distribution and release by coherent anti-stokes Raman scattering microscopy. *Anal. Chem.* **78**, 8036–8043 (2006).

89. Kang, E., Robinson, J., Park, K. & Cheng, J.-X. Paclitaxel distribution in poly(ethylene

glycol) / poly(lactide-co- glycolic acid) blends and its release visualized by coherent anti-Stokes Raman scattering microscopy. *J. Control. Release* **122**, 261–268 (2007).

90. Kang, E. *et al.* Application of coherent anti-Stokes Raman scattering microscopy to image the changes in a paclitaxel-poly(styrene-b-isobutylene-b-styrene) matrix pre- and post-drug elution. *J. Biomed. Mater. Res. - Part A* **87**, 913–920 (2008).

91. Windbergs, M. *et al.* Chemical imaging of oral solid dosage forms and changes upon dissolution using coherent anti-stokes raman scattering microscopy. *Anal. Chem.* **81**, 2085–2091 (2009).

92. Jurna, M. *et al.* Coherent anti-stokes raman scattering microscopy to monitor drug dissolution in different oral pharmaceutical tablets. *J. Innov. Opt. Health Sci.* **2**, 37–43 (2009).

93. Wurpel, G. W. H., Schins, J. M. & Müller, M. Chemical specificity in three-dimensional imaging with multiplex coherent anti-Stokes Raman scattering microscopy. *Opt. Lett.* **27**, 1093–1095 (2002).

94. Pope, I., Langbein, W., Watson, P. & Borri, P. Simultaneous hyperspectral differential-CARS, TPF and SHG microscopy with a single 5 fs Ti:Sa laser. *Opt. Express* **21**, 7096 (2013).

95. Rocha-Mendoza, I., Langbein, W., Watson, P. & Borri, P. Differential coherent anti-Stokes Raman scattering microscopy with linearly chirped femtosecond laser pulses. *Opt. Lett.* **34**, 2258–2260 (2009).

96. Di Napoli, C. *et al.* Chemically-specific dual/differential CARS micro-spectroscopy of saturated and unsaturated lipid droplets. *J. Biophotonics* **7**, 68–76 (2014).

97. Woodbury, E. J. & Ng, W. K. Ruby laser operation in the near IR. *Proc. Inst. Radio Eng.* **50**, 2347–2348 (1962).

98. Tipping, W. J., Lee, M., Serrels, A., Brunton, V. G. & Hulme, A. N. Stimulated Raman scattering microscopy: An emerging tool for drug discovery. *Chem. Soc. Rev.* **45**, 2075–2089 (2016).

99. Freudiger, C. W. *et al.* Label-Free Biomedical Imaging with High Sensitivity by Stimulated Raman Scattering Microscopy. *Science (80-.).* **322**, 1857–1861 (2008).

100. Min, W., Freudiger, C. W., Lu, S. & Xie, X. S. Coherent nonlinear optical imaging: Beyond fluorescence microscopy. *Annu. Rev. Phys. Chem.* **62**, 507–530 (2011).

101. Bocklitz, T. *et al.* Invited Article: Comparison of hyperspectral coherent Raman scattering microscopies for biomedical applications. *APL Photonics* **3**, 092404 (2018).

102. Cleff, C. *et al.* Ground-state depletion for subdiffraction-limited spatial resolution in coherent anti-Stokes Raman scattering microscopy. *Phys. Rev. A - At. Mol. Opt. Phys.* **86**, 1–11 (2012).

103. Cheng, J.-X., Volkmer, A. & Xie, X. S. Theoretical and experimental characterization of coherent anti-Stokes Raman scattering microscopy. *J. Opt. Soc. Am. B* **19**, 1363 (2002).

104. Fu, D. *et al.* Quantitative chemical imaging with multiplex stimulated Raman scattering microscopy. *J. Am. Chem. Soc.* **134**, 3623–3626 (2012).

105. Bae, K. *et al.* Epi-Detected Hyperspectral Stimulated Raman Scattering Microscopy for Label-Free Molecular Subtyping of Glioblastomas. *Anal. Chem.* **90**, 10249–10255 (2018).

106. Vartiainen, E. M., Rinia, H. A., Müller, M. & Bonn, M. Direct extraction of Raman line-shapes from congested CARS spectra. *Opt. Express* **14**, 3622 (2006).

107. Liu, Y., Lee, Y. J. & Cicerone, M. T. Broadband CARS spectral phase retrieval using a time-domain Kramers-Kronig transform. *Opt. Lett.* **34**, 1363–1365 (2009).

108. Chung, C.-Y., Boik, J. & Potma, E. O. Biomolecular imaging with coherent nonlinear vibrational microscopy. *Annu. Rev. Phys. Chem.* **64**, 77–99 (2013).

109. Li, Y., Wang, Z., Mu, X., Ma, A. & Guo, S. Raman tags: Novel optical probes for intracellular sensing and imaging. *Biotechnol. Adv.* **35**, 168–177 (2017).

110. Hong, S. *et al.* Live-cell stimulated Raman scattering imaging of alkyne-tagged biomolecules. *Angew. Chemie - Int. Ed.* **53**, 5827–5831 (2014).

111. Hu, F. *et al.* Vibrational Imaging of Glucose Uptake Activity in Live Cells and Tissues by Stimulated Raman Scattering. *Angew. Chemie - Int. Ed.* **54**, 9821–9825 (2015).

112. Zhao, Z., Shen, Y., Hu, F. & Min, W. Applications of vibrational tags in biological imaging by Raman microscopy. *Analyst* **142**, 4018–4029 (2017).

113. Beatty, K. E. *et al.* Fluorescence visualization of newly synthesized proteins in mammalian cells. *Angew. Chemie - Int. Ed.* **45**, 7364–7367 (2006).

114. Jao, C. Y. & Salic, A. Exploring RNA transcription and turnover in vivo by using click chemistry. *Proc. Natl. Acad. Sci.* **105**, 15779–15784 (2008).

115. Yamakoshi, H. *et al.* Imaging of EdU, an alkyne-tagged cell proliferation probe, by Raman

microscopy. *J. Am. Chem. Soc.* **133**, 6102–6105 (2011).

116. Wei, L. *et al.* Live-cell imaging of alkyne-tagged small biomolecules by stimulated Raman scattering. *Nat. Methods* **11**, 410–412 (2014).

117. Lee, H. J. *et al.* Assessing Cholesterol Storage in Live Cells and C. elegans by Stimulated Raman Scattering Imaging of Phenyl-Diyne Cholesterol. *Sci. Rep.* **5**, 1–10 (2015).

118. Van Manen, H. J., Lenferink, A. & Otto, C. Noninvasive imaging of protein metabolic labeling in single human cells using stable isotopes and Raman microscopy. *Anal. Chem.* **80**, 9576–9582 (2008).

119. Li, J. & Cheng, J. X. Direct visualization of de novo lipogenesis in single living cells. *Sci. Rep.* **4**, 1–8 (2014).

120. Wei, L., Yu, Y., Shen, Y., Wang, M. C. & Min, W. Vibrational imaging of newly synthesized proteins in live cells by stimulated Raman scattering microscopy. *Proc. Natl. Acad. Sci.* **110**, 11226–11231 (2013).

121. Wei, L. *et al.* Imaging complex protein metabolism in live organisms by stimulated raman scattering microscopy with isotope labeling. *ACS Chem. Biol.* **10**, 901–908 (2015).

122. Shi, L., Shen, Y. & Min, W. Visualizing protein synthesis in mice with in vivo labeling of deuterated amino acids using vibrational imaging. *APL Photonics* **3**, 092401 (2018).

123. Farese, R. V & Walther, T. C. Lipid Droplets Finally Get a Little R-E-S-P-E-C-T. *Cell* **139**, 855–860 (2009).

124. Matthäus, C. *et al.* Noninvasive imaging of intracellular lipid metabolism in macrophages by Raman microscopy in combination with stable isotopic labeling. *Anal. Chem.* **84**, 8549–8556 (2012).

125. Alfonso-García, A., Pfisterer, S. G., Riezman, H., Ikonen, E. & Potma, E. O. D38-cholesterol as a Raman active probe for imaging intracellular cholesterol storage. *J. Biomed. Opt.* **21**, 061003 (2015).

126. van Manen, H.-J., Kraan, Y. M., Roos, D. & Otto, C. Single-cell Raman and fluorescence microscopy reveal the association of lipid bodies with phagosomes in leukocytes. *Proc. Natl. Acad. Sci.* **102**, 10159–10164 (2005).

127. Xie, X. S., Yu, J. & Yang, W. Y. Perspective - Living cells as test tubes. *Science (80-.).* **312**, 228–230 (2006).

128. Weeks, T., Schie, I., den Hartigh, L. J., Rutledge, J. C. & Huser, T. Lipid-cell interactions in human monocytes investigated by doubly-resonant coherent anti-Stokes Raman scattering microscopy. *J. Biomed. Opt.* **16**, 021117 (2011).

129. Zhang, D., Slipchenko, M. N. & Cheng, J. X. Highly sensitive vibrational imaging by femtosecond pulse stimulated raman loss. *J. Phys. Chem. Lett.* **2**, 1248–1253 (2011).

130. Stiebing, C. *et al.* Real-time Raman and SRS imaging of living human macrophages reveals cell-to-cell heterogeneity and dynamics of lipid uptake. *J. Biophotonics* **10**, 1217–1226 (2017).

131. Fu, D. *et al.* In vivo metabolic fingerprinting of neutral lipids with hyperspectral stimulated raman scattering microscopy. *J. Am. Chem. Soc.* **136**, 8820–8828 (2014).

132. El-Mashtoly, S. F. *et al.* Label-free imaging of drug distribution and metabolism in colon cancer cells by Raman microscopy. *Analyst* **139**, 1155–1161 (2014).

133. Bergner, G. *et al.* Quantitative detection of C-deuterated drugs by CARS microscopy and Raman microspectroscopy. *Analyst* **136**, 3686–3693 (2011).

134. Fu, D. *et al.* Imaging the intracellular distribution of tyrosine kinase inhibitors in living cells with quantitative hyperspectral stimulated Raman scattering. *Nat. Chem.* **6**, 614–622 (2014).

135. Hu, F. *et al.* Supermultiplexed optical imaging and barcoding with engineered polyynes. *Nat. Methods* **15**, 194–200 (2018).

136. Raman, C. V. & Krishnan, K. S. A new type of secondary radiation. *Nature* **121**, 501–502 (1928).

137. Schie, I. W. & Huser, T. Label-free analysis of cellular biochemistry by Raman spectroscopy and microscopy. *Compr. Physiol.* **3**, 941–956 (2013).

138. Fox, M. *Optical Properties of Solids*. *Oxford University Press* (2001).

139. Krafft, C., Dietzek, B., Schmitt, M. & Popp, J. Raman and coherent anti-Stokes Raman scattering microspectroscopy for biomedical applications. *J. Biomed. Opt.* **17**, 040801 (2012).

140. Cheng, J. X. & Xie, X. S. *Coherent Raman scattering microscopy*. *Coherent Raman Scattering Microscopy* (2012).

141. Rodriguez, L. G., Lockett, S. J. & Holtom, G. R. Coherent anti-Stokes Raman scattering

microscopy: A biological review. *Cytom. Part A* **69**, 779–791 (2006).

142. Evans, C. L. & Xie, X. S. Coherent Anti-Stokes Raman Scattering Microscopy: Chemical Imaging for Biology and Medicine. *Annu. Rev. Anal. Chem.* **1**, 883–909 (2008).

143. Müller, M. & Zumbusch, A. Coherent anti-Stokes Raman Scattering Microscopy. *Chemphyschem* **8**, 2156–70 (2007).

144. Lotem, H., Lynch, R. T. & Bloembergen, N. Interference between Raman resonances in four-wave difference mixing. *Phys. Rev. A* **14**, 1748–1755 (1976).

145. Cheng, J.-X. & Xie, X. S. Coherent Anti-Stokes Raman Scattering Microscopy: Instrumentation, Theory, and Applications. *J. Phys. Chem. B* **108**, 827–840 (2004).

146. Evans, C. L., Potma, E. O. & Xie, X. S. Coherent anti-Stokes Raman scattering spectral interferometry: determination of the real and imaginary components of nonlinear susceptibility χ^(3) for vibrational microscopy. *Opt. Lett.* **29**, 2923–2925 (2004).

147. Potma, E. O., Evans, C. L. & Xie, X. S. Heterodyne coherent anti-Stokes Raman scattering (CARS) imaging. *Opt. Lett.* **31**, 241–243 (2006).

148. Di Napoli, C. *Label-free multiphoton microscopy of intracellular lipids using Coherent anti-Stokes Raman Scattering (CARS) (PhD Thesis)*. (Cardiff University, 2014).

149. Duncan, M. D., Reintjes, J. & Manuccia, T. J. Scanning coherent anti-Stokes Raman microscope. *Opt. Lett.* **7**, 350–352 (1982).

150. Cheng, J.-X. Coherent anti-Stokes Raman scattering microscopy. *Appl. Spectrosc.* **61**, 197–208 (2007).

151. Fu, Y., Wang, H., Shi, R. & Cheng, J.-X. Characterization of photodamage in coherent anti-Stokes Raman scattering microscopy. *Opt. Express* **14**, 3942–3951 (2006).

152. Cheng, J., Volkmer, A., Book, L. D. & Xie, X. S. An Epi-Detected Coherent Anti-Stokes Raman Scattering (E-CARS) Microscope with High Spectral Resolution and High Sensitivity. *J. Phys. Chem. B* **105**, 1277–1280 (2001).

153. Hashimoto, M., Araki, T. & Kawata, S. Molecular vibration imaging in the fingerprint region by use of coherent anti-Stokes Raman scattering microscopy with a collinear configuration. *Opt. Lett.* **25**, 1768–1770 (2000).

154. Hellerer, T., Enejder, A. M. K. & Zumbusch, A. Spectral focusing: High spectral resolution spectroscopy with broad-bandwidth laser pulses. *Appl. Phys. Lett.* **85**, 25–27

(2004).

155. Rocha-Mendoza, I., Langbein, W. & Borri, P. Coherent anti-Stokes Raman microspectroscopy using spectral focusing with glass dispersion. *Appl. Phys. Lett.* **93**, 201103-1-201103–3 (2008).

156. Langbein, W., Rocha-Mendoza, I. & Borri, P. Single source coherent anti-Stokes Raman microspectroscopy using spectral focusing. *Appl. Phys. Lett.* **95**, 081109 (2009).

157. Volkmer, A., Book, L. D. & Xie, X. S. Time-resolved coherent anti-Stokes Raman scattering microscopy: Imaging based on Raman free induction decay. *Appl. Phys. Lett.* **80**, 1505–1507 (2002).

158. Marks, D. L. & Boppart, S. A. Nonlinear Interferometric Vibrational Imaging. *Phys. Rev. Lett.* **92**, 123905 (2004).

159. Kee, T. W., Zhao, H. & Cicerone, M. T. One-laser interferometric broadband coherent anti-Stokes Raman scattering. *Opt. Express* **14**, 3631–3640 (2006).

160. Listenberger, L. L. & Brown, D. A. Fluorescent detection of lipid droplets and associated proteins. in *Current Protocols in Cell Biology* 24.2.1-24.2.11 (2007). doi:10.1002/cpcb.7

161. Schindelin, J. *et al.* Fiji - an Open Source platform for biological image analysis Johannes. *Nat. Methods* **9**, 676–682 (2012).

162. Kim, J. & Park, H. Fast nonnegative matrix factorisation: An active-set-like method and comparisons. *SIAM J. Sci. Comput.* **33**, 3261–3281 (2011).

163. Rinia, H. A., Burger, K. N. J., Bonn, M. & Müller, M. Quantitative label-free imaging of lipid composition and packing of individual cellular lipid droplets using multiplex CARS microscopy. *Biophys. J.* **95**, 4908–4914 (2008).

164. Bonn, M., Müller, M., Rinia, H. A. & Burger, K. N. J. Imaging of chemical and physical state of individual cellular lipid droplets using multiplex CARS microscopy. *J. Raman Spectrosc.* **40**, 763–769 (2009).

165. Bartz, R. *et al.* Lipidomics reveals that adiposomes store ether lipids and mediate phospholipid traffic , . *J. Lipid Res.* **48**, 837–847 (2007).

166. Chen, B.-C., Sung, J., Wu, X. & Lim, S.-H. Chemical imaging and microspectroscopy with spectral focusing coherent anti-Stokes Raman scattering. *J. Biomed. Opt.* **16**, 021112 (2011).

167. Diem, M. *Modern Vibrational Spectroscopy and Micro-Spectroscopy: Theory, Instrumentation and Biomedical Applications*. *Modern Vibrational Spectroscopy and Micro-Spectroscopy: Theory, Instrumentation and Biomedical Applications* (2015). doi:10.1002/9781118824924

168. De Gelder, J., De Gussem, K., Vandenabeele, P. & Moens, L. Reference database of Raman spectra of biological molecules. *J. Raman Spectrosc.* **38**, 1133–1147 (2007).

169. Verma, S. P. & Wallach, D. F. H. Raman spectra of some saturated, unsaturated and deuterated C 18 fatty acids in the HCH-deformation and CH-stretching regions. *Biochim. Biophys. Acta (BBA)/Lipids Lipid Metab.* **486**, 217–227 (1977).

170. Ya, F., Shuang, L. & Da-Peng, X. Raman spectra of oleic acid and linoleic acid. *Guang Pu Xue Yu Guang Pu Fen Xi / Spectrosc. Spectr. Anal.* **33**, 3240–3243 (2013).

171. Czamara, K. *et al.* Raman spectroscopy of lipids: A review. *J. Raman Spectrosc.* **46**, 4–20 (2015).

172. Gachet, D., Billard, F., Sandeau, N. & Rigneault, H. Coherent anti-Stokes Raman scattering (CARS) microscopy imaging at interfaces: evidence of interference effects. *Opt. Express* **15**, 10408 (2007).

173. Henne, W. M., Reese, M. L. & Goodman, J. M. The assembly of lipid droplets and their roles in challenged cells. *EMBO J.* **37**, e98947 (2018).

174. Walther, T. C., Chung, J. & Farese Jr., R. V. Lipid Droplet Biogenesis. *Annu. Rev. Cell Dev. Biol.* **33**, 491–510 (2017).

175. Kohlwein, S. D., Veenhuis, M. & van der Klei, I. J. Lipid droplets and peroxisomes: Key players in cellular lipid homeostasis or a matter of fat-store'em up or burn'em down. *Genetics* **193**, 1–50 (2013).

176. Thiam, A. R., Farese, R. V. & Walther, T. C. The biophysics and cell biology of lipid droplets. *Nat. Rev. Mol. Cell Biol.* **14**, 775–786 (2013).

177. Barbosa, A. D. & Siniossoglou, S. Function of lipid droplet-organelle interactions in lipid homeostasis. *Biochim. Biophys. Acta - Mol. Cell Res.* **1864**, 1459–1468 (2017).

178. Barbosa, A. D. *et al.* Lipid partitioning at the nuclear envelope controls membrane biogenesis. *Mol. Biol. Cell* **26**, 3641–3657 (2015).

179. Hong, H., Yang, Y., Zhang, Y. & Cai, W. Non-Invasive Cell Tracking in Cancer and

Cancer Therapy. *Curr. Top. Med. Chem.* **10**, 1237–1248 (2010).

180. Swirski, F. K. *et al.* A near-infrared cell tracker reagent for multiscopic in vivo imaging and quantification of leukocyte immune responses. *PLoS One* **2**, 1–7 (2007).

181. Foster, A. E. *et al.* In vivo fluorescent optical imaging of cytotoxic T lymphocyte migration using IRDye800CW near-infrared dye. *Appl. Opt.* **47**, 5944–5952 (2008).

182. Guo, Y., Cordes, K. R., Farese, R. V. & Walther, T. C. Lipid droplets at a glance. *J. Cell Sci.* **122**, 749–752 (2009).

183. Carlson, L. A. & Oro, L. The Effect of Nicotinic Acid on the Plasma Free Fatty Acids. *Acta Med. Scand.* **172**, 641–645 (1962).

184. Blondin, D. P. *et al.* Inhibition of Intracellular Triglyceride Lipolysis Suppresses Cold-Induced Brown Adipose Tissue Metabolism and Increases Shivering in Humans. *Cell Metab.* **25**, 438–447 (2017).

185. Hann, M. M. Molecular obesity, potency and other addictions in drug discovery. *Medchemcomm* **2**, 339–443 (2011).

186. Greer, T., Sturm, R. & Li, L. Mass spectrometry imaging for drugs and metabolites. *J. Proteomics* **74**, 2617–2631 (2011).

187. Rubakhin, S. S., Jurchen, J. C., Monroe, E. B. & Sweedler, J. V. Imaging mass spectrometry: Fundamentals and applications to drug discovery. *Drug Discov. Today* **10**, 823–837 (2005).

188. Prideaux, B. & Stoeckli, M. Mass spectrometry imaging for drug distribution studies. *J. Proteomics* **75**, 4999–5013 (2012).

189. Trim, P. J. *et al.* Matrix-assisted laser desorption/ionization-ion mobility separation-mass spectrometry imaging of vinblastine in whole body tissue sections. *Anal. Chem.* **80**, 8628–8634 (2008).

190. Römpp, A. & Spengler, B. Mass spectrometry imaging with high resolution in mass and space. *Histochem. Cell Biol.* **139**, 759–783 (2013).

191. Zavalin, A., Yang, J., Haase, A., Holle, A. & Caprioli, R. Implementation of a gaussian beam laser and aspheric optics for high spatial resolution MALDI imaging MS. *J. Am. Soc. Mass Spectrom.* **25**, 1079–1082 (2014).

192. Passarelli, M. K. *et al.* Single-Cell Analysis: Visualizing Pharmaceutical and Metabolite

Uptake in Cells with Label-Free 3D Mass Spectrometry Imaging. *Anal. Chem.* **87**, 6696–6702 (2015).

193. Newman, C. F. *et al.* Intracellular Drug Uptake - A Comparison of Single Cell Measurements Using ToF-SIMS Imaging and Quantification from Cell Populations with LC/MS/MS. *Anal. Chem.* **89**, 11944–11953 (2017).

194. Wurtman, R. J., Hefti, F. & Melamed, E. Precursor control of neurotransmitter synthesis. *Pharmacol. Rev.* **32**, 315–335 (1981).

195. Sainio, E. L., Pulkki, K. & Young, S. N. L-tryptophan: Biochemical, nutritional and pharmacological aspects. *Amino Acids* **10**, 21–47 (1996).

196. Richard, D. M. *et al.* L-tryptophan: Basic metabolic functions, behavioural research and therapeutic indications. *Int. J. Tryptophan Res.* **2**, 45–60 (2009).

197. Dougherty, D. M. *et al.* Comparison of 50- and 100-g L-tryptophan depletion and loading formulations for altering 5-HT synthesis: Pharmacokinetics, side effects, and mood states. *Psychopharmacology (Berl).* **198**, 431–445 (2008).

198. Palego, L., Betti, L., Rossi, A. & Giannaccini, G. Tryptophan Biochemistry: Structural, Nutritional, Metabolic, and Medical Aspects in Humans. *J. Amino Acids* **2016**, 1–13 (2016).

199. Tretter, L., Patocs, A. & Chinopoulos, C. Succinate, an intermediate in metabolism, signal transduction, ROS, hypoxia, and tumorigenesis. *Biochim. Biophys. Acta - Bioenerg.* **1857**, 1086–1101 (2016).

200. Smith, R. A. J., Porteous, C. M., Gane, A. M. & Murphy, M. P. Delivery of bioactive molecules to mitochondria in vivo. *Proc. Natl. Acad. Sci.* **100**, 5407–5412 (2003).

201. Elkalaf, M., Tuma, P., Weiszenstein, M., Polák, J. & Trnka, J. Mitochondrial Probe Methyltriphenylphosphonium (TPMP) Inhibits the Krebs Cycle Enzyme 2- Oxoglutarate Dehydrogenase. *PLoS One* **11**, 1–16 (2016).

202. Ross, M. F. *et al.* Accumulation of lipophilic dications by mitochondria and cells. *Biochem. J.* **400**, 199–208 (2006).

203. Ross, M. F. *et al.* Rapid and extensive uptake and activation of hydrophobic triphenylphosphonium cations within cells. *Biochem. J.* **411**, 633–645 (2008).

204. Mukhopadhyay, A. & Weiner, H. Delivery of drugs and macromolecules to mitochondria.

Adv. Drug Deliv. Rev. **59**, 729–738 (2007).

205. Kelso, G. F. *et al.* Prevention of mitochondrial oxidative damage using targeted antioxidants. *Ann NY Acad Sci* **959**, 263–274 (2002).

206. Bishop, T., St-Pierre, J. & Brand, M. D. Primary causes of decreased mitochondrial oxygen consumption during metabolic depression in snail cells. *Am. J. Physiol. - Regul. Integr. Comp. Physiol.* **282**, 372–382 (2002).

207. Murphy, M. P. Targeting lipophilic cations to mitochondria. *Biochim. Biophys. Acta - Bioenerg.* **1777**, 1028–1031 (2008).

208. Anderson, B. J. Paracetamol (Acetaminophen): Mechanisms of action. *Paediatr. Anaesth.* **18**, 915–921 (2008).

209. Graham, G. G., Davies, M. J., Day, R. O., Mohamudally, A. & Scott, K. F. The modern pharmacology of paracetamol: Therapeutic actions, mechanism of action, metabolism, toxicity and recent pharmacological findings. *Inflammopharmacology* **21**, 201–232 (2013).

210. Jozwiak-Bebenista, M. & Nowak, J. Z. Paracetamol: Mechanism of action, applications and safety concern. *Acta Pol. Pharm. - Drug Res.* **71**, 11–23 (2014).

211. Feldman, M. & Burton, M. E. Histamine2-Receptor Antagonists - Standard therapy for acid-peptic diseases. *N. Engl. J. Med.* **323**, 1672–1680 (1990).

212. Parsons, M. E. & Ganellin, C. R. Histamine and its receptors. *Br. J. Pharmacol.* **147**, 127–135 (2006).

213. Marty, F. M. & Boeckh, M. Maribavir and human cytomegalovirus-what happened in the clinical trials and why might the drug have failed? *Curr. Opin. Virol.* **1**, 555–562 (2011).

214. Biron, K. K. *et al.* Potent and Selective Inhibition of Human Cytomegalovirus Replication by 1263W94. *Antimicrob. Agents Chemother.* **46**, 2365 (2002).

215. Prichard, M. N. Function of human cytomegalovirus UL97 kinase in viral infection and its inhibition by maribavir. *Rev. Med. Virol.* **19**, 215–229 (2009).

216. Chuang, C. H. & Chen, Y. T. Raman scattering of L-tryptophan enhanced by surface plasmon of silver nanoparticles: Vibrational assignment and structural determination. *J. Raman Spectrosc.* **40**, 150–156 (2009).

217. Suzuki, M. & Shimanouchi, T. Infrared and Raman spectra of succinic acid crystal. *J. Mol.*

Spectrosc. **28**, 394–410 (1968).

218. Pogorzelec-Glaser, K. *et al.* Structure and molecular dynamics of bis-1H-1,2,4-triazole succinic acid complex crystals. *CrystEngComm* **13**, 3698–3709 (2011).

219. Shi, L. *et al.* Optical imaging of metabolic dynamics in animals. *Nat. Commun.* **9**, (2018).

220. Norton, R. S. & Bradbury, J. H. Kinetics of hydrogen-deuterium exchange of tryptophan and tryptophan peptides in deutero-trifluoroacetic acid using proton magnetic resonance spectroscopy. *Mol. Cell. Biochem.* **12**, 103–111 (1976).

221. Marcsisin, S. R. & Engen, J. R. Hydrogen exchange mass spectrometry: what it is and what can it tell is? *Anal. Bioanal. Chem.* **397**, 967–972 (2010).

222. Nguyen Thi, Y., Rademann, K. & Emmerling, F. Direct evidence of polyamorphism in paracetamol. *CrystEngComm* **17**, 8967–9244 (2015).

223. Kolesov, B. A., Mikhailenko, M. A. & Boldyreva, E. V. Dynamics of the intermolecular hydrogen bonds in the polymorphs of paracetamol in relation to crystal packing and conformational transitions: A variable-temperature polarized Raman spectroscopy study. *Phys. Chem. Chem. Phys.* **13**, 14243–14253 (2011).

224. Nanubolu, J. B. & Burley, J. C. Investigating the recrystallization behavior of amorphous paracetamol by variable temperature Raman studies and surface raman mapping. *Mol. Pharm.* **9**, 1544–1558 (2012).

225. Shende, C., Smith, W., Brouillette, C. & Farquharson, S. Drug stability analysis by Raman spectroscopy. *Pharmaceutics* **6**, 651–662 (2014).

226. Manuela Garrido, E., Garrido, J., Calheiros, R., Marques, M. P. M. & Borges, F. Fluoxetine and norfluoxetine revisited: New insights into the electrochemical and spectroscopic properties. *J. Phys. Chem. A* **113**, 9934–9944 (2009).

227. Mathlouthi, M., Seuvre, A. M. & Koenig, J. L. F.T.-I.R. and laser-raman spectra of d-ribose and 2-deoxy-d-erythro-pentose (‘2-deoxy-d-ribose’). *Carbohydr. Res.* **122**, 31–47 (1983).

228. Zhao, Y., Bower, A. J., Graf, B. W., Boppart, M. D. & Boppart, S. A. Imaging and Tracking of Bone Marrow-Derived Immune and Stem Cells. *Methods Mol. Biol.* **1052**, 57–76 (2013).

229. Zhao, Y. *et al.* Longitudinal label-free tracking of cell death dynamics in living engineered

human skin tissue with a multimodal microscope. *Biomed. Opt. Express* **5**, 3699 (2014).

230. Graf, B. W. *et al.* In vivo multimodal microscopy for detecting bone-marrow- derived cell contribution to skin regeneration. *J. Biophotonics* **7**, 96–102 (2014).

231. Li, J. *et al.* Investigating the healing mechanisms of an angiogenesis-promoting topical treatment for diabetic wounds using multimodal microscopy. *J. Biophotonics* **11**, 1–7 (2018).

232. Chen, Z. *et al.* Multicolor live-cell chemical imaging by isotopically edited alkyne vibrational palette. *J. Am. Chem. Soc.* **136**, 8027–8033 (2014).

233. Jardé, T. *et al.* Wnt and Neuregulin1/ErbB signalling extends 3D culture of hormone responsive mammary organoids. *Nat. Commun.* **7**, (2016).

234. Almond, L. M., Hoggard, P. G., Edirisinghe, D., Khoo, S. H. & Back, D. J. Intracellular and plasma pharmacokinetics of efavirenz in HIV-infected individuals. *J. Antimicrob. Chemother.* **56**, 738–744 (2005).

235. Lee, W. A. *et al.* Selective Intracellular Activation of a Novel Prodrug of the Human Immunodeficiency Virus Reverse Transcriptase Inhibitor Tenofovir Leads to Preferential Distribution and Accumulation in Lymphatic Tissue. *Antimicrob. Agents Chemother.* **49**, 1898–1906 (2005).

236. Colletti, L. M. *et al.* Methods to measure the intracellular concentration of unlabeled compounds within cultured cells using liquid chromatography/tandem mass spectrometry. *Anal. Biochem.* **383**, 186–193 (2008).

237. Mateus, A., Matsson, P. & Artursson, P. Rapid measurement of intracellular unbound drug concentrations. *Mol. Pharm.* **10**, 2467–2478 (2013).

238. Gordon, L. J. *et al.* Direct Measurement of Intracellular Compound Concentration by RapidFire Mass Spectrometry Offers Insights into Cell Permeability. *J. Biomol. Screen.* **21**, 156–164 (2016).

DISSEMINATION OF INFORMATION

Parts of this work were presented at the following conferences:

1. **D. Boorman**, I. Pope, F. Masia, W. Langbein, S. Hood, P. Borri and P. Watson. 'Optimising CARS microscopy to detect isotope labelled lipids', *Poster presentation*, EMBL Industry Workshop: Imaging in Pharma R and D, Heidelberg, Germany, 8-10 Feb 2017.

2. **D. Boorman**, I. Pope, W. Langbein, S. Hood, P. Borri and P. Watson. 'Optimisation of multimodal CARS microscopy for detection of isotope-labelled molecules', *Poster presentation*, Bio-Nano-Photonics Symposium, Cardiff, UK, 18-19 Sept 2017.

3. **D. Boorman**, I. Pope, W. Langbein, S. Hood, P. Borri and P. Watson. 'Optimisation of multimodal CARS microscopy for detection of isotope-labelled molecules', *Oral presentation*, Bioimaging Expertise Network Symposium, GlaxoSmithKline, Stevenage, UK, 11-12 June 2018.

4. **D. Boorman**, I. Pope, W. Langbein, S. Hood, P. Borri and P. Watson. 'Optimisation of multimodal CARS microscopy for detection of isotope-labelled molecules', *Poster presentation*, Drug Metabolism Discussion Group/Swedish Academy of Pharmaceutical Sciences Joint Open Meeting, Gothenburg, Sweden, 16-18 Oct 2018.

5. **D. Boorman**, I. Pope, W. Langbein, S. Hood, P. Borri and P. Watson. 'Optimisation of multimodal CARS microscopy for detection of isotope labelled molecules', *Oral presentation*, SPIE Photonics West, San Francisco, California, United States, 2-7 Feb 2019. Paper published in Proceedings of the SPIE 10890, *Label-free Biomedical Imaging and Sensing (LBIS)*, 1089005, 2019.

6. **D. Boorman**, I. Pope, W. Langbein, S. Hood, P. Borri and P. Watson. 'Optimisation of multimodal CARS microscopy for detection of isotope-labelled molecules', *Oral presentation*, Bioimaging Expertise Network Symposium, GlaxoSmithKline, Stevenage, UK, 20-22 May 2019.

APPENDICES

Appendix A

In Chapter 6 of the main body of the thesis, Figure 6.5 showed hyperspectral CARS datasets acquired from cytoplasmic regions of 100 μM D5-Trp-treated HeLa cells over the spectral range, 1900-2200 cm^{-1}. However, the acquired Raman spectra for D5-Trp dissolved in water, as shown in Figure 6.1, suggested positioning of the CD-associated peak at 2300 cm^{-1}, outside of the targeted spectral range. Thus, hyperspectral CARS datasets were reacquired over a larger spectral range, but as these data could not be acquired prior to thesis submission, they are included as an appendix to the main body of the thesis. Spatial and spectral data outputs are shown in Figure A1.

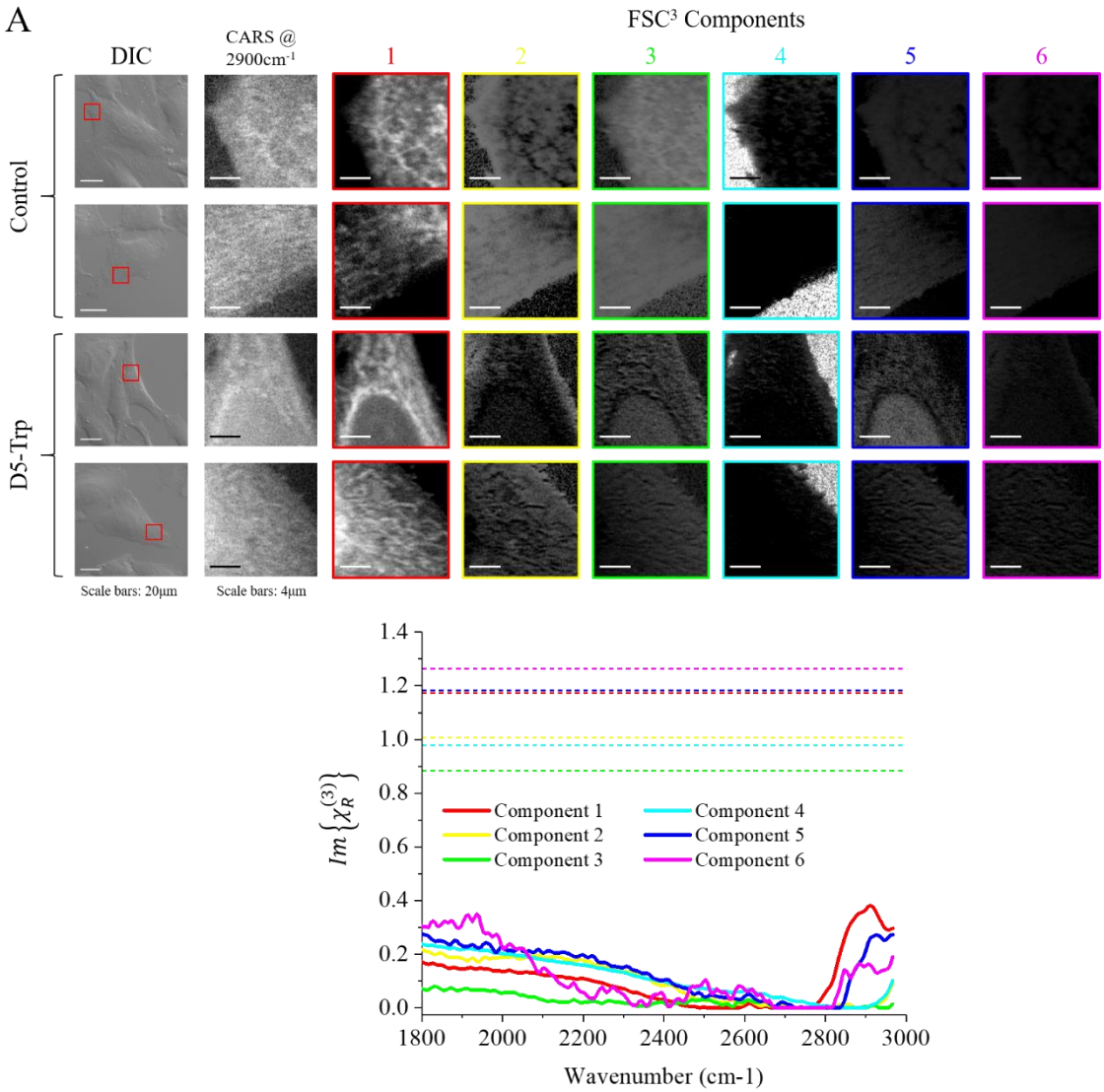

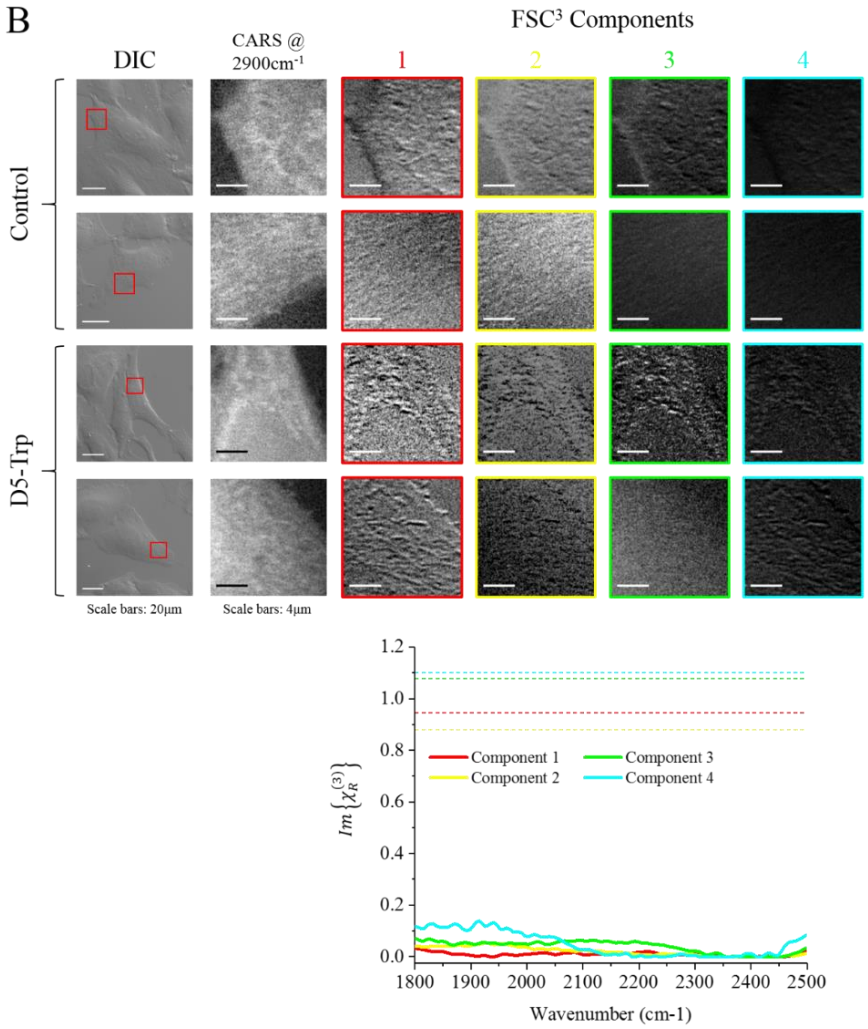

Figure A1 | Spatial and spectral FSC^3 outputs following application to hyperspectral CARS datasets acquired from cytoplasmic regions of HeLa cells exposed to 100 μM D5-Trp or water (vehicle control) for 24 hours. Spectral ranges of 1800-3000 cm^{-1} (A) and 1800-2500 cm^{-1} (B) were utilised, and the spatially resolved images for six (A) and four (B) separate chemical components, along with associated spectra showing the phase-retrieved imaginary part of the normalised CARS susceptibility $Im\left\{\chi_R^{(3)}\right\}$ are displayed. The corresponding real parts are shown as averages, indicated by horizontal dashed lines. DIC was utilised for initial selection of cells, and the single wavenumber CARS image shows cellular structure based on a combined lipid/protein signal. Scale bars show 20 μm in DIC images and 4 μm in CARS images.

Appendix B

In Chapter 6 of the main body of the thesis, Figure 6.14 showed hyperspectral CARS datasets acquired from cytoplasmic regions of 100 μM D4-Para-treated HeLa cells over the spectral range, 1900-2200 cm^{-1}. However, the acquired Raman spectra for pure D4-Para, as shown in Figure 6.5, showed peaks at 2244 cm^{-1}, 2278 cm^{-1} and 2314 cm^{-1}, all of which lay outside of the targeted spectral range. Thus, hyperspectral CARS datasets were reacquired over a larger spectral range and the spatial and spectral outputs are displayed in Figure A2.

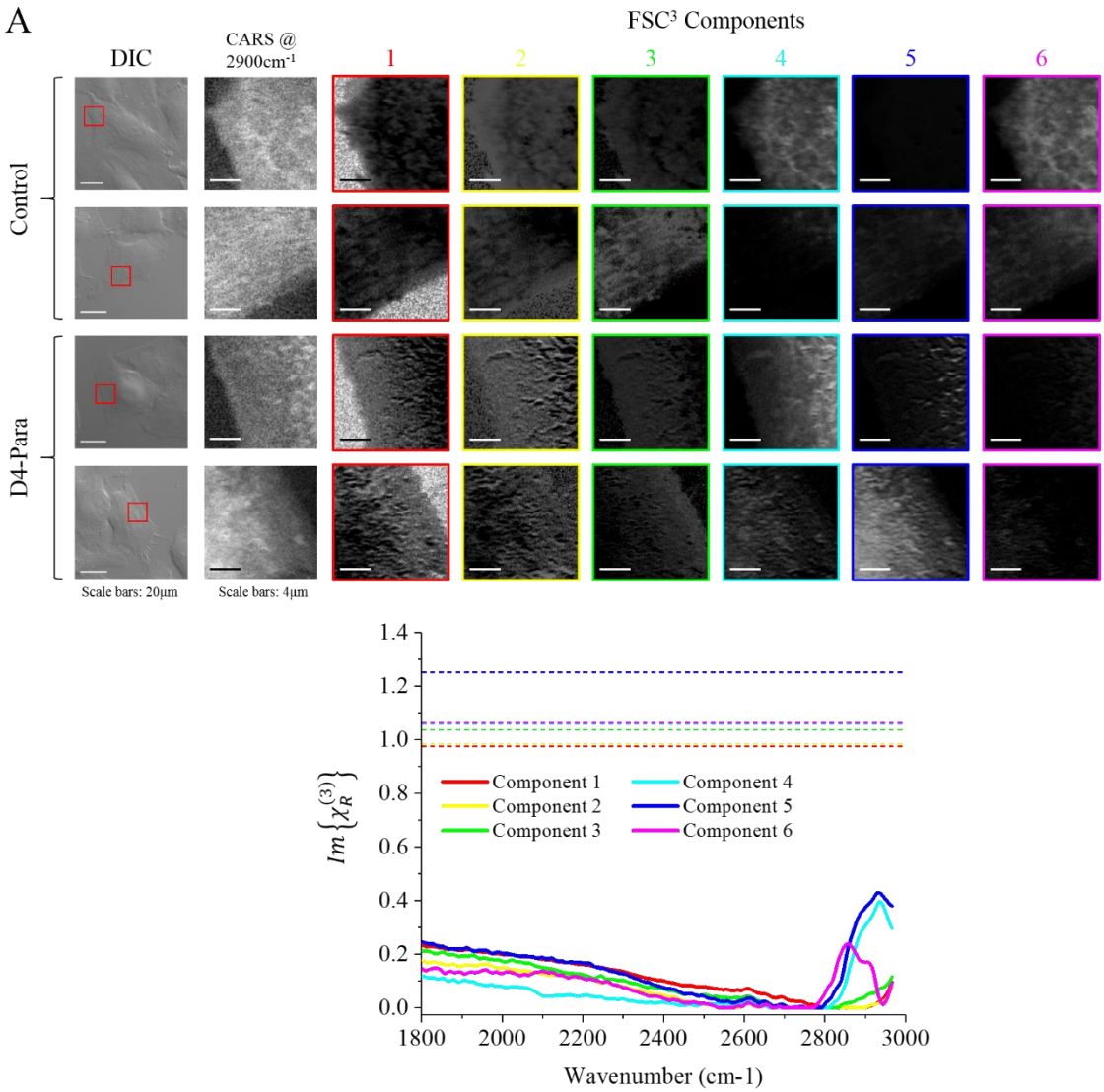

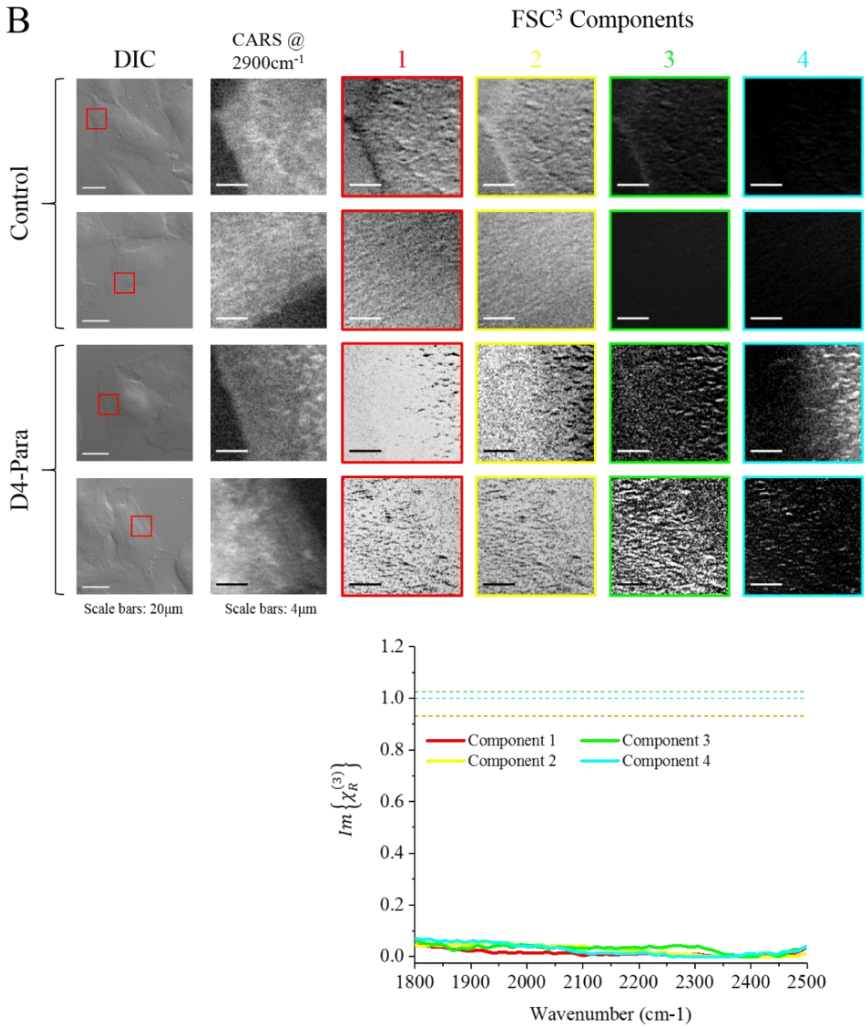

Figure A2 | Spatial and spectral FSC^3 outputs following application to hyperspectral CARS datasets acquired from cytoplasmic regions of HeLa cells exposed to 100 μM D4-Para or a 50:50 water/methanol solution (vehicle control) for 24 hours. Spectral ranges of 1800-3000 cm^{-1} (A) and 1800-2500 cm^{-1} (B) were utilised, and the spatially resolved images for six (A) and four (B) separate chemical components, along with associated spectra showing the phase-retrieved imaginary part of the normalised CARS susceptibility $Im\left\{\chi_R^{(3)}\right\}$ are displayed. The corresponding real parts are shown as averages, indicated by horizontal dashed lines. DIC was utilised for initial selection of cells, and the single wavenumber CARS image shows cellular structure based on a combined lipid/protein signal. Scale bars show 20 μm in DIC images and 4 μm in CARS images.